^{61}Cu/^{67}Cu theranostic pair production, chemical separation and radiolabeling

Inaugural dissertation
of the Faculty of Science,
University of Bern

presented by
Nadia Zandi
From Iran

Supervisor of the doctoral thesis:
Prof. Dr. Andreas Türler
Department of Chemistry, Biochemistry and Pharmaceutical Sciences
(University of Bern)

^{61}Cu/^{67}Cu theranostic pair production, chemical separation and radiolabeling

Inaugural dissertation

of the Faculty of Science,

University of Bern

presented by
Nadia Zandi
From Iran

Supervisor of the doctoral thesis:
Prof. Dr. Andreas Türler
Department of Chemistry, Biochemistry and Pharmaceutical Sciences
(University of Bern)

Accepted by the Faculty of Science.

Bern, 29.10.2021

The Dean
Prof. Dr. Zoltan Balogh

CONTENTS **Pages**

SUMMARY

CHAPTER 1, INTRODUCTION

SUMMARY

Historical relations between physics and medicine accelerated with the discovery of X-ray radiation and shortly thereafter with the discovery of radioactivity in the 19th century. At present, the term medical physics refers to physicists whose work is mainly concerned with medical applications of radiation. One of the most prominent applications of physics and chemistry in the medical field is nuclear medicine. Nuclear medicine can be defined as the medical specialization that uses radionuclides to investigate organ metabolism and to provide diagnosis and therapeutic interventions. The origin of nuclear medicine and radiopharmaceutical chemistry was started with the fundamental research started by George De Hevesy, and the first cyclotron was built by Ernest Orlando Lawrence in 1930. About 95% of the radiopharmaceuticals are employed in nuclear medicine for diagnosis, while the rest are used for therapy. A radiopharmaceutical consists of two components: a radionuclide and a pharmaceutical compound. First, a pharmaceutical compound is chosen that preferentially targets a given receptor or other cellular targets, then an appropriate radionuclide is attached to it for diagnosis or therapy. According to the available data at the International Atomic Energy Agency (IAEA), 134 countries use nuclear medicine facilities and equipment. Due to the rising prevalence of NCDs (Non-Communicable Diseases), the availability of new tracers, and the high demand for early and accurate diagnoses, NCD are expected to be the fastest-growing segment in nuclear medicine. There is an increasing demand for a personalized medicine approach in this era with scientific and technological developments. Several factors have resulted in the growth of personalized medicine, such as advances in molecular biology, a better understanding of processes, and more excellent knowledge of individual diseases' mechanisms.

Theranostics, which is a combination of therapy and diagnosis, has introduced a new chapter in the field of nuclear medicine for providing personalized treatment to the patient. Among the different radioisotopes, Cu offers several radioisotopes potentially appropriate for use in nuclear medicine. One of the most promising pairs is ^{61}Cu/^{67}Cu that could be applied in theranostic applications. However, its optimized production and its availability in large quantity have been among the main challenges in nuclear medicine and constitute our inspiration to start this Ph.D. study.

This thesis was performed in the framework of the Sinergia project “PHOtonuclear Reactions (PHOR): Breakthrough Research in Radionuclides for Theranostics” funded by Swiss National Science Foundation (SNSF). This enterprise is based on a collaboration among the Department of Chemistry, Biochemistry, and Pharmacy (DCBP) and the Laboratory of High Energy Physics (LHEP) of the University of Bern, and the Federal Institute of Metrology (METAS).

This thesis is structured in 5 chapters:

The first chapter introduces and deals with the basics of radiopharmaceutical chemistry and different production methods. In addition, the first chapter presents an introduction of nuclear medicine and its applications in diagnosis and therapy, along with introducing different radionuclide production facilities such as cyclotron, reactor, and electron accelerators. Chapter two focuses on the investigation of ^{61}Cu and ^{67}Cu production through different nuclear reactions and finally production of ^{61}Cu by irradiation of ^{64}Zn using a proton cyclotron at SWAN Isotopen AG at Inselspital Bern and production of ^{67}Cu via irradiations of ^{68}Zn with Bremsstrahlung generated by a 22 MeV Microtron at METAS. Chapter three introduces a novel method based on an evaporation technique for the efficient separation of Cu from the irradiated Zn targets, followed by a liquid chemical separation using extraction chromatography. To achieve this, an automated system (using a Modular-Lab PharmTracer system) was developed and installed in the framework of this thesis. With this automated system, Cu was completely separated and purified from the irradiated Zn targets. Moreover, in chapter three, radiolabeling of Cu with DOTA peptide was investigated. In chapter four, as a part of this study, the production of further potentially suitable radionuclides for medical applications such as ^{167}Tm, ^{165}Er, and ^{135}La were investigated. Chapter five gives a summary of all processes that were considered and employed in this Ph.D. thesis and provides an outlook for further studies in the near future.

CHAPTER 1
INTRODUCTION

1.1 Cancer and cancer therapy

Cancer occurs when cells start dividing in an abnormal and uncontrolled way. This behavior may cause growth, which is called a tumor. Cancerous tumors are malignant and are able to spread into or invade nearby tissues, and, afterward move to other places in the body through the bloodstream or the lymph system. Cancer cells differ from normal cells. One crucial difference is that cancer cells are less specialized than normal cells, whereas normal cells differentiate into very distinct cell types with specific functions. Cancer cells are able to influence the normal cells and blood vessels that surround a tumor—an area known as the microenvironment [1]. There are more than 200 types of cancers known such as lung cancer, brain cancer, blood cancer etc. [2, 3]. Solid tumors can occur in several places, such as bones, muscles and organs. However, blood cancers are completely different from solid cancers. Blood cancers affect the white blood cells whose function is fighting against infections. There are three major types of blood cancer named leukemia, lymphoma, and myeloma. Myeloma cancer is located in the bone marrow and affects plasma cells, which produce antibodies that can attack diseases and infections and thus damage or weaken bone. Myeloma can be treated with radiation therapy or targeted radionuclide therapy. Leukemia, a cancer of the blood cells starts in the bone marrow and spreads through the bloodstream. The bone marrow produces mutated cells, which can spread into the blood, where they crowd out healthy blood cells. This type of blood cancer may need aggressive treatment. Finally, lymphomas affect the cells in the lymphatic system, and then immune cells grow out of control [2].

Different types of cancer treatment such as surgery, external radiation therapy, internal radiation therapy, targeted radionuclide therapy, and chemotherapy depend mainly on the type of cancer and how advanced it is.

Surgery is an invasive procedure in which the tissue will be removed from the body by a surgeon.

Radiation therapy has been used for cancer treatment for more than 100 years (after the discovery of X-rays by Wilhelm Röntgen in 1895). It was found that exposure to them caused living tissue to have an adverse effect upon the duration of exposure. The observation of a burn on the chest of scientists who carried radioactive material in their jackets was exploited to treat

a variety of tumors. Afterward, in 1934, Irene and Pierre Joliot-Curie discovered that they could produce radioactive elements that were not initially radioactive and just can be produced by exposing stable elements to alpha particles or neutrons [4, 5, 6].

Radiation therapy can be categorized into internal and external therapy. Currently, radiation therapy is considered as one of the most widely used treatment modalities, with approximately 50% of patients with localized tumors in developed countries. Ionizing radiations (i.e., X-rays and γ-radiations) are used in radiation therapy to damage cancer cells. Using radiation therapy, many different cellular components such as lipids, proteins, and nucleic acids are damaged [7, 8, 9]. In external radiation therapy, the source of radiation (such as ^{60}Co) is placed outside the body and therefore exposes the entire body to radiation, including both cancerous and normal tissue. The influence of ionizing radiation in external radiation therapy is not only limited to cancer cells but also damages surrounding non-cancerous healthy cells. The side effects rely on the dose and treated area of the body. In external radiation therapy, a high dose of X-rays and γ-radiation is required. The X-rays are generated outside the patient's body via an electron accelerator such as Linear Electron Accelerator called LINAC. External radiation therapy is mainly used for the cancer treatment of the head, neck, lung, and breast [8, 9].

Internal radiation therapy is a treatment in which the radiation source is put in or near the tumor that is able to allow delivering a radiation dose to cancerous cells and, therefore, reduces the damage to surrounding non-cancerous cells. For this purpose, the radiation source is enclosed into a container such as a rod, tube, or needle. Internal radiation therapy is called brachytherapy when implants are put for an extended period of time. Some of the used radionuclides in brachytherapy are ^{192}Ir and ^{103}Pd, which are employed for breast and prostate cancer treatment. It is worth pointing out that internal radiation therapy is used for cancer treatment of the prostate, vagina, uterus, etc. [10, 11, 12, 13].

The method of targeted radionuclide therapy stands for the selective accumulation of radionuclide-containing pharmaceuticals in cancer cells only, to prevent undesirable influencing of normal cells. On this basis, the use of high-affinity molecules as carriers to the cancer cells for the employed radionuclides are the main feature of targeted radionuclide therapy. In this

method, pharmaceuticals are often injected intracavitary or intravenously. After the injection, these drugs enter the bloodstream where they can finally reach the target (which is a target molecule placed on the surface of the tumor cell). The attached radionuclide to the pharmaceutical can directly interact and influence the tumor cell. An advantage of targeted radionuclide therapy is not only the precision of selectively destroying tumor cells but also the patients well-fare. This is due to the relatively fast clearance (however, some radiopharmaceuticals such as antibody-based ones have slow clearance and long half-life, so they are in the bloodstream for extended periods of time [14]) and subsequently affecting the tumor without any additional interventions (within this period of time) [15, 16]. The radionuclide selection in targeted radionuclide therapy is of great importance and requires complying with several requirements, including the radiative decay mode, radionuclide half-life, binding to a wide variety of carrier molecules, large-scale production, ability to be used as theranostic pair application, etc. In targeted radionuclide therapy, β-emitters, α-emitters, and Auger electron emitters are considered to provide the highest therapeutic efficiency due to providing more substantial destruction of biological systems at a given dose called biological effectiveness compared to X-rays and γ-radiation (see Fig. 1.1). Importantly, β-particles, α-particles, and Auger electrons have different ranges in tissue. Alpha and beta particles have a range of, 40–100 μm and 50–12,000 μm, respectively, while Auger/conversion electrons possess a very short range of only 0.002–0.5 μm. The importance of the range stems from the fact that delivery of the radiolabeled compounds carrying a radionuclide with a short-range requires it to be extremely close to or directly in/near the cell nucleus to lead to DNA damage [17, 18, 19]. Accordingly, Auger electron-emitting radionuclides are appropriate only for internalizing, DNA seeking pharmaceuticals.

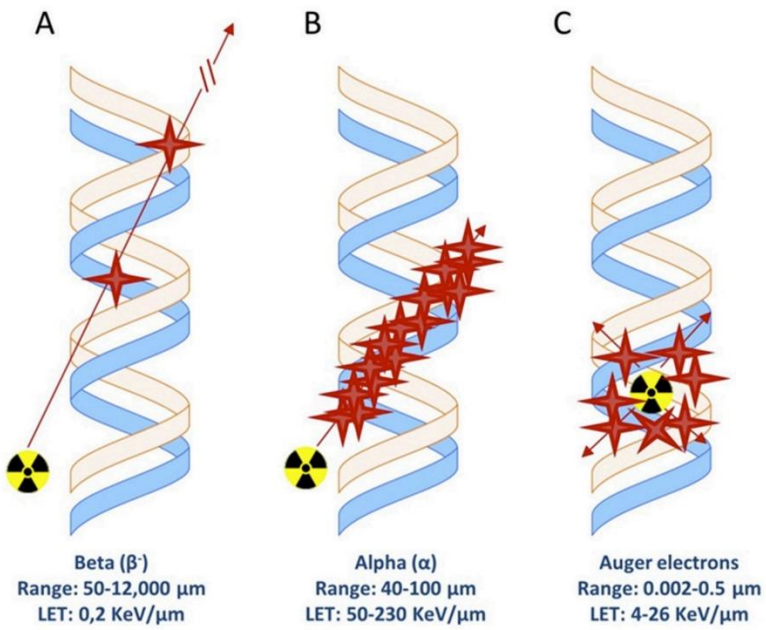

Fig. 1.1 Schematic view of ionization events due to interaction of (A) β-particles, (B) α-particles, and (C) Auger electrons. LET stands for the Linear Energy Transfer and is defined as the average amount of deposited energy per unit path length of an ionizing particle/radiation along its track. The LET of particles is higher than the LET of X-rays and γ. The LET of X-rays and g-radiation increases with increasing atomic number of the absorber. Moreover, the LET decreases by increasing the incident particle/radiation energy. Increasing the LET results in increased biological effectiveness [17, 20].

In targeted radionuclide therapy, the half-life of the radionuclide should be longer (although not much longer) than the time required for the pharmaceutical preparation, to be delivered to the clinic, including injection into the patient, and the time required to localize a tumor. However, it should not be too long due to increased absorbed doses in the cancerous tissue and the undesirable irradiation of surrounding areas. The long half-life of radionuclides and/or a long biological half-life make patients themselves a source of radioactivity and they contaminate clinical facilities such as liquid waste disposal systems. Considering all of these factors, an optimal half-life from six hours to seven days is usually assumed appropriate for isotopes used for radionuclide therapy [4, 15, 21]. The most frequently used radionuclides for targeted

radionuclide therapy are ^{177}Lu, ^{90}Y, and ^{131}I, so that in almost 90% of clinical practice, beta-emitting radionuclides are employed. This is due to their appropriate emission characteristics and cost-effectiveness in production. ^{131}I can be employed in both visualization and therapy and exhibits successful applications for different malignant tumors, including thyroid cancer. One disadvantage of ^{131}I-tyrosine is the release of free ^{131}I to the blood stream of patients. Moreover, γ-radiation emitted by ^{131}I can pose radiation hazards for the healthcare personnel and patient family members. ^{90}Y is an alternative to ^{131}I because it is a pure beta-minus emitter and its ionizing radiation is mostly limited to the patient's organism and, therefore, has a lower radiation hazard compared to ^{131}I. ^{90}Y has a shorter half-life, higher energy of β-particles, and higher retention in cancerous cells compared to ^{131}I. Over the last decade, the use of ^{177}Lu for targeted radionuclide therapy has attracted considerable attention due to its advantage in lower beta-minus energy and an equally or even better complex formation constant with the DOTA chelator [15, 10, 22, 23, 24]. ^{67}Cu is an ideal radionuclide for targeted radionuclide therapy, considering the ability to pair with ^{61}Cu and ^{64}Cu as a theranostic application. However, ^{67}Cu has not entered into clinical use yet due to large-scale production difficulties [25, 26, 27, 28, 29].

The application of α-emitting radionuclides in targeted radionuclide therapy has been investigated and attracted great attention due to their high relative biological effectiveness and higher Linear Energy Transfer (LET) compared to β-emitting radionuclides. ^{211}At, ^{225}Ac, ^{223}Ra, and ^{227}Th are among the best candidates for α-emitters. Some of the associated problems with the application of α-emitting radionuclides in targeted radionuclide therapy are presence of daughter products with a long half-life that causing patient isolation (e.g., β-emitter ^{207}Bi as the daughter product ^{211}At) and the potential tendency of them to self-radiolysis and partial drug destruction because of their radioactivity [15, 23, 30, 26, 31].

Chemotherapy was introduced for the chemical treatment of diseases by Paul Ehrlich, who received the Nobel Prize for Medicine in 1908. Up to now, more than a hundred different chemical drugs have been approved for cancer treatment. These drugs affect cells at different phases of the cell cycle. Most chemotherapeutic drugs are cell cycle-specific, and act on cells undergoing division, and are most effective in the case of high growth fraction malignancies (e.g., hematologic cancers). The capability to kill cells using chemotherapeutic drugs exhibits a dose-

related plateau and therefore is not increasing with further increased dosage [9, 32, 33]. This is due to the fact that at a certain time point, only a subset of cells is fully drug-sensitive [9, 32, 33]. However, cell cycle non-specific drugs exhibit a linear dose-response curve and are shown to be effective for both cases of low and high growth fraction tumors [9, 32, 33, 34, 35].

1.2 Nuclear medicine

Nuclear medicine is an area of medicine in which small amounts of radioactive materials or radiopharmaceuticals are used in the diagnosis and treatment of disease. Nuclear medicine comprises two applications; clinical diagnostics and radionuclide therapy. In diagnostic nuclear medicine, radiographers use equipment such as Single Photon Emission Computed Tomography (SPECT) or Positron Emission Tomography (PET) to produce images to makes cancerous tissues visible. However, in radionuclide therapy, the specialist person uses radiation to treat cancer and tissue defects [10, 21].

in 1899, in Stockholm, Thor Stenbeck started the treatment of a 49-year-old woman's basal-cell carcinoma of the skin of the nose and delivered more than 100 treatments in 9 months. Also, at the same time, Tage Sjörgen started curing a squamous cell epithelioma with fifty treatments for 30 months. Then after, in 1907, Louis Wickham and Paul Desgrais, treated a child with erectile angioma using beta therapy delivered by applying an external source of ^{226}Ra (see Fig. 1.2) [36].

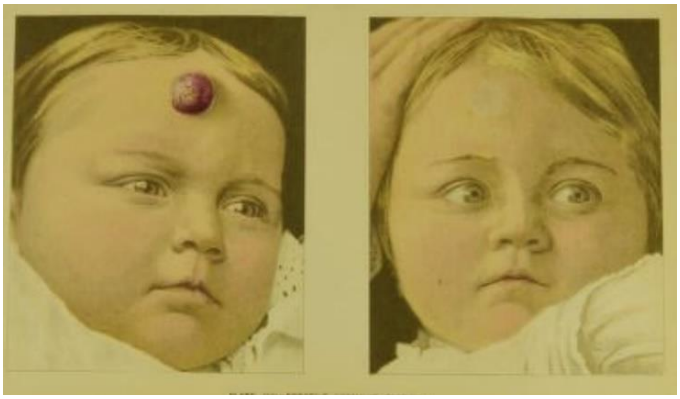

Fig. 1.2 Child with an erectile angioma cured with repetitive irradiations with ^{226}Ra in 1907 [36]

As reviewing the nuclear medicine history, in 1943, George de Hevesy received the Nobel prize for the invention of the radiotracer technology. In radiotracer technology, a radiotracer is a chemical compound in which one or more atoms have been replaced by an appropriate radionuclide (e.g., ^{14}C, ^{32}P) and is used to explore the mechanism of chemical reactions by tracing the radionuclide [37]. In studying the metabolic processes of plants and animals, radiotracer technology is an important process in the industry [38]. It is usually used to diagnose specific causes of inefficiency in a process operation and investigate processes related transport of sediments where a cost-benefit ratio can be obtained from process optimization [38].

In 1948, Seidlin reported success in treating a patient with thyroid cancer with ^{131}I, a beta-minus emitter. In this study, doses from 500 to 2000 mCi of ^{131}I were administered orally to patients on non-restricted diets and thereafter, urine was collected and studied for radioactive iodine content. Forty-eight hours after the dose was administrated, invivo readings were performed with a Geiger-Mueller counter to measure the degree of localization of ^{131}I in the thyroid gland and the metastases. However, the cases that listed as negative results are those in which it was not possible to demonstrate such a concentration of ^{131}I [39, 40].

By the 1950s, the clinical use of nuclear medicine spread as researchers globally increased their knowledge of detecting radioactivity and using radionuclides to monitor the processes. Later, the Society of Nuclear Medicine was officially formed in 1954 in Spokane, Washington, USA, and in 1960 they launched the Journal of Nuclear Medicine for the first time, which became the most well-known journal associated with this field [41, 42].

1.2.1 Imaging modalities

1.2.1.1 SPECT

Single Photon Emission Computed Tomography (SPECT) is a tomographic medical imaging technique using gamma rays and is able to provide 3D information. The SPECT technique needs delivery of gamma-emitting radionuclides (such as ^{99m}Tc and ^{123}I) into the bloodstream. The radionuclide is attached to a specific ligand to create a radioligand (that is described in the radiopharmaceutical section), and the combination of radiopharmaceuticals is carried and bound

to a place of interest in the body. A nuclear de-excitation event occurs, and the excited nucleus decays into a more stable form and releases a γ-ray photon. These photons traverse the patient's tissues and interact with the electrons of atoms in the tissue through Compton scattering or photoelectric absorption*. Once the gamma-ray photon exits the patient's body, it interacts with a collimator (which consists of a high density and high atomic number element like tungsten or lead that leads photons to enter the detector under a defined angle). Photons that can succeed in passing the collimator are those that have the appropriate angle of incidence for optimum image resolution. The detector consists of a scintillation crystal (such as NaI (Tl) crystal) coupled with photomultiplier tubes (PMT) (see Fig. 1.3). Once a scintillation crystal absorbs photons, it emits visible light. This visible light then interacts with a PMT, which generates an amplified electronic signal through the photoelectric effect. Multiple-detector-based SPECT systems surrounding the patient are to provide higher detection efficiency [43, 44].

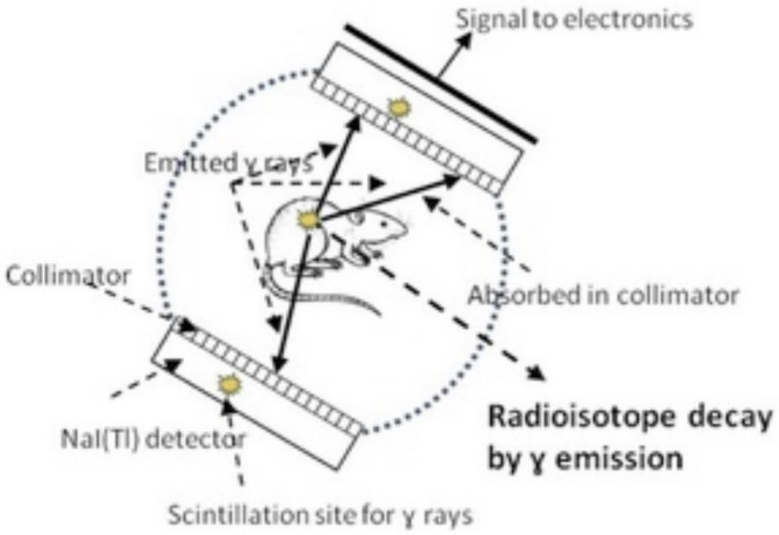

Fig. 1.3 Schematic view of SPECT [45]

* Compton scattering refers to the inelastic scattering of photons from a free (or a loosely bound) electron. Photoelectric absorption refers to a process when a photon interacts with a tightly bound orbital electron (inner shell electron in an atom), then through this process, electron can be ejected from the atom and referred to as photoelectron.

1.2.1.2 PET

Positron Emission Tomography (PET) imaging is a functional imaging technique that uses radioactive substances to reveal the metabolic function of tissues and organs. In PET imaging, a positron emitting radioactive tracer is injected into the body, and the two annihilation photons that are produced back-to-back after positron annihilation are detected by a large number of detectors (see fig. 1.4) operated in coincidence mode. Measured pulses are reconstructed into either 2D slice images or 3D representations. Since PET can detect tissue metabolism (similar to SPECT, in the case of gamma emitting radionuclides), it can provide molecular-level information much earlier than any anatomic changes are visible. Dynamic Whole-Body (DWB) PET can demonstrate organ function. DWB PET is performed within reasonable clinical imaging times and enables a generation of multiple PET images [46]. In comparison between PET and SPECT, image quality is the most common comparison point. Based on previous studies, SPECT resolution is at about 10 mm, and SPECT cannot provide a quantifiable estimate of the blood flow while PET provides high resolution (about 2.5 mm) and dynamic PET provide quantitative estimates of blood flow and how tissue is actually behaving [47, 48].

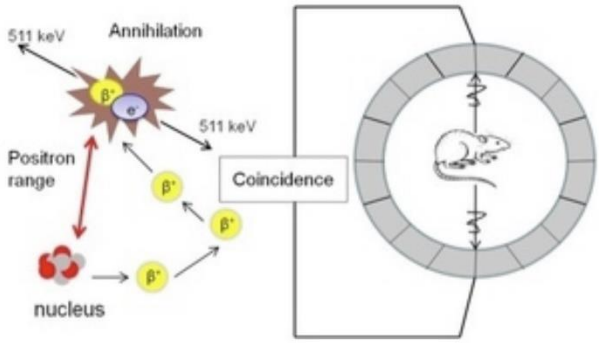

Fig. 1.4 Schematic view of PET [45]

1.2.1.3 Magnetic resonance imaging (MRI)

MRI is a medical imaging method that uses strong magnetic fields and radio waves to form pictures of the anatomy of the body (see Fig. 1.5). Hydrogen nuclei that are in tissues consist of a proton which is very sensitive to magnetic fields. The MRI scanner produces a radiofrequency current that creates a magnetic field. Then, the protons (in the tissue) absorb the energy from the magnetic field, are deflected, and jump to a higher energy state. When the magnetic field of the MRI scanner is turned off, the protons return to their normal spin, and the return process produces a radio signal that is measured by receivers in the scanner [49]. Protons in different types of tissues return to their normal spins at different rates, so regarding that, the scanner can distinguish among different types of tissue.

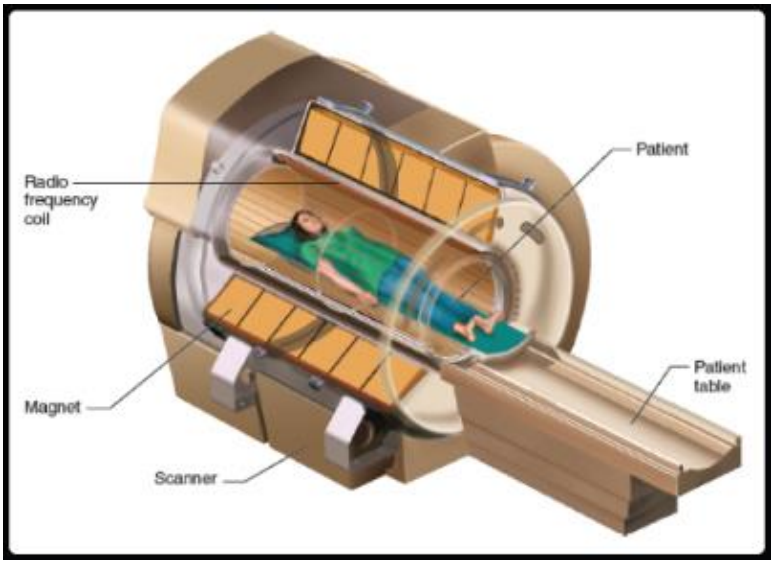

Fig. 1.5 Schematic view of MRI [50]

1.2.1.4 SPECT/CT, SPECT/MRI

SPECT can be combined with other modalities (CT and MRI) to provide precise information. This technology allows the combination of the exquisite anatomic details provided by CT with the functional and physiologic information provided by SPECT. Hybrid imaging technology (refers to the fusion of two or more imaging modalities to form a new technique) has the potential of providing an image with increased specificity and localization, thus providing more accurate diagnosis [51]. The original motivation to produce a combined SPECT/CT system was raised to provide improved anatomical localization of the SPECT radiopharmaceutical and to improve the capability of the SPECT system to provide images with correction for the photon scattering and attenuation that lead to degradation of the image. In other words, the CT data are used to correct tissue attenuation in the SPECT imaging [52, 53]. In the SPECT/CT system, the CT and SPECT scanners are positioned (see Fig. 1.6 a) so that the patient is enabled to be moved directly from the CT scanner to the SPECT scanner by an extension of the CT table.

Fig. 1.6 (a) Schematic of a SPECT/CT system. Position of the SPECT scanner adjacent to the multi–detector row CT scanner (MDCT), (b) Schematic of a SPECT/MRI system. [54, 55]

SPECT can also be combined with MRI to provide precise information (see Fig. 1.6 b). However, the implementation of a combined SPECT/MRI system has not yet happened in clinical practice due to the incompatibility between SPECT components (like PMT tube) and magnetic field in MRI. Recent developments include using silicon photomultipliers (SiPM) and new detector technologies like semiconductors (which have immunity to intense magnetic fields) to solve the problem of incompatibility [56, 57].

1.2.1.5 PET/CT, PET/MRI

PET can be combined with other modalities (CT and MRI) to acquire sequential images from both devices in the same session, which then are combined into a single image (see Fig. 1.7). In the case of PET/CT, the functional imaging obtained by PET is more precisely aligned or correlated with anatomic imaging obtained by CT. PET/CT system has revolutionized medical imaging by adding precision of anatomic localization to functional imaging, which is a lack in pure PET imaging.

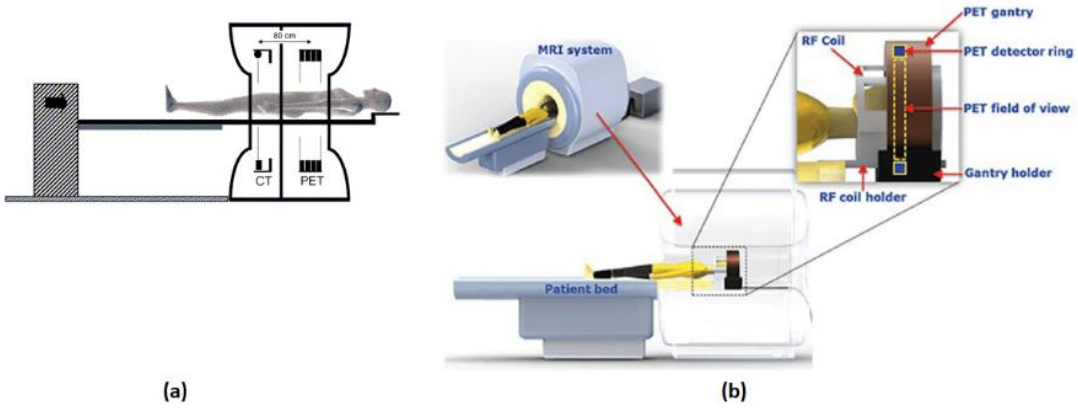

Fig.1.7 (a) Schematic of PET/CT system. CT is positioned in front of a PET scanner, and centers of imaging fields are separated by 80 cm (b) Schematic of PET/MRI system [58, 55].

In the case of a PET/MRI system, combined PET and MRI is an emerging technology that aims to capitalize the advantages of MRI, including increased soft tissue contrast and lack of ionizing radiation exposure. However, PET-MRI systems are more costly than PET/CT systems due to the inherent costs of MRI compared to CT technology [59]. Both PET/CT and PET/MRI have some strengths and limitations. As an example, PET/CT are more available compared with PET/MRI; however, PET/MRI delivers better contrast for functional-imaging capabilities [59, 60].

1.2.2 Suitable radionuclides for SPECT

Radionuclides used for SPECT emit low energy γ-rays. Gamma emission occurs when a nuclide, which is in an excited state, decays to the ground state with the emission of a quantum of high-energy electromagnetic radiation (gamma-ray). In this case, there is no change in the mass number or atomic number during the emission of a gamma-ray (see Eq. 1.1).

$$ {}^{A}_{Z}PExcited\ state^{*} \rightarrow {}^{A}_{Z}Ground\ state + {}^{0}_{0}\Upsilon. \qquad \text{Eq. 1.1} $$

In the SPECT process, first, a tracer is injected into the bloodstream, and then the tracer emits gamma rays (see more details in SPECT section) [61].

Examples of commonly used radionuclides for imaging are ^{99m}Tc and ^{123}I. After injection or administered orally, the concentration of radionuclides in tumors and organs can be made visible with a SPECT system by detection of the emitted gamma (as discussed above).

^{99m}Tc with a half-life of about 6 hours is the most widely used radionuclide in diagnosis, which decays to ^{99}Tc through a gamma emission of 141 keV [62, 63]. There are two common ways for the production of ^{99m}Tc via nuclear reactor and a cyclotron. A large majority of ^{99m}Tc is produced in nuclear reactors. More precisely, ^{99}Mo is produced in a nuclear reactor with thermal neutron bombardment of enriched uranium targets or through neutron activation of ^{98}Mo [64]. Then ^{99}Mo (with a half-life of 67 hours) decays by emitting a beta particle to ^{99m}Tc. The ^{99}Mo/^{99m}T generator system is based on the principle that the shorter-lived radioactive daughter nuclide (^{99m}Tc) can be easily and repeatedly isolated from ^{99}Mo [64]. However, a Coordinated Research Project (CRP) on Accelerator-based production of ^{99}Mo/^{99m}Tc as an alternative to Non-HEU Production was initiated. There are different potential methods for the production of ^{99m}Tc from accelerators. The direct production of ^{99m}Tc through ^{100}Mo(p,2n)^{99m}Tc reaction using accelerators is one of the proposed alternatives. Usable quantities of ^{99m}Tc are produced through the ^{100}Mo(p,2n)^{99m}Tc reaction, which has a peak in the cross-section at 15–16 MeV. Using this reaction, 350 GBq (>9 Ci) of ^{99m}Tc, is produced (using 18 MeV protons, 250μA, 6 h irradiation), which could supply a large metropolitan area [65].

^{123}I with a half-life of 13.2 hours decays 100% by electron capture to ^{123}Te and emits gamma radiation with predominant energy of 159 keV. ^{123}I can be produced through different reactions (such as ^{124}Te(p, 2n)^{123}I, ^{123}Te(p, n)^{123}I, ^{122}Te(d, n)^{123}I and ^{124}Xe(p, pn)^{123}Xe: ^{123}I) [66]; however, the most common reaction for the production of ^{123}I is ^{124}Te(p, 2n)^{123}I reaction on highly enriched ^{124}Te with the useful proton energy range of 26-20 MeV. The reason for a highly enriched ^{124}Te target is due to the production of ^{124}I contamination through ^{125}Te(p, 2n)^{124}I reaction [66]. In the production of radiopharmaceuticals, the specific radioactivity (A_s, which is defined as the radioactivity per mass of a labeled compound) must be assessed. However, conventionally radioactivity per mol is termed as specific radioactivity. The maximum specific activity of ^{123}I of biological interest is 237 Ci/μmol [67].

1.2.3 Suitable radionuclides for PET

β^+ emitting radionuclides refer to those nuclides which are located on the neutron deficient side of the line of beta stability (see Fig. 1.8), and the energy difference between the initial state and final state must be more than 1.022 MeV [68]. A beta-plus particle is named a positron, which is the antimatter of an electron. The difference in atomic and mass number of parent and its daughter results in a neutron, a positron, and a neutrino production (See Eq. 1.2 & Fig. 1.9). The positron then scatters off other electrons before its kinetic energy is low enough to annihilate with an electron and send off two 511 keV photons under 180 degrees (See Fig. 1.10). The location of the annihilation reaction is not the same as where the beta-plus emitting nuclide decayed. The higher the positron energy, the further away the positron travels before annihilation, which causes lower imaging resolution and less accuracy in tumor position determination.

$$ {}^{A}_{Z}Parent \rightarrow {}^{A}_{Z-1}Daughter + e^{+} + \nu + Energy. \qquad \text{Eq. 1.2} $$

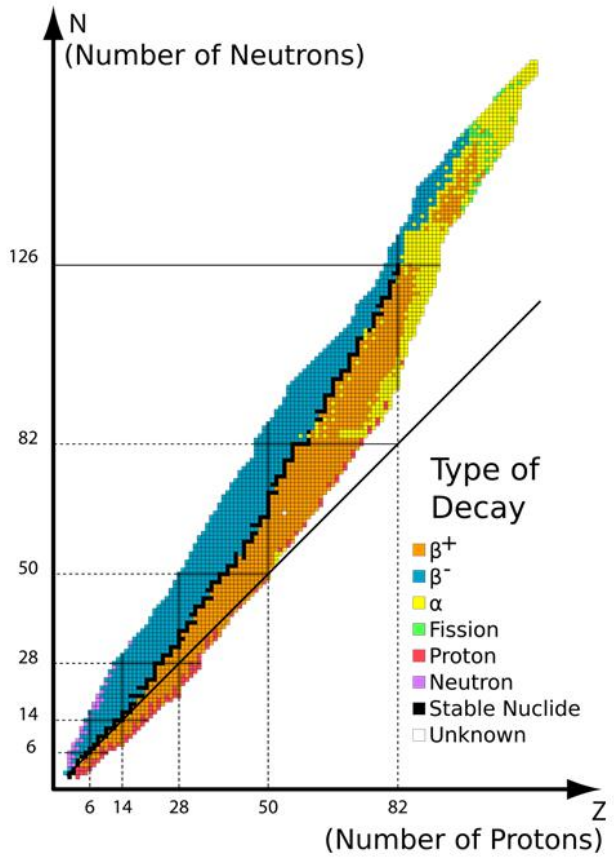

Fig. 1.8 Graph of nuclides (isotopes) by type of decay [69]

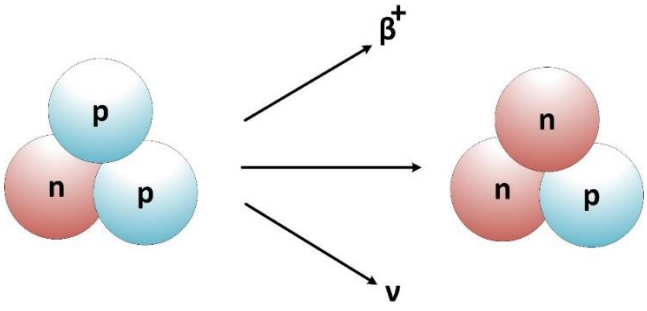

Fig. 1.9 β^+ decay scheme

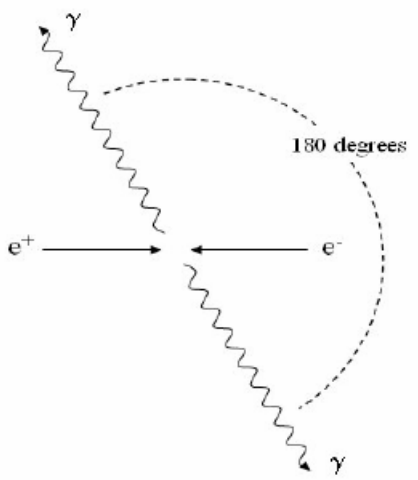

Fig. 1.10 Electron-positron annihilation scheme [70]

Radionuclides used in PET imaging are mostly nuclides with short half-lives (see Table 1.1). These radionuclides are incorporated into compounds or into molecules that bind to receptors of the cancer cells (for more details, see radiopharmaceutical section). The most common radionuclides for PET imaging are ^{18}F, ^{11}C, ^{15}O, ^{13}N, ^{124}I, and ^{68}Ga. ^{18}F (with a half-life of 109 min) is the most commonly used radiotracer in clinical PET imaging for labeling an FDG molecule. This ^{18}F-FDG radiotracer is used mostly in scans for oncology and neurology and makes up the large majority of the radiotracers (>95%) used in PET imaging [71]. This is mainly due to the short half-life of ^{18}F, which is preferred for imaging, and lack of additional gamma emission (which causes better resolution). ^{18}F is produced through proton irradiation of water enriched in the ^{18}O isotope by a cyclotron. Two important factors that have an effect on the production yield of ^{18}F are the proton beam energy and the beam current being used. One can expect approximately 167 GBq of ^{18}F during one hour of irradiation with a 14–19 MeV proton beam at a beam current of 50 μA [72].

^{11}C with a half-life of 20 min is a suitable radionuclide for PET imaging. While there are several routes for producing ^{11}C, the ^{14}N(p,α)^{11}C reaction using nitrogen gas can be considered as an important reaction in the context of routine production and use in biomedical research. Regarding the experimental data, the expected activity for one hour of irradiation with a 4–17 MeV proton beam at a beam current of 50 μA is 405 GBq [66, 73].

^{15}O with a half-life of 2 min is another radionuclide that can be used for PET imaging. There are several routes for the production of ^{15}O via a PET cyclotron such as $^{15}N(p,n)^{15}O$ (with a proton energy range of 4-10) and $^{12}C(\alpha,n)^{15}O$ (with an alpha energy range of 12-30). Regarding the previously published studies, the production yield via the $^{15}N(p,n)^{15}O$ reaction was 2976MBq with a beam intensity of 40 μA [74].

^{68}Ga with a half-life of 68 min is an interesting radionuclide for PET imaging. ^{68}Ga mostly is obtained via a $^{68}Ge/^{68}Ga$ generator or through the $^{68}Zn(p,n)^{68}Ga$ reaction. In a $^{68}Ge/^{68}Ga$ generator, the long-lived parent ^{68}Ge (with a half-life of 271 d) is usually obtained by a proton cyclotron through the $^{69}Ga(p,2n)^{68}Ge$ reaction or though the $^{66}Zn(\alpha, 2n)\ ^{68}Ge$ reaction. Regarding the previous experimental data, $^{68}Zn(p,n)^{68}Ga$ nuclear reaction resulted in the highest radioactivity of up to 1445 MBq/μAh compared to other production routes [75, 76].

Table 1.1 Decay characteristics for some PET radionuclides [77]

Radionuclides	Half-Life	$E\beta^{+}_{av}$ [keV]	Branching ratio* ($I_{\beta+}$)
^{15}O	2 min	735	100
^{13}N	10 min	491	100
^{11}C	20 min	385	100
^{18}F	110 min	242	100
^{68}Ga	1.1 h	740	88
^{61}Cu	3.3 h	309	51
^{43}Sc	3.8 h	419	70
^{44}Sc	4 h	596	94.3
^{64}Cu	12.7 h	124	17.4
^{86}Y	14.7 h	217	11
^{152}Tb	17.5 h	210	6
^{124}I	4.1 d	192	11

*Branching Ratio (BR) is the ratio of the number of particles that decay via a specific decay mode with respect to the total number of particles that decay via all decay modes [78].

1.3 Radiopharmaceuticals

Radiolabeled molecules, called “radiopharmaceuticals,” are considered an essential element in nuclear medicine [79, 80]. A radiopharmaceutical comprises two components, including a radionuclide and a pharmaceutical. The characteristics of these two components determine the usefulness of a radiopharmaceutical. For diagnostic purposes the radionuclide of choice needs to be easily detected by radiation detectors and result in minimal radiation dose to the patient. Ideally, the pharmaceutical of choice should be safe and non-toxic for the human body [81].

In detail, the metallic-based radiopharmaceutical is a metallic radionuclide that has been combined with a chelator which is a small molecule that can form very stable complexes with radionuclides. However, non-metallic radionuclides (e.g., ^{15}O, ^{18}F, and ^{11}C) allow radiolabeling without the help of chelators [82]. There are two main requirements for the chelator choice. First, the chelator must form stable complexes with the radionuclide that are stable in human serum. Second, it must be possible to react the chelator with biomolecules (that deliver the radionuclide to the organ of interest) without affecting its chelating properties [83].

Most chelators (e.g., dodecane tetraacetic acid; DOTA) are simple molecules that are easily manufactured. These chelators can be chemically linked to a variety of tumor seeking peptides such as the Prostate-Specific Membrane Antigen (PSMA). Bifunctional Chelating Agents (BFCAs) are employed to stabilize the link between the radionuclide complex and the carrier moiety of the radiopharmaceutical [84]. There are several BFCAs that are used as a cross-linker between the carrier and the radionuclide. [85]. In Fig. 1.11, a schematic view of a standard four-component radiopharmaceutical consisting of a radionuclide complexed by a bifunctional chelator that connects this entity via a linker to a bioconjugate is shown in details.

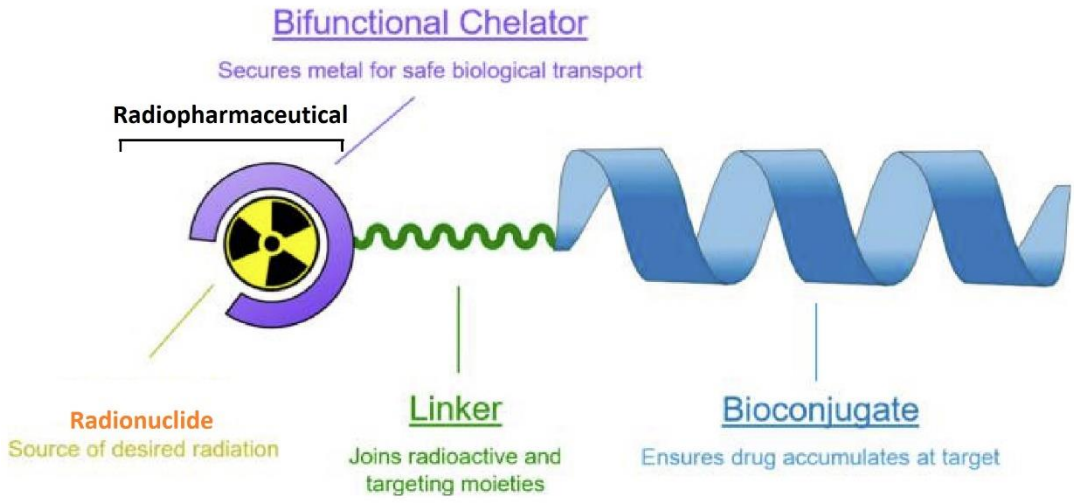

Fig. 1.11 Schematic view of a four-component radiopharmaceutical compound [86]

Receptors are macromolecular structures composed of proteins on the cell surface that can receive and transduce signals. These signals carry chemical messengers which are able to bind to

a receptor and eventually lead to some form of cellular or tissue response. It is worth pointing out that the retention of the receptor radiopharmaceutical is because of their binding to receptor sites. As can be seen in Fig.1.12, the radiopharmaceutical is fixed to the cancer cells through interaction with specific receptors, which are found on the cell surface. The binding affinity between the ligand and receptor is of great importance in determining the extent of accumulation of radioactivity to tumor cells. High binding affinity to non-receptors or other receptors can cause a high background radioactivity in imaging [87].

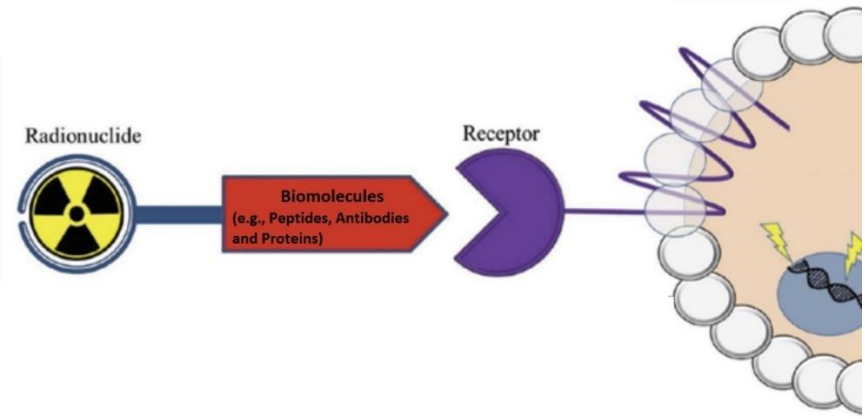

Fig. 1.12 Schematic representation of accumulation of radionuclides to cancer cells through binding with specific receptors [88]

1.3.1 Labeled peptides and antibodies

A peptide is a short string of amino acids (mostly comprising two to some tens of amino acids) that is employed to target specific receptors expressed by the tumor cell [89]. The peptide can be labeled with an appropriate radionuclide to localize the radionuclide in the cancer cells. As can be seen in Fig. 1.13, the radionuclide attaches to the chelator and then the compound will be connected to a peptide using a linker. The first radiolabeled peptide (^{111}In-pentetreotide, ^{111}In-DTPA-octreotide, OctreoScan) was used in the diagnosis of neuroendocrine tumors and approved by the US Food and Drug Administration (FDA) [90]. Radiolabeled peptides are various in terms of therapeutic or diagnostic applications. The majority of these radiolabeled peptides

are used in oncology, where they can be used in diagnostic imaging and therapy by changing the radionuclide. Radiolabeled peptides are also being used in cardiac imaging and neurology [90].

Peptides are easier absorbed in the body compared to proteins. This is due to the fact that peptides are smaller and more broken down compared to proteins. Peptides can be categorized based on their application and localization in the body such as Edotreotide ($C_{65}H_{92}N_{14}O_{18}S_2$) or DOTATOC which mimics natural somatostatin pharmacologically, or the prostate-specific membrane antigen (PSMA), a transmembrane protein expressed in all types of prostatic tissue. Fig. 1.14 shows a schematic structure of DOTATOC and PSMA [91, 92]. A pharmacokinetic modifying (PKM) linker (Fig. 1.13) is used to modify the radiotracer's pharmacokinetics and improve the excretion kinetics of radiolabeled biomolecules [93, 94].

An antibody is a large Y-shaped protein employed by the immune system, which its function is to neutralize foreign objects, such as viruses and bacteria. Human antibodies are categorized into five isotypes (IgM, IgD, IgG, IgA, and IgE) that provide each isotype with distinct characteristics and functions. IgG, which constitutes 70-75% of human antibodies, is the most abundant antibody isotype in the blood (plasma). IgM mostly circulates in the blood and comprises about 10% of human antibodies. IgA (accounting for 10-15% of human antibodies) is abundant in saliva, breast milk, serum, and intestinal fluid. IgE (with no more than 0.001% of human antibodies) and IgD (with less than 1% of human antibodies) have functions in protecting against parasites and involvement in the induction process of antibody production in white blood cells of the lymphocyte.

Antibodies have mainly three functions; 1) Antibodies are inside the bloodstream and mucosa and bind to foreign substances such as pathogens and toxins and inactivate them. 2) Antibodies have functions in destroying bacterial cells by punching holes in the cell wall. 3) Antibodies facilitate phagocytosis of foreign substances by using phagocytic cells. Phagocytosis is a process in which a cell takes in bacteria, dead host cells, parasites, or cellular and foreign debris. Phagocytosis occurs after the foreign body (for example, a bacterial cell), has bound to receptors that exist on the surface of the phagocyte [95].

Radiolabeled antibodies were studied for the first time in the case of tumor detection by single-photon imaging. It was shown that radiolabeled antibodies could be effective in the treatment of lymphoma. Many monoclonal antibodies could be used to treat cancer. Monoclonal antibodies (mAb) are made by cloning (a process of generating a genetically identical copy of a cell or an organism) of 1 cell (white blood cell) [96, 97]. Monoclonal antibodies are an identical population of antibodies that bind to a single epitope of the antigen [96]. Some monoclonal antibodies are also used in immunotherapy because they can help turn the immune system against cancer. For example, some monoclonal antibodies help the immune system to better recognize and destroy cancer cells by marking them. Other monoclonal antibodies helping the immune cells kill the cancer cells by bringing T cells close to cancer cells. T cells are one of the most important type of white blood cells of the immune system and have a crucial role in the adaptive immune response. Radiolabeled antibodies used in minimal (or even small-size) metastatic disease have presented promising clinical efficacy while in solid tumors that are less accessible to large molecules (such as antibodies), clinical efficacy is limited [98]. As shown in Fig. 1.15, the concept of radiolabeling of antibodies and peptides is similar and consists of chelator, linker and radionuclide.

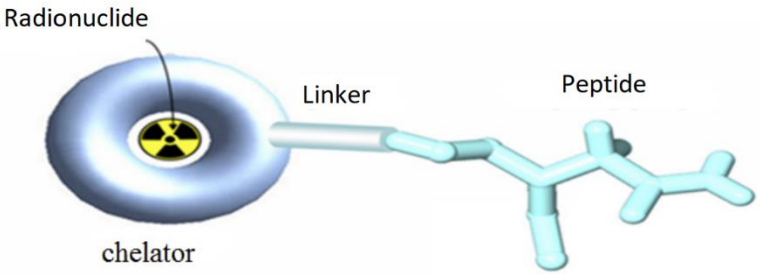

Fig. 1.13 Schematic representation of radiolabeling process with peptide [99]

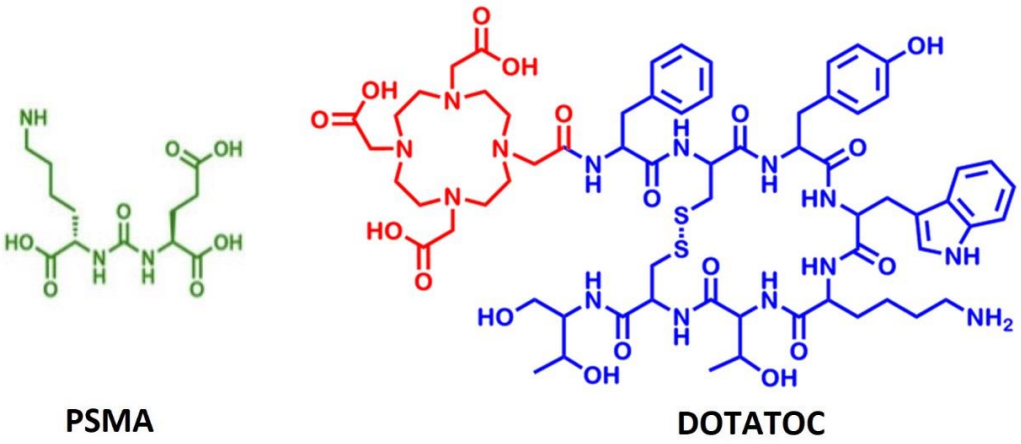

Fig. 1.14 Schematic view of PSMA* (formula depends on PSMA type) and DOTATOC ($C_{65}H_{92}N_{14}O_{18}S_2$) [100, 101]

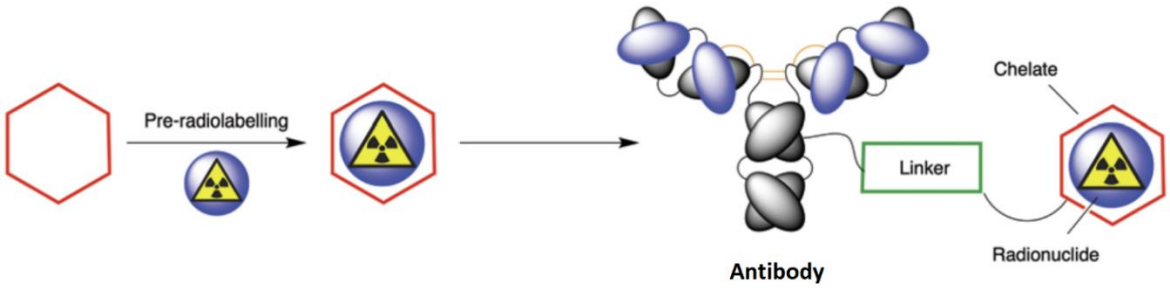

Fig. 1.15 Schematic representation of radiolabeling process with antibody [102]

1.3.2 Analogs

All cells in the body use glucose to get energy. But cancer cells use almost 200 times more glucose than normal cells. Tumors that start in the thin, flat cells in the lungs require even more glucose. Through this process, cancer cells grow quickly and divide faster. ^{18}F-fluorodeoxyglucose (FDG) is a radiotracer used in positron emission tomography (PET) and can be actively transported across the blood-brain barrier and phosphorylated within cells. FDG uptake shows the tissue glucose

metabolism and is high in high-grade tumors [103]. Through ^{18}F-FDG PET/CT, malignant lesions are detected by identifying regions with increased glycolytic metabolism. However, it is shown that increased ^{18}FDG uptake is not only in malignant lesions but also in inflammatory or infectious lesions. So, ^{18}FDG uptake can be observed also in other lesions in the neck, head, pelvis, bones, or vasculature.

FDG uptake patterns are classified as focal or diffuse FDG uptake in the thyroid. In focal uptake, lesions were defined as areas of increased tracer uptake compared to the surrounding structures by the thyroid, and this focal pattern is associated with a 25–50% risk of malignancy (Fig. 1.16). However, diffuse FDG uptake by the thyroid gland is defined as FDG uptake in the whole thyroid gland (Fig. 1.17) [104].

^{18}FDG also can be used for Cardiac imaging. Positron Emission Tomography (PET) utilizing ^{18}FDG is considered the most sensitive modality for detecting myocardial viability in coronary artery disease. Based on the reports, ^{18}FDG PET imaging has a benefit over ^{99m}Tc- SPECT in understanding functional recovery in patients with impaired left ventricular function. The diagnostic accuracy of ^{18}F-FDG PET shows sensitivity being superior to other techniques (SPECT, echocardiography, and cardiac MRI); however, cardiac PET is not as widely available as other techniques [105].

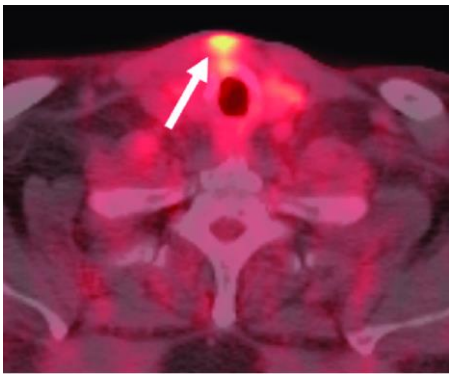

Fig. 1.16 Focal ^{18}FDG uptake in thyroid tissue where axial fused PET/CT shows focal uptake in the soft tissues (shown with arrow) in the anterior neck superficial to the thyroid gland [106]

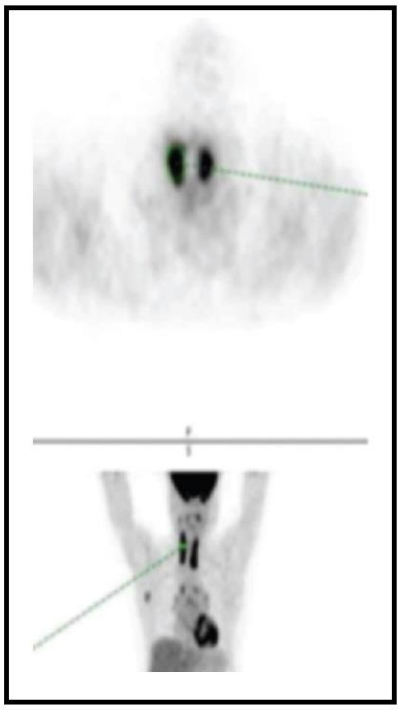

Fig. 1.17 Diffuse ^{18}FDG uptake in thyroid gland. As is shown, FDG uptake is in the whole thyroid gland [107]

1.3.3 Therapeutic radionuclides

Targeted radionuclide therapy or radiotherapy is a cancer treatment that uses high doses of radiation to shrink and kill the cancer cells. In radionuclide therapy, mostly radionuclides which emit β^- or α-particles are used [68].

1.3.3.1 Alpha (α) decay

Alpha decay occurs in heavy nuclides with many nucleons. In this process, the parent nuclide emits a helium nucleus (α-particle) (see Eq. 1.3).

$$^{A}_{Z}Parent^{*} \rightarrow {}^{A-4}_{Z-2}Daughter + {}^{4}_{2}He + Energy \qquad \text{Eq. 1.3}$$

Targeted alpha therapy is a therapeutic option in patients with multiple micro-metastases. In this process, by attaching an α-emitting radionuclide to a biological molecule with targeting

capabilities, the activity as a high radiation dose is delivered to cancerous cells [68]. An alpha particle is an energetic positively charged helium nucleus with an energy range of 4-9 MeV. Because alpha particles have a short path length, known as a high linear energy transfer (LET), it deposits about 1500 times more energy per unit path length than a β^- particle [68].

Some of the α-emitting radionuclides, which have been investigated and used in animals or humans, are listed in Table. 1.2. Among them, ^{225}Ac is particularly attractive due to its relatively long half-life ($T_{1/2}$=10 days), making it appropriate for vector molecules with longer biological half-life and internalizing peptides [108]. Moreover, ^{225}Ac decays by four alpha particles successively (all half-lives are under 1 hour), which can improve the treatment.

Table 1.2 Characteristics of selected alpha emitting radionuclides [77]

Radionuclides	Half-Life	Decay mode (%)	Eα[MeV] (Iα[%])
^{213}Po	4.2 µs	α (100)	8.3 (100)
^{212m}Po	45.1 s	α (99.9)	11.6 (97)
^{213}Bi	45.6 m	α (2) β^- (97.9)	5.5 (7.4) 5.8 (93)
^{212}Bi	60.5 m	α (35.9) β^- (64.1)	6 (69.9) 6.1 (27.12)
^{149}Tb	4.2 h	α (16.7) EC (72.1)	3.967(16.7)
^{211}At	7.2 h	α (41.8) EC (57.9)	5.869(41.8)
^{225}Ac	10 d	α (100)	5.829(50.7) 5.793 (18) 5.731(10) 5.791(8.6) 5.637(4.5) 5.723(2.9)
^{223}Ra	11.4 d	α (100)	5.6 (25.7) 5.7 (52.6)

1.3.3.2 Beta radiation therapy

Beta decay occurs in the nuclides that are neutron-rich. The neutral neutron decays into a proton (p), an electron (e^-), and one electron antineutrino (See Fig. 1.18 & Eq. 1.4).

$$ {}^{A}_{Z}Parent \rightarrow {}^{A}_{Z+1}Daughter + e + \nu_e^- + Energy \qquad \text{Eq. 1.4} $$

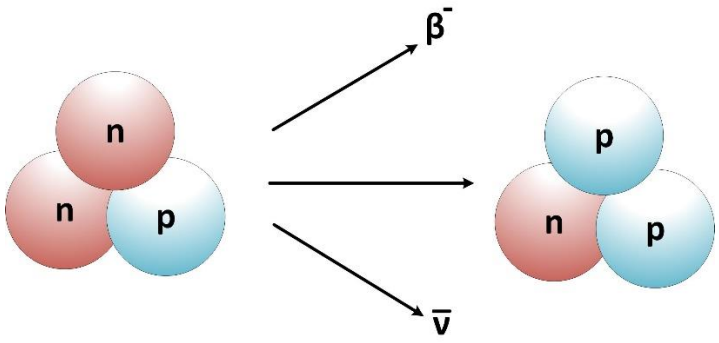

Fig. 1.18 Beta decay scheme

Beta particles are electrons with energies of 18 keV up to several MeV that penetrate tissue up to 10 mm. In comparison with alpha particles, beta particles ionize differently (lower LET) and have a larger range in tissue. In this case, more particles are required to cause lethal damage to cancer cells. ^{177}Lu, ^{131}I and ^{90}Y are the widest radionuclides used in clinics because of their suitable emission characteristics and affordable production [46]. ^{131}I is used in both visualization and therapy in order to implement many malignant tumors successfully [109]. However, ^{90}Y has been replaced mostly by ^{177}Lu in cancer therapy due to kidney damage. Some other clinically used beta emitting radionuclides are listed in Table 1.3.

Table 1.3 Characteristics of selected beta-emitting radionuclides [77]

Radionuclides	Half-Life	Decay mode (%)	$E\beta^-_{av}$ [keV]
^{67}Cu	61.83 h	β^- (100)	156
^{90}Y	2.7 d	β^- (100)	933
^{177}Lu	6.7 d	β^- (100)	148
^{161}Tb	6.9 d	β^- (100)	201
^{131}I	8.0 d	β^- (100)	192
^{32}P	14.3 d	β^- (100)	695

1.3.4 Theranostic radionuclides

Theranostic radionuclide is the term used for nuclides that can be applied for diagnosis and radiation therapy. This can be achieved by radionuclides that emit both therapeutic (e.g., α or β^-) and diagnostic (e.g., γ or β^+) radiation [110] or by two radionuclides of the same element (isotopes) that are separately employed for imaging and therapy (see Fig. 1.19) [111]. Using theranostic radiopharmaceuticals is relatively new. The most significant advantage of theranostics is that it can be applied to monitor the therapy course during treatment [111]. The first and famous theranostic radiopharmaceutical used in nuclear medicine was ^{131}I. Another widely used radionuclides in theranostic applications is ^{177}Lu. ^{131}I and ^{177}Lu are beta emitters and low energy gamma emitters and these agents can be employed for both imaging and therapy

simultaneously. It is necessary that the production of these radionuclides occurs in non-carrier* added form. The currently available radionuclide pairs are illustrated in Fig. 1.20 with some other used therapeutic and diagnostic radionuclides.

To reach the main goal of theranostics, new radionuclides which have optimum decay characteristics and chemical properties are needed [112]. Currently, one of the interesting pseudo-theranostic pairs is ^{68}Ga/ ^{177}Lu in which ^{177}Lu-labelled counterpart for radionuclide therapy are combined with ^{68}Ga-labelled compounds for PET diagnostics (a standard dose of ^{177}Lu and ^{68}Ga are between 5.55–7.4 GBq, and 200.0 MBq, respectively). Also, [^{68}Ga] Ga-PSMA-11 for diagnosis of metastasized prostate cancer was successfully used for subsequent treatment with ^{225}Ac (a standard dose of ^{225}Ac is about 6 MBq) in the form of [^{225}Ac] Ac-PSMA-617 (see Fig. 1.21) [112, 113, 114].

Another very interesting pair for theranostics is ^{61}Cu/^{67}Cu labeled with DOTATOC that can be used for neuroendocrine tumors (NETs). NETs are neoplasms, which arise from the nervous systems and cells of the endocrine system. They commonly occur in the intestine; however, they also have been found in the lung, pancreas and the rest of the body. The ^{61}Cu/^{67}Cu pair can be considered as a promising theranostic pair due to having appropriate half-lives for diagnosis and therapy, respectively (^{61}Cu with a half-life of 3.3 h and ^{67}Cu with a half-life of 61.8 h). Moreover, ^{61}Cu, which emits β^+ particles with an energy of 1.22 MeV and high Branching Ratio (BR=60%), is much better than ^{64}Cu with BR of 17.7% (note that the higher BR results in smaller patient doses). ^{67}Cu as a therapeutic radionuclide has a dual application for therapy and imaging, it emits β^- particles with an average energy of 141 keV and gamma-rays of 93 and 185 keV make it ideal for both radionuclide therapy and SPECT [115].

* A preparation of a radioactive isotope which is essentially free from stable isotopes of the corresponding element. Minimizing contamination and high specific activity of the radioisotopes can be achieved when they are prepared in no-carrier added form.

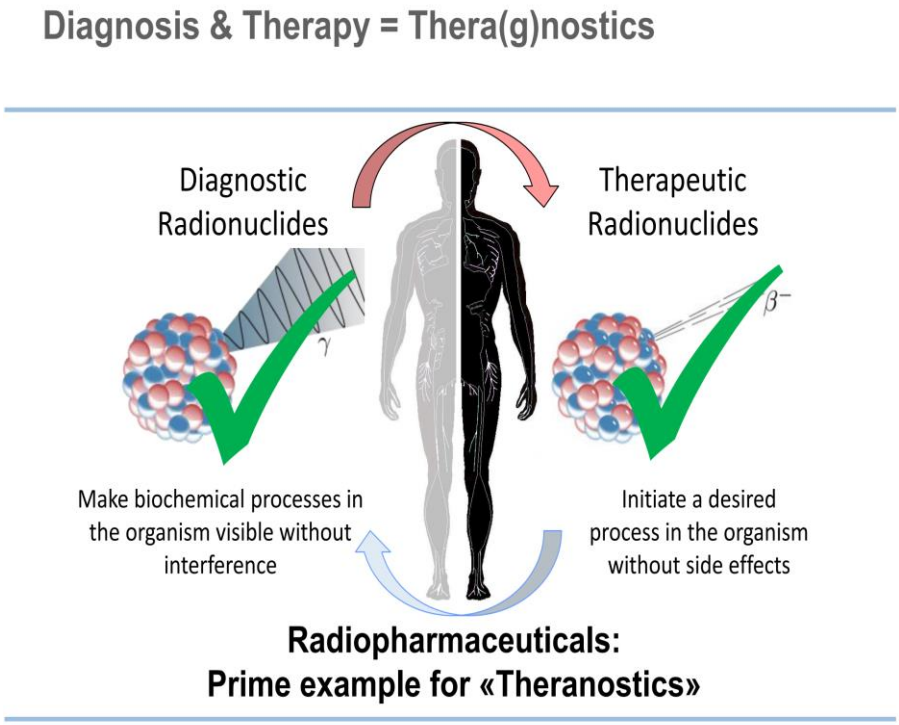

Fig. 1.19 Theranostics approach diagram [112]

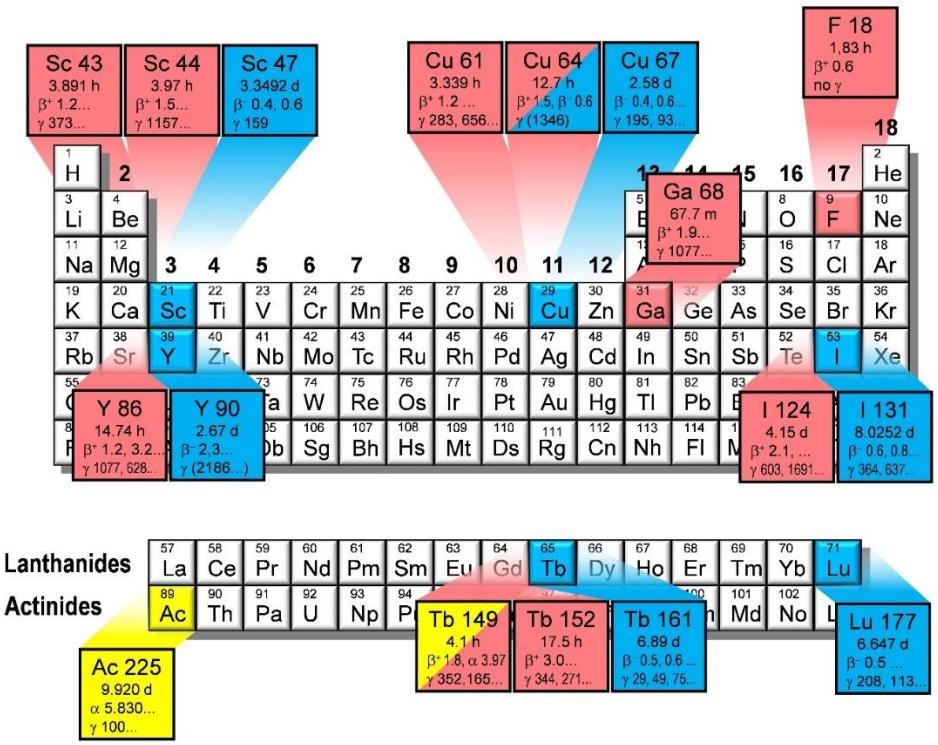

Fig. 1.20 Periodic table of the elements for diagnostic radionuclides suitable for therapeutic and PET radionuclides [112]

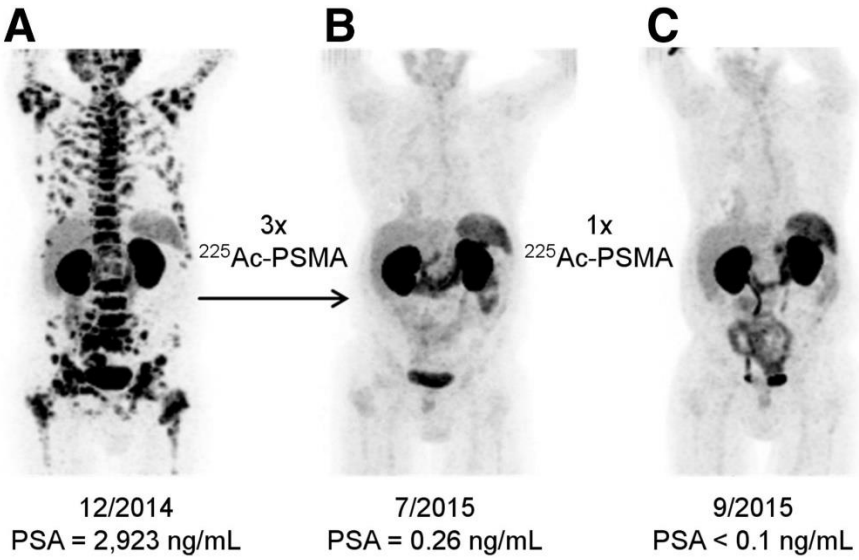

Fig. 1.21 ^{68}Ga-PSMA-11 PET/CT scans of a patient. Pretherapeutic tumor spread (A), restaging 2 mo after third cycle of ^{225}Ac-PSMA-617 (B), and restaging 2 mo after one additional consolidation therapy (C). This research was originally published in JNM. © SNMMI [112]

1.4 Radionuclide production methods

1.4.1 Cyclotron production

A cyclotron consists of different parts, which include: an ion source, a magnet, two D-shaped electrodes, and an acceleration chamber [116]. The function of each part is described as follows:

The ion source produces an ion which can be a proton, deuteron, helium nucleus (^{3}He, ^{4}He), or a heavy ion. Then the particle is accelerated from the center (see Fig. 1.22), and a high-frequency voltage is applied between two "D"-shaped metal electrodes [117]. Two D-shaped electrodes are located between the poles of an electromagnet with a static magnetic field *B*. Using this magnetic field, the particle path will be bent in a circle due to the Lorentz force, which is perpendicular to their direction of motion while the particle is inside the "D"-shaped metal electrode the voltage is switched to achieve further acceleration across the gap (see Fig. 1.22). So, the particle energy in a cyclotron can be obtained through a formula as Eq. 1.5 [118]:

$$E = \frac{q^2 B^2 R^2}{2m}, \qquad \text{Eq. 1.5}$$

where *q* is particle charge, *B* is the magnetic field, *R* is the acceleration radius, and *m* is the charged particle's mass.

The first cyclotron devoted to medical applications was installed at Washington University in St. Louis in 1941 for ^{32}P, ^{77}As, and the production of other radionuclides [119]. Depending on the function for which they are intended, cyclotrons come in different sizes, but the basic characteristics of all cyclotrons are the same.

Medical cyclotrons (level I to level III with energy lower than 20 MeV) [120] mostly accelerate negative ions, and after acceleration by removing electrons using a striper foil, the accelerated negative charges convert to positive charged ion. However, higher energy cyclotrons (level IV to level VI) [120] accelerate positive ions. Extraction of the beam in positive ion cyclotrons is different compared to negative charge ion cyclotrons. In a positive ion cyclotron, the beam is extracted using a deflector at negative extraction voltage, which bends the accelerated positive ion out of the B-field (see Fig. 1.23). [121]. However, in modern cyclotrons, for negative charge

ions, the extraction of the beam is by using stripper foils (such as carbon foils) which remove the two electrons attached to the accelerated ion, let the magnetic field reverse the curvature of the positively charged particles' path and extract the particles out of the cyclotron (see Fig. 1.24).

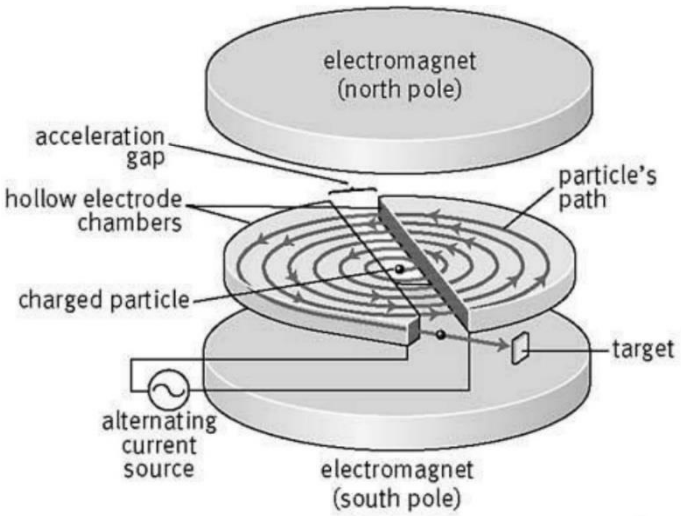

Fig. 1.22 Cyclotron set up for particle acceleration [122]

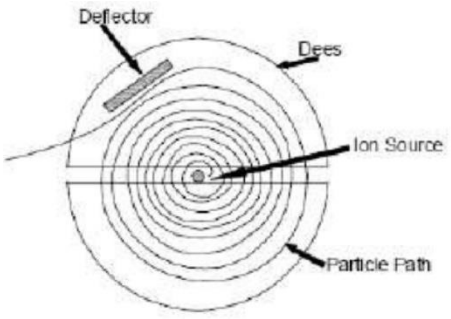

Fig. 1.23 Extraction mechanism in a positive ion cyclotron using a deflector [123]

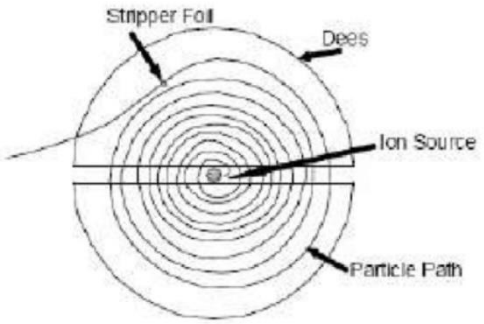

Fig. 1.24 Extraction mechanism in a negative ion cyclotron using a stripper foil [123]

1.4.2 Nuclear reactor production

Nuclear research reactors can be used for radionuclide production. Radionuclides are produced in a nuclear reactor by exposing target materials to the neutron flux for an appropriate time. Before the irradiation, target materials are sealed in a primary irradiation capsule and then loaded in special places assigned for irradiation in nuclear research reactors (see Fig. 1.25). In this production method, the neutron's energy, neutron flux, activation cross-section for the desired reaction, and characteristics of the target material determine the rate of production [124]. The amount of neutron flux for radionuclide production in research reactors should be 10^{13} to 10^{14} $n/cm^2.s$ which depends on the power of the nuclear reactor. Nuclear research reactors are used mostly for therapeutic radionuclide production such as ^{131}I, ^{177}Lu and ^{32}P [125].

In general, there are two different types of nuclear reactors, the first one are nuclear power plants and the second one are nuclear research reactors. The former is used for heat generation and subsequent electricity production; however, the latter one is for different scientific research fields; in particular, for radionuclide production. Nuclear power plants work at high temperature and pressure and, therefore, the reactor core is within a pressure vessel which prevents any accessibility; in particular, near the fuels where the neutron flux is high. Moreover, they usually are working at power that means they usually work continuously since the startup time until the time of refueling (usually once per year for water-cooled reactors) or the time which is related to a safety shutdown (frequent shutdown in nuclear power plant leads to some safety

considerations). Accordingly, it can reasonably be argued that most nuclear power plants are not suitable for radionuclide production purposes. In contrast to nuclear power plants, nuclear research reactors are working at a suitable temperature and pressure (usually atmospheric condition), and the core is easily accessible for target irradiation.

The problem associated with nuclear reactor production is that many research reactors are considered as no longer reliable due to old age and are planned to be shut down in a few years [126].

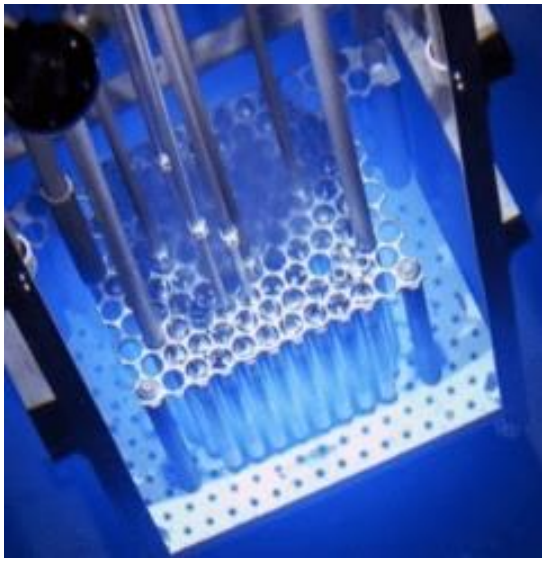

Fig. 1.25 Nuclear reactor used for radionuclide production [127]

1.4.3 Electron accelerators

Electron accelerators are one of the other alternatives for radionuclide production using photonuclear reactions. Electron accelerators come as different types, such as linear accelerator, Rhodotron, and Microtron, which operate based on different electron acceleration methods and electron beam energy. In the following, these types of accelerators are discussed.

1.4.3.1 Linear accelerators

Linear accelerators are based on microwave technology to accelerate electrons. In a linear accelerator, electrons acquire energy while moving on a linear path. A linear accelerator will receive the electron beam from an electron source, bunch it at a given RF frequency and then accelerate it [128]. Electrons are accelerated through electric fields and are bent and focused through magnetic fields (see Fig 1.26). In a linear accelerator, the bunch of electrons will collide with a target located at the end of the accelerating electrodes and produce photons through the Bremsstrahlung process. Photon energies larger than 8 MeV are required to induce photonuclear reactions on the production target [129] (see more details in section 1.5.2). Electron Linacs are capable of producing photons with sufficiently high energies and intensities for radionuclide production [128, 130]. Through photonuclear reactions, the electron Linac is useful for radionuclide production. Regarding this issue, Argonne National Laboratory installed an upgraded 55 MeV electron Linac, which can produce a number of various medical isotopes through photonuclear reactions [130].

Commercially available Linacs are from the company MEVEX in Canada with an optimum energy of 33 MeV for ^{99}Mo production. The electron energy of this type of Linac is up to 35 MeV and the beam power is up to 120 kW [131].

Actually, using Linac has a disadvantage associated with radionuclide production. Since beam pulses are very short in Linacs (because of the high applied RF), and due to the high intensity of the beam (about 300 mA during a beam pulse), a considerable amount of energy is deposited on the converter target in a very short time leading to a high temperature rise.

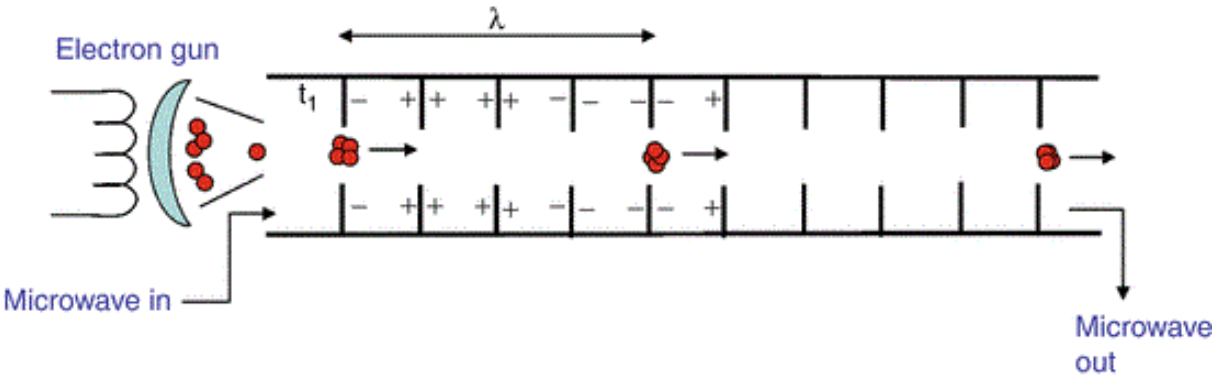

Fig. 1.26 Scheme of the electron Linac acceleration method [132]

1.4.3.2 Microtron accelerator

In a Microtron, the electrons which revolve in a uniform magnetic field are accelerated each time by passing through an electric field. In a Microtron, the electrons' momentum increases, and particle paths are different for each pass (see Fig. 1.27).

In a Microtron, the particle paths are different for each pass due to the electrons' increasing momentum. In this case, the slow electrons need an electric field oscillation and the faster electrons need an integer multiple of this oscillation. There are some advantages associated with Microtron over a linear accelerator which are its simplicity, ease of energy selection, compact size, low energy dispersion and more efficient acceleration (due to circular rotation compared to the longitudinal direction in the linear accelerators for the same output electron energy, see Figs. 1.26 & 1.27) [133].

A Microtron exists at METAS (Federal Institute of Metrology) in Switzerland, which has a maximum energy of 22 MeV and beam currents up to 20 μA. This system is equipped with a target that converts the primary electron beam into a high flux photon spectrum of up to about 20 MeV photon energy. This Microtron is a suitable photon source for the production of ^{67}Cu, ^{47}Sc, or ^{225}Ac for first test experiments.

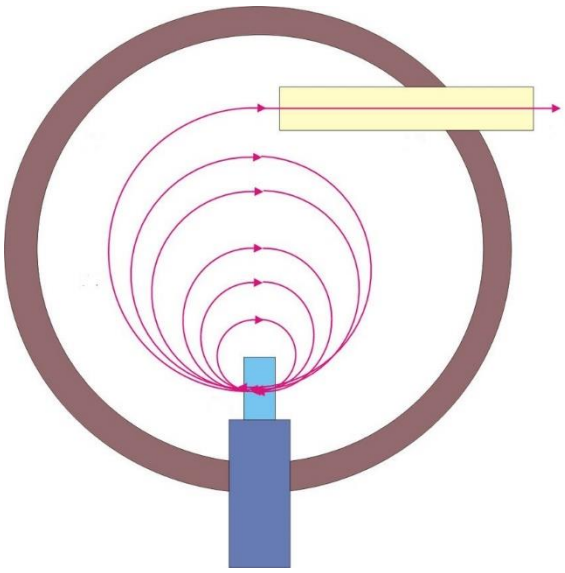

Fig. 1.27 Microtron basis for electron acceleration [133]

1.4.3.3 Rhodotron accelerator

A Rhodotron is a high-power electron beam accelerator, which can accelerate electrons to high energies (up to 40 MeV) and allows for efficient radionuclide production through photonuclear interaction (see Fig. 1.28a). A Rhodotron works based on “re-circulating” a beam through successive diameters of a single coaxial cavity resonating in metric waves (see Fig. 1.28b) [134]). As can be seen in Fig. 1.28, a Rhodotron also is able to provide different beams with different electron beam energies depending on the number of passages through the cavity and acceleration voltage.

Rhodotrons have been invented and patented by the IBA company. Commercially available Rhodotrons are available from the company IBA (40 MeV and 125 kW beam power). In this commercial Rhodotron, the maximum number of passes of an electron is 12, and the energy gain with each pass is 3.3 MeV.

For efficient radionuclide production, the high-energy and high-power (or high-current) Rhodotron model TT300-HE is desirable; however, the problem associated with such an electron

accelerator is the considerable amount of heat that is deposited in the converter target, which causes a sharp temperature rise and, therefore, mechanical instability.

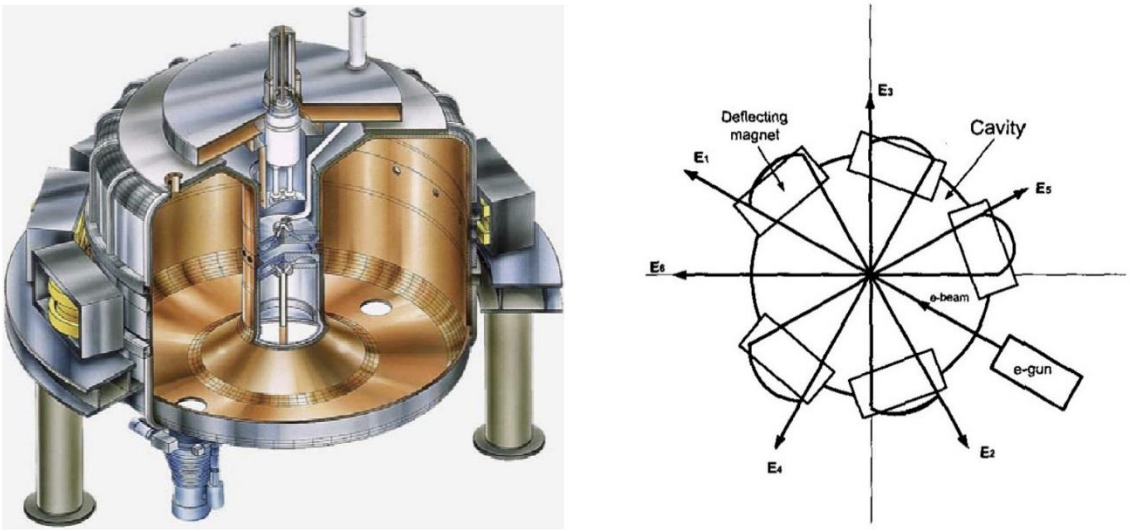

Fig. 1.28 a) Schematic representation of a Rhodotron accelerator, b) Rhodotron mechanism scheme, where E_i is the electron beam with different energy [134, 135]

1.5 ^{61}Cu/^{67}Cu theranostic pair

The selection of suitable radionuclides for theranostic applications is of great importance and requires some properties: 1) appropriate half-life, which is close to the biological half-life of the radionuclide in the desired tissue); 2) existence of two different isotopes that are suitable for both imaging and therapy; 3) lack of high-energy gamma-ray emission, 4) availability and cost-effective production of the radionuclide and 5) suitable chemical properties, i.e. suitable chelators. As such, copper isotopes are an excellent option for theranostic applications due to their appropriate half-lives and their decay properties (β^+, β^-, or EC), which are suitable for both imaging and therapy [136].

^{61}Cu, with a half-life of 3.3 h, is a positron emitting radioisotope that can be used for PET imaging. ^{61}Cu (E_{β^+}= 1.22 MeV, BR (%)=60) has a much higher abundance of positron emission than ^{64}Cu (E_{β^+}= 0.65 MeV, BR (%)=17.7), that allows use in smaller doses [137, 138].

^{67}Cu is a great candidate to be is used as a therapeutic isotope due to its appropriate half-life, and its dual application for therapy and imaging and it is a non-essential element for the body. The nuclide ^{67}Cu ($T_{1/2}$ = 62.83 h) emits β^- particles with an average energy of 141 keV, and γ-rays (93 keV, BR (%)=16.1, and 185 keV, BR (%)= 48.7) make it ideal both for radionuclide therapy and SPECT imaging [139].

It is ideal if therapeutic radiopharmaceuticals localize in the tumor in sufficient concentration, which is called a target-specific radiopharmaceutical. Copper radioisotopes (^{61}Cu/^{67}Cu) are able to bind with a chelator and a targeting biomolecule and are very suitable for preparing chelates for the use as a theranostic application. However, ^{67}Cu is also able to be used as a theranostic radionuclide by itself due to simultaneous use in radionuclide therapy coupled with SPECT technology [139]. In the following, ^{61}Cu and ^{67}Cu production through different reaction channels were investigated.

1.5.1 ^{61}Cu production routes

Radionuclide production for use in biomedical procedures is obtained through nuclear reactions in charged particle bombardments in accelerators or from nuclear reactors. Regardless of the production method, the beams (in accelerators)/ neutron flux (in nuclear reactors) must have enough energy required in the region of interest of the excitation function for the production of desired radionuclides and sufficient beam-current/flux to give practical yields. Another factor playing a significant role in the selection of the production method is that the reaction method must be chosen so that the product is produced in a non- carrier added form. In addition, the nuclear absorption cross-section, which represents the total probability of a nuclear reaction, should be as high as possible to allow for a high yield production of the desired radionuclide [140, 141]. For ^{61}Cu production, the most suitable nuclear reactions are ^{61}Ni(p,n)^{61}Cu, ^{nat}Ni(α,x)^{61}Cu, and ^{64}Zn(p,α)^{61}Cu (see Fig. 1.29). In the following, these reaction routes are considered in detail. It is worth pointing out that the feasibility of ^{61}Cu production in high radionuclide purity and amount to allow radiolabeling is the main objective for the selection of the best reaction route [142-144].

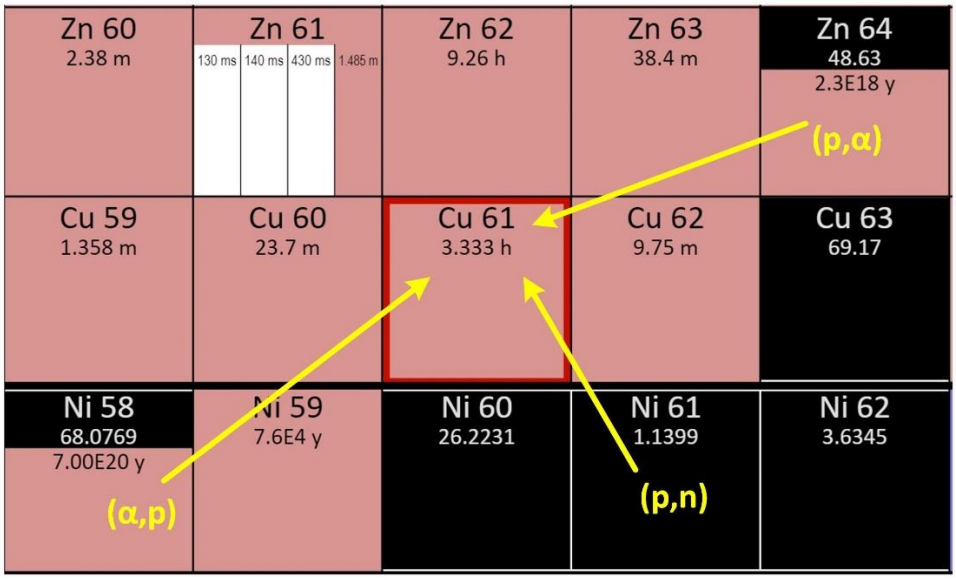

Fig. 1.29 ^{61}Cu different production routes

^{nat}Ni(p,x)^{61}Cu reaction route

^{61}Cu can be produced from ^{61}Ni and ^{62}Ni via (p,n) and (p,2n) reaction channels, respectively. The production of ^{61}Cu via these reaction channels results in a high yield due to high cross-sections (> 300 mb). Regarding the experimental published data, the beneficial energy ranges to produce ^{61}Cu from a ^{61}Ni target are proton energies from 5–20 MeV, and the maximum cross-section is 418 mb at 10 MeV [145]. Due to low impurities' production, this reaction can be considered one of the desirable production routes. Regarding the experimental published data, ^{61}Cu was produced with a maximum yield of 144 mCi using enriched ^{61}Ni target ($37 per mg). Ni targets were prepared using an electroplating technique and then irradiated with approximately 14.7 MeV protons on the CS-15 cyclotron at Washington University [145, 146].

$^{nat}Ni(\alpha,x)^{61}Cu$ reaction route

^{61}Cu can be produced via alpha-particle irradiation on natural or enriched Ni targets. The natural Ni target is composed of two stable isotopes ^{58}Ni (68.0%) and ^{60}Ni (26.2%). Using these reaction channels, ^{61}Cu can be produced with alpha-particle energies in the range between 8-24 MeV. It should be noted that the $^{58}Ni(\alpha,p)^{61}Cu$ reaction is the only contributing channel in the energy range of 3–24 MeV (with a maximum cross-section of 501 mb at the energy of 15 MeV), while the threshold energy of the ^{60}Ni $(\alpha,p2n)^{61}Cu$ reaction channel is at 18 MeV (with a maximum cross-section of 278 mb at the energy of 40 MeV). So, due to the higher abundance of ^{58}Ni target, lower threshold energy of the $^{58}Ni(\alpha,p)^{61}Cu$ reaction, and higher cross-sections, one can conclude that production of ^{61}Cu via the $^{58}Ni(\alpha,p)^{61}Cu$ reaction is economical and practical [146, 147].

$^{64}Zn(p,\alpha)^{61}Cu$ reaction route

The production of ^{61}Cu from ^{64}Zn target via proton-induced nuclear reactions is regarded as an attractive option due to low impurity production and high obtainable yield. According to published data [145], the best energy range for ^{61}Cu production is 6–25 MeV, and the maximum-cross section is 25 mb at an energy of 13 MeV. Moreover, regarding the high natural abundance of ^{64}Zn target (48.6%), the target would be cost-effective (about 1.2 $ per mg). However, the low cross-section in comparison with the $^{61}Ni(p,n)^{61}Cu$ reaction, can be satisfied by irradiation of a tick target of ^{64}Zn.

Regarding the previously published study [148], ^{61}Cu was produced from ^{64}Zn with 99.30% isotopic enrichment (about 1.2 $ per mg). The irradiations were performed at two different cyclotrons. One cyclotron was a CC 18/9 (Efremov Institute, Russia) in Turku, and the second one was a Cyclone 18/9 (IBA, Louvain la Neuve, Belgium) in Rossendorf. The targets were irradiated with both cyclotrons for 0.5–3 h with various beam currents. Regarding the results, an activity of ^{61}Cu obtained was 290 MBq and 339 MBq at the Cyclone 18/9 (with a beam current of 12 μA) and CC 18/9 (with a beam current of 30 μA) cyclotrons, respectively [148].

Nuclear model calculation for cyclotron production of ^{61}Cu as a PET imaging

Authors: Mahdi Sadeghi, Nadia Zandi, Mahdi Bakhtiari

Journal of radioanalytical and nuclear chemistry, 292:777–783 (2012)

Highlights: ^{61}Cu with a half-life of 3.3 h, offers some advantages over ^{64}Cu when using it for PET imaging [138]. In the paper presented in the following, cyclotron production of ^{61}Cu via different reactions has been investigated. The ALICE/ASH and TALYS-1.2 codes were used to calculate excitation functions for proton, alpha and deuteron induced reactions on different targets that lead to the production of ^{61}Cu using intermediate beam energy cyclotrons [149, 150]. In addition, the data obtained from this study was compared with the reported experimental data. Regarding the results presented in the paper, the theoretically obtained results were in good agreement with the reported experimental data. Moreover, optimal thicknesses of the targets and physical yield were obtained by calculating the stopping and range of ions in matter for each reaction. Finally, considering the possibilities to produce ^{61}Cu and the existing facilities and materials, we used the ^{nat}Ni(p,x)^{61}Cu reaction to test the target preparation. Accordingly, natural nickel (99.99% purity, purchased from Aldrich) was electroplated on a gold-coated copper backing with 48 µm thickness and 11.69 cm^2 area (for more details, refer to the attached paper).

Contributions: My contribution to the publication consisted of performing the theoretical calculations, investigating the results and writing the manuscript.

J Radioanal Nucl Chem (2012) 292:777–783
DOI 10.1007/s10967-011-1557-1

Nuclear model calculation for cyclotron production of ^{61}Cu as a PET imaging

Mahdi Sadeghi · Nadia Zandi · Mahdi Bakhtiari

Received: 11 October 2011 / Published online: 21 December 2011

Abstract ^{61}Cu is positron emitter and can be used as the PET and molecular imaging. In this study cyclotron production of ^{61}Cu via ^{61}Ni(p,n)^{61}Cu, ^{nat}Ni(p,x)^{61}Cu, ^{nat}Ni(d,x)^{61}Cu, ^{nat}Ni(α,x)^{61}Cu, ^{nat}Zn(p,x)^{61}Cu and ^{59}Co(α,2n)^{61}Cu reactions was investigated. The ALICE/ASH (hybrid and GDH models) and TALYS-1.2 codes were used to calculate excitation functions for proton, alpha and deuteron induced on ^{nat}Ni, proton on ^{61}Ni and ^{nat}Zn and also alpha-particle on ^{59}Co targets that lead to the production of ^{61}Cu radioisotopes using intermediate energy accelerators. In addition, we compared the data obtained from in this study with the reported measurement by experimental data. Moreover, optimal thickness of the targets and physical yield were obtained by stopping and range of ions in matter code for each reaction. Eventually ^{61}Ni(p,n)^{61}Cu and ^{59}Co(α,2n)^{61}Cu reaction to produce ^{61}Cu in no-carrier added state with high production yield was suggested. Finally the ^{nat}Ni(p,x)^{61}Cu reaction was employed to test the target preparation using electroplating technique.

Keywords Excitation function · ^{61}Cu · Physical yield · TALYS-1.2 · ALICE/ASH · Ni electroplating

M. Sadeghi (✉)
Agricultural, Medical & Industrial Research School, Nuclear Science and Technology Research Institute, P.O. Box 31485/498, Karaj, Tehran, Iran
e-mail: msadeghi@nrcam.org

N. Zandi
Department of Nuclear Engineering and Physics, Amir-kabir University of Technology, Tehran, Iran

M. Bakhtiari
Department of Physics, Boroujerd Branch, Islamic Azad University, Boroujerd, Iran

Introduction

Copper has many radio-nuclides (^{60}Cu, ^{61}Cu, ^{62}Cu, ^{64}Cu, and ^{67}Cu) that can be used in nuclear medicine and molecular imaging [1, 2]. ^{61}Cu offers several advantages over other Cu radioisotopes for labeling radiopharmaceuticals for positron emission tomography (PET). Interestingly, it has been shown that the tomographic images obtained using ^{61}Cu are superior to those using ^{64}Cu, based on the larger abundance of positrons emitted by ^{61}Cu compared with ^{64}Cu [3]. ^{61}Cu is a positron emitter ($T_{1/2} = 3.33$ h, β^+: 62%, EC: 38%), with excellent potentials for application in the PET method and molecular imaging [4]. Molecular imaging is a new biomedical research discipline enabling the visualization, characterization, and quantification of biologic processes taking place at the cellular and sub-cellular levels within intact living subjects including patients [5].

In our previous articles, we evaluated cyclotron production parameters of ^{172}Lu, ^{93m}Mo, ^{122}Sb, and ^{109}Cd via various codes and compared with existing data [6–9]. In this work, several methods for ^{61}Cu production using TALYS-1.2 and ALICE/ASH (hybrid and GDH models) codes have been studied. There are different methods to produce ^{61}Cu via proton, deuteron and alpha particles on various targets such as ^{nat}Ni, ^{61}Ni, ^{nat}Zn, ^{nat}Cu and ^{59}Co [10–34]. The aim of the presented study is to compare the calculated cross sections for the production of ^{61}Cu via different reactions with incident particle energy up to 50 MeV as a part of systematic studies on particle-induced activations on metal targets, theoretical calculation of physical yield, calculation of target thickness requirement and suggestion for optimum reaction to produce ^{61}Cu. Theoretical calculation of physical yield and target thickness was done using Stopping and Range of Ions in Matter

(SRIM) code [35]. To find the aberration amount of the acquired data from in this study and experimental data, and TENDL-2010 [36], they were compared with each other. Eventually natural nickel target was prepared using the electroplating technique.

Materials and methods

Excitation function

Excitation functions of ^{61}Ni(p,n)^{61}Cu, ^{nat}Ni(p,x)^{61}Cu, ^{nat}Ni(d,x)^{61}Cu, ^{nat}Ni(α,x)^{61}Cu, ^{nat}Zn(p,x)^{61}Cu and ^{59}Co(α,2n)^{91}Cu reactions were calculated using TALYS-1.2 and ALICE/ASH (hybrid and GDH models) codes [37, 38]. According to results an optimum energy range was determined and employed to avoid the formation of radionuclide impurities and decrease the excitation functions of inactive impurities as far as possible.

The TALYS 1.2 code

The TALYS program simulates nuclear reactions that involve gammas, neutrons, protons, deuterons, tritons, ^{3}He and α-particles in the incident energy range from 1 keV to 200 MeV for target nuclides of mass 12 and heavier. The TALYS code was designed to calculate total and partial cross sections, residual and isomer production cross sections, discrete and continuum γ-ray production cross sections, energy spectra, angular distributions, double differential spectra, as well as recoil cross sections. The TALYS code takes into account three types of reaction mechanisms: DIR [coupled channel analysis, distorted wave born approximation, etc.], PEQ (one- and two-component exciton models), and EQ (Hauser–Feshbach model) [37].

ALICE/ASH code

The ALICE/ASH code is an advanced version of the original Blann code [38]. The code calculates energy and angular distributions of particles emitted in nuclear reactions, residual nuclear yields, and total non-elastic cross-sections for nuclear reactions induced by particles and nuclei with energies up to 300 MeV [38]. Concerning the implementation in the code, the models are describing the pre-compound composite particle emission and fast γ-emission, different approaches for the nuclear level density calculation [39] and the model for the fission fragment yield calculation. The geometry dependent hybrid (GDH) model is used for the description of the pre-equilibrium particle emission. Intra-nuclear transition rates are calculated using the effective cross section of nucleon–nucleon interactions in nuclear matter. The equilibrium emission of particles is described by the Weisskopf–Ewing model without detail consideration of angular momentum.

Calculation of the physical yield and the target thickness

Enhance of the projectile energy, beam current, and time of bombardment increase the production yield. Theoretical physical yield can be calculated by the following equation:

$$Y = \frac{N_L H}{M} I\left(1 - e^{-\lambda t}\right) \int_{E_1}^{E_2} \left(\frac{dE}{d(\rho x)}\right)^{-1} \sigma(E)\, dE \qquad (1)$$

where Y is the activity of the product (in Bq), N_L is the Avogadro number, H is the isotope abundance of the target nuclide (%), M is the mass number of the target element (g), $\sigma(E)$ is the cross-section at energy E (mb), I is the projectile current (μA), $dE/d(\rho x)$ is the stopping power (MeV/mg/cm^2), λ is the decay constant of the product and t is the time of irradiation (h). The physical yields were deduced using the measured cross-sections by using the Simpson numerical integral method from Eq. 1. To predict theoretical physical yields calculated by means of the acquired cross-section data and stopping powers of projectiles in target material, a nuclear code named SRIM [35] was used. According to the SRIM code, the required thickness of the target was calculated for each reaction. The physical thickness of the target layer that was calculated by SRIM code is for 90° geometry beam toward the target. To better heat transfer on the surface of the target and the beam cover all surface of the target (11.69 cm^2), 6° geometry beam toward the target during the bombardment was performed [40]. So required layer thickness will be less with coefficient 0.1.

Results and discussion

Excitation function of ^{61}Ni(p,n)^{61}Cu reaction

According to TALYS-1.2 code, beneficial energy range of the projectile particle (proton) to produce ^{61}Cu from ^{61}Ni target is 5–20 MeV that maximum cross section is 418 mb at 10 MeV (Fig. 1). To limit the production of impurities ^{60}Cu (23.7 m) and ^{58}Co (70.86 days) and to attain its benefit energy range, the 5–9 MeV energy range was considered. In this reaction, data obtained from TALYS-1.2, ALICE/ASH and TENDL-2010 are in good agreement with the previous published results (Fig. 2). Accordingly this reaction is suggested as one of the best method to production of ^{61}Cu in no carrier state. The calculated

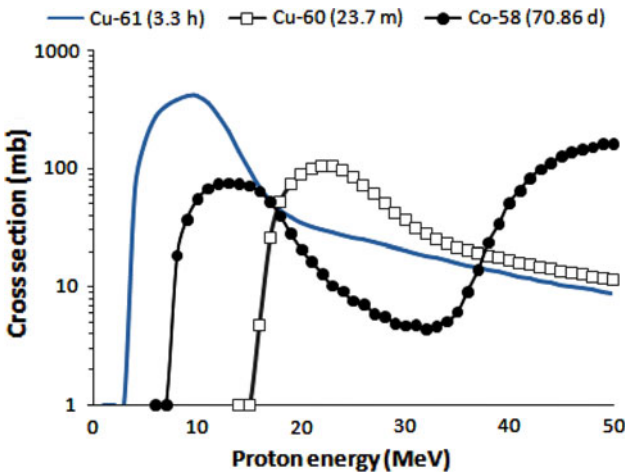

Fig. 1 Excitation function of ^{61}Ni(p, x)^{61}Cu reaction calculated by TALYS-1.2 code

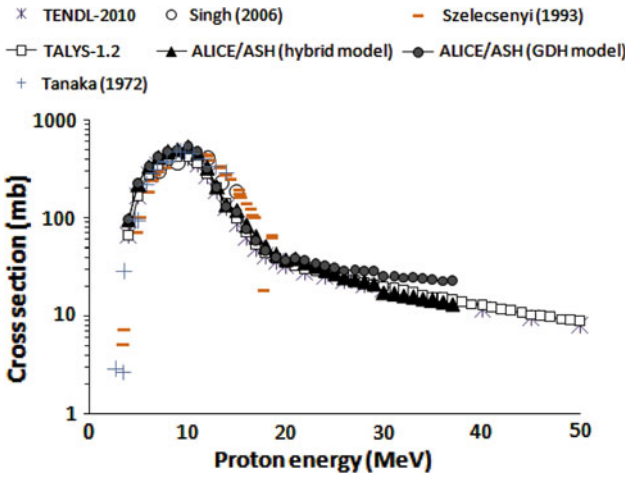

Fig. 2 Excitation function of ^{61}Ni(p, x)^{61}Cu reaction calculated by ALICE/ASH (hybrid and GDH models) and TALYS-1.2 codes and experimental data

Table 1 ^{61}Cu physical yield and target thickness for various reactions

Reaction	Energy range (MeV)	Target thickness (μm)	Theoretical physical yield (MBq/μA h)
^{61}Ni(p,x)^{61}Cu	20 → 5	77.2	1379.7
^{nat}Ni(p,x)^{61}Cu	24 → 17	47.0	68.0
^{nat}Ni(d,x)^{61}Cu	14 → 3	23.8	52.8
^{nat}Ni(α,x)^{61}Cu	21 → 8	6.2	167.2
^{nat}Zn(p,x)^{61}Cu	25 → 6	56.5	110.7
^{59}Co(α,2n)^{61}Cu	35 → 16	153.2	249

physical yield is 1379.7 MBq/μA h. The recommended target thickness was calculated using the SRIM code (Table 1).

Excitation function of ^{nat}Ni(p,x)^{61}Cu reaction

In this study excitation functions of the proton-induced reaction on natural nickel were measured by TALYS-1.2 and ALICE/ASH (hybrid and GDH models) codes and compared to existing data (Fig. 3). Regarding to TALYS-1.2 code data for this reaction, ^{61}Cu has a maximum cross-section of about 13 mb at 21 MeV; its beneficial excitation functions occur between 17 and 24 MeV. Because of very low cross section to produce ^{61}Cu, this reaction basically is not suggested as the one of the best reaction to produce ^{61}Cu especially as the medically application. As the natural nickel is composed of five stable isotopes (Table 2), the ^{nat}Ni(p,x)^{61}Cu reaction leading to the formation of the ^{60}Cu (23.7 m), ^{59}Cu (81.5 s) and ^{58}Cu (3.2 s) impurities in this energy range. Figure 4 shows the comparison between cross section values reported by Saleh [10], Michel [11, 12] and Barrandon [13] and the results of nuclear model calculations employing the different theoretical calculations. Almost in all energy regions, calculated data from TALYS-1.2 and ALICE/ASH codes are in good agreement with the cross section value reported by experimental data. According to SRIM-2006 code the required target thickness to achieve this energy range should be 47.0 μm for 6° geometry beam toward the target (Table 1). The physical yield of ^{61}Cu was obtained 68.0 MBq/μA h.

Excitation function of ^{nat}Ni(d,x)^{61}Cu reaction

Excitation functions based on TALYS-1.2 code calculation are shown in Fig. 5 at different decay channels after deuteron bombardment of natural nickel. According to Fig. 5 the ^{nat}Ni(d,x)^{61}Cu reaction leading to the formation of the $^{60/58/57}$Co and ^{60}Cu impurities in 3–14 MeV. To restrict production of impurities as far as possible, 3–8 MeV is

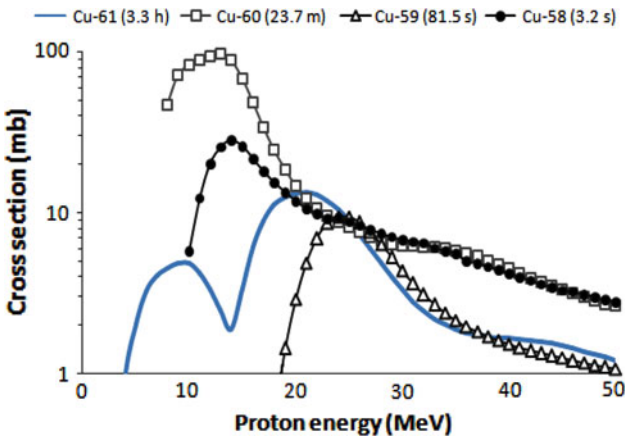

Fig. 3 Excitation function of ^{nat}Ni(p, x)^{61}Cu reaction calculated by TALYS-1.2 code

Table 2 Isotopes abundance of ^{nat}Ni

Isotope	Abundance (%)
^{58}Ni	68.07
^{60}Ni	26.22
^{61}Ni	1.14
^{62}Ni	3.63
^{64}Ni	0.92

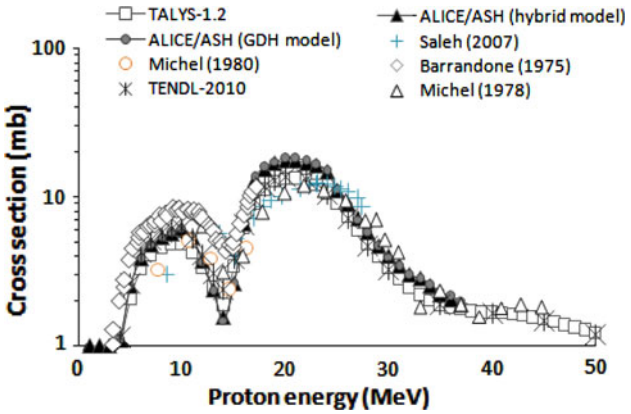

Fig. 4 Excitation function of ^{nat}Ni(p, x)^{61}Cu reaction calculated by ALICE/ASH (hybrid and GDH models) and TALYS-1.2 codes and experimental data

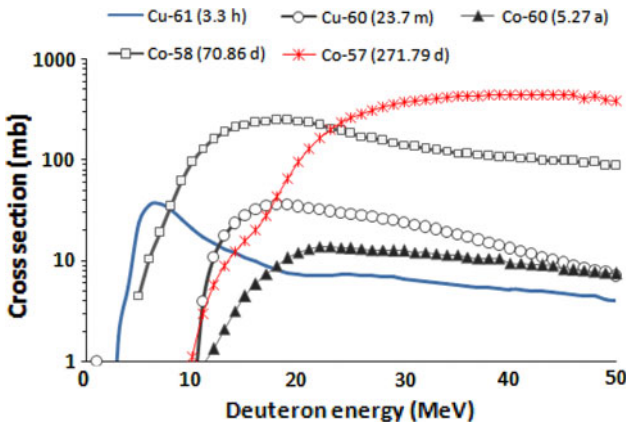

Fig. 5 Excitation function of ^{nat}Ni(d, x)^{61}Cu reaction calculated by TALYS-1.2 code

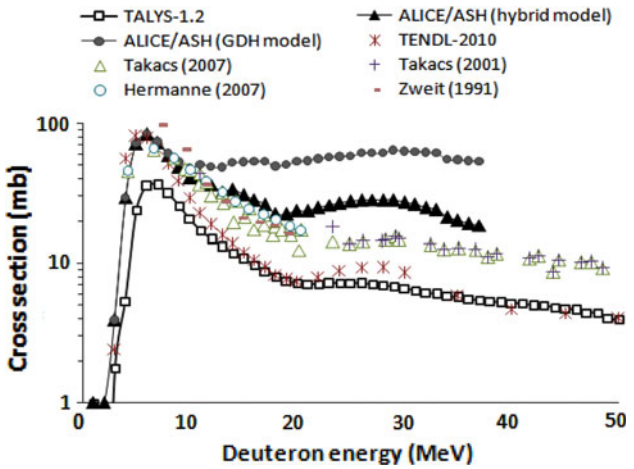

Fig. 6 Excitation function of ^{nat}Ni(d, x)^{61}Cu reaction calculated by ALICE/ASH (hybrid and GDH models) and TALYS-1.2 codes and experimental data

presented as the beneficial range of energy. Figure 6 shows the comparison between cross section values reported by Takacs et al. [16, 17], Hermanne et al. [18], Zweit [27] and the results of nuclear model calculations employing the different theoretical calculations. It should be noted that TALYS-1.2 code predicted cross sections for ^{nat}Ni(d,x)^{61}Cu reaction are lower than ALICE/ASH, TENDL-2010 and experimental data. In the maximum value point to production of ^{61}Cu at 6 MeV, the ALICE/ASH (hybrid and GDH models), TENDL-2010 and experimental data are in good agreement with each others. According to the SRIM code the required thickness of target is 23.8 μm for 6° geometry of the beam toward the target (Table 1). The physical yield of ^{61}Cu was obtained 52.8 MBq/μA h.

Excitation function of ^{nat}Ni(α,x)^{61}Cu reaction

Using the ^{nat}Ni(α,x)^{61}Cu reaction to produce ^{61}Cu, the best range of incident energy was assumed 8–21 MeV whose maximum cross section by TALYS-1.2 code is 345 mb at 15 MeV (Fig. 7). In this energy range, $^{63/62/60}$Cu, $^{63/61}$Zn are simultaneously produced. ^{63}Cu is a stable isotope and could not be separated by chemical methods; therefore this reaction does not lead to produce ^{61}Cu in no-carrier added state [41, 42]. Figure 8 shows the comparison between previous published results and the results of nuclear model calculations employing the different theoretical calculations. As can be seen on Fig. 8, the predicted data by TALYS-1.2, ALICE/ASH codes and data obtained from TENDL-2010 are in acceptable agreement with Takacs et al. [14], Singh et al. [15] and Michel et al. [26]. The calculated physical yield is 167.2 MBq/μA h. The recommended target thickness was calculated using the SRIM code (Table 1).

Excitation function of ^{nat}Zn(p,x) ^{61}Cu reaction

Although natural zinc are composed of five stable isotopes (^{64}Zn 48.6%, ^{66}Zn 27.9%, ^{67}Zn 4.1%, ^{68}Zn 18.8% and ^{70}Zn

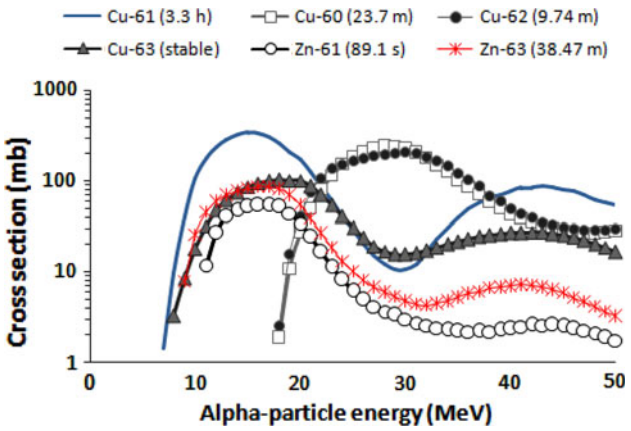

Fig. 7 Excitation function of ^{nat}Ni(α, x)^{61}Cu reaction calculated by TALYS-1.2 code

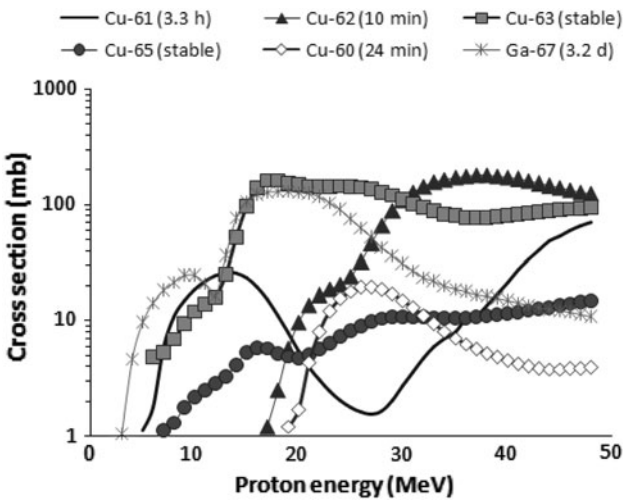

Fig. 9 Excitation function of ^{nat}Zn(p, x)^{61}Cu reaction calculated by TALYS-1.2 code

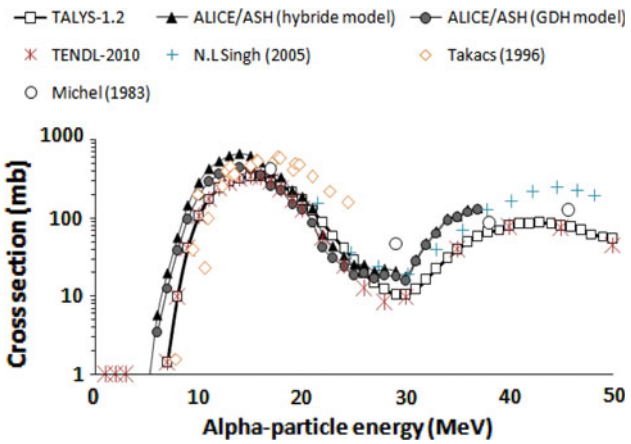

Fig. 8 Excitation function of ^{nat}Ni(α, x)^{61}Cu reaction calculated by ALICE/ASH (hybrid and GDH models) and TALYS-1.2 codes and experimental data

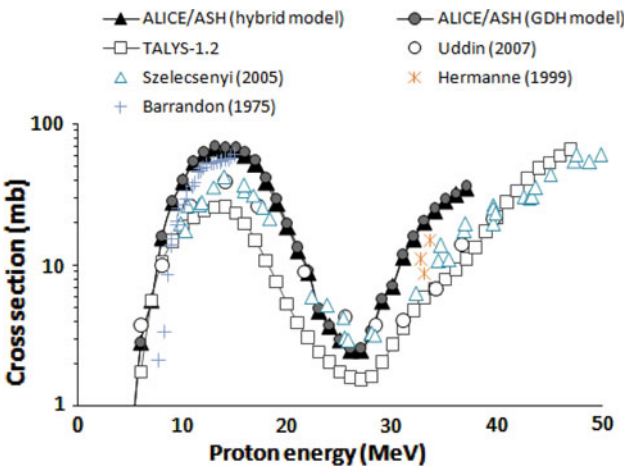

Fig. 10 Excitation function of ^{nat}Zn(p, x)^{61}Cu reaction calculated by ALICE/ASH (hybrid and GDH models) and TALYS-1.2 codes and experimental data

0.6%) but ^{61}Cu can be produced from only channel of ^{64}Zn. Figure 9 presents the excitation function for ^{61}Cu production via ^{nat}Zn(p,x) ^{61}Cu reaction. According to the figure, the best energy range for ^{61}Cu production is 6–25 MeV and the maximum cross section (25.5 mb) appears at 13 MeV. In this energy range there are some impurities such as $^{60/63/65}$Cu and ^{67}Ga. Since ^{63}Cu and ^{65}Cu are stable isotopes and could not be separated by chemical methods, this reaction does not lead to production of ^{61}Cu in no-carrier added form. The results obtained from in this study and the previous published experimental data are compared in Fig. 10. Recommended thickness of the target is 56.5 μm for 6° geometry beam toward the target (Table 1). Theoretical physical yield in view of the chosen energy range is 110.7 MBq/μA h.

Excitation function of ^{59}Co(α,2n) ^{61}Cu reaction

Through this reaction to produce ^{61}Cu the best range of incident energy was assumed 16–35 MeV that maximum cross-section is 292 mb at 25 MeV. In this energy range ^{57}Co (271.7 days), ^{58}Co (70.8 days), and ^{62}Cu (10 min) impurities are simultaneously produced (Fig. 11). To avoid ^{57}Co production, its beneficial excitation functions occur between 16 and 27 MeV. As the natural cobalt is composed of 1 stable isotope (^{59}Co 100%), this reaction is considered the best reaction to no-carrier added production of ^{61}Cu at cyclotron. Figure 12 shows the comparison of calculated data obtained from in this study and previous experimental data. Physical yield and target thickness were calculated by

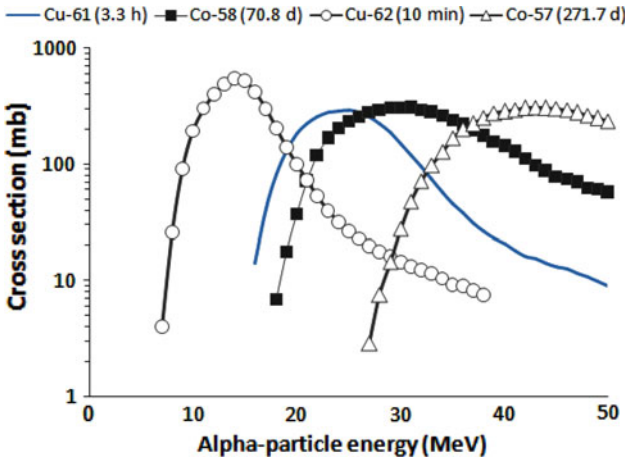

Fig. 11 Excitation function of ^{59}Co(α, 2*n*)^{61}Cu reaction calculated by TALYS-1.2 code

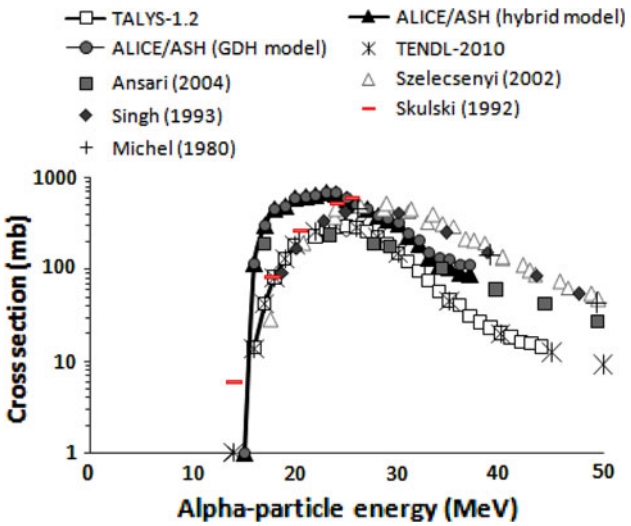

Fig. 12 Excitation function of ^{59}Co(α, 2*n*)^{61}Cu reaction calculated by ALICE/ASH (hybrid and GDH models) and TALYS-1.2 codes and experimental data

considering TALYS-1.2 code and SRIM data (Table 1). Recommended thickness of the target is 153.2 μm for 6^0 geometry beam toward the target (Table 1). The calculated physical yield is 249 MBq/μA h.

Target preparation

Among the possibilities to produce ^{61}Cu, with respect to existing facilities, we employed ^{nat}Ni(*p*,*x*)^{61}Cu reaction to test the target preparation. The medical application require highly enriched ^{61}Ni target. The natural nickel target was prepared by stack foil technique reported by Saleh et al. [10]. High purity Ni foils (99.9%) from Goodfellow Metals Ltd UK, of thickness (12.6 and 25.2 mm) were used as targets (circular foils of 10 mm diameter) [10]. In this study we employed electroplating technique to prepare ^{nat}Ni target. Natural nickel (99.99% purity, Aldrich) was electroplated on a gold-coated copper backing (48 μm thickness, 11.69 cm^2). Appropriate quantities of nickel metal were dissolved in hot 6 M nitric acid and evaporated to dryness. The residue was treated with concentrated sulfuric acid followed by dilution with de-ionized water. The volume of the solution was adjusted to approximately 400 mL with de-ionized water. The PH was then adjusted to 3–4 with concentrated sodium hydroxide and the final volume was 450 mL. This solution was transferred to the cell and used for electroplating with a 50 mA cm^2 dc current density at 45 °C temperature. The complete electroplating process took 12 h [43].

Conclusions

In this work we employed ALICE/ASH (hybrid and GDH models) and TALYS-1.2 codes to calculation the excitation functions of ^{61}Ni(*p*,*n*)^{61}Cu, ^{nat}Ni(*p*,*x*)^{61}Cu, ^{nat}Ni(*d*,*x*)^{61}Cu, ^{nat}Ni(α,*x*)^{61}Cu, ^{nat}Zn(*p*,*x*)^{61}Cu and ^{59}Co(α,2*n*)^{61}Cu reactions. The ^{61}Cu physical yield was evaluated with attention to excitation function and stopping power. Among these possibilities to produce ^{61}Cu, ^{nat}Ni(α,*x*)^{61}Cu, ^{61}Ni(*p*,*n*)^{61}Cu and ^{59}Co(α,2*n*)^{61}Cu reactions have higher cross sections compared to other reactions but bombardment ^{nat}Ni via alpha particles doesn't lead to produce ^{61}Cu in no-carrier added form. Therefore, ^{61}Ni(*p*,*n*)^{61}Cu and ^{59}Co(α,2*n*)^{61}Cu reactions are considered as the best reaction to no-carrier added production of ^{61}Cu at cyclotron.

References

1. Watanabe S, Iida Y, Suzui N, Katabuchi T, Ishii S, Kawachi N, Hanaoka H, Matsuhashi S, Endo K, Ishioka NS (2009) Production of no-carrier-added ^{64}Cu and applications to molecular imaging by PET and PETIS as a biomedical tracer. J Radioanal Nucl Chem 280:199–205
2. Katabuchi T, Watanabe S, Ishioka NS, Iida Y, Hanaoka H (2008) Production of ^{67}Cu via the ^{68}Zn(*p*,2*p*)^{67}Cu reaction and recovery of ^{68}Zn target. J Radioanal Nucl Chem 277:467–470
3. Jalilian AR, Sabet M, Rowshanfarzad P, Kamali-dehghan M, Akhlaghi M, Mirzaii M (2006) Optimization of the production of [^{61}Cu]diacetyl-bis(N4-methylthiosemicarbazone) for PET studies. J Radioanal Nucl Chem 269:147–154
4. Jalilian AR, Nikzad M, Zandi H, Nemati Kharat A, Rowshanfarzad P, Akhlaghi M, Bolourinovin F (2008) Preparation and evaluation of [^{61}Cu]-thiophene-2-aldehyde thiosemicarbazone for PET studies. Nucl Med Rev 11:41–47
5. Massoud TF, Cambhir SS (2003) Molecular imaging in living subjects: seeing fundamental biological processes in a new light. Genes Dev 17:545–580

6. Sadeghi M, Enferadi M, Nadi H (2010) Study of the cyclotron production of ^{172}Lu: an excellent radiotracer. J Radioanal Nucl Chem 286:259–263
7. Sadeghi M, Enferadi M, Nadi H, Tenreiro C (2010) A novel method for the cyclotron production no-carrier-added ^{93m}Mo for nuclear medicine. J Radioanal Nucl Chem 286:141–144
8. Sadeghi M, Enferadi M, Aboudzadeh M, Sarabadani P (2010) Production of ^{122}Sb for the study of environmental pollution. J Radioanal Nucl Chem 287:585–589
9. Sadeghi M, Mirazaee M, Gholamzadeh Z, Karimian A, Novin FB (2009) Targetry and radiochemistry for no-carrier-added production of ^{109}Cd. Radiochim Acta 97:113–116
10. Saleh FS, AlMugren KS, Azzam A (2007) Excitation functions of (p, x) reactions on natural nickel between proton energies of 2.7 and 27.5-MeV. Appl Radiat Isot 65:104–113
11. Michel R, Brinkmann G (1980) On the depth-dependent production of radionuclides ('A' between 44 and 59) by solar protons in extraterrestrial matter. J Radioanal Nucl Chem 59:467–510
12. Michel R, Weigel H, Herr W (1978) Proton-induced reactions on nickel with energies between 12 and 45 MeV. Z Phys A 286:393–400
13. Barrandon JN, Debrun JL, Kohn A, Spear RHA (1975) Study of the main radioisotopes obtained by irradiation of Ti, V, Cr, Fe, Ni, Cu and Zn with protons from 0 to 20 MeV. Nucl Instrum Meth 127:269–278
14. Takacs S, Tarkanyi F, Kovacs Z (1996) Excitation function of alpha-particle induced nuclear reactions on natural nickel. Nucl Instrum Methods B 113:424–428
15. Singh NL, Mukherjee S, Gadkari MS (2005) Excitation functions of alpha induced reactions on natural nickel up to 50 MeV. Int J of Mod Physics Part E 14:611–629
16. Takacs S, Tarkanyi F, Kiraly B, Hermanne A, Sonck M (2007) Evaluated activation cross sections of longer-lived radionuclides produced by deuteron-induced reactions on natural nickel. Nucl Instrum Methods B 260:495–507
17. Takacs S, Szelecsenyi F, Tarkanyi F, Sonck M, Hermanne A, Shubin A, Dityuk A, Mustafa MG, Youxiang Zh (2001) New cross-sections and inter-comparison of deuteron monitor reactions on Al, Ti, Fe, Ni and Cu. Nucl Instrum Methods B 174:235–258
18. Hermanne A, Tarkanyi F, Takacs S, Kovalev SF, Ignatyuk A (2007) Activation cross sections of the 64Ni(d, 2n) reaction for the production of the medical radionuclide ^{64}Cu. Nucl Instrum Methods B 258:308–312
19. Singh BP, Sharma M, Musthafa MM, Bhardwaj HD, Prasad R (2006) A study of pre-equilibrium emission in some proton- and alpha-induced reactions. Nucl Instrum Methods A 562:717–720
20. Szelecsenyi F, Blessing G, Qaim SM (1993) Excitation functions of proton induced nuclear reaction on enriched ^{61}Ni and ^{64}Ni: possibility of production of no-carrier-added ^{61}Cu and ^{64}Cu at a small cyclotron. Appl Radiat Isot 44:575–580
21. Tanaka S, Furukawa M, Chiba M (1972) Nuclear reactions of nickel with protons up to 56 MeV. J Inorg Nucl Chem 34:2419–2426
22. Uddin MS, Khandaker MU, Kim KS, Lee YS, Kim GN (2007) Excitation functions of the proton induced nuclear reactions on ^{nat}Zn up to 40 MeV. Nucl Instrum Methods B 258:313–320
23. Tarkanyi F, Takacs S, Ditroi F, Hermanne A, Sonck M, Shubin YN (2004) Excitation functions deuteron induced nuclear reactions on natural zinc up to 50 MeV. Nucl Instrum Methods B 217:531–550
24. Szelecsenyi F, Suzuki K, Kovacs Z, Takei M, Okada K (2001) Alpha beam monitoring via ^{nat}Cu^{+} alpha processes in the energy range from 40 to 60 MeV. Nucl Instrum Methods B 184:589–596
25. Hermanne A, Szelecsenyi F, Sonck M, Takacs S, Tarkanyi F, Vanden WP (1999) New cross section data on ^{68}Zn(p, 2n)^{67}Ga and ^{nat}Zn(p, xn)^{67}Ga nuclear reactions for the development of a reference data base. J Radioanal Nucl Chem 240:623–630
26. Michel R, Brinkmann G, Stock R (1983) Integral excitation functions of alpha-induced reaction on titanium, iron and nickel. Radiochim Acta 32:173–178
27. Zweit J, Smith AM, Downey S, Sharma HL (1991) Excitation functions for deuteron induced reactions in natural nickel: production of no-carrier-added ^{64}Cu from enriched ^{64}Ni targets for positron emission tomography. Appl Radiat Isot 42:193–197
28. Al-Saleh FS, Al-Harbi AA, Azzam A (2006) Excitation functions of proton induced nuclear reactions on natural copper using a medium-sized cyclotron. Radiochim Acta 94:391–396
29. Szelecsenyi F, Suzuki K, Kovacs Z, Takei M, Okada K (2002) Production possibility of $^{60,\ 61,\ 62}$Cu radioisotopes by alpha induced reactions on cobalt for PET studies. Nucl Instrum Methods B 187:153–163
30. Ansari MA, Alslam MA, Sathik NPM, Ismail M, Rashid MH (2004) Excitation functions of alpha-induced reaction in cobalt and pre-equilibrium effects. Int J Mod Phys E 13:585
31. Singh NL, Agraval S, Rama Rao J (1993) Excitation function for alpha-particle-induced reactions in light-mass nuclei. Can J Phys 71:115
32. Skulski W, Fornal B, Broda R, Jastrzebski J, Koczon P, Kownacki J, Opacka M, Pawlat T, Pienkowski L, Plociennik W, Sieniawski J, Singh PP, Styczen J, Wrzesinski J (1992) Mass and charge release by the evaporation of particles from compound nuclei around mass 60. Z fuer Phys A Hadrons Nucl 342:61–66
33. Michel R, Brinkmann G (1980) Alpha-induced reactions on cobalt. Nucl Phys Sect A 338:167–189
34. Szelecsényi F, Kovács Z, Suzuki K, Okada K, van der Walt TN, Steyn GF, Mukherjee S (2005) Production possibility of ^{61}Cu using proton induced nuclear reactions on zinc for PET studies. J Radioanal Nucl Chem 263:539–546
35. Ziegler JF, Biersack JP, Littmark U (2006) The code of SRIM–the stopping and range of ions in matter. IBM Research, New York
36. Koning AJ, Rochman D (2010) TENDL-2010: TALYS-based evaluated nuclear data. Nuclear Research and Consultancy Group (NRG) Petten, The Netherlands. http://www.talys.eu/tendl-2010. Accessed 8 Dec 2010
37. Koning AJ, Hilairey S, Duijvestijn M (2009) TALYS-1.2: a nuclear reaction program. User manual, NRG, Netherlands, http://www.talys.eu/download-talys. Accessed 22 Dec 2009
38. Broeders CHM, Konobeyev AY, Korovin YA, Lunes VP, Blann M (2006) ALICE/ASH–Pre-compound and evaporation model code system for calculation of excitation functions, energy and angular distributions of emitted particles in nuclear reaction at intermediate energies, FZK-7183. http://bibliothek.fzk.de/zb/berichte/FZKA7183.pdf. Accessed June 2006
39. Konobeyev AY, Korovin, YA, Pereslavtsev PE (1997) Code ALICE/ASH for calculation of excitation functions, energy and angular distributions of emitted particles in nuclear reactions. Obninsk Institute of Nuclear Power Engineering, Obninsk
40. Sadeghi M, Zandi N, Afarideh H (2011) Targetry and specification of ^{167}Tm production parameters by different reactions. J Radioanal Nucl Chem. doi:10.1007/s10967-011-1422-2
41. Naught M, Wilkinson A, Nic M, Jirat J, Kosata B, Jenkins A (2006) IUPAC, compendium of chemical terminology. XML on-line corrected version: http://goldbook.iupac.org. ISBN 0-9678550-9-8. doi:10.1351/goldbook
42. de Goeij JJM, Bonardi ML (2005) How do we define the concepts specific activity, radioactive concentration, carrier, carrier-free and no-carrier-added? J Radioanal Nucl Chem 263:13–18
43. Sadeghi M, Amiri M, Roshanfarzad P, Avila M, Tenreiro C (2008) Radiochemical studies relevant to the no-carrier added production of $^{61,\ 64}$Cu at a cyclotron. Radiochim Acta 96:399–402

1.5.2 ^{67}Cu production routes

^{67}Cu can be produced via different methods using proton, deuteron, and heavy-ion accelerators, electron accelerators, and nuclear reactors (see Fig. 1.30). In each method, the probability of a nuclear reaction is assessed by the cross-section as a function of the energy. Thus exact knowledge of the individual values is of uppermost importance, especially when optimization of the product yield and radionuclide purity is considered.

In recent years the most limiting factor for using ^{67}Cu in clinical trials was its availability. Although studies on ^{67}Cu production started about 45 years ago in nuclear reactors since the last decades, its production shifted to particle accelerators due to some problems associated with nuclear reactors and also the higher quality of the ^{67}Cu product that is required for its medical use in targeted therapy [151, 152].

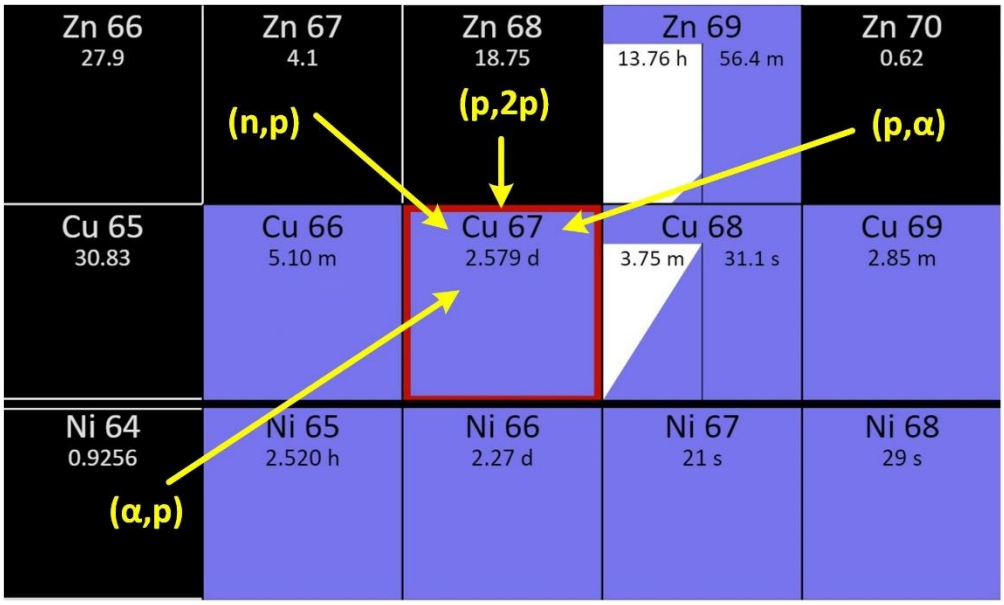

Fig. 1.30 ^{67}Cu different production routes

$^{68}Zn(p,2p)^{67}Cu$ reaction route

^{67}Cu can be produced through irradiation of an enriched ^{68}Zn target at a proton accelerator. A number of earlier experimental data can be found in the literature about the production of ^{67}Cu by proton irradiations on enriched ^{68}Zn or natural Zn targets.

Regarding TENDL data [153], the maximum cross-section for ^{67}Cu through the $^{68}Zn(p,2p)^{67}Cu$ reaction channel amounts to 22 mb at energy of 70 MeV [154]. According to published data, the energy threshold for production of ^{67}Cu using a proton accelerator is at about 30 MeV. A cyclotron with energies above 35 MeV is considered a high-energy cyclotron [155], and the number of research cyclotrons generating such high-energy protons is limited. Therefore, this reaction cannot be regarded as the best reaction route to provide sufficient activities per year regarding the low cross-section of the reaction in most available cyclotrons.

Based on a previously published study (using the 70 MeV proton cyclotron at the ARRONAX facility), the yield of ^{67}Cu obtained in the energy range 35-70 MeV is 24.25 MBq/μAh.

Among other studies, some authors studied ^{67}Cu production using a high energy proton beam (660 MeV). Such a high energy range is not reasonable for cost-effectiveness and commercial production of ^{67}Cu [155, 156].

$^{70}Zn(p,\alpha)^{67}Cu$ reaction route

One of the other possible routes to the production of ^{67}Cu is proton irradiation of enriched ^{70}Zn with a cyclotron. According to previously published data, the maximum cross-section for the production of ^{67}Cu from this reaction is 14 mb at an energy of 17 MeV [157]. Regarding previous published study, the thick-target yield of ^{67}Cu through the irradiation of 100 % enriched ^{70}Zn material was 38 MBq/μAh [158].

Although ^{67}Cu production through this reaction channel does not require a high energy cyclotron, the very low abundance of ^{70}Zn in natural zinc (below 1 %) does not make this reaction channel cost-effective with a sufficient production yield [158].

$^{64}Ni(\alpha,p)^{67}Cu$ reaction route

Regarding Skakun in 2004 [159], the maximum cross-section for this reaction is 36 mb at an energy of 20 MeV. According to the data, the production of ^{67}Cu by irradiation of ^{64}Ni metal targets yielded activities of 544 kBq/μAh. Thus this reaction cannot provide high enough activities due to the low cross-sections.

Although the production activity using a ^{64}Ni target is lower than that using a Zn target via the $^{68}Zn(p, 2p)^{67}Cu$ or $^{nat}Zn(p,x)^{67}Cu$ channels, the quality (specific activity and radionuclide purity) is much better [160].

$^{67}Zn(n,p)^{67}Cu$ reaction route

The production of ^{67}Cu is feasible by neutron irradiation of ^{67}Zn targets through the $^{67}Zn(n,p)^{67}Cu$ reaction channel [161, 162]. However, this method requires fast neutrons with energies above 1 MeV, which requires a fast nuclear reactor. Since the number of fast neutron reactors is limited globally and due to the low cross-sections of this reaction channel, this method is not considered the best for routine production of ^{67}Cu.

Based on a previously published study, neutron irradiation of highly enriched ^{67}Zn targets in a thermal neutron reactor yielded 29.6 MBq/g ^{67}ZnO of ^{67}Cu and due to the highly enriched target, production of undesired isotopes, particularly ^{65}Zn and ^{69m}Zn, was reduced significantly which would be detrimental to the recovery of valuable target material [162]. The target material in the study was zinc oxide since oxides targets are ideal for reactor-based irradiations, as they dissolve readily in mineral acids and are simple to work with.

Photonuclear reaction through $^{68}Zn(\gamma,p)^{67}Cu$

Currently, charged-particle reactions with proton, deuteron, or alpha and neutron-induced fission are considered the main routes for producing diagnostics and therapeutic radioisotopes. But, unfortunately, some disadvantages come along with both production techniques. As mentioned above, nuclear reactors are planned to be shut down in a few years due to problems concerning safety and, also security concerns [163]. Concerning the production using cyclotrons,

although they may not have such risks compared to nuclear reactors, they can only produce a limited range of medical radionuclides and very limited activities, especially for therapeutic radionuclides. Due to these problems, using a high-intensity and high-energy photon beam for radioisotope production through photonuclear reaction is becoming an option. Additionally, the photonuclear radioisotope production method allows obtaining high specific activities for radioisotopes, which are not produced in adequate quantities to satisfy current demands. In this technique, when a photon is incident on a nucleus, the excited nucleus decays to release the excitation energy. The most probable decays are single or multi neutron emission and, after that, proton emission.

The cross-section for photonuclear reactions is usually at energies from 8 to 30 MeV which are called Giant Dipole Resonances (GDR) (see Fig. 1.31 & Fig. 1.32) [164, 165]. Several de-excitation events such as nuclear fission, emission of neutrons or gamma rays, or combinations of these usually occur through GDR. The photons for irradiating photo-nuclear reaction's targets are commonly produced as Bremsstrahlung radiation [166] using electron accelerators. Bremsstrahlung radiation is electromagnetic radiation given off mainly by an electron due to a sudden slowing down or deflection caused by another charged particle's electric field (see Fig. 1.33). In the photonuclear reaction process, the high electron beam hits to a converter target, and through Bremsstrahlung radiation, photons are produced. Convertor should be a material with high atomic density and high melting points such as tantalum or tungsten. After that, photons hit the production target for radioisotope production (see Fig. 1.34).

The theoretical estimated activity of ^{67}Cu through irradiation of enriched ^{68}Zn target, via photonuclear production, is 16.25 (GBq/125 kW.d). This calculation has been done via MCNPX code for a high energy 40 MeV Rhodotron, with 125 kW power [167]. Regarding the experimental published data [168], the yield for the irradiation of natural zinc target via a 41 MeV Linac with a beam current of 200 μA, obtained 10.33 mCi/g.day (382.21 MBq/g.day). It should be noted that regarding Fig. 1.32, there is a huge discrepancy between TENDL and experimental data, and it emphasizes the need for further experimental measurements.

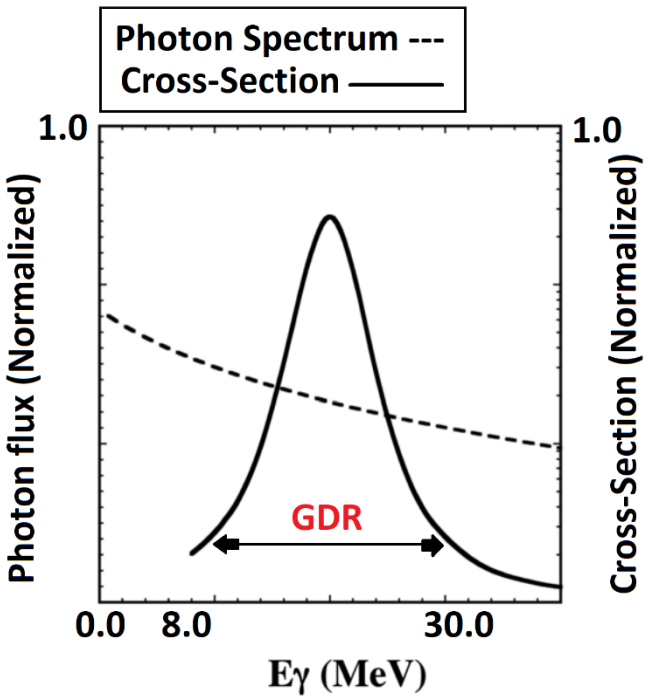

Fig. 1.31 GDR region for photonuclear reaction. The GDR region is defined as a range in cross-section in which most photon-absorption reactions for almost all of the nuclei occur at. In this region (which is in the photon energy range of 8-30 MeV for most middle and heavy mass nuclei), the nucleus acts as a whole, and a collective oscillation of all protons against all neutrons in a nucleus happens. The schematic representation for the Bremsstrahlung photon flux variations as a function of photon energy reveals a decreasing trend of photon flux with increasing photon energy. This implies that not all of the incident photons contribute to photonuclear reactions, and in fact, only those whose energy are in the GDR range can be considered for radionuclide production.

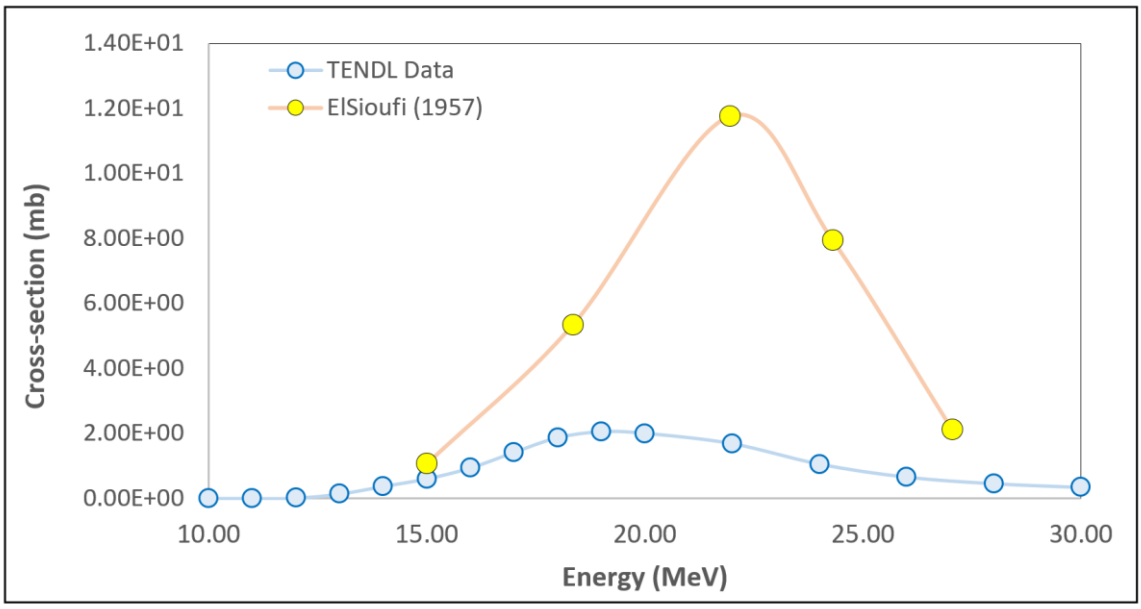

Fig. 1.32 Cross-section of ^{67}Cu via $^{68}Zn(\gamma,p)^{67}Cu$ reaction obtained through TENDL compared with experimental data[169]

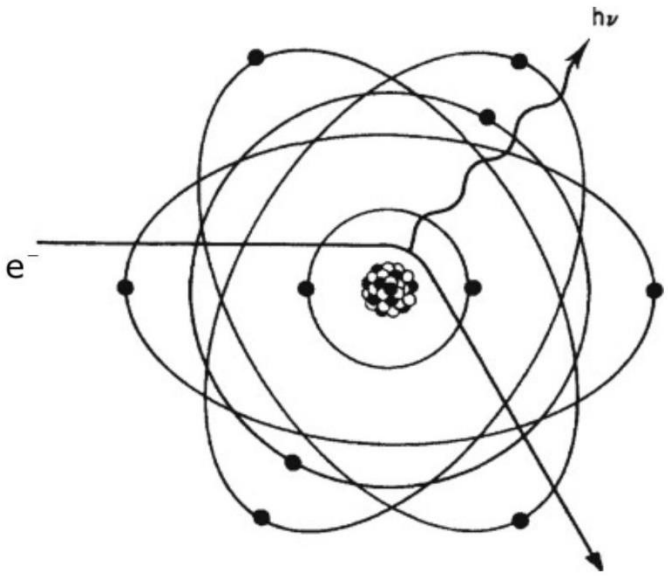

Fig. 1.33 Bremsstrahlung radiation [170]

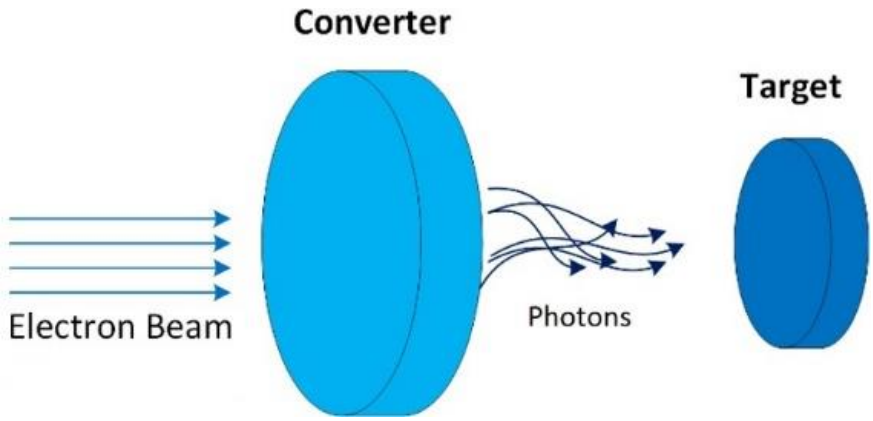

Fig. 1.34 Photonuclear reaction process for radioisotope production

1.6 Radiochemical separation

Radiochemistry is the discipline dedicated to the study of the chemical and physical properties of radionuclides. Using nuclear reactions, stable nuclides are transformed to radioactive ones and it is needed to separate the nuclide of interest from other radioactive and non-radioactive nuclides that are present. This can be achieved by performing radiochemical separation consisting of conventional separation techniques adapted to radiochemistry's special needs.
There are different methods to separate copper from the zinc target after irradiation. Each technique has its radiochemical yield, and can be considered depending on the application of the radioisotope.

1.6.1 Solvent extraction

Solvent extraction, also called liquid-liquid extraction, is when the compounds are first mixed and then separated based on their relative solubilities in two different immiscible liquids. Mixing has an effect on the extraction, which produces little droplets with a large surface for transfer. Immiscible liquids are usually aqueous solution and an organic solvent and separate into layers after being intensively mixed (see Fig. 1.35) [171]. Immiscible liquids that do not dissolve in one another form layers when put together. This is due to the fact that each liquid differs in polarity. In this case, one particular liquid is on top and another is on the bottom depending on their density. The method of extraction usually is performed by a separatory funnel. First, the liquid mixture is added to the separatory funnel. Then the extraction solvents are added to the funnel. When extracting solvent is mixed with a solution containing solute, then solute from the original solvent gets transferred into an extracting solvent. When stirring is stopped the extracting solvent forms a separate layer and now contains the solute of interest. Based on the Nernst law [172], when a solute component that is soluble in both solvents is added, it gets distributed between them. Then molecules of the solute pass from solvent A to B and from B to A. Finally, at dynamic equilibrium, the rate at which molecules of the solute pass from one solvent to the other is balanced. Then (see Eq. 1.6),

$$\frac{Concentration\ of\ X\ in\ A}{Concentration\ of\ X\ in\ B} = K_D \qquad \text{Eq. 1.6}$$

where K_D is distribution coefficient.

The solvent extraction method for separation of copper from Zn targets is based on two steps; 1.) selective extraction of Cu dithizonate ($CuDz_2$, where dithizonate is $C_{13}H_{12}N_4S$) into an organic solvent from a dilute acidic solution of the bulk Zn target, 2.) back extraction of Cu into the aqueous phase. The separation of Cu and Zn target was previously studied by solvent extraction with copper-dithizone [173]. Regarding the previous studies, copper dithizonate has a large extraction constant value* in acid solution compared to other metals present in the solution of the irradiated Zn target.

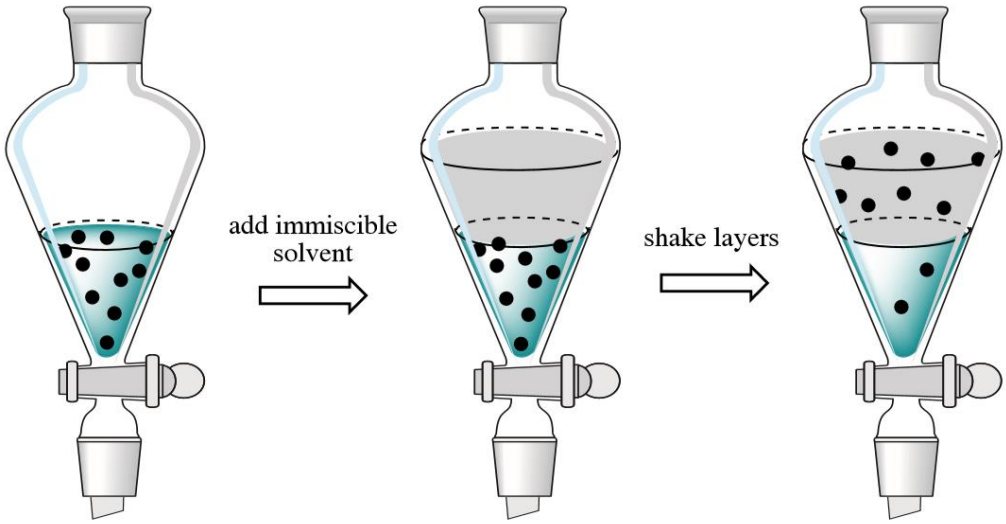

Fig. 1.35 Schematic of solvent extraction method [174]

1.6.2 Extraction chromatography

Extraction chromatography is an extraction process performed in a multi-stage manner on a packed column. This technique combines the selectivity and diversity of solvent extraction with the high extraction efficiencies of column separation. In this technique, there is a stationary phase that consists of one or more ionophores dissolved in an organic solvent and they are

* extraction constant is the concentration ratio of a chemical in one phase to the concentration in a second phase when the two concentrations are at equilibrium.

immobilized on a porous material (see Fig. 1.36). The porous material is usually composed of porous silica with particle sizes ranging between 50 and 150 µm. One of the commercially used columns in this process is TEVA resin which was developed by Horwitz et al. [175].

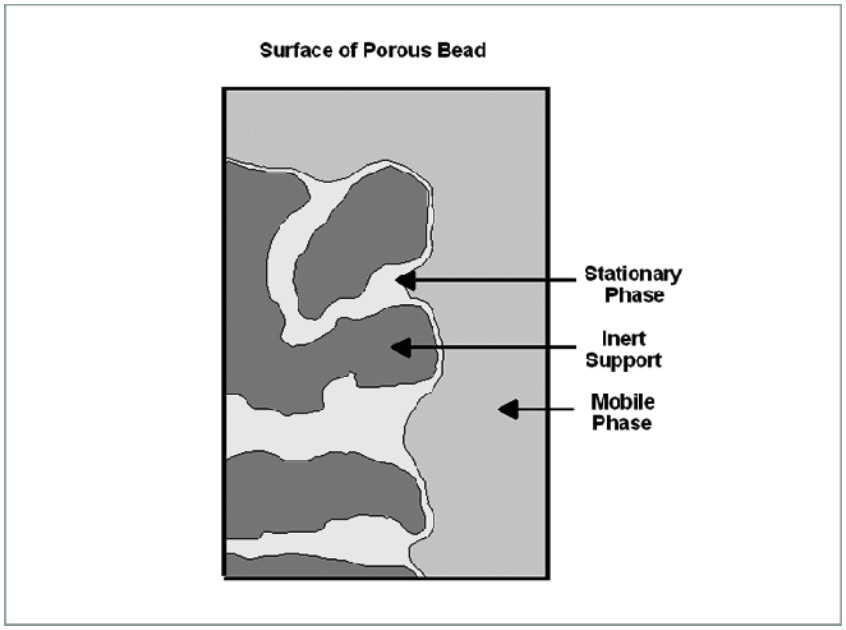

Fig. 1.36 Extraction chromatography resin bead [176]

1.6.3 Exchange chromatography

Ion exchange chromatography refers to a process allowing the separation of ions based on their affinity to ion exchangers. The principle of separation is, therefore, by reversible exchange of ions between the ions present on the ion exchangers and the target ions in the sample solution. The ion-exchange chromatography like other chromatography consists of both mobile and stationary phases. The mobile phase is an aqueous buffer into which the sample has been introduced, and the stationary phase is usually an inert organic matrix [177]. All ion exchange chromatography depends on electrostatic interactions between the resin groups and the element of interest. Since buffer pH and ionic strength dramatically affect element binding to the column, it is important to ensure that buffer pH is properly selected. It is better to readjust buffer pH after adjusting salt concentration and to be sure that buffer counterions are compatible and have the

same charge as the resin. In this case, for negatively charged cation exchange resins, phosphate buffers are the best choice. There are two types of chromatography to separation of the elements; anion-exchange chromatography and cation-exchange chromatography [178, 179]. However, it has been shown that anion-exchange chromatography can also be used as the second step after cation-exchange chromatography for metal separation such as Cu from Zn, which needs some additional steps such as heating to dryness [178, 179].

1.6.3.1 Cation-exchange chromatography

Cation-exchange chromatography is a form, which is used to separate ions or ionic complexes based on their net surface charge. Cation-exchange chromatography uses a negatively charged ion exchange resin with an affinity for ions or ionic complexes having net positive surface charges (see Fig. 1.37).

Regarding Fig. 1.37, in the cation-exchange chromatography process, metal ions (e.g., Cu^{+2}) that are initially contained in an aqueous solution are exchanged with ions initially contained in a solid resin (see Fig. 1.37). This process can be illustrated by reaction (see Eq. 1.7) [180, 181].

$$\overline{R^{-}H^{+}} + A^{+} \rightarrow \overline{R^{-}A^{+}} + H^{+} \qquad \text{Eq. 1.7}$$

where R is the ion exchanger; A^{+} is a positively charged metal ion

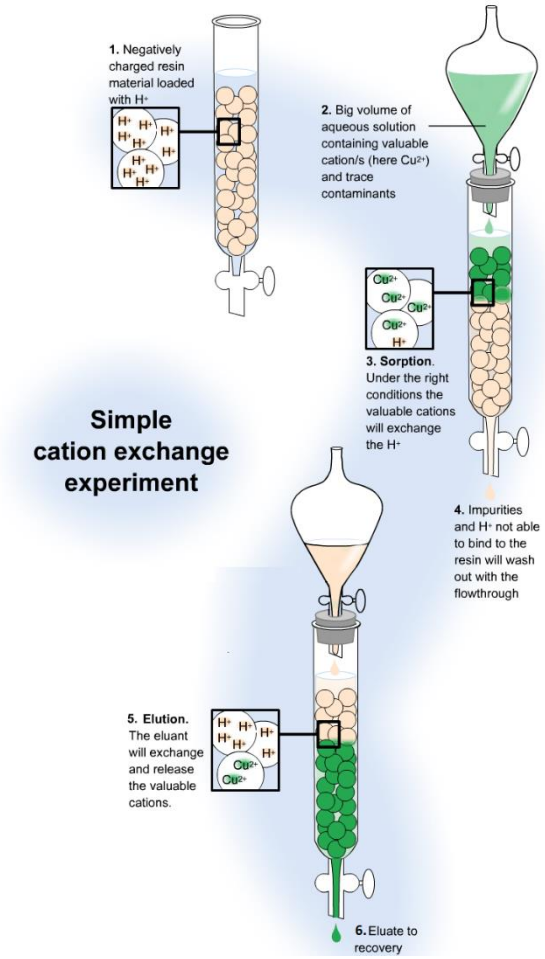

Fig. 1.37 Schematic diagram of a cation exchange chromatography [182]

The separation of Cu from the Zn target can be performed mostly by a TK201 resin (Triskem International, France). The selectivity of the resin for elements is presented as the weight distribution ratio (Dw), which can be obtained by radiotracer measurements. Dw, is obtained by measuring the amount of a given metal ion taken up by a measured weight of resin from a given volume of an aqueous solution [176] (see Eq. 1.8).

$$D_w = \frac{A_0 - A_s}{A_s} \cdot \frac{mL}{g} \qquad \text{Eq. 1.8}$$

where $A_0 - A_S$ = activity sorbed on a known weight of the resin (g), and A_S = the activity in a known volume (mL) of solution.

1.6.3.2 Anion-exchange chromatography

This technique moves the interaction that exists between charged molecules in a sample and oppositely charged moieties in the stationary phase of the chromatography matrix. Anion-exchange chromatography uses a positively charged ion exchange resin with an affinity for ions or ionic complexes having net negative surface charges (see Fig. 1.38). In this technique, the charge is easily manipulated by the pH of the buffer used. The crude sample containing ions or ionic complexes is used as the liquid phase. When the liquid phase passes through the chromatographic column, ions or ionic complexes bind to oppositely charged sites in the stationary phase. Then the separated molecules eluted using a solution of varying ionic strength (see Fig. 1.38) [178, 179]. The process involving anions is called anion exchange (see Eq. 1.9).

$$\overline{R^+Y^-} + B^- \rightarrow \overline{R^+B^-} + Y^- \qquad \text{Eq. 1.9}$$

where B^- and Y^- are anions or negatively charged metal ion complexes [182].

Regarding the IAEA TECDOC-1955 [179], Cu was separated from the irradiated Zn target through ion-exchange chromatography in two processes. First, the solution was passed through a cation exchange column (AG 50W), and then the column was washed with 9 M HCl to remove Zn and Cu ions. Afterward, the solution in 6 M HCl passed through the anion exchange column (AG 1X8). Then Cu was eluted by 2 M HCl (see Fig. 1.39). Regarding the study, a radionuclide purity of more than 97% was obtained [179].

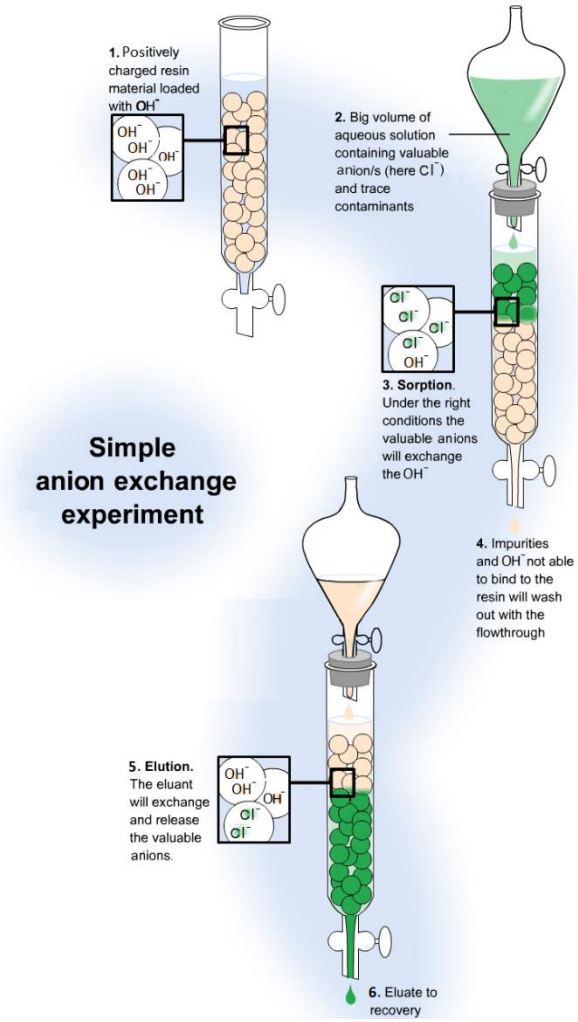

Fig. 1.38 Schematic diagram of an anion exchange chromatography [182]

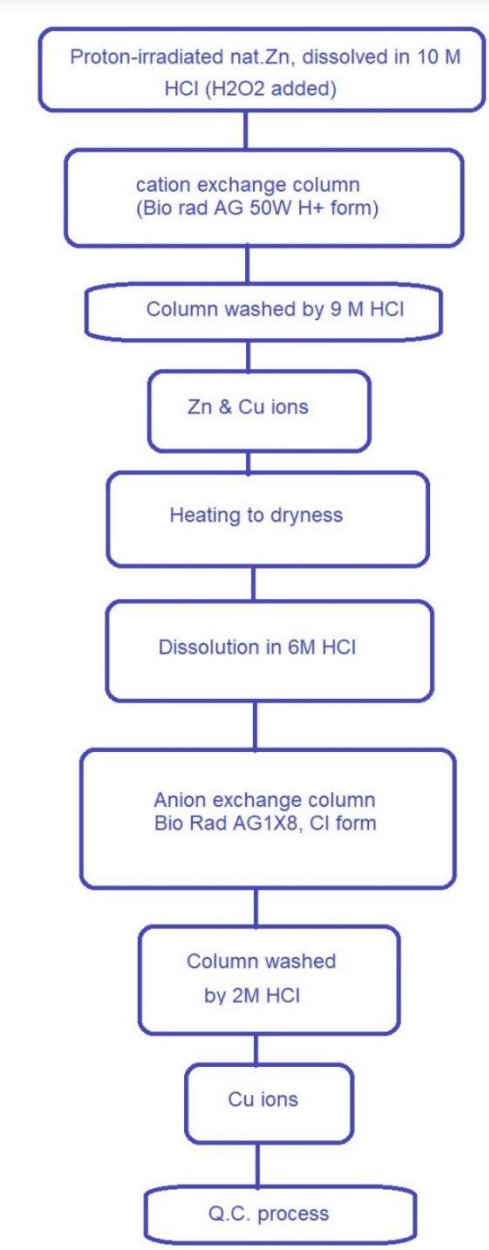

Fig. 1.39 Schematic steps for the separation of ^{61}Cu from an irradiated Zn target (courtesy of A. Jalilian, IAEA, Austria) [179]

1.6.4 Evaporation technique or distillation

The principle in this method is based on different vapor pressures at the same temperature. So, regarding the fact that the vapor pressure of Zn is much higher than that of Cu at the same temperature (see Fig. 1.40), Zn can be transferred into the gas phase at elevated temperatures while Cu with low vapor pressure remains in the solid phase and cannot be evaporated. On this basis, it is possible to separate Zn from Cu or other metals at temperatures above 900 ^{0}C at atmospheric pressure [183]. Ma et al., used the evaporation technique to separate and recover Zn form other elements. Regarding their results, Zn was successfully separated by this technique under vacuum conditions [183].

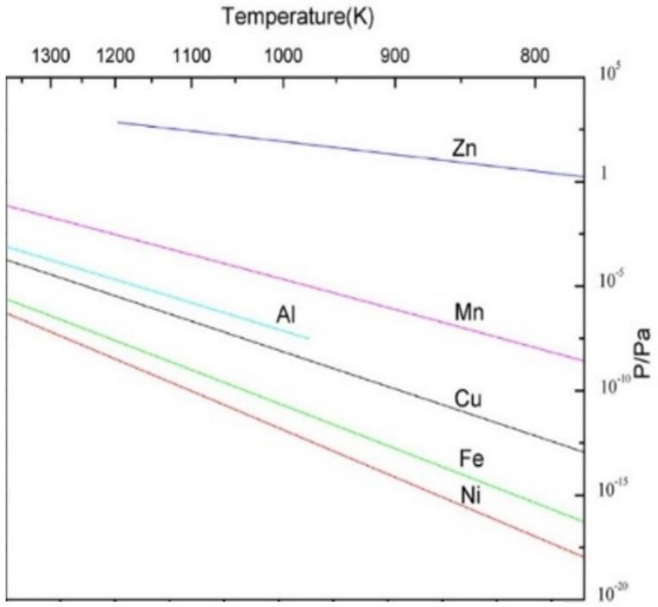

Fig. 1.40 Relationship between saturation vapor pressure and temperature for various metals [183]

1.7 Radiolabeling with Cu isotopes

An important requirement for the application of radiopharmaceuticals is the formation of a thermodynamically stable and kinetically inert complex of the radionuclide with an appropriate chelator, which is linked to the targeting agent (peptide). The coordination of Cu(II) has previously been investigated with different chelators and peptides, including ATSM, PSMA, DOTATOC, and DOTATATE [184, 185, 186, 173, 175]. For example, ATSM (Dithiosemicarbazone) was recently

labeled with ^{61}Cu for head and neck cancer diagnostics [186, 185]. ATSM labeled with Cu isotopes is considered a promising hypoxia marker for PET, which has been found to be predictive of the outcome of radiotherapy treatment [185]. Furthermore, ^{64}Cu-PSMA-617 also was studied for PET imaging of prostate cancer [173]. Prostate-Specific Membrane Antigen (PSMA) is a cell surface protein that shows overexpression in PC cells and restricted expression in normal tissue [185]. ^{64}Cu-DOTATOC was also investigated for PET–CT imaging of neuroendocrine tumors (NETs), which need sophisticated imaging modalities due to the fact that tumors originate in different parts of the body and have different clinical symptoms [187]. NETs are usually found in the lungs and gastrointestinal tract. DOTATOC, also known as edotreotide, is a chelator plus a targeting molecule used to treat gastro-entero-pancreatic neuroendocrine tumors and can be labeled with Cu radioisotopes (Fig. 1.41). Moreover, ^{64}Cu-DOTATATE was recently studied for patients with positive neuroendocrine tumors (NETs). Regarding this study, the radiochemical purity of ^{64}Cu-DOTATATE was higher than 95% [188].

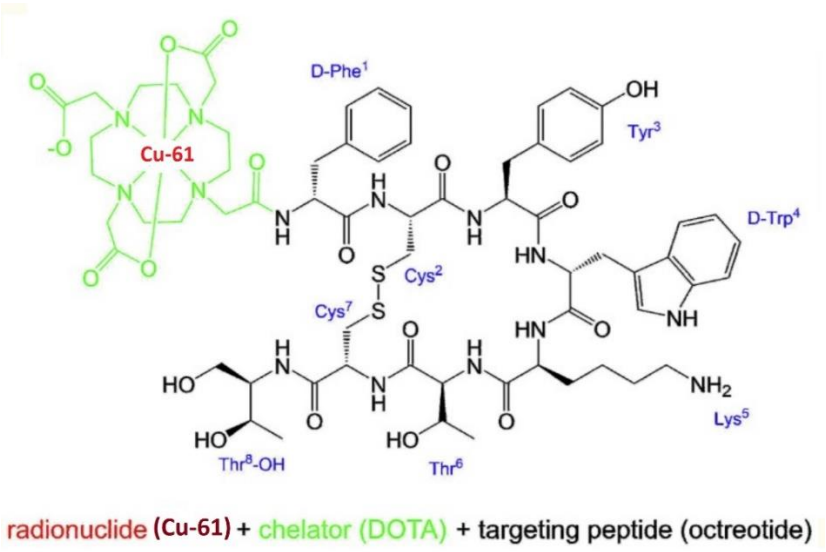

Fig. 1.41 Radiolabeling schematic of DOTATOC with ^{61}Cu [189]

1.8 Status of research of $^{61}Cu/^{67}Cu$

^{61}Cu with a half-life of 3.3 h is a positron-emitting radionuclide, which emits β^+ particles with an energy of 1.22 MeV and high BR (60%). ^{61}Cu is considered as one of the most interesting radionuclides for nuclear medicine research because of its appropriate nuclear properties and ease of production. [115]. Compared to ^{64}Cu with a BR of 17.7%, ^{61}Cu has much higher BR (60%), resulting in smaller doses and more than three times the detection sensitivity when PET imaging is used. On this basis, ^{61}Cu production via different reaction routes has been investigated in the literature [190]. A review in ^{61}Cu production methods showed that cyclotron production of ^{61}Cu with protons as a projectile is of upmost interest due to the possibility of ^{61}Cu production in high activity required for radiolabeling. As an illustration, in 2005, Szelecsényi et al. produced a high activity of about 1.4 GBq/μAh via the bombardment of ^{nat}Zn using 67–60 MeV protons [191]. It is Worth pointing out that the use of ^{nat}Zn results in the production of several Ga (^{63}Ga, ^{64}Ga, ^{65}Ga, ^{66}Ga, ^{67}Ga, ^{68}Ga, ^{69}Ga, ^{70}Ga) and Zn (^{62}Zn, ^{63}Zn, ^{64}Zn, ^{65}Zn, ^{66}Zn, ^{67}Zn, ^{68}Zn, ^{69}Zn, ^{70}Zn) isotopes with a mixture of stable, short and long half-lives [192]. So, significantly better results can be obtained using enriched ^{64}Zn targets. In addition, this method produces no-carrier added ^{61}Cu, and therefore, is appropriate from the chemical separation point of view [193]. Among the other possibilities, cyclotron production of $^{61}Ni(p,n)^{61}Cu$ and $^{62}Ni(p,2n)^{61}Cu$ require the very low isotopic abundance ^{61}Ni (about 1.13%) and ^{62}Ni (3.59%) as an enriched target [194]. Additionally, $^{63}Cu(p,t)^{61}Cu$ and $^{65}Cu(p,t2n)^{61}Cu$ nuclear reaction routes produce ^{61}Cu in carrier added form with low specific activity (for more details on the definition of specific activity, refer to Appendix B). Some preliminary studies and clinical trials evaluated the potential clinical role of ^{61}Cu for diagnostic purposes [195, 196]. For example, ATSM (Dithiosemicarbazone) was recently labeled with ^{61}Cu for head and neck cancer diagnosis [197, 198]. Regardless of the researches performed in ^{61}Cu, large-scale ^{61}Cu production, and clinical application are limited and still in preclinical studies.

^{67}Cu is one of upmost interest in production and application as a therapeutic radionuclide; however, its use is restricted due to its low availability. ^{67}Cu with a half-life of 2.6 d fits in many cases with the biological half-lives of many pharmaceutical compounds. Moreover, the mean beta-decay energy of ^{67}Cu with 0.141 MeV is appropriate for therapeutic application. The emitted

gamma-rays of ^{67}Cu (184.6 keV, 93.1 keV, and 91.3 keV) are comparable in intensities and can be used for SPECT. Different production routes of ^{67}Cu via cyclotron [199], nuclear research reactor [200], and electron accelerator [201] have been studied in the literature [202]. ^{67}Cu production in the (p,2p) nuclear reaction on natural Zn leads to ^{67}Cu production with low specific activity because of significant quantities of co-produced stable Cu isotopes [203, 204]. Accordingly, using an enriched ^{68}Zn can be useful; however, the (p,2p) reaction for ^{67}Cu production requires a high-energy proton beam (the threshold is 30 MeV), which is rare [200, 202]. As an illustration for ^{67}Cu production through the (p,2p) reaction, reported yields of about 0.503 MBq/μAh and 6.5 MBq/μAh for the irradiation of respectively, 29 g natural ZnO and 3.7 g of enriched ZnO (99% enriched in ^{68}Zn) could be found in the literature [202]. An alternative route for ^{67}Cu production is via the ^{70}Zn(p,α)^{67}Cu reaction. This method of ^{67}Cu production is very costly due to the very low isotopic abundance of ^{70}Zn in natural Zn (about 0.6 %). Even with the use of a highly enriched ^{70}Zn (99.7%) target, the production yield is still low (8.14-15.5 kBq/mg mAh) [202, 205]. ^{67}Cu production in nuclear research reactors via the (n,p) nuclear reaction on ^{67}Zn requires fast neutrons, which can be produced in fast nuclear reactors. These types of nuclear reactors are extremely limited in use. As an illustration for ^{67}Cu production via fast neutrons, it was shown that about 0.13 MBq/h g ZnO (93.0% enriched in ^{67}Zn) for 1.5 $\times 10^{12}$ n/cm^{2}s fast neutron flux could be obtained [200]. An attractive, alternative production route for ^{67}Cu relies on the photonuclear reaction on enriched ^{68}Zn through the (γ,p) reaction. It was shown that the production of up to 600 GBq/day could be obtained using a 35 MeV e-Linac with 100 kW beam power, enough to treat 60 patients/day [206]. Accordingly, among all production routes, the production investigation via photonuclear reaction is of upmost interest. ^{67}Cu chemical separation, and its use for radioimmunotherapy were reviewed in the literature [201]. ^{67}Cu radiolabeling also was investigated in the literature recently [207, 208]. Regarding the study performed in 2017, ^{67}Cu was used for labeling cyclam-RAFT-c(-RGDFK-)4 for ovarian cancer peritoneal metastases [207]. However, ^{67}Cu is only in the clinical trial phase due to some problems associated with large-scale production. Indeed, for large-scale production, one should move to high-energy and high-power electron beam accelerators. By providing such facilities, ^{67}Cu can enter the market for clinical application [209].

1.9 Aims of the thesis

Cancer treatment is of great importance in all countries and particularly attracted considerable attention in economically developed as well as developing countries where cancer is the first and the second frequent cause of death, respectively. Early detection advancement (known as diagnostics), in addition to improvement in new treatment modalities (known as therapeutics), are among the leading purposes in nuclear medicine (in which about 95% of the radiopharmaceuticals are employed for diagnosis, while the rest are used for therapy). If the same pharmaceutical is radiolabeled with radionuclides that are suitable for diagnostic and therapeutic applications, this is referred to the theranostics. Theranostic matched isotope pairs are those, where the employed radionuclides are from the same chemical element. One of the most promising pairs is ^{61}Cu/^{67}Cu due to the appropriate properties, including radioactive decay, β-particle energy, γ-radiation energies, and potential radiolabeling with different peptides.

The investigation of optimized ^{61}Cu/^{67}Cu production routes for radiopharmaceutical applications is the first aim of this project. The cyclotron-based ^{61}Cu production through the (p,α) reaction (as one of the best ^{61}Cu production routes) and microtron ^{67}Cu production through photonuclear (γ,p) reaction is the next aim of the project. Irradiations were performed at the 18 MeV proton cyclotron of SWAN Isotopen AG and at METAS (Federal Institute of Morphology), respectively.

The next aim of this thesis was to introduce a novel and innovative two-step semi-automated radiochemical separation method for the efficient radiochemical separation of a micro amounts of Cu from the irradiated bulk Zn target. For this purpose, two different connected successive processes were designed and applied to efficiently perform the radiochemical separation. The first step relied on the difference in evaporation temperature. While the second step is based on a semi-automated extraction chromatography to separate Cu from the remaining traces of Zn inside the sample. As the final aim of the thesis, radiolabeling of ^{61}Cu with an appropriate peptide is performed and the radiolabeling purity is investigated using Thin-Layer Chromatography (TLC) to demonstrate the possible potential use of the final product for clinical purposes.

CHAPTER 2
^{61}Cu/^{67}Cu THERANOSTIC PAIR PRODUCTION

2.1 Introduction

In this study, the production of ^{61}Cu from a ^{64}Zn target via proton-induced nuclear reactions is regarded as an attractive option due to low impurity production and high obtainable yield. In this project, a solid Zn target was used for the irradiation at the cyclotron. It is worth pointing out that a PET medical cyclotron solid target consists of the target material deposited onto a backing plate cooled by water and possibly by helium gas flow. Solid targets can be prepared through different methods such as rolling, pressing and mechanical reshaping, and electrodeposition [210]. The choice of techniques is usually based on a compromise between the cost of implementation and the approach to fulfilling the requirements. One of the most common techniques for solid target preparation is pressing in which thicknesses of hundreds of μm to some mm [210] can be achieved, but this technique is not suitable for hard materials.

Additionally, as a part of the study, ^{67}Cu production through photonuclear (γ,p) reaction was performed. Currently, charged-particle reactions with proton, deuteron, or alpha and neutron-induced fission are considered the main routes for producing diagnostics and therapeutic radioisotopes. But, unfortunately, some disadvantages come along with both production techniques (for more details, refer to introduction chapter).

2.2 Materials and Methods

2.2.1 Chemicals

Enriched ^{64}Zn metal pieces were purchased from Trace Sciences International company, Canada, with 99.4% purity (see Table 2.1 & Table 2.2 for isotopic and chemical impurities) and were used as the target for ^{61}Cu production. Natural Zn foil (purchased from Goodfellow, USA) was used as the target for ^{67}Cu production. The main chemical impurities of the Zn foil are given in table 2.3. Moreover, enriched ^{68}Zn (for ^{67}Cu production with higher activity compared to natural Zn target) was purchased from Trace Sciences International, Canada, with 97.8% purity (see Table 2.4 & Table 2.5 for isotopic and chemical impurities).

Table 2.1 Isotopic composition of ^{64}Zn, given from certificate (Trace Sciences International, Canada)

Isotope	64	66	67	68	70
Enrichment (%)	99.4	0.39	0.04	0.17	<0.01

Table 2.2 Chemical impurities in ^{64}Zn target, given from certificate (Trace Sciences International, Canada)

Element	Impurity measurements (ppm)
Al	10
Ca	8
Cd	<3
Cu	30
Fe	30
K	<10
Mg	10
Na	50
Pb	<10
Si	70

Table 2.3 Chemical impurities of the natural Zn foil, given form certificate (Goodfellow, USA)

Element	ppm
Ag	15
Bi	1
Ca	2
Cd	5
Cu	10
Fe	5
Pb	10
Si	3
Sn	5

Table 2.4 Isotopic composition of ^{68}Zn, given from certificate (Trace Sciences International company, Canada)

Isotope	64	66	67	68	70
Enrichment (%)	0.99	0.81	0.38	97.8	0.02

Table 2.5 Chemical impurities in ^{68}Zn target, given from certificate (Trace Sciences International company, Canada)

Element	Impurity measurements (ppm)
Al	20
Ca	6
Cd	100
Cu	5
Fe	50
K	<10
Mg	40
Na	5
Pb	200
Si	20

2.2.2 Instruments used for measurements

The activity of the produced ^{67}Cu (before and after chemical separation) was identified and quantified by γ-ray spectrometry using an N-type high-purity germanium (HPGe) coaxial detector (Ortec, USA) and the InterSpec software (see Fig. 2.1). A dose calibrator (ISOMED 2010, Nuclear–Medizintechnik Dresden GmbH, Germany) (see Fig. 2.1) was employed for the quantitative determination of the ^{61}Cu activity and calibrated for ^{18}F.

HPGe Detector

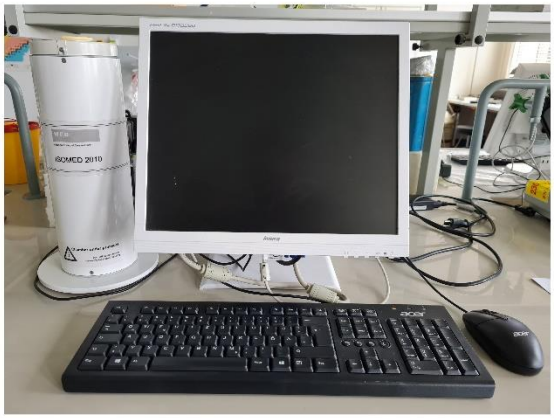

Dose Calibrator

Fig. 2.1 HPGe detector setup for gamma spectroscopy and dose calibrator

2.2.3 Irradiations of targets for ^{61}Cu production

Regarding the investigations of the ^{61}Cu production routes performed before, ^{61}Cu production using enriched ^{64}Zn targets through the ^{64}Zn(p,α)^{61}Cu was considered the best route due to high-yield production and optimal proton energies (which makes production on available low energy cyclotrons possible) [211].

Accordingly, 500 mg enriched ^{64}Zn metal pieces were used for target preparation. Since Zn evaporates at atmospheric pressure at above 900 ^{0}C (close to the boiling point of Zn), the metallic ^{64}Zn piece was evaporated inside an oven at a temperature of about 950 ^{0}C, and then the produced Zn powder was obtained and gathered. This technique helped us to purify the Zn target and to convert it to powder form. Then, the next step was to press enriched ^{64}Zn powder in the form of a pellet. To make the targets, 85 mg enriched ^{64}Zn powder was pressed with 2 tons of pressure (see Fig. 2.2). The thickness and diameter of the target were measured to be 0.5 mm and 6 mm, respectively.

After solid target preparation using a press, the pellet was placed inside a magnetically closing coin as the target holder (Fig. 2.3). The target coin is cooled during the irradiation using water cooling from the back and direct helium gas cooling the target coin from the front part. The material employed for the coin has to provide high thermal conductivity and the lowest chemical reactivity. Usually, two materials are chosen: aluminum EN AW-6082 or pure niobium (In our work, we used aluminum EN AW-6082). The back part of the coin should be able to completely stop the protons to avoid contamination of the cooling water, especially when dealing with high-energy cyclotrons [212].

Fig. 2.2 Hydraulic press for making pellets. A pressure of 2 tons was used to press the ^{64}Zn target

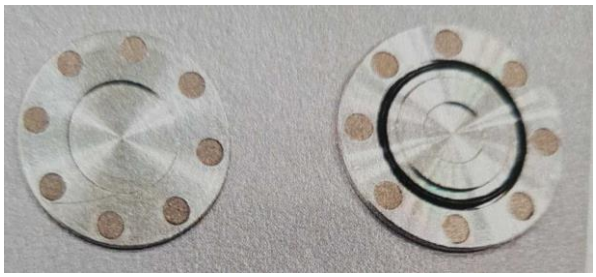

Fig. 2.3 Front cover (left) and back part (right) of the coin for inserting the ^{64}Zn target inside, preparing for irradiation [212]

Later the prepared solid ^{64}Zn target was irradiated with a proton beam of 25 µA at an energy of 15 MeV for 2 hours at the Bern medical cyclotron at SWAN Isotopen AG. Then, the irradiated target was inserted automatically in a shuttle (Fig. 2.4) which was then transferred outside the cyclotron bunker by the TEMA Sinergie transfer system (Fig. 2.5). This system transfers the shuttle to the receiving station in the second bunker. For this study, several irradiations have been performed.

Fig. 2.4 Coin and shuttle for target irradiation and delivery

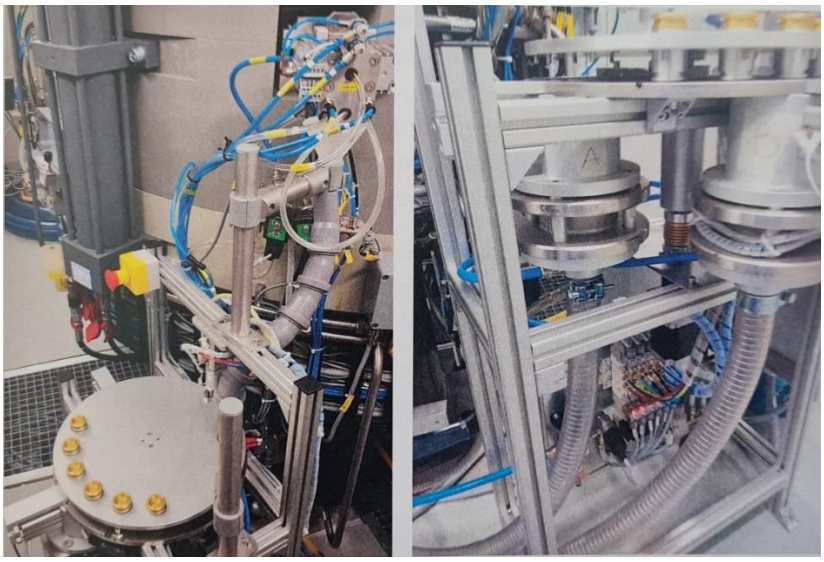

Fig. 2.5 Target irradiation station and delivery system (TEMA) for the irradiated targets at Bern medical cyclotron [212]

2.2.4 Irradiations for ^{67}Cu production

In this study, ^{67}Cu was produced through the photonuclear interaction based on the ^{68}Zn(γ,p)^{67}Cu nuclear reaction route. The reaction ^{68}Zn(γ,p)^{67}Cu is considered promising and applicable for obtaining ^{67}Cu in non-carrier added form and also large production yield. In the photonuclear reaction method, radionuclides are produced through irradiation of targets with high-energy photons. So, producing considerable photon flux is of great importance for large-scale production.

Accordingly, the ^{68}Zn target was irradiated at the Microtron at METAS (Federal Office of Metrology). METAS has a Scanditronics M22 Microtron electron accelerator that produces electron beam energies from 5.3 MeV to 22.4 MeV and is equipped with two beamlines [213]. One beamline is used for producing therapeutic photons, mainly for dosimetric studies. The second beamline is mainly used for research purposes.

In this case, the Microtron at METAS with an electron beam energy of 22 MeV and an electron beam current of 20 µA (see Fig. 2.6) was used to irradiate 450 mg natural Zn foil. Irradiation of natural zinc resulted in ^{65}Zn production through the ^{66}Zn(γ,n)^{65}Zn reaction. The produced ^{65}Zn can conveniently be used as a tracer during the radiochemistry process.

Later, a 413 mg enriched ^{68}Zn, was irradiated to prevent the co-production of radionuclidic impurities. The irradiation time was 8 hours.

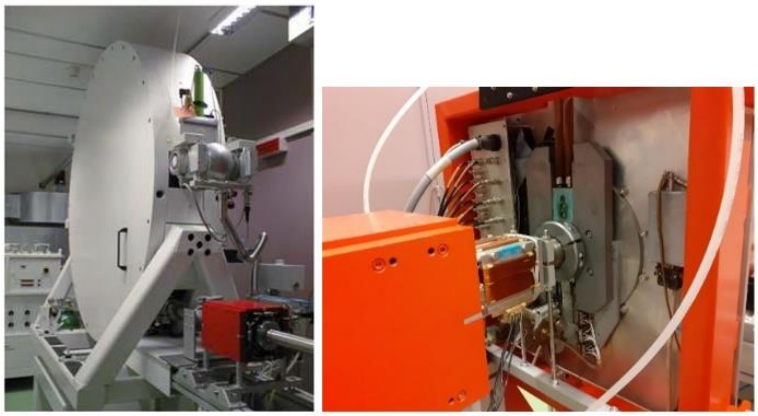

Fig. 2.6 Microtron and target set-up for irradiations at METAS

2.3 Results

2.3.1 ^{61}Cu production

^{61}Cu production was achieved by irradiation of an enriched ^{64}Zn target at the Bern medical cyclotron at SWAN Isotopen AG (See Table 2.6). After 1 hour of cooling time, the shuttle containing the coin was transferred via a lead container (Fig. 2.7) to the department of chemistry, biochemistry, and pharmacy (DCBP) of the University of Bern. Due to the irradiated target's high activity, two pieces of equipment were designed by Adrian Bigler and Ronald Zingg at the workshop at DCBP to open the shuttle and the irradiated coin, respectively (see Figs. 2.8 and 2.9). The first one is the shuttle opening device, designed to open the shuttle easily without radiation dose exposure to the fingers. The second piece of equipment, which is named “Coin-Master”, allows to open the coin and remove the irradiated Zn target safely. Using this equipment, the irradiated coin is inserted into the coin-master (Fig. 2.9) with long tweezers and then, by pushing and pulling the handle, the coin is opened, and after that, by turning back the equipment, the irradiated target pellet falls out of the coin. Evidently, the dose exposure is reduced significantly due to a reduced manual contact with the coin.

Fig. 2.7 Transport box for a lead container containing the shuttle with the irradiated target coin

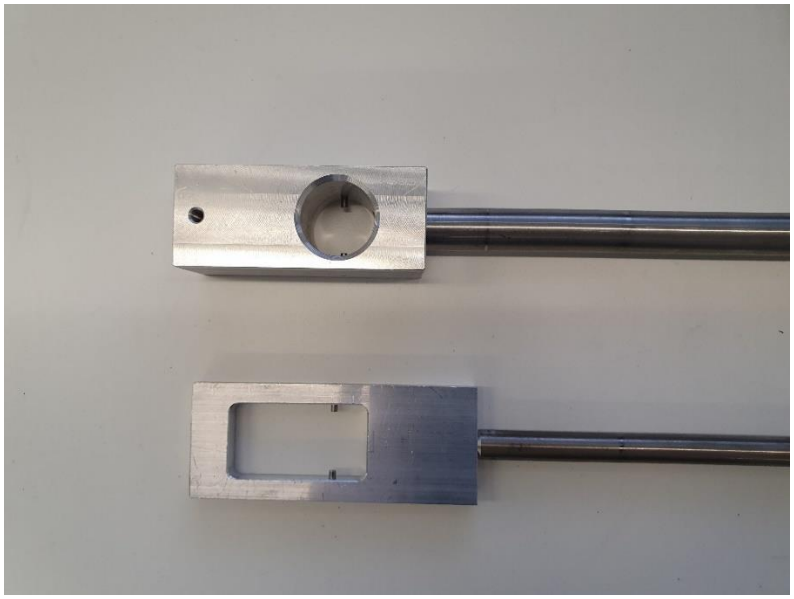

Fig. 2.8 Shuttle opening device

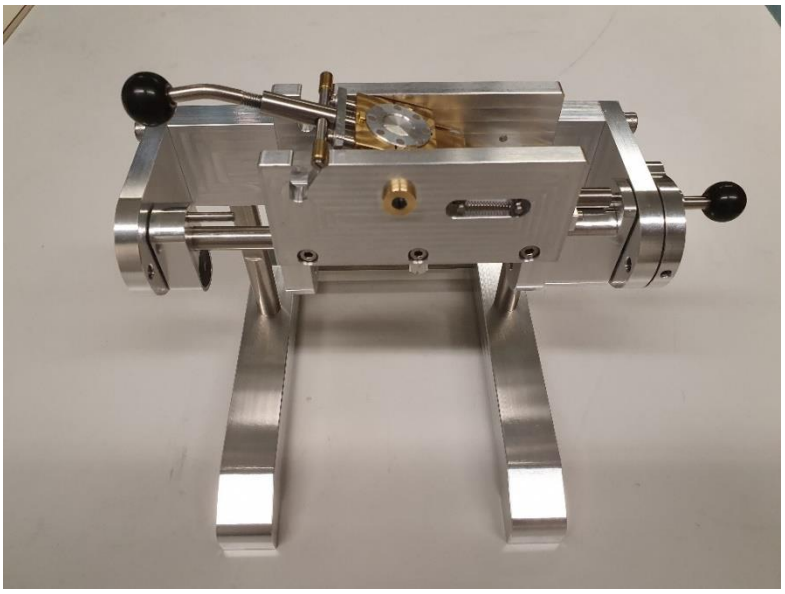

Fig. 2.9 Coin-Master for opening the irradiated coin

Finally, due to the high activity of the target, the ^{64}Zn target was inserted into a dose calibrator to measure the activity.

Table 2.6 details of ^{64}Zn target irradiations at the cyclotron at SWAN Isotopen AG for ^{61}Cu production

Target	Thickness (µm)	Irradiation time (h)	Irradiation Beam current (µAh)	Irradiation Energy (MeV)	^{61}Cu Activity at EOB (Experimental) (GBq)	^{61}Cu Activity at EOB (Theoretical*) (GBq)
^{64}Zn	345	2	10.9	11.63	0.684	0.626
^{64}Zn	320	2.2	11.26	11.63	0.750	0.662
^{64}Zn	330	4	18.8	11.69	1.35	0.910
^{64}Zn	500	3.5	18.8	11.69	2.17	2.01

*The theoretical activity calculations were performed using the IAEA Medical Isotope Browser (see: https://www-nds.iaea.org/relnsd/isotopia/isotopia.html)

After a few days and a reduction of the activity, one sample of the irradiated ^{64}Zn target was measured with both the HPGe detector (Fig. 2.10 shows the peaks of ^{61}Cu including 66.7, 281.9, 371.9, 509.8, 587.3, 654.68, 815.1, 839.6, 907.1 and 1183.6 keV) and the dose calibrator. Since the measurement via HPGe detector was taken after chemical separation, no impurities were observed in the peak. The reason for measurement after the chemical separation is due to the high activity of the target at the initial time of the process, which could not be measured via HPGe detector due to saturation of the detector even at a large distance.

Regarding the data (Table. 2.7), the correlation factor for the dose calibrator is about 1.5. Fig. 2.11 shows the decay scheme of ^{61}Cu.

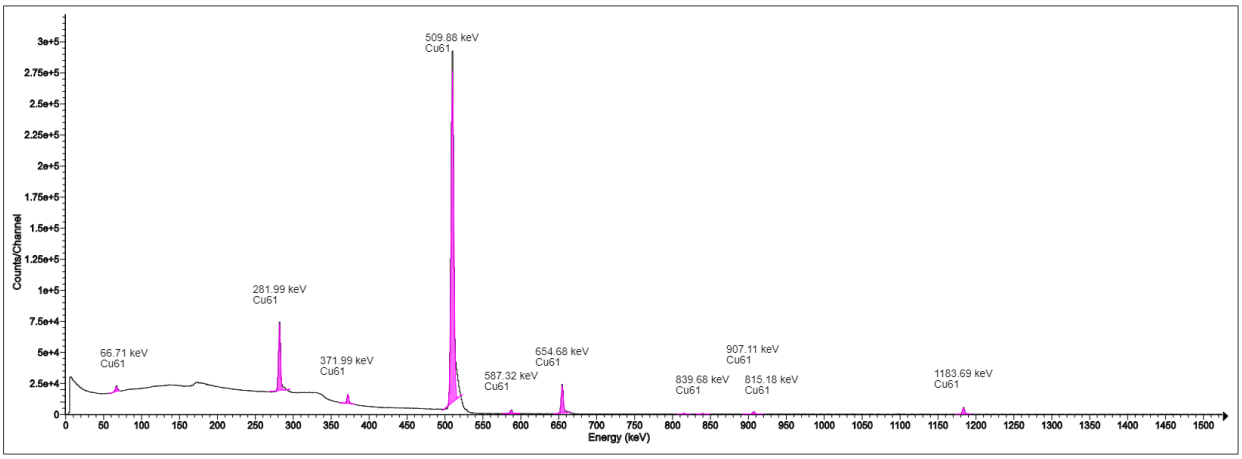

Fig. 2.10 Peaks of ^{61}Cu measured with a HPGe detector

Table 2.7 Correlation factor between HPGe detector and dose calibrator for measuring the activities

Activity measured by HPGe	Energy/Branching ratio	Activity measured by dose calibrator	Correlation factor
0.113 MBq	283 keV/12.7 %	0.17 MBq	1.50
0.116 MBq	511 keV/123 %	0.17 MBq	1.46
0.112 MBq	373 keV/2.1 %	0.17 MBq	1.52

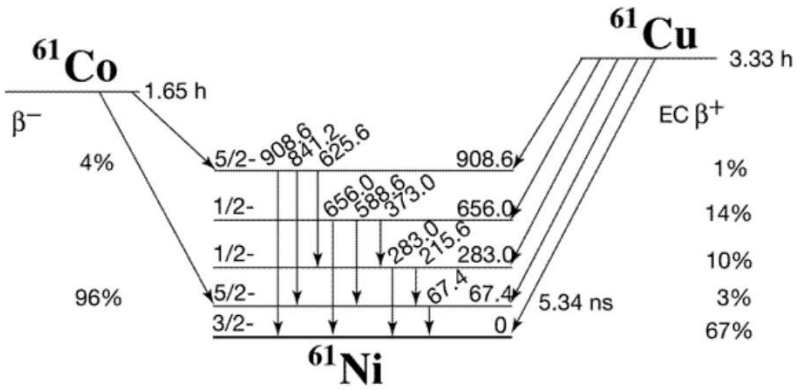

Fig. 2.11 Decay scheme of ^{61}Cu with specification of gamma branching ratio at an energy of 283 keV

2.3.2 ^{67}Cu irradiation

In this study, ^{67}Cu was produced through the irradiation of enriched ^{68}Zn and natural Zn targets at METAS. The ^{67}Cu activity was quantitatively determined with a HPGe detector (See Table 2.8). Figures 2.12 and 2.13 show the peaks of ^{67}Cu produced after irradiation through the ^{68}Zn(γ, p)^{67}Cu reaction for natural Zn and enriched ^{68}Zn targets, respectively. Regarding the peaks measured by the HPGe detector, ^{67}Cu was recognized through the peaks 93 and 184 keV.

Table 2.8 details of Zn target irradiations at Microtron at METAS for ^{67}Cu production

Target	Mass (mg)	Irradiation time (h)	Beam current µA	^{67}Cu Activity at EOB (kBq)	^{65}Zn Activity at EOB (kBq)
Natural Zn foil	369	7	21	8.6	3.9
Natural Zn foil	474	8	17.7	12.3	5.7
^{68}Zn metal basis (97.8%)	413	7	20	260.9	not detected

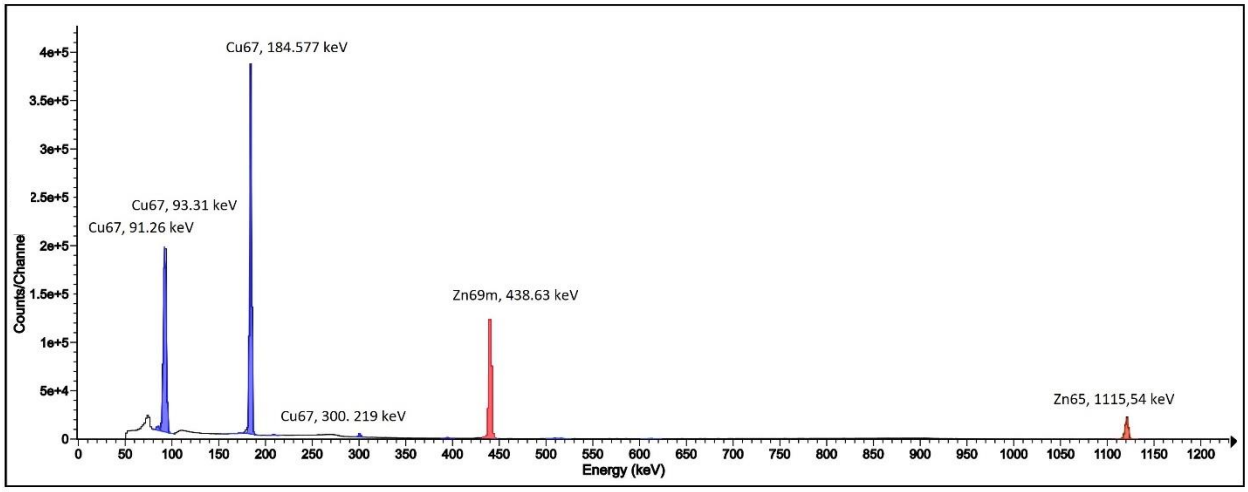

Fig. 2.12 Peaks of ^{67}Cu and ^{65}Zn measured with a HPGe detector after irradiation of a natural Zn target

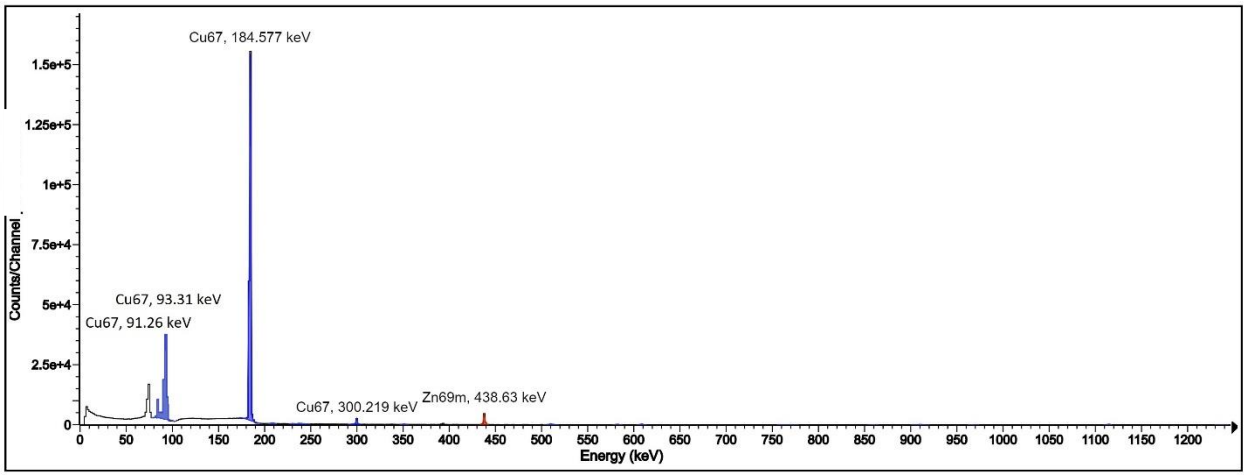

Fig. 2.13 Peaks of ^{67}Cu measured with a HPGe detector after irradiation of an enriched ^{68}Zn target

2.4 Discussion

This section of the thesis focused on the production of ^{61}Cu and ^{67}Cu at a cyclotron and a Microtron, respectively. In the case of ^{61}Cu production, the Zn target irradiation has already been investigated in previous studies [145, 214, 148]. In our study, an enriched ^{64}Zn (metal pieces) was purchased as the target material. Using the evaporation technique (see more details in chapter 3), the material was purified and converted to powder form. Using this technique, pellet targets of different thicknesses and diameters were made. In looking at the literature, Asad et al., in 2015 [145] used an enriched ^{64}Zn target for ^{61}Cu production through the ^{64}Zn(p,α)^{61}Cu reaction. However, using a foil target, which has limitations concerning the preparation of targets in different thicknesses, could be considered as a disadvantage of their study. In our work, irradiations were performed at the Bern medical cyclotron at SWAN Isotopen AG. As can be seen in Fig. 2.10, many gamma-ray energy peaks from ^{61}Cu were recognized in the HPGe gamma-ray spectrum confirming ^{61}Cu production in the irradiated Zn target. As discussed above, it is worth mentioning that no other impurities (short-or longer-lived side products) were observed after the chemical separation (see section 2.3.1). Moreover, several Zn target irradiations were performed with different beam currents, target thicknesses, and irradiation times (see Table 2.6). The results of the theoretical activity calculations using the IAEA Medical Isotope Browser were also presented in Table 2.6. As can be seen, the theoretical calculations slightly underestimate the experimental measurements probably due to the lack of accurate available cross-sections values for different proton beam energies or using the dose calibrator to estimate ^{61}Cu production activity. As Table 2.6 reveals, by increasing the thickness of the target from 330 µm to 500 µm, the beam current from 11 µA-h to 18.8 µA-h and the irradiation time from 2 to 3.5 h, the ^{61}Cu activity was increased by a factor of three up to 2.17 GBq at EOB. For facilitating comparison, Asad et al. in 2015 produced ^{61}Cu through the irradiation of enriched ^{64}Zn foil targets via 11.7 MeV proton beam energy and 20-40 µA beam current [145]. Regarding their results, the yield at EOB of enriched foil targets was obtained as 48.5-98.5 MBq/µA-h, which is relatively close to our results (115.4 MBq/µA-h). In another study, Thieme et al. in 2013 [148] used the electroplating technique to prepare enriched ^{64}Zn target. The irradiations of the targets were performed at two different cyclotrons, Cyclone 18/9 (Rossendorf) and CC 18/9 (Turku), which

differ in proton beam energy and maximal beam current. In their study, the targets were irradiated with various beam currents and different irradiation times. Regarding their results, the maximum yield they obtained was 44.8 MBq/μA-h through the irradiation of 164 mg of enriched ^{64}Zn targets via Cyclone 18/9 [148]. On this basis, compared to our results (115.4 MBq/μA-h), they obtained around 2.6 times less activity at EOB. Finally, according to the discussion presented in the introduction section of this chapter and results presented in our study and similar works, ^{61}Cu production through the ^{64}Zn(p,α)^{61}Cu reaction can be considered one of the best production routes for large-scale production.

In the case of ^{67}Cu production, ^{67}Cu was produced through the photonuclear interaction based on the ^{68}Zn(γ,p)^{67}Cu nuclear reaction route. Accordingly, natural and enriched ^{68}Zn targets were irradiated at the Microtron at METAS. The gamma-ray energy peaks of ^{67}Cu were detected with the HPGe detector for both natural and enriched Zn targets in Fig. 2.12 and Fig. 2.13, respectively. As can be seen in Fig. 2.12, ^{65}Zn and ^{69m}Zn were co-produced through the ^{66}Zn(γ,n)^{65}Zn and ^{70}Zn(γ,n)^{69m}Zn reaction, respectively, for the natural Zn target. However, in the case of using enriched ^{68}Zn target (see Fig. 2.13), ^{65}Zn was not detected, and ^{69m}Zn was observed in a relatively low quantity compared to the natural Zn target (less than 1.4% of the total activity). The results of the performed irradiation for ^{67}Cu production are presented in Table. 2.8. As can be seen, using the enriched ^{68}Zn target (in the last experiment) led to a significant increase (about 21 times more) in the activity of ^{67}Cu at EOB compared to the use of a natural Zn target (from 12.3 kBq to 260.9 kBq). However, this significant increase is not only due to using an enriched target but also due to reducing the distance between the target holder and the converter at the Microtron facility at METAS to increase the number of photons reaching the target. It is worth pointing out that ^{67}Cu production through the photonuclear interaction was also studied in the literature [215, 216]. As an illustration, Hovhannisyan et al., in 2021 [216], investigated ^{67}Cu production through photonuclear interaction. Regarding their results, ^{67}Cu was produced by irradiating natural Zn targets via bremsstrahlung photons with energies of 30 and 40 MeV. The specific activities of ^{67}Cu were obtained as 75.48 and 175.75 kBq/μA-h-g at EOB for bremsstrahlung maximum energies of 30 and 40 MeV, respectively. This significant increase in their production yield compared to our results (4.5 kBq/μA-h-g for enriched ^{68}Zn target, which corresponds to 0.83 kBq/μA-h-g for the

natural Zn target) is due to using high energy photons generated from the Linac accelerator LUE-75 [216]. In another study, Aliev et al. [215] also investigated ^{67}Cu production via photonuclear interaction using the 55 MeV electron accelerator RTM55 of the Skobeltsyn. Regarding their results, ^{67}Cu was produced by the irradiation of natural Zn in higher activities than our study (about 133 times more) due to target irradiation with high energy photons. Finally, one can reasonably conclude that among all of the ^{67}Cu production routes (see introduction section in this chapter), production with photonuclear interaction could be considered as a very promising route if high energy and high power electron beam accelerators are provided.

2.5 Conclusion

In this section of the study, production of ^{61}Cu and ^{67}Cu via cyclotron and photonuclear interaction were investigated, respectively. ^{61}Cu was produced by irradiation of an enriched ^{64}Zn target at the Bern medical cyclotron with an activity of 2.17 GBq in the final experiment which is relatively close to the theoretical value calculated using the IAEA Medical Isotope Browser. Regarding such high activities, which are required for the successful radiolabeling, this production route can be efficient for large-scale production. In the case of ^{67}Cu production, ^{67}Cu was produced through the irradiation of enriched ^{68}Zn target at METAS and the activity obtained was 260.9 kBq. However, this low activity is due to the non-availability of a high electron energy and high power electron accelerator facility in Switzerland and is not sufficient for labeling purposes.

CHAPTER 3

AUTOMATED RADIOCHEMICAL SEPARATION OF COPPER FROM IRRADIATED ZINC TARGET AND RADIOLABELING

3.1 Introduction

In this section of the study, radiochemical separation of Cu from Zn target was performed. On this basis, the evaporation technique and extraction chromatography (see introduction chapter) were used for the implementation of the project. Accordingly, some new designs were developed. After the radiochemical separation, radiolabeling of the DOTA peptide with obtained ^{61}Cu was performed, and the radiolabeling yield was measured.

3.2 Materials and methods

3.2.1 Chemicals

TK201 columns (particle size 50-100 µm, purchased from Triskem, France) were used to separate Zn from produced Cu through extraction chromatography. Chemical isolation was performed with ultra-pure (TraceSelect VWR international GMbH, Switzerland), hydrochloric acid (HCl, 37% Suprapur, Sigma-Aldrich, Switzerland), and H_2O_2 (ultratrace 30%). The radiolabeling section was performed with DOTATOC (GMP grade from ABX Advanced biochemical compounds, Germany), sodium acetate buffer (from Sigma-Aldrich, Switzerland), Ammonium acetate (Sigma-Aldrich, 99.5%, Switzerland).

3.2.2 Instruments used for measurements

The activity of produced ^{67}Cu (before and after chemical separation) was identified and quantified by γ-ray spectrometry using an N-type high-purity germanium (HPGe) coaxial detector (Ortec, USA) and the InterSpec software. A dose calibrator (ISOMED 2010, Nuclear–Medizintechnik Dresden GmbH, Germany) was employed for the quantitative determination of the ^{61}Cu activity. The radiolabeling purity of the samples was measured using Thin Layer Chromatography (TLC, Eckert & Ziegler Eurotope GMBH). A Modular-Lab PharmTracer synthesis module (Eckert & Ziegler, Germany) was used to perform the automated chemical separation.

3.3 Automated radiochemical separation of Cu from irradiated Zn targets

The radiochemical separation for separating Cu from Zn targets was implemented in two steps. The first step is performed for the separation of Cu from bulk Zn through a novel evaporation technique and the second step is an automated extraction chromatography that is performed to separate Cu from the remaining traces of Zn and other impurities inside the sample (see Fig. 3.1).

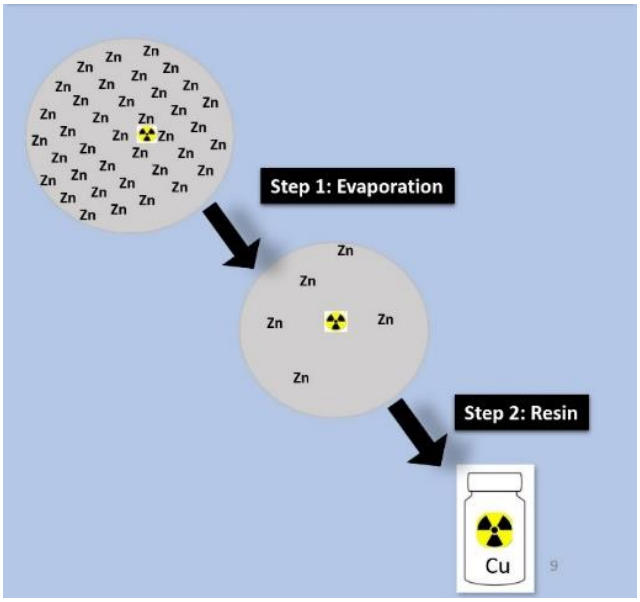

Fig. 3.1 Radiochemistry steps used in this study to separate Cu from Zn target

3.3.1 Evaporation technique or distillation

In this study, we used the evaporation technique to separate Cu from the irradiated Zn target. For this purpose, a design based on the evaporation technique was introduced (Figs. 3.2, 3.3 & 3.4). The concept of our design is to separate Cu from the irradiated Zn target based on the difference in vapor pressure temperature (see Fig. 1.40) and boiling points (which are 907 ^{0}C and 2562 ^{0}C for Zn and Cu, respectively). Accordingly, in contrast to Cu, Zn is evaporated at a temperature above 900 ^{0}C (at atmospheric pressure) and is deposited and collected in a cold section. This entire process was implemented in a quartz tube that consisted of two parts (see Fig. 3.2). The first part is exposed to heat (to evaporate the Zn target), and the second part is cooled by a water flow circulation. In the following, the details of the entire process and design are presented.

Regarding Fig. 3.2, (1) is for the inlet of argon gas inside the vessel. This step was performed to let argon gas blow inside the quartz tube (that is shown in Fig. 3.3) for about 5 minutes through an inlet connection (1) (see Fig. 3.2). This step is for removing oxygen inside the quartz tube and prohibiting oxidation of the Zn target. Then, the quartz tube containing the irradiated target at the conical bottom was put inside a heater, and the heater was warmed up to above 900 ^{0}C, (for efficient evaporation, we selected the temperature above the boiling point of Zn, which is 907^{0}C. The sample was left at this temperature for about 1 hour, and throughout this process, argon gas was blown inside the quartz tube as a carrier gas, which prohibits oxidation of the Zn target and transports the evaporated Zn towards the cool part. After a cooling time of about 5 min, the acid was injected inside the glass through the connection (2) (see Fig. 3.2), and the dissolved Cu at the bottom of the quartz tube withdrawn. (3) and (4) are inlet and outlet for water flow in the spiral cooler, (5) is an outlet of argon gas passing through the charcoal (activated carbon) to absorb volatile radioactive components (e.g., traces of Ga). However, this design was not further used for extraction of Cu and next chemical separation step (extraction chromatography). The reason is that Zn was collected not only in the cooler section but also on the wall of the quartz vessel, which was due to the low temperature gradient in the first design. Additionally, as can be seen in Fig. 3.4, recycling of the evaporated Zn was not possible due to the fact that the spiral water cooling tube was inside another glass tube, which resulted in the deposited Zn being not accessible for recycling purposes. On this basis, a new design was employed.

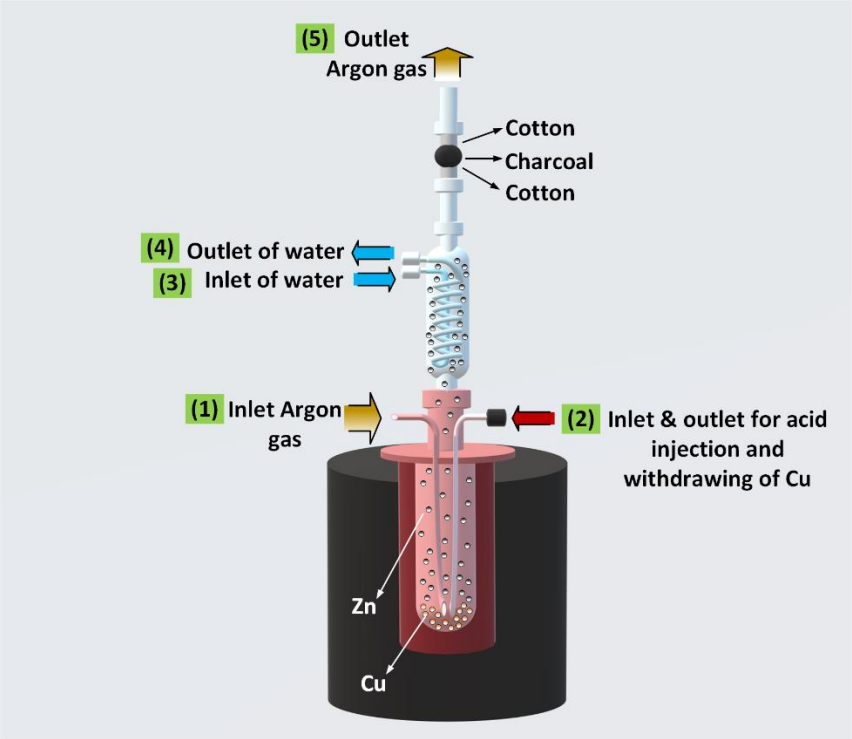

Fig. 3.2 Evaporation technique to separate Cu from bulk Zn (first design)

Fig. 3.3 Designed quartz glass for radiochemical separation in this study (first design)

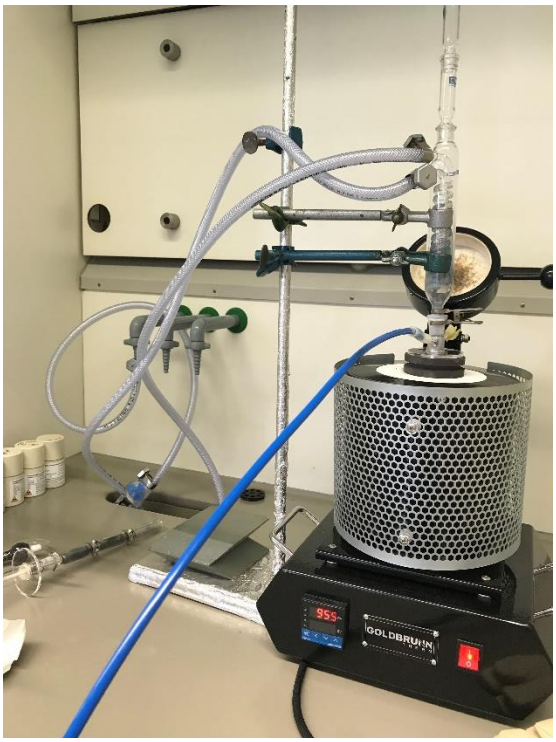

Fig. 3.4 First setup for the separation of Cu from Zn target based on the evaporation technique

Another design was also implemented for the separation of Cu from the Zn target using the evaporation technique (see Figs 3.5, 3.6 & 3.7). Regarding the new design in Figure 3.5, 1) is the inlet for entering argon gas inside the vessel, 2) is for acid injection and withdrawing the dissolved Cu at the bottom of the quartz tube using a T-shape connection (3-way valve), 3) is an inlet at the top for the cooling finger (see Figs. 3.5 & 3.7), which is employed to accumulate Zn 4) is an outlet of argon gas and 5) and 6) are inlet and outlet for water flow in the cooling finger and 7) is a photograph of the second design of the quartz glass tube. The quartz tube with the irradiated target at the conical bottom was put inside a heater, and the heater was warmed-up to 900 ^{0}C. The sample was left at this temperature for about 1 hour.

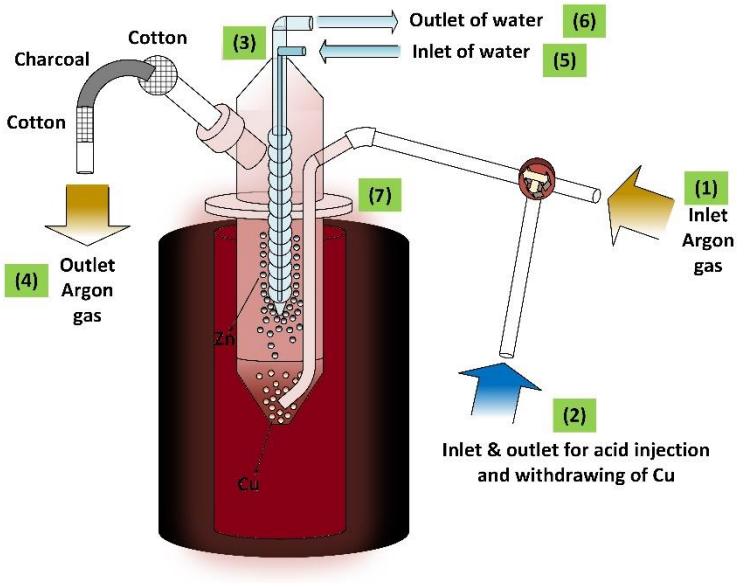

Fig. 3.5 Evaporation technique to separate Cu from bulk Zn (second design)

Fig. 3.6 Designed quartz glass for radiochemical separation in this work (second design)

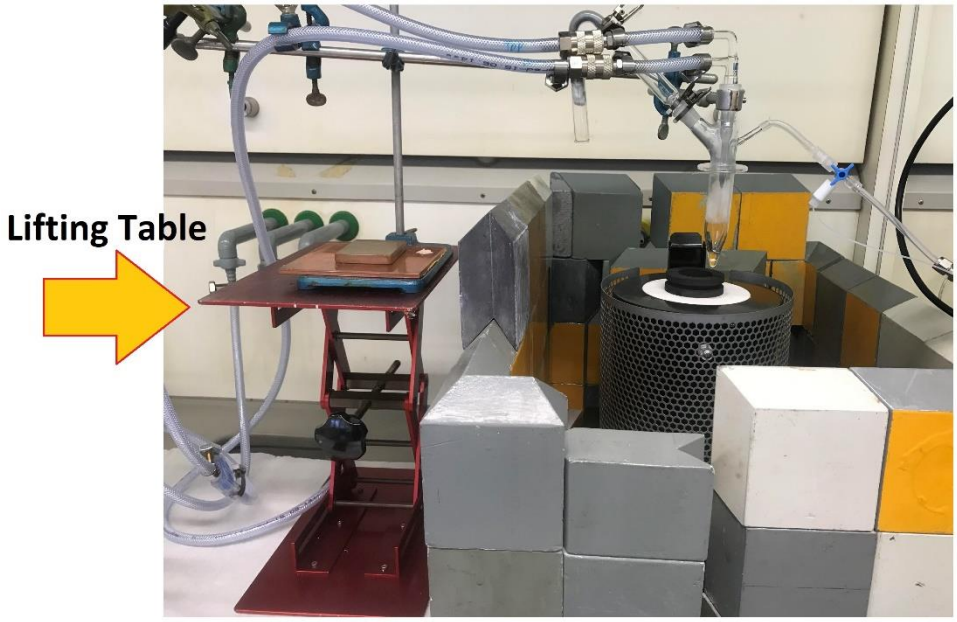

Fig. 3.7 Designed set up for the evaporation technique (second design)

After evaporation of Zn, the quartz tube was lifted out of the oven with a lifting table called labor-boy (see Fig. 3.7) and cooled to room temperature using a fan. Then, most of the radioactive Cu was dissolved in 6 mL 8M HCl and transferred to the subsequent clean-up using extraction chromatography with TK201 resin (more details are presented in the next chemical separation step).

3.3.2 Automated extraction chromatography

In the first step of the chemical separation using the evaporation technique, most of the Zn was separated; however, for removing the remaining Zn (i.e., in the form of ZnO) and other impurities in the sample, a second step of separation (extraction chromatography via TK201 resin) was used. TK201 resin is based on a tertiary amine and contains a small amount of long-chained alcohol as a radical scavenger to increase its radiolysis stability [176]. For the implementation of extraction chromatography, the residue of the evaporation process containing the Cu inside the vessel (in the first step of chemical separation) was dissolved and taken out using 8 M HCl acid. Using highly concentrated HCl was due to the fact that Cu metal can be dissolved in such a high concentration of HCl acid. Fig. 3.8 shows the selectivity of the TK201 resin for a wide range of elements in HCl.

All Dw values (see chapter 1, section 1.6.3.1) in these graphs were obtained through radiotracer measurements [176]. According to the available data presented in Fig. 3.8 for TK201 resin in HCl, at all HCl concentrations, Zn has higher retention on the column than Cu. In other words, at 8M HCl, Cu and Zn are well retained on the TK201 resin with Dw values of about 30 for Cu and about 140 for Zn.

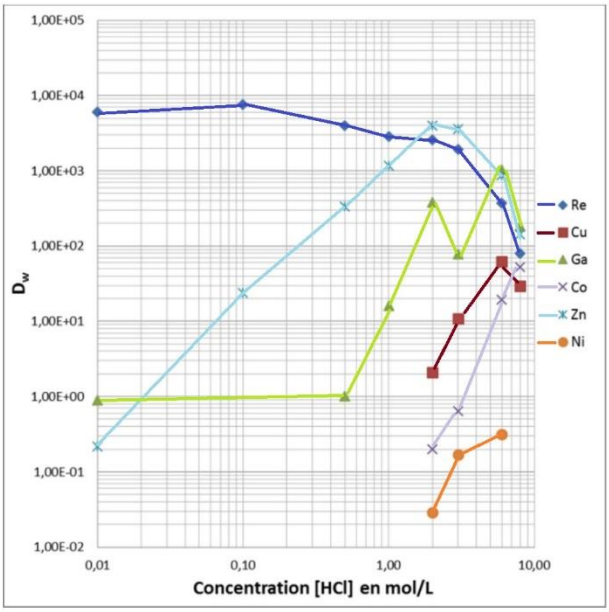

Fig. 3.8 Dw values of selected elements on TK201 Resin in HCl [176]

For the implementation of the automated extraction chromatography step, an Eckert & Ziegler Modular-Lab PharmTracer synthesis module was used. The Modular-Lab PharmTracer is usually used for routine production of radiopharmaceuticals and research. This equipment contains cassettes containing all the components for a particular synthesis. There are some commercially available cassettes and software. E.g. ^{68}Ga DOTATOC, ^{177}Lu DOTATOC and ^{90}Y DOTA-peptides synthesis. Its setup consists of a 4-fold module (SLM-4), a Heater Reaction Module (HRM), and a Syringe Module (SYM) (see Fig. 3.9).

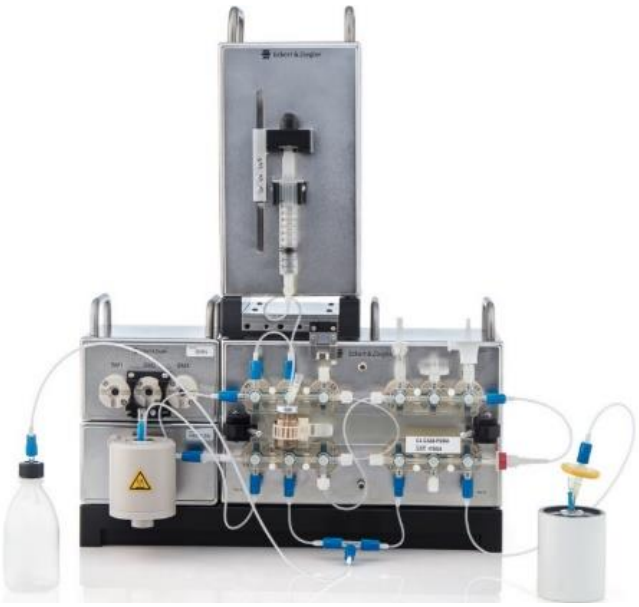

Fig. 3.9 Modular-Lab PharmTracer set up

For using Eckert & Ziegler Modular-Lab PharmTracer, first, the procedure must be programmed using modular software. With this software, programming of projects to develop own synthesis processes is possible. The software contains an intuitive graphical interface to create projects by dragging and dropping symbols. In the following, the process of implementation is described. The details of the process of the implementation is as follows:

In the first step of automated extraction chromatography, a 2 mL TK201 column automatically was conditioned with 7 mL H_2O and then with 6 mL 8 M HCL [217]. Then after conditioning the column, the T-shape connection was turned and put in the other direction to inject the solution into the vessel and 3 mL 8 M HCl acid with 1.5 mL H_2O_2 (ultratrace 30%) was injected into the vessel to dissolve the residue of the evaporation process containing the Cu. Then the solution inside the vessel was taken out and gain injected inside the vessel and this process repeated four times. Afterward, the next 3 mL 8 M HCl were added, and then after a waiting time of 10 min, the solution at the bottom of the glass was automatically transferred from the oven to the TK201 column in the cassette (see Figs. 3.10 and 3.11).

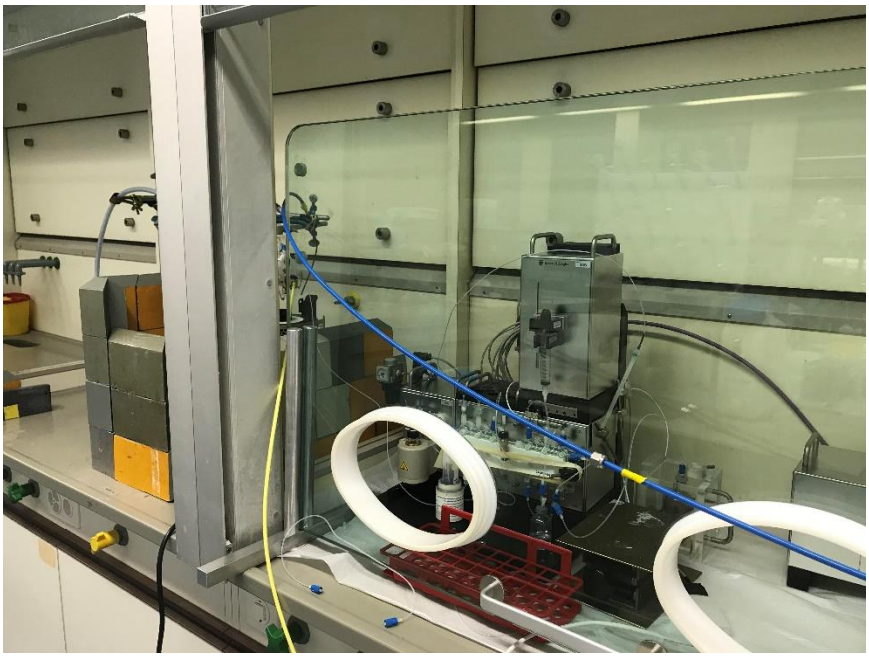

Fig. 3.10 Joined two-steps chemical separation mechanisms

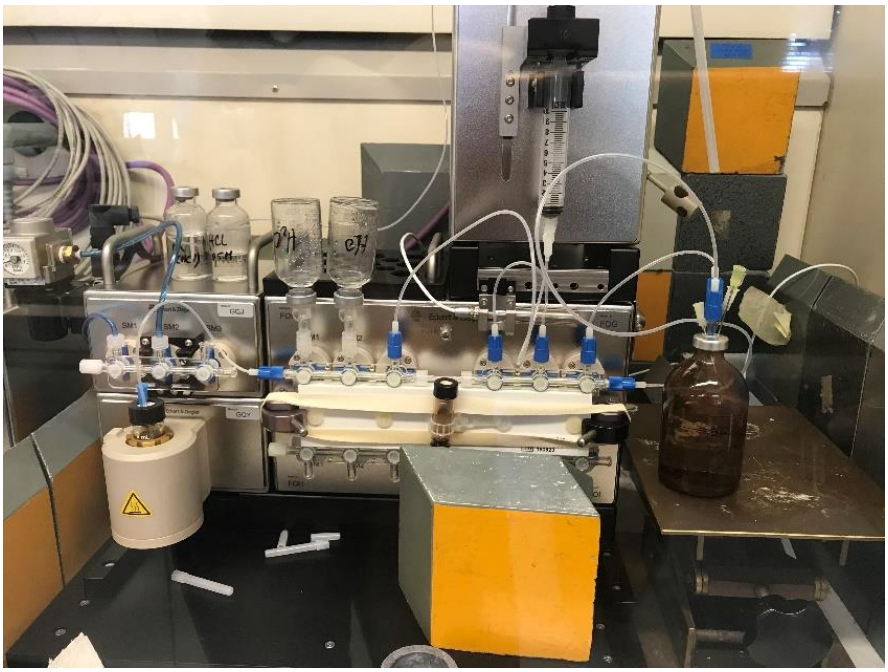

Fig. 3.11 Modular-Lab system setup

In the next step, the solution containing the dissolved Cu and traces of Zn was passed through the TK-201 column and Cu and Zn were retained.

The column was then washed with 4 mL of NaCl (5 M) in 0.05 M HCl to decrease residual acidity on the resin [217]. The total chloride concentration was obtained 5.05 M. Finally, the TK-201 column was again washed with 8 mL 0.05 M HCl acid to elute [^{61}Cu]$CuCl_2$ while Zn was still retained with Dw values of about 6. The vial containing the copper was measured using an HPGe detector and a dose calibrator to measure the activity.

3.4 Radiolabeling of DOTATOC with ^{61}Cu

In this section, radiolabeling of ^{61}Cu is being discussed. In the case of ^{67}Cu, the obtained activities were too low to perform labeling studies. Therefore, the radiolabeling with ^{61}Cu was investigated. For the radiolabeling of DOTATOC with ^{61}Cu, the activity of ^{61}Cu in the eluate was first determined with a dose calibrator and was about 800 MBq at the time of starting the radiolabeling. The radiolabeling of DOTATOC was performed with a hydrochloric solution of Cu^{2+}. The $CuCl_2$, which was prepared after cassette separation, was incubated with the 50 µg DOTATOC at a pH of 5.5 sodium acetate buffer (10 M) at 80 ^{0}C for about 20 min. The purity of the labeled compound was measured by TLC. The TLC plates (Silica-gel 60, Merck) were prepared using 1 M ammonium acetate (Sigma-Aldrich, 99.5%) as a mobile phase.

3.5 Results and discussion

3.5.1 Automated radiochemical separation of Cu from the irradiated Zn target

There is some literature for the separation of Cu from Zn target through different methods [179, 173]. Regarding the IAEA TECDOC [179], The Cu was separated from the irradiated Zn target in two steps through cation exchange column (AG 50W) and anion exchange column (AG 1X8) and obtained more than 99% radionuclide purity [179]. However, Gopalakrishna et al., in 2018, used solvent extraction to separate Cu from Zn target and yields >90 %, were achieved [173].

In this work, separation of Cu from Zn target was performed in two steps, involving the evaporation technique and extraction chromatography. In the first setup Zn was collected not only in the cooler, but also on the wall of the quartz vessel, which was due to the low temperature gradient in the first design. Additionally, as can be seen in Fig. 3.4, recycling of the evaporated Zn was not possible due to the fact that the spiral water cooling tube was inside another glass tube which resulted in the deposited Zn being not accessible for recycling purposes. On this basis, a new design was employed (see Fig.s 3.5 & 3.6) and the evaporated Zn deposited only on the surface of the cooling finger (see Fig. 3.12). Due to maximizing the temperature gradient in the new design the evaporated Zn could easily be removed after finishing the evaporation process. Therefore, the Zn can be recycled for further use (see Fig. 3.12). A lifting table (labor-boy) was used to lift the quartz vessel out of the oven, which had a strong effect on the cooling time of the vessel. This cooling time was about 5 minutes and is necessary since injection of the HCl in the vessel with a temperature above 100 ^{0}C would result in the evaporation of the solution.

Fig. 3.12 Deposited Zn on the cooling finger (second design)

In the next step, an automated extraction chromatography using a TK201 column was performed to purify the Cu and to remove remaining Zn and other impurities in the sample. Accordingly, some experiments were performed to improve the results. On this basis, experiments were performed with different acid solutions and molarities. In the two first experiments, 30 mL 8 M

HCl acid was injected into the vessel (without mixing with H_2O_2) for extracting the Cu from the vessel. The results obtained from the experiments showed that we were not able to extract most of the Cu from the vessel, and it remained at the bottom of the quartz glass. Moreover, as can be seen in Table 3.1, for the first two experiments, most of the extracted Cu from the vessel went to the waste instead of the vials. This is due to the fact that, the quartz glass was washed several times with a total of 30 mL HCl and this caused Cu to start breaking through the column. In experiment No. 3, a little amount of H_2O_2 was added to the quartz glass (100 µL), to investigate whether that influenced the dissolution of Cu. As can be seen in Table 3.1, this significantly affected the dissolution of the residue of the evaporation process containing the Cu, and therefore, much more of the Cu (compared to the experiments No. 1 and 2) was extracted from the quartz glass. Additionally, the total volume of HCl for washing the glass decreased from 30 mL to 22 ml. This resulted in a reduced amount of Cu breaking through the column. Finally, in the last experiment, a higher amount of H_2O_2 (1.5 mL) was added to the quartz glass vessel and it was observed that the amount of Cu remaining in the quartz glass was significantly reduced (Table 3.1). Importantly, by decreasing the total volume of HCl for washing the glass (from 23 mL in the experiment 3 to 6 mL in the experiment No. 4), almost all of the Cu was collected in the vials instead of going to the waste (see Table. 3.1).

Table 3.1 Relative measured activity in each part of the process compared to the total activity

Experiment No.	Vials	Glass	Column	Waste	Lost (e.g., in tubes and cassette)
1. Without H_2O_2	21%	33%	3.2%	42.1%	0.7%
2. Without H_2O_2	30%	23%	3.5%	42.4%	1.1%
3. With H_2O_2	70%	17%	0.9%	11.1%	1%
4. With H_2O_2	88%	11%	0.6%	0.3%	0.1%

In the case of ^{67}Cu production, ^{65}Zn which was produced through the ^{66}Zn(γ,n)^{65}Zn reaction could be used as a tracer (see Fig. 2.12). Afterwards, the vial containing most of the activity was measured with the HPGe detector and ^{65}Zn was not observed (see Fig. 3.13).

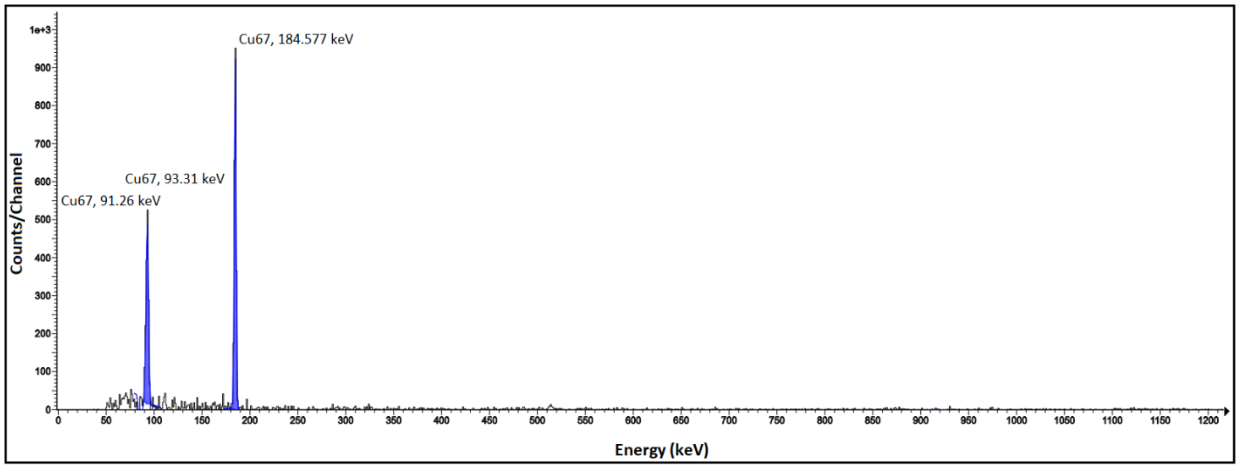

Fig. 3.13 Peaks of ^{67}Cu measured by HPGe detector after chemical separation (with background subtraction)

3.5.2 Radiolabeling of DOTATOC with ^{61}Cu

In the radiolabeling section, in the first experiment, the $CuCl_2$, which was prepared after cassette separation, was incubated with the DOTATOC and a different buffer solution (ascorbic acid solution 0.1 g/mL $C_6H_8O_6$; see Table 3.2). Then the pH of the solution was measured, and it was too acidic (around pH 1) due to using 8M HCl in the separation process for removing the Cu from the glass tube. Regarding the TLC after radiolabeling, no peaks corresponding to radiolabeled DOTATOC could be observed (see Fig. 3.14). However, in the second experiment, regarding the TLC result, DOTATOC was labeled with ^{61}Cu with a 73% labeling yield (see Fig. 3.15 and Table 3.2), but the solution was still too acidic. To solve the problem, two steps were performed. First, in the chemistry section (extraction chromatography), after loading the TK201 column with the irradiated target solution in 8M HCl, the column was then washed with 4 mL of NaCl in 0.05 M HCl to decrease residual acidity on the resin. Secondly, for the radiolabeling section, sodium acetate (10 M) was used as a buffer solution for incubating $CuCl_2$ with the DOTATOC.

Evaluation information

Method: n.a. (version -)
Method description: -
User: admin

Activity graph, sensor: EOL-SY-AD

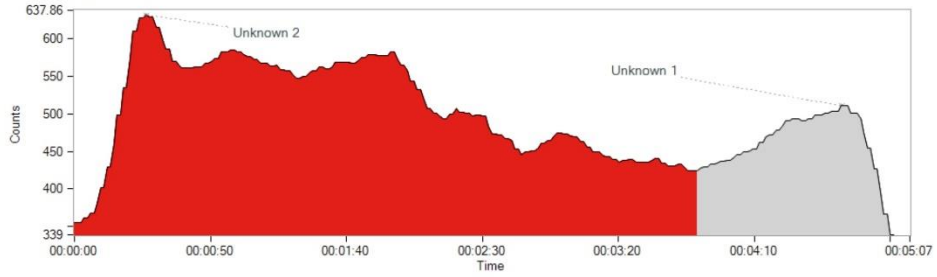

Activity summary

No	Identifier	Area	Percentage	Amount	Max Time	Start Time	End Time	Maximum	% Total	Retention time	Flag
1	Unknown 2	117041.05	78.05		00:00:26	00:00:00	00:03:49	632	77.84	00:01:50	
2	Unknown 1	32907.05	21.95		00:04:41	00:03:49	00:04:59	511	21.89	00:04:24	
	Unallocated Area	406.8							0.27		
	Total Area	150354.9							100		
	2 Peaks	149948.1	100						99.73		

Fig. 3.14 TLC result for the first experiment

Evaluation information

Method: n.a. (version -)
Method description: -
User: admin

Activity graph, sensor: EOL-SY-AD

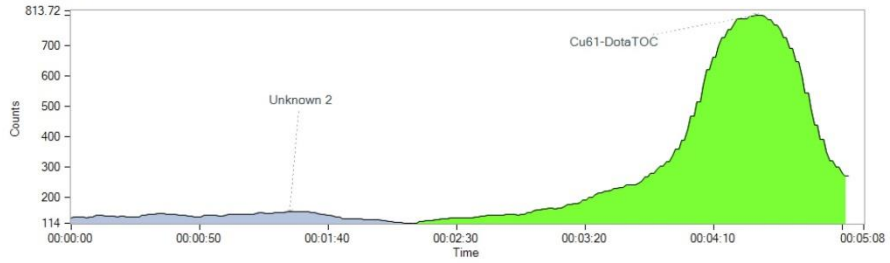

Activity summary

No	Identifier	Area	Percentage	Amount	Max Time	Start Time	End Time	Maximum	% Total	Retention time	Flag
1	Unknown 2	17945.99	23.6		00:01:25	00:00:00	00:02:09	153	23.38	00:01:04	
2	Cu61-DotaTOC	58085.17	76.4		00:04:26	00:02:13	00:05:01	800	75.66	00:04:03	
	Unallocated Area	735.5							0.96		
	Total Area	76766.65							100		
	2 Peaks	76031.16	100						99.04		

Fig. 3.15 TLC result for the second experiment

Table 3.2 Different parameters for radiolabelling of DOTATOC for different experiments.

Experiment No.	pH	Buffer Solution	Activity (MBq)	Radiolabeling Purity (%)
1. ^{61}Cu in ascorbic acid buffer	~1	ascorbic acid solution 0.1 g/mL $C_6H_8O_6$	188	-
2. ^{61}Cu in ascorbic acid buffer	~3	ascorbic acid solution 0.1 g/mL $C_6H_8O_6$	145	73
3. ^{61}Cu in sodium acetate buffer	5.5	sodium acetate (10 M)	800	97

Afterward, based on the TLC results in the third experiment, the ^{61}Cu-DOTATOC was obtained with more than 97% labeling yield (see Fig. 3.16). Regarding the results, 22.7 (radiolabeled ^{61}Cu MBq/ nmol of peptide) was obtained.

Evaluation information

Method: n.a. (version -)
Method description: -
User: admin
Activity background correction: Activated, manually defined, 3 points

Activity graph, sensor: EOL-SY-AD

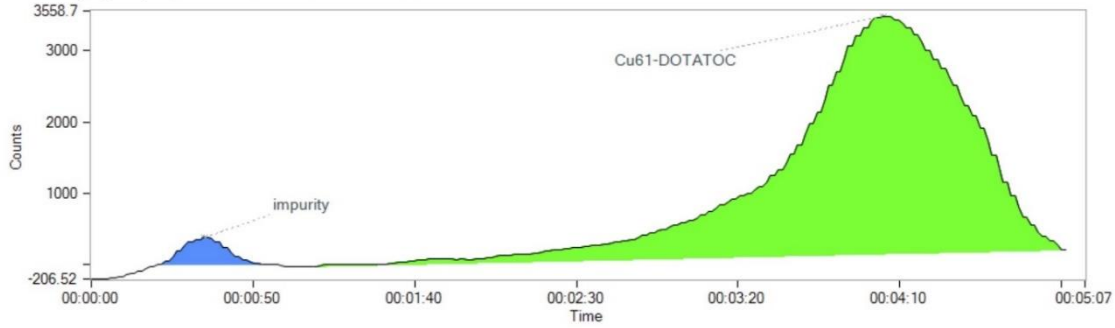

Activity summary

No	Identifier	Area	Percentage	Amount	Max Time	Start Time	End Time	Maximum	% Total	Retention time	Flag
1	impurity	5857.28	2.67		00:00:34	00:00:21	00:00:52	376.48	2.43	00:00:35	
2	Cu61-DOTATOC	213824.35	97.33		00:04:04	00:01:08	00:05:01	3484.83	88.83	00:03:56	
	Unallocated Area	21022.46							8.73		
	Total Area	240704.1							100		
	2 Peaks	219681.64	100						91.27		

Fig. 3.16 ^{61}Cu-DOTATOC labeling yield measured with TLC

3.6 Conclusion

In this section of the study, separation of Cu from Zn target was implemented through a novel automated system in two steps, involving an evaporation technique and extraction chromatography. In the evaporation technique, a new and novel setup was developed, which included a quartz tube containing a cooling finger that allows the evaporated Zn to collect around it and which can be easily removed. Afterward, the solution was automatically transferred to the next step (extraction chromatography with TK201 resin), which was performed to remove remaining Zn in the solution. Regarding the results, through the automated system, Cu was separated completely from the Zn target. In the radiolabeling section, DOTATOC was labeled with ^{61}Cu with more than 97% labeling yield (22.7 MBq/nmol of peptide).

CHAPTER 4

ADDITIONAL STUDIES TOWARDS SOME POTENTIAL RADIONUCLIDES IN NUCLEAR MEDICINE

4.1 Targetry and specification of ^{167}Tm production parameters by different reactions

Authors: Mahdi Sadeghi, Nadia Zandi, Hossein Afarideh

Journal of Radioanalytical and Nuclear Chemistry, 291:731–738 (2012)

Highlights: ^{167}Tm with a half-life of 9.25 d and γ-ray of 208 keV can be used as a complex with hydroxy ethylene diamine tetra-acetic acid (HEDTA) for tumor and bone studies in nuclear medicine. This study first describes excitation functions of some major reaction channels calculated by ALICE/ ASH and TALYS-1.0 codes, and then calculated data were compared to the earlier published experimental data and TENDL-2010 database. Additionally, physical yield and optimal thickness of the targets were obtained by SRIM (stopping and range of ions in matter) code [218] for each reaction channel. At the next step, the targetry of Er_2O_3 on a Cu substrate through sedimentation technique was performed, and the prepared target was irradiated with the proton beam energy of 15 MeV and beam current of 20 μA [219]. The yield of about 3.2 MBq/ μA h was experimentally obtained.

Contributions: I performed the theoretical calculations using TALYS and ALICE code. I also performed the targetry of Er_2O_3 on a Cu substrate through sedimentation technique and performed the calculation of theoretical and physical yields. Furthermore, I wrote the manuscript.

J Radioanal Nucl Chem (2012) 291:731–738
DOI 10.1007/s10967-011-1422-2

Targetry and specification of ^{167}Tm production parameters by different reactions

Mahdi Sadeghi · Nadia Zandi · Hossein Afarideh

Received: 22 June 2011 / Published online: 20 September 2011

Abstract In recent years, there has been a rapid expansion in the use of radio nuclides for therapeutic purposes. Thulium–167 is an important radionuclide ($T_{1/2} = 9.25$ d) due to it could be used for tumor and bone studies in nuclear medicine. ^{167}Tm complexed with hydroxy ethylene diamine tetra-acetic acid (HEDTA) could be used with the aim of bone imaging. ^{167}Tm emits a prominent γ ray of 208 keV energy and low energy electrons. This study describes calculations on the excitation functions of ^{165}Ho(α,2n)^{167}Tm, ^{167}Er(p,n)^{167}Tm, ^{nat}Er(d,xn)^{167}Tm and ^{nat}Er(p,xn)^{167}Tm reactions by ALICE/ASH (hybrid and GDH models) and TALYS-1.0 codes. In addition, calculated data by codes were compared to experimental data that earlier were published and TENDL-2010 database. Moreover, optimal thickness of the targets and physical yield were obtained by SRIM (stopping and range of ions in matter) code for each reaction. According to the results, the ^{167}Er(p,n)^{167}Tm and ^{165}Ho(α,2n)^{167}Tm reactions are suggested as the best method to produce ^{167}Tm owing to minimum impurities. The TALYS-1.0 code, predict the maximum cross-section of about 382 mb at 11 MeV and 849 mb at 26 MeV for ^{167}Er(p,n)^{167}Tm and ^{165}Ho(α,2n)^{167}Tm reactions, respectively. Finally, deposition of $^{nat}Er_2O_3$ on Cu substrate was carried out via the sedimentation method. The 516 mg of erbium(III)oxide with 103.2 mg of ethyl cellulose and 8 mL of acetone were used to prepare a $^{nat}Er_2O_3$ layer of 11.69 cm^2. ^{167}Tm was produced via the ^{nat}Er(p,n)^{167}Tm nuclear process at 20 μA current and 15 → 7 MeV protons beam (1 h). Yield of about 3.2 MBq ^{167}Tm per μA h were experimentally obtained.

Keywords Excitation function · Thulium-167 · Nuclear medicine · Physical yield · TALYS-1.0 · ALICE/ASH · Target thickness

M. Sadeghi (✉)
Agricultural, Medical & Industrial Research School, Nuclear Science and Technology Research Institute,
P.O. Box 31485/498, Karaj, Tehran, Iran
e-mail: msadeghi@nrcam.org

N. Zandi · H. Afarideh
Department of Nuclear Engineering and Physics, Amir-kabir, University of Technology, P.O. Box 4155-4494, Tehran, Iran

Introduction

In recent years, there has been a fast growth in the make use of radio nuclides for therapeutic functions [1, 2]. Thulium–167 has been proposed as a useful agent for tumor and bone studies having a half-life of 9.25 days. ^{167}Tm emits a prominent γ-ray of 208 keV energy and low energy electrons. The Auger-electron emitters ^{167}Tm had high TND (the ratio of the absorbed dose rate to the tumors and the normal tissue) values for tumors weighing less than 1 mg and can be produced with high specific activities [1–6]. There is direct and indirect reactions to production of ^{167}Tm as follow [7–15]:

$^{165}\mathrm{Ho}(\alpha, 2n)^{167}\mathrm{Tm}$
$^{167}\mathrm{Er}(p, n)^{167}\mathrm{Tm}$
$^{nat}\mathrm{Er}(p, xn)^{167}\mathrm{Tm}$
$^{nat}\mathrm{Er}(d, xn)^{167}\mathrm{Tm}$
$^{167}\mathrm{Er}(d, 2n)^{167}\mathrm{Tm}$
$^{169}\mathrm{Tm}(p, 3n)^{167}\mathrm{Yb} \rightarrow {}^{167}\mathrm{Tm}$
$^{nat}\mathrm{Yb}(p, x)^{167}\mathrm{Lu} \rightarrow {}^{167}\mathrm{Yb} \rightarrow {}^{167}\mathrm{Tm}$
$^{168}\mathrm{Yb}\ (p, x)^{167cum}\mathrm{Tm}$
$^{nat}\mathrm{Er}(\alpha, xn)^{167}\mathrm{Yb} \rightarrow {}^{167}\mathrm{Tm}$
$^{nat}\mathrm{Hf}(p, x)^{167}\mathrm{Lu} \rightarrow {}^{167}\mathrm{Yb} \rightarrow {}^{167}\mathrm{Tm}$

This study describes calculations on the excitation functions of ^{165}Ho(α,2n)^{167}Tm, ^{167}Er(p,n)^{167}Tm, ^{nat}Er(d,xn)^{167}Tm and ^{nat}Er(p,xn)^{167}Tm reactions by ALICE/ASH (hybrid and GDH models) and TALYS-1.0 codes. In this study, the excitation functions of ^{167}Tm for the various reactions with incident particle energy up to 50 MeV were calculated and compared with experimental previous published data. ALICE/ASH (hybrid and GDH models) and TALYS-1.0 codes have been used to perform these calculations. Theoretical calculation of physical yield and target thickness was done using SRIM code (stopping and range of ions in matter). To find the aberration amount of the acquired data and experimental data, and TENDL-2010, they were compared with each other. Finally, according to the results, the best reaction to prevent formation radioactive and non radioactive impurities as far as possible to production ^{167}Tm was chosen. Targets' essential thickness and suitable method for preparing target was investigated.

Materials and methods

Calculation of excitation function

Excitation function of ^{167}Er(p,n)^{167}Tm, ^{nat}Er(p,xn)^{167}Tm, ^{165}Ho(α,2n)^{167}Tm and ^{nat}Er(d,xn)^{167}Tm reactions was calculated using ALICE/ASH and TALYS-1.0 codes [16, 17]. Further, an optimum energy range was determined so that formation of radionuclide impurities is avoided as far as possible.

The ALICE/ASH code

The ALICE/ASH code can be applied for the calculation of excitation functions, energy and angular distribution of secondary particles in nuclear reactions induced by nuclei with the energy up to 300 MeV [16]. The hybrid model and the geometry dependent hybrid model (GDH) can be used for the calculation of particle spectra. In the GDH model the pre-equilibrium spectrum of nucleons is calculated as follows:

$$\frac{d\sigma}{d\varepsilon_x} = \pi\lambda^{-2}\sum_{i=0}^{\infty}(2l+1)T_L \times \sum_{i=0}^{\infty}R_x(n)\frac{w(p-1,h,U)}{W(p,h,E)}\cdot\frac{\lambda_x^e}{\lambda_x^e+\lambda_x^+}g\ \mathrm{D}\ (n)$$

T_L is the transmission coefficient for 1th partial wave; R_x (n) is the number of nucleons of x-type in the n-excitation state, g is the single particle level density equal to A/14 ; λ_x^e is the emission rate of nucleon. This code uses the Weisskopf–Ewing evaporation model, the Bohr–Wheeler model for fission, and the geometry-dependent hybrid model for pre compound decay. This hybrid model is relevant to the pre-compound decay but not to the compound decay. The geometry-dependent hybrid model is a further revision of the hybrid model.

TALYS code

TALYS is a computer code system for the analysis and prediction of nuclear reactions. The basic objective behind its construction is the simulation of nuclear reactions that involve neutrons, photons, protons, deuterons, tritons, 3He- and alpha-particles, in the 1 keV-200 MeV energy range and for target nuclides of mass 12 and heavier. It covers an energy range from 1 keV to 200 MeV [17].

The pre-equilibrium particle emission is described using the two component excitation model. This model implements new expression for the internal transition rates and new parameterization of the average squared matrix element for the residual interaction, which is obtained using the optical model potential [17]. The phenomenological model is used for the description of the pre-equilibrium complex particle emission. The equilibrium particle emission is described using the Hauser–Feshbach model.

TENDL-2010

TENDL is a nuclear data library which provides the output of the TALYS nuclear model code system for direct use in both basic physics and applications. The third version is TENDL-2010, which is based on both default and adjusted TALYS calculations and data from other sources [18].

Calculation of the physical yield and the target thickness

Theoretical physical yield can be calculated by the following equation:

$$Y = \frac{N_L H}{M} I\left(1 - \mathrm{e}^{-\lambda t}\right)\int_{E_1}^{E_2}\left(\frac{dE}{d(\rho x)}\right)^{-1}\sigma(E)\,dE$$

where Y is the activity of the product (in Bq), N_L is the Avogadro number, H is the isotope abundance of the target nuclide (%), M is the mass number of the target element (g), $\sigma(E)$ is the cross-section at energy E (mb), I is the projectile current (μA), $dE/d(\rho x)$ is the stopping power (MeV/mg/cm^2), λ is the decay constant of the product and t is the time of irradiation (h).

SRIM (stopping and range of ions in matter) code [19] was used to calculation the required thickness of the target. The physical thickness of the target layer that was calculated by SRIM code is for 90° geometry beam toward the target. To better heat transfer on the surface of the target

and the beam cover all surface of the target (11.69 cm^2), 6° geometry beam toward the target during the bombardment was performed. So required layer thickness will be less with coefficient 0.1.

Result and discussion

^{167}Er(p,n)^{167}Tm reaction

To produce ^{167}Tm from ^{167}Er, sedimentation technique were used by Tarkanyi et al. in 2010 [8], they determined the excitation functions of proton induced reaction on the targets containing erbium oxide. Consequently, it has been obtained the maximum cross-section of 455 mb at 10.8 MeV. The target samples were prepared of highly enriched erbium oxide, $^{167}Er_2O_3$ powder, via sedimentation technique. Subsequently, small amount of erbium-oxide powder was suspended in EtOH/H_2O and let to settle slowly onto an Al backing of 13.0 mm diameter and 0.1 mm thickness [8].

The experimental data and the results of the nuclear model calculations of the ^{167}Er(p,n)^{167}Tm reaction are given in Fig. 2. According to TALYS-1.0 code, data for ^{167}Er(p,n)^{167}Tm reaction, beneficial range of proton energy to produce ^{167}Tm from ^{167}Er target is 6–15 MeV that maximum cross-section is 382 mb at 11 MeV (Fig. 1). The cross-section data from TALYS-1.0 and ALICE/ASH (hybrid and GDH models) codes showed that bombarding ^{167}Tm with proton particles leads to produce ^{166}Tm (7.7 h) in 6–15 MeV. ^{166}Tm (7.7 h) has short half life compared to ^{167}Tm and can be reduced by choosing proper energy range. As can be seen on Fig. 2, The TALYS-1.0 and

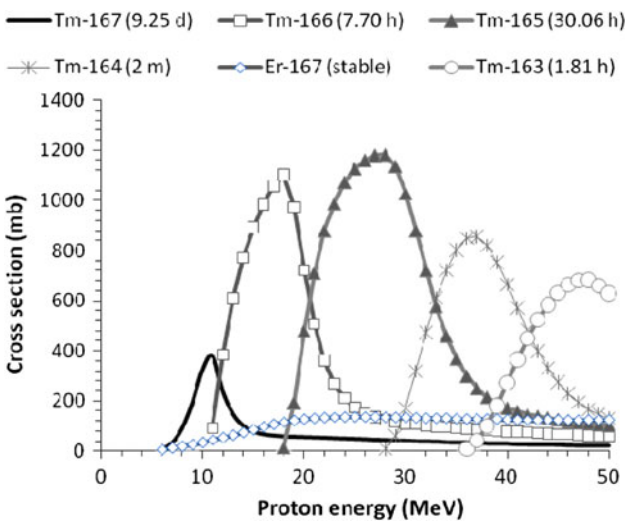

Fig. 1 Excitation function of ^{167}Er(p,n)^{167}Tm reactions calculated by TALYS-1.0 code

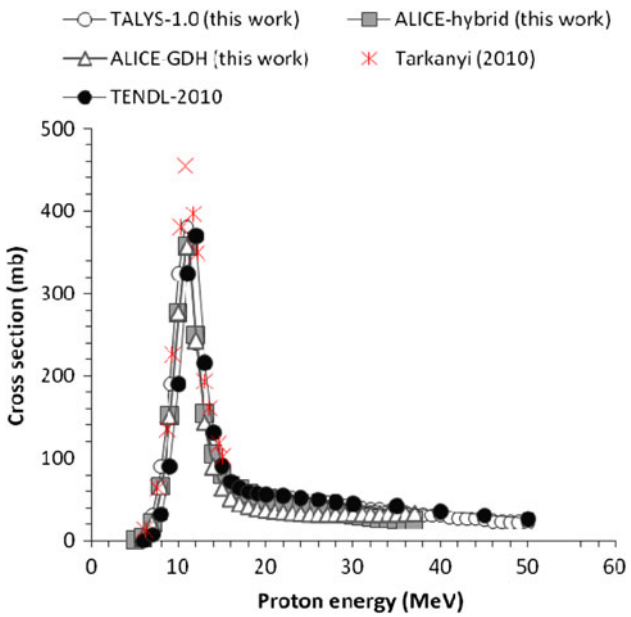

Fig. 2 Excitation function of ^{167}Er(p,n) ^{167}Tm reaction calculated by ALICE/ASH (hybrid and GDH models) and TALYS-1.0 codes and experimental data

ALICE (hybrid and GDH models) calculated results codes are in good agreement with the cross section values reported by Tarkanyi et al. in 2010 [8]. Considering the excitation function and SRIM data we conclude that 6–15 MeV is the optimal energy range for production of ^{167}Tm which leads to physical yield of 5.8 MBq/μA h and required thickness of target is 51.3 μm for 6° geometry of the beam toward the target (Table 1).

^{nat}Er(p,xn) ^{167}Tm reaction

In 2008 Tarkanyi et al. [9], investigated production of ^{167}Tm on erbium up to 70 MeV and found the maximum value of cross section is about 358 mb at 18.8 MeV. In this part of study we calculated the excitation functions of ^{nat}Er (p,xn) ^{167}Tm reaction by ALICE/ASH (hybrid and GDH models) and TALYS-1.0 codes and compared with cross section values reported by Tarkanyi et al. [9] in Fig. 4. Regarding to TALYS-1.0 code data for ^{nat}Er(p,xn) ^{167}Tm reaction, ^{167}Tm has a maximum cross-section of about 323 mb at 19 MeV; its beneficial excitation functions occur between 7 and 23 MeV. As the natural erbium is composed of six stable isotopes (Table 2), ^{169}Tm (stable), ^{168}Tm (93.1 d), ^{166}Tm (7.7 h), ^{165}Tm (30.06 h) and ^{164}Tm (2 min) are simultaneously produced in this energy range (Fig. 3). Actually ^{169}Tm is an stable isotope; therefore, this reaction doesn't lead to production of ^{167}Tm in no carrier-added form [20, 21].

In fact, separation of isotopic contamination ^{169}Tm is not possible by chemical methods. Although, ^{168}Tm

Table 1 ^{167}Tm physical yield and target thickness for various reactions

Reaction	Energy range (MeV)	Target thickness (μm)	Theoretical physical yield (MBq/μA h)
^{167}Er(p,n)^{167}Tm	15 → 6	51.3	5.8
^{nat}Er(p,xn)^{167}Tm	15 → 7	51.0	4.2
^{165}Ho(α,2n)^{167}Tm	34 → 17	18.0	4.9
^{nat}Er(d,xn)^{167}Tm	70 → 10	505.5	16.7

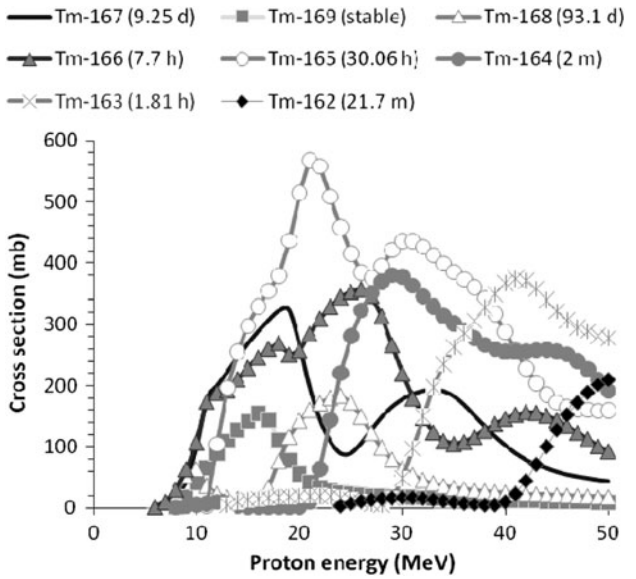

Fig. 3 Excitation function of ^{nat}Er(p,xn)^{167}Tm reaction calculated by TALYS-1.0 code

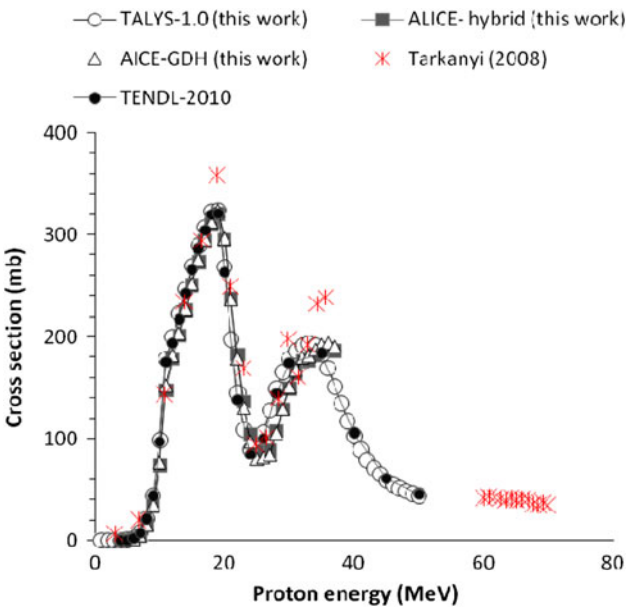

Fig. 4 Excitation function of ^{nat}Er(p,xn)^{167}Tm reaction calculated by ALICE/ASH (hybrid and GDH models) and TALYS-1.0 codes and experimental data

Table 2 Isotopes abundance of ^{nat}Er

Isotope	Abundance (%)
^{162}Er	0.14
^{164}Er	1.61
^{166}Er	33.6
^{167}Er	22.95
^{168}Er	26.8
^{170}Er	14.9

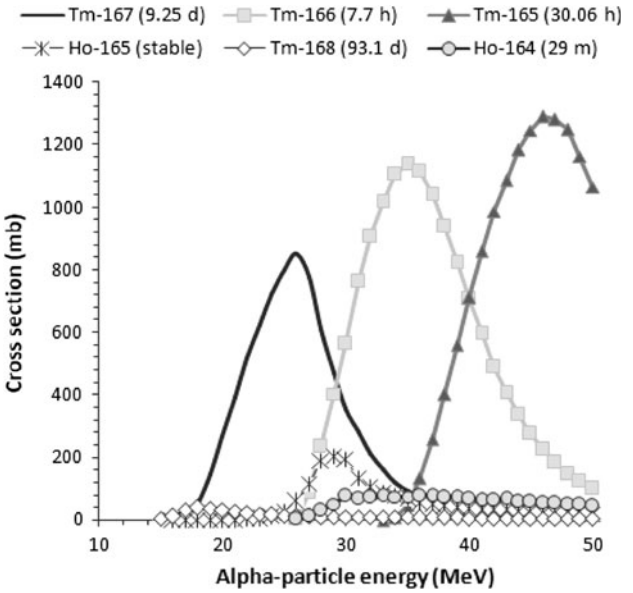

Fig. 5 Excitation function of ^{165}Ho(α,2n)^{167}Tm reaction calculated by TALYS-1.0 code

(93.1 d) half life is more than ^{167}Tm (9.25 d), but other produced radioisotope can be reduced by choosing proper energy range. The physical yield of ^{167}Tm was obtained 4.2 MBq/μA h. According to the SRIM code the required thickness of target is 51 μm for 6° geometry of the beam toward the target (Table 1).

^{165}Ho(α,2n) ^{167}Tm reaction

Holmium can be used to produce ^{167}Tm via alpha-particles bombardment. Furthermore, ^{165}Ho(α,2n)^{167}Tm reaction was determined one of the considerable reactions due to its mono-isotopic (^{165}Ho, 100% natural abundance). The acquired data from TALYS-1.0 code showed that ^{167}Tm has full benefit excitation function of 17–34 MeV (Fig. 5). Bombarding ^{165}Ho with alpha-particles leads to production of ^{166}Tm, ^{168}Tm and ^{164}Ho impurities at the energy range of 17–34 MeV. To limit the produce isotope and non-isotope impurities and to attain its benefit energy range, the 17–26 MeV energy range was considered. As can be seen

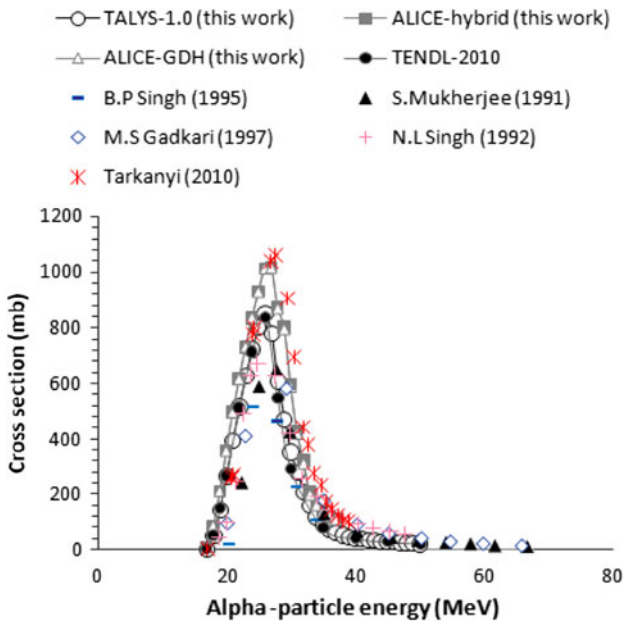

Fig. 6 Excitation function of ^{165}Ho(α,2n)^{167}Tm reaction calculated by ALICE/ASH (hybrid and GDH models) and TALYS-1.0 codes and experimental data

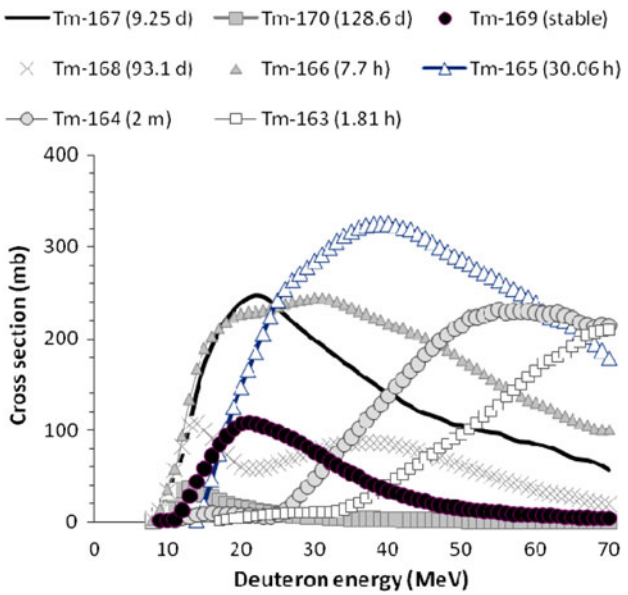

Fig. 7 Excitation function of ^{nat}Er(d,xn)^{167}Tm reactions calculated by TALYS-1.0 code

on Fig. 6, the ALICE and TALYS results are in acceptable agreement with the cross-section values reported by Gadkari [22], Singh [23], Singh [24], Mukherjee [25] and Tarkanyi et al. [7]. The calculated physical yield is 4.9 MBq/μA h. The recommended target thickness was calculated using the SRIM code (Table 1).

^{nat}Er(d,xn)^{167}Tm reaction

Excitation function of the deuteron induced reaction on ^{nat}Er was calculated and evaluation of the acquired data showed that the range of energy to produce ^{167}Tm is 10 to 70 MeV. TALYS-1.0 code predicted the maximum cross section to be about 247 mb at 22 MeV (Fig. 7). In this energy range there is lots of impurities and ^{169}Tm isotope (stable) will be produced. Accordingly, this reaction doesn't lead to ^{167}Tm production in no carrier-added state [20, 21]. According to SRIM code the thickness has to be 505.5 μm for 6° geometry beam toward the target and the physical yield is 16.7 MBq/μA h (Table 1). The calculated data are compared with the cross section values reported by Tarkanyi et al. [11] (Fig. 8). It should be noted that TALYS-1.0 code predicted cross sections for ^{nat}Er(d,xn)^{167}Tm reaction is lower than ALICE/ASH, TENDL-2010 and experimental data.

Target preparation

Among the possibilities to produce ^{167}Tm, with respect to existing facilities, we employed ^{nat}Er(p,x)^{167}Tm reaction to

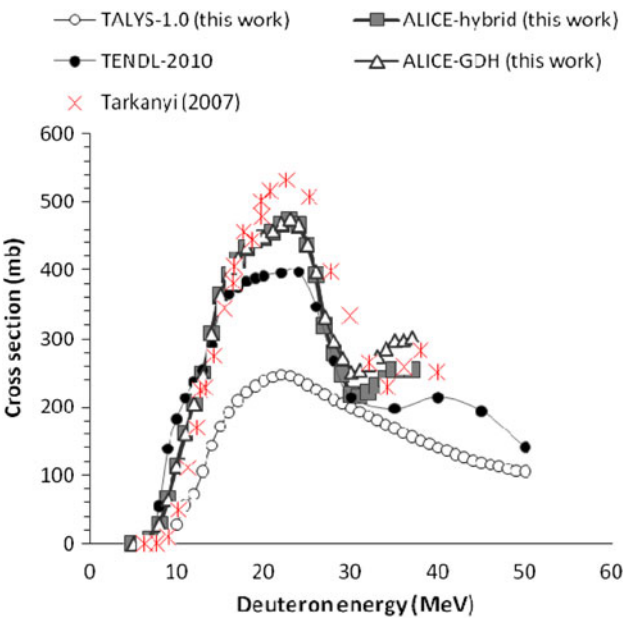

Fig. 8 Excitation function of ^{nat}Er(d,xn)^{167}Tm reaction calculated by ALICE/ASH (hybrid and GDH models) and TALYS-1.0 codes and experimental data

test the target preparation, the target quality, the irradiation and the thick target yield. The medical application require highly enriched ^{167}Er target.

A suspension of 103.2 mg ethyl cellulose ($C_{20}H_{38}O_{11}$, Aldrich), 516 mg $^{nat}Er_2O_3$ (Aldrich, 99.99%) and 8 mL acetone was employed to prepare a $^{nat}Er_2O_3$ layer deposited on copper substrate. According to SRIM code the thickness has to be 510 μm for 90° geometry beam toward the target. To minimize the thickness of the

erbium(III)oxide layer and to increase heat transfer, a 6° geometry beam toward the target is preferred, in which this case a 51 μm $^{nat}Er_2O_3$ layer is recommended. Physical thickness of erbium oxide layer is chosen as for a given beam/target angle geometry to provide bombarding beam exit energy of about 7 MeV. The $^{nat}Er_2O_3$ suspension solution was stirred for several minutes and loaded into cylinder of the upper disk immediately. A particular device made of Teflon (PTFE) was constructed. It consists of two plates of 19 × 10 cm^2 surface and 3 cm height. The upper plate contains an elliptical window of 11.69 cm^2 (same as the copper substrate). The copper substrate was placed between these two plates, the upper part is fitted on it with six supporting pins and it is sealed by an *O*-ring fitted-window [26–30]. The solution evaporated slowly through the hole at the room temperature after about 24 h.

Adhesion agent amount and target quality control

Adhesion is an important factor for adhering and coating among physical properties of the samples. Insufficient amount of ethyl cellulose causes poor adhesiveness of deposited erbium(III)oxide layer. On the other hand, their over abundance reduces thermal conductivity of the target. To optimize the quantity for maximum adhesion and thermo-stability of $^{nat}Er_2O_3$ layer, the samples were examined with different quantities of EC with respect to $^{nat}Er_2O_3$ (Table 3). Homogeneity of the $^{nat}Er_2O_3$ layer, which may affect the production rate of ^{167}Tm, was determined by standard deviation of the layer thickness measured at several spots by micrometer, while the morphology by SEM (see Fig. 9). Results of the thermal shock tests and adhesion agent amount are given in Table 3.

Irradiation

The $^{nat}Er_2O_3$ target was bombarded in this study. ^{167}Tm was produced via proton induced reactions on erbium(III)oxide at the AMIRS (Cyclone-30, IBA, Belgium) cyclotron with 15 MeV protons at 20 μA current beam for 1 h.

Conclusions

In this study we employed ALICE/ASH (hybrid and GDH models) and TALYS-1.0 codes to calculation the excitation

Table 3 Influence of ethyl cellulose (EC) amount and thermal shock test with 8 mL acetone for 516 mg $^{nat}Er_2O_3$

W(EC) (mg)	W(EC)/W(Er_2O_3) (%)	t_d (mg cm^{-2})	Adhesion[a]	Comments	200 °C	300 °C
77.4	15	43.4	Tolerable	Porous	Stable	Unstable
103.2	20	43.9	Excellent	Reflective, smooth	Stable	Stable
129	25	42.8	Excellent	Reflective, smooth	Stable	Unstable, peeling off
154.8	30	41.7	Unfavourable	Porous	Unstable	Unstable, peeling off

The heating of the target for 60 min followed by submersion of the hot target in cold water (8 °C)

t_d = calculated thickness of the deposit on Cu backing

[a] Adhesion at room temperature

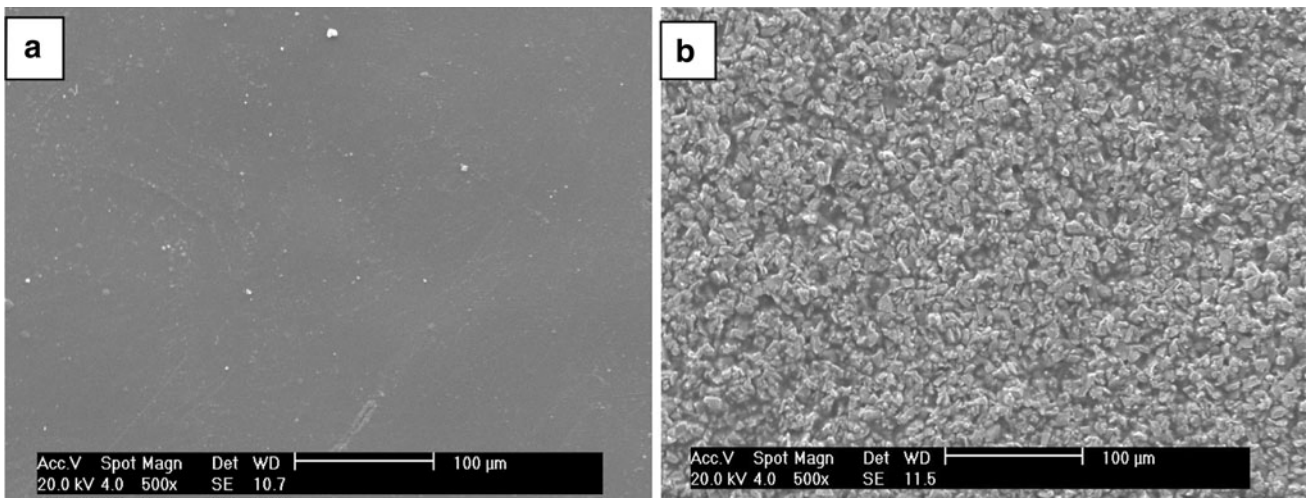

Fig. 9 SEM of erbium oxide deposit on the Cu backing: **a** for 516 mg of $^{nat}Er_2O_3$, 103.2 mg of EC, and 8 mL of acetone suspensions (no crack was observed), **b** respectively for 516 mg, 77.4 mg and 8 mL

functions of ^{165}Ho(α,2n)^{167}Tm, ^{167}Er(p,n)^{167}Tm, ^{nat}Er(d,xn)^{167}Tm and ^{nat}Er(p,xn)^{167}Tm reactions. Accordingly, ^{167}Er(p,n)^{167}Tm and ^{165}Ho(α,2n) ^{167}Tm reactions are suggested as the best method to produce ^{167}Tm because of minimum impurities; Additionally, lower thickness of the target is another advantage of those reactions.

A suspension of 103.2 mg ethyl cellulose, 516 mg $^{nat}Er_2O_3$ and 8 mL acetone was employed to prepare a $^{nat}Er_2O_3$ layer deposited on copper substrate. According to SEM scans, observation of neither crack formation nor pit on the surface indicated a good adhesion for the target preparation of ^{167}Tm. Sedimented $^{nat}Er_2O_3$ target was irradiated by 15 MeV protons. Through the irradiation of 516 mg $^{nat}Er_2O_3$ at 20 μA beam current for 1 h, yield of about 3.2 MBq/μA h was found (using γ-ray spectroscopy), which is 24% less compared to the yield calculated from the excitation function. Production of ^{167}Tm from ^{nat}Er(p,xn)^{167}Tm reaction is not suitable because of lots of impurities and simultaneously isotope stable (^{169}Tm) production. Therefore, in order to the cyclotron production of no-carrier-added ^{167}Tm from Er, highly enriched ^{167}Er target, is suggested.

References

1. Sadeghi M, Bakht MK, Mokhtari L (2011) Practicality of the cyclotron production of radiolanthanide^{142}Pr: a potential for therapeutic applications and biodistribution studies. J Radioanal Nucl Chem 288:937–942
2. Bakht MK, Sadeghi M (2011) Internal radiotherapy techniques using radiolanthanide praseodymium-142: a review of production routes, brachytherapy, unsealed source therapy. Ann Nucl Med. doi:10.1007/s12149-011-0505-z
3. Ando A, Ando I, Sakamoto K, Hiraki T, Hisada K, Takeshita M (1983) Affinity of ^{167}Tm-citrate for tumor and liver tissue. Eur J Nucl Med Mol Imaging 8:440–446
4. Beyer GJ, Franke WG, Hennig K, Johannsen BA, Khalkin VA, Kretzschmar M, Lebedev NA, Munze R, Novgorodov AF, Thieme K (1978) Comparative kinetic studies of simultaneously injected ^{167}Tm and ^{67}Ga citrate in normal and tumour bearing mice. Appl Radiat Isot 29:673–681
5. Uusijärvi H, Bernhardt P, Rösch F, Maecke HR, Forssell-Aronsson E (2006) Electron- and positron-emitting radiolanthanides for therapy: aspects of dosimetry and production. J Nucl Med 47:807–814
6. Yano Y, Chu P (1975) Cyclotron-produced thulium-167 for bone and tumor scanning. Inter J Nucl Med Biol 2:135–139
7. Tárkányi F, Hermanne A, Király B, Takács S, Ignatyuk AV (2010) Study of excitation functions of alpha-particle induced nuclear reactions on holmium for ^{167}Tm production. Appl Radiat Isot 68:404–411
8. Tárkányi F, Hermanne A, Takács S, Király B, Spahn I, Ignatyuk AV (2010) Experimental study of the excitation functions of proton induced nuclear reactions on ^{167}Er for production of medically relevant ^{167}Tm. Appl Radiat Isot 68:250–255
9. Tárkányi F, Takács S, Hermanne A, Ditrói F, Király B, Baba M, Ohtsuki T, Kovalev SF, Ignatyuk AV (2008) Study of activation cross sections of proton induced reactions on erbium for practical applications. Nucl Instrum Methods B 266:4872–4876
10. Hermanne A, Adam Rebeles R, Tárkányi F, Takács S, Király B, Ignatyuk AV (2011) Cross sections for production of longer lived 170, 168, 167Tm in 16 MeV proton irradiation of natEr. Nucl Instrum Methods Phys Res B 269:695–699
11. Tárkányi F, Hermanne A, Király B, Takács S, Ditrói F, Baba M, Ohtsuki T, Kovalev SF, Ignatyuk AV (2007) Study of activation cross-sections of deuteron induced reactions on erbium: production of radioisotopes for practical applications. Nucl Instrum Methods Phys Res Sect B 259:829–835
12. Hermanne A, Adam Rebeles R, Tárkányi F, Takács S, Spahn I, Ignatyuk AV (2011) High yield production of the medical radioisotope 167Tm by the 167Er(d, 2n) reaction. Appl Radiat Isot 69:475–481
13. Tárkányi F, Hermanne A, Takács S, Ditrói F, Király B, Yamazaki H, Baba M, Mohammadi A, Ignatyuk AV (2009) Activation cross-sections of proton induced nuclear reactions on ytterbium up to 70 MeV. Nucl Instrum Methods Phys Res Sect B 267:2789–2801
14. Király B, Tárkányi F, Takács S, Hermanne A, Kovalev SF, Ignatyuk AV (2008) Excitation functions of alpha-induced nuclear reactions on natural erbium. Nucl Instrum Methods Phys Res B 266:549–554
15. Scholz KL, Sodd VJ, Blue JW (1976) Production of thulium-167 for medical use by irradiation of lutetium, hafnium, tantalum and tungsten with 590 MeV protons. Appl Radiat Isot 27:263–266
16. Broeders CHM, Konobeyev AYu, Korovin YuA, Lunes VP, Blann M (2006) ALICE/ASH–Pre-compound and evaporation model code system for calculation of excitation functions, energy and angular distributions of emitted particles in nuclear reaction at intermediate energies, FZK-7183. http://bibliothek.fzk.de/zb/berichte/FZKA7183.pdf
17. Koning AJ, Hilaire SD, Duijvestijn MC (2007) TALYS-1.0. In: Proceedings of the international conference on nuclear data for science and technology, Nice, 2007
18. Koning A J, Rochman D (2010) TENDL-2010: TALYS-based evaluated nuclear data library. Nuclear Research and Consultancy Group (NRG) Petten, The Netherlands, http://www.talys.eu/tendl-2010
19. Ziegler JF, Biersack JP, Littmark U (2006) The code of SRIM—the stopping and range of ions in matter. IBM Research, New York
20. de Goeij JJM, Bonardi ML (2005) How do we define the concepts specific activity, radioactive concentration, carrier, carrier-free and no-carrier-added? J Radioanal Nucl Chem 263:13–18
21. Naught M, Wilkinson A, Nic M, Jirat J, Kosata B, Jenkins A (2006) IUPAC, compendium of chemical terminology. XML on-line corrected version: http://goldbook.iupac.org. ISBN 0-9678550-9-8. doi:10.1351/goldbook
22. Gadkari MS, Patel HB, Shah DJ, Singh NL (1997) Study of preequilibrium decay in(a, xn) reactions in holmium up to 70 MeV. Physica Scripta 55:147–151
23. Singh BP, Prasad R (1995) Measurement and analysis of excitation functions for the reactions 165Ho(a, xn) (x = 1–3) in the energy range 10–40 MeV. Physica Scripta 51:440–445
24. Singh NL, Agarrwal S, RamaRao J (1992) Pre-equilibrium neutron emission in alpha particle induced reactions. J Phys 18:927–934
25. Mukherjee S, MohanRao AV, RamaRao J (1991) Pre-equilibrium analysis of the excitation functions of (a, xn) reactions on silver and holmium. Nuovo Cimento 104:863–874
26. Sadeghi M, Zali A, Sarabadani P, Majdabadi A (2009) Targetry of $SrCO_3$ on a copper substrate by sedimentation method for the cyclotron production no-carrier-added ^{86}Y. Appl Radiat Isot 67:2029–2032

27. Sadeghi M, Enferadi M, Nadi H (2010) A novel method for the cyclotron production no-carrier-added ^{93m}Mo for nuclear medicine. J Radioanal Nucl Chem 286:141–144
28. Sadeghi M, Enferadi M, Nadi H (2010) Study of the cyclotron production of ^{172}Lu: an excellent radiotracer. J Radioanal Nucl Chem 286:259–263
29. Sadeghi M, Enferadi M, Aboudzadeh M, Sarabadani P (2010) Production of ^{122}Sb for the study of environmental pollution. J Radioanal Nucl Chem 287:585–589
30. Sadeghi M, Alipoor Z, Kakavand T (2010) Target preparation of RbCl on a copper substrate by sedimentation method for cyclotron production. Nuklenika 55:303–306

4.2 Radiochemical studies relevant to cyclotron production of the therapeutic radionuclide ^{167}Tm

Authors: Nadia Zandi, Mahdi Sadeghi, Hossein Afarideh, Mostafa Yarmohamadi

Journal of Radiochim. Acta 100:915–918 (2012)

Highlights: In this study, ^{167}Tm (with a half-life of 9.25 d) was produced via the ^{nat}Er(p,xn)^{167}Tm nuclear reaction with 15 MeV protons at a beam current of 20 μA. Then, the radiochemical separation of ^{167}Tm from a solution of the irradiated Er target in hydrochloric acid was performed using di-(2-Ethylhexyl) phosphoric acid (HDEHP) in n-hexane and in chloroform separately. Moreover, the effect of HDEHP with different concentrations on extraction efficiency was investigated. Finally, the radiochemical yield of ^{167}Tm was obtained about 80±5% using n-hexane/HDEHP (1 M).

Contributions: In this study, I contributed to the radiochemical separation and investigation of different concentrations on extraction efficiency. Furthermore, I wrote the manuscript.

Radiochim. Acta **100**, 915–918 (2012) / **DOI** 10.1524/ract.2012.1987

Radiochemical studies relevant to cyclotron production of the therapeutic radionuclide ^{167}Tm

By N. Zandi[1]*, M. Sadeghi[2], H. Afarideh[1] and M. Yarmohamadi[2]

[1] Department of Nuclear Engineering and Physics, Amir-Kabir University of Technology, P.O. Box 4155-4494, Tehran, Iran
[2] Agricultural, Medical and Industrial Research School, Nuclear Science and Technology Research Institute, P.O. Box 31485/498, Karaj, Tehran, Iran

(Received September 16, 2011; accepted in final form May 2, 2012)
(Published online October 15, 2012)

^{167}Tm / $^{nat}Er_2O_3$ *target / Cyclotron production / Radiochemical separation / Solvent extraction / Production yield*

Summary. Thulium-167, having a half-life of 9.25 d, is an important therapeutic radionuclide. It was produced *via* the $^{nat}Er(p,xn)^{167}Tm$ nuclear reaction by irradiation of a sedimented target with 15 MeV protons at a beam current of 20 μA. Radiochemical separation of ^{167}Tm from a solution of the irradiated erbium target in hydrochloric acid was performed using di-(2-ethylhexyl) phosphoric acid (HDEHP) in *n*-hexane and in chloroform separately. The effect of different molarities of HDEHP on extraction efficiency was investigated. The radiochemical yield of ^{167}Tm amounted to about 80 ± 5% while using *n*-hexane/HDEHP (1 M). The experimentally obtained production yield was about 3.2 MBq/μA h. It was comparable with the theoretical value of 4.1 MBq/μA h obtained from nuclear model calculations using the TALYS and EMPIRE codes.

1. Introduction

^{167}Tm ($T_{1/2} = 9.25$ d) emits a prominent γ-ray of 208 keV energy, low energy electrons (< 200 keV) and X-rays. Hence it can be used in nuclear medicine, especially for therapy [1–3]. Tumor imaging was done with ^{167}Tm-citrate because of strong tumor affinity and suitable physical characteristics [4]. ^{167}Tm accumulated in *via*ble tumor tissue and tissue containing viable and necrotic tumor tissue [5]. Many researchers measured experimentally excitation functions for the formation of ^{167}Tm by different projectiles on various targets. There are three direct principal routes to produce ^{167}Tm at a cyclotron:

(i) the bombardment of ^{nat}Er with proton and deuteron, *i.e.* the $^{nat}Er(p,xn)^{167}Tm$ and $^{nat}Er(d,xn)^{167}Tm$ reactions [6–8];
(ii) the bombardment of ^{167}Er with proton and deuteron, *i.e.* the $^{167}Er(p,n)^{167}Tm$ and $^{167}Er(d,2n)^{167}Tm$ reactions [9, 10] and
(iii) alpha induced reaction on ^{165}Ho, *i.e.* the $^{165}Ho(\alpha,2n)^{167}Tm$ reaction [11].

Also ^{167}Tm can be produced through the indirect reactions [12–14]: $^{169}Tm(p,3n)^{167}Yb \rightarrow {}^{167}Tm$, $^{nat}Yb(p,x)^{167}Lu \rightarrow {}^{167}Yb \rightarrow {}^{167}Tm$, $^{nat}Er(\alpha,xn)^{167}Yb \rightarrow {}^{167}Tm$ and $^{nat}Hf(p,x)^{167}Lu \rightarrow {}^{167}Yb \rightarrow {}^{167}Tm$.

The separation of lanthanides is notoriously difficult and many processes have been used over the years with varied levels of success. In 1950, Fitch and Russel reported on the ion-exchange separation of lanthanides using complexing agents, and careful control of pH and ion concentration [15]. Over the last forty years, solvent extraction technique was extensively used. The selectivity in solvent extraction for the neighbors of lanthanides is generally low because they are chemically very similar.

In recent years separation of thulium and erbium were reported with resin containing 1-hexyl-4-ethyloctyl isopropylphosphonic acid (HEOPPA) by Wang *et al.* [16], α-hydroxyisobutyric acid (α-HIB) by Schwantes *et al.* [17], a mixture of acidic phosphorus based reagents by Xianglan *et al.* [18] and ion imprinted polymer particles *via* solid phase extraction by Kala *et al.* [19].

The aim of this work was to produce ^{167}Tm by developing a target that has sufficient stability at high power beam bombardment, and separating ^{167}Tm from the irradiated target by solvent extraction [18, 20] using di-(2-ethylhexyl) phosphoric acid (HDEHP) into *n*-hexane and into chloroform separately. Attention was also devoted to the excitation functions and stopping power of protons in erbium oxide (using SRIM code) [21]. We calculated theoretical physical yield [22] and compared it with the experimental production yield.

2. Experimental

2.1 ^{167}Tm production

A suspension of ethyl cellulose ($C_{20}H_{38}O_{11}$, Aldrich), $^{nat}Er_2O_3$ (Aldrich, 99.99%) and acetone was used to prepare a $^{nat}Er_2O_3$ layer deposited on copper substrate (8.7 g/cm^3) [7, 23].

For production of ^{167}Tm, the target was bombarded with 15 MeV protons for 1 h at 20 μA beam current. The energy range and power density at the target were 15–6 MeV and 15.4 W cm^{-2}, respectively.

*Author for correspondence (E-mail: nadia_zandi@yahoo.com).

2.2 Ethyl cellulose removal

The irradiated target was dissolved with 50 mL acetone. The obtained solution was evaporated to near dryness, the residue was dissolved in 12 M HCl (50 mL) and the obtained solution was filtered with Whatman-41 filter paper for removing the residual ethyl cellulose. Washing the filter with 12 M HCl following the filtration ensures ethyl cellulose removal and radiothulium elution.

2.3 Tm/Er separation technique

The first extraction was performed into *n*-hexane/HDEHP. A 10 mL portion of aqueous feed solution ($ErCl_3$ and $TmCl_3$) was equilibrated with 2.5 mL of the organic solvent (1 M HDEHP) in a separatory funnel by shaking the two phases vigorously for 5 min and then allowing the phases to separate for at least 10 min. The organic phase was washed four times. Thulium and erbium were extracted into the organic phase (HDEHP in *n*-hexane) which was then transferred into a separatory funnel and was washed with 8 M HC1 (80 mL). In this condition, $ErCl_3$ was back extracted into aqueous phase and $TmCl_3$ remained in the organic phase [20].

2.4 Chemical and radionuclidic purity control

To determine percentage of Er impurity in the final solution, separation was repeated in cold. Weighed amounts of Er_2O_3 and Tm_2O_3were dissolved in 12 M HCl and mixed. Afterwards the separation procedure was carried out using the same process as explained for 1 M *n*-hexane/HDEHP. The obtained solution was examined by ICP-AES. Identification and assay of gamma-ray emitting radionuclide was carried out using γ-ray spectrometry with a high purity (HPGe) detector (Canberra™ model GC1020-7500SL).

3. Results and discussion

3.1 Tm/Er separation

Solvent extraction of ^{167}Tm from irradiated erbium(III)oxide target hydrochloric solution, was carried out using *n*-hexane/HDEHP (1 M) and the radiochemical yield was 80 ± 5%. Thulium was effectively separated from ethyl cellulose (EC) and erbium.

3.2 Effect of HDEHP molarities on extraction of thulium

The extraction was performed into *n*-hexane/HDEHP and also into chloroform/HDEHP with different molarities of HDEHP (0.5, 0.75, 1, 1.5 and 2 M) to find the condition under which the Tm and Er separate more efficiently. The results showed that by extraction into *n*-hexane/HDEHP (1 M), the thulium and erbium were extracted more into organic phase and in the latest stage (back extraction) Tm was separated from Er more efficiently. Indeed, *n*-hexane/HDEHP (1 M), is the best condition to separate Tm from Er compared to other conditions (Fig. 1).

3.3 Chemical and radionuclidic purity control

The solution obtained after separation of Tm from Er in nonradioactive test was analyzed by ICP-AES. The amount of Er impurity detected for the prepared solution (1 M *n*-hexane/HDEHP) was 4.7 ppm. Through the irradiation of $^{nat}Er_2O_3$ (the entire $^{nat}Er_2O_3$ target was dissolved in acetone), yield of about 3.2 MBq ^{167}Tm per μA h was experimentally obtained (Table 1). Using the (HPGe) detector (Canberra™ model GC1020-7500SL) thulium-167 was mainly identified by the following γ peaks: 208 keV (41%), 57 keV (4.6%) [24].

3.4 Experimental production yield

As the natural erbium is composed of six stable isotopes (^{162}Er = 0.14%; ^{164}Er = 1.61%; ^{166}Er = 33.6%; ^{167}Er = 22.9%; ^{168}Er = 26.8%; ^{170}Er = 14.9%), ^{167}Tm is produced mainly *via* two channels, *i.e.* ^{167}Er$(p,n)^{167}$Tm and ^{168}Er$(p,2n)^{167}$Tm reactions. Indeed the yield obtained from this study is contribution of two reactions. ^{168}Er$(p,2n)^{167}$Tm reaction has a high cross section to produce ^{167}Tm in this energy range (about 930 mb at 15 MeV) [25] and as can be seen in Table 1, by considering TALYS-1.0 code [26], the

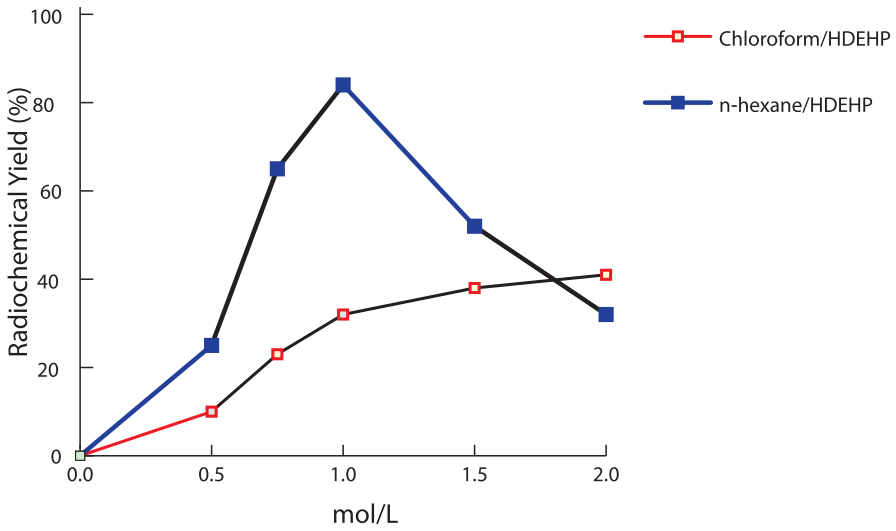

Fig. 1. Separation of Tm from Er using di-(2-ethylhexyl) phosphoric acid (HDEHP) in *n*-hexane and chloroform with different molarities of HDEHP.

Table 1. Yields of ^{167}Tm in proton irradiation of erbium.

Reaction	Energy range (MeV)	Yield (MBq/μA h)	Reference
^{nat}Er(p, xn)^{167}Tm	15–6	3.2	This work
	15–6	4.1	Theoretical calculation[a]
	15–6	4.2	Theoretical calculation[b]
^{167}Er(p, n)^{167}Tm	15–6	5.8	Theoretical calculation[a]
	15–6	6.2	Theoretical calculation[b]
^{168}Er($p, 2n$)^{167}Tm	15–6	10.3	Theoretical calculation[a]
	15–6	10.5	Theoretical calculation[b]

a: Theoretical calculation by TALYS-1.0 code (this work);
b: Theoretical calculation by EMPIRE (3.1 Rivoli) code (this work).

theoretical yield obtained from ^{168}Er and ^{167}Er is 10.3 and 5.8 MBq/μAh respectively. Somewhat similar values were obtained using the EMPIRE (3.1 Rivoli) code [27]. Therefore with respect to isotopic abundance, the theoretical yield from natural erbium is calculated as 4.1 MBq/μA h. This theoretical yield is comparable to our experimental yield of 3.2 MBq/μA h.

The experimental yield is slightly lower because of the use of $^{nat}Er_2O_3$ target as compared to ^{nat}Er target assumed in calculations. The proton induced reaction considered here leads to ^{167}Tm in no-carrier-added form.

4. Conclusion

The sedimentation technique was successfully applied to prepare a target for cyclotron production of ^{167}Tm. The radiothulium produced *via* proton bombardment of natural Er_2O_3 was separated from hydrochloric acid solution sufficiently using *n*-hexane/HDEHP (1 M).

References

1. Beyer, G. J., Franke, W. G., Hennig, K., Johannsen, B. A., Khalkin, V. A., Kretzschmar, M., Lebedev, N. A., Münze, R., Novgorodov, A. F., Thieme, K.: Comparative kinetic studies of simultaneously injected ^{167}Tm and ^{67}Ga citrate in normal and tumor bearing mice. Appl. Radiat. Isot. **29**, 673 (1978).
2. Uusijärvi, H., Bernhardt, P., Rösch, F., Maecke, H. R., Forssell-Aronsson, E.: Electron- and positron-emitting radiolanthanides for therapy: Aspects of dosimetry and production. J. Nucl. Med. **47**, 807 (2006).
3. Yano, Y., Chu, P.: Cyclotron-produced thulium-167 for bone and tumor scanning. Inter. J. Nucl. Med. Biol. **2**, 135 (1975).
4. Ando, A., Ando, I., Sakamoto, K., Hiraki, T., Hisada, K., Takeshita, M.: Affinity of ^{167}Tm-citrate for tumor and liver tissue. Eur. J. Nucl. Med. Mol. Imaging **8**, 440 (1983).
5. Ando, A., Ando, I., Sanada, S., Hiraki, T., Takeuchi, T., Hisada, K., Tonami, N.: Relationship between the bio distributions of radioactive metal nuclides in tumor tissue and the physicochemical properties of these metal ions. Annals. Nucl. Med. **13**, 83 (1999).
6. Hermanne, A., Adam Rebeles, R., Tárkányi, F., Takács, S., Király, B., Ignatyuk, A. V.: Cross sections for production of longer lived ^{170,168,167}Tm in 16 MeV proton irradiation of ^{nat}Er. Nucl. Instrum. Methods B **269**, 695 (2011).
7. Tárkányi, F., Hermanne, A., Király, B., Takács, S., Ditrói, F., Baba, M., Ohtsuki, T., Kovalev, S. F., Ignatyuk, A. V.: Study of activation cross-sections of deuteron induced reactions on erbium: production of radioisotopes for practical applications. Nucl. Instrum. Methods B **259**, 829 (2007).
8. Tárkányi, F., Takács, S., Hermanne, A., Ditrói, F., Király, B., Baba, M., Ohtsuki, T., Kovalev, S. F., Ignatyuk, A. V.: Study of activation cross sections of proton induced reactions on erbium for practical applications. Nucl. Instrum. Methods B **266**, 4872 (2008).
9. Tárkányi, F., Hermanne, A., Takács, S., Király, B., Spahn, I., Ignatyuk, A. V.: Experimental study of the excitation functions of proton induced nuclear reactions on ^{167}Er for production of medically relevant ^{167}Tm. Appl. Radiat. Isot. **68**, 250 (2010).
10. Hermanne, A., Adam Rebeles, R., Tárkányi, F., Takács, S., Spahn, I., Ignatyuk, A. V.: High yield production of the medical radioisotope ^{167}Tm by the ^{167}Er(d,2n) reaction. Appl. Radiat. Isot. **69**, 475 (2011).
11. Tárkányi, F., Hermanne, A., Király, B., Takács, S., Ignatyuk, A. V.: Study of excitation functions of alpha-particle induced nuclear reactions on holmium for ^{167}Tm production. Appl. Radiat. Isot. **68**, 404 (2010).
12. Tárkányi, F., Hermanne, A., Takács, S., Ditrói, F., Király, B., Yamazaki, H., Baba, M., Mohammadi, A., Ignatyuk, A. V.: Activation cross-sections of proton induced nuclear reactions on ytterbium up to 70 MeV. Nucl. Instrum Methods B **267**, 2789 (2009).
13. Scholz, K. L., Sodd, V. J., Blue, J. W.: Production of thulium-167 for medical use by irradiation of lutetium, hafnium, tantalum and tungsten with 590 MeV protons. Appl. Radiat. Isot. **27**, 263 (1976).
14. Király, B., Tárkányi, F., Takács, S., Hermanne, A., Kovalev, S. F., Ignatyuk, A. V.: Excitation functions of alpha-induced nuclear reactions on natural erbium. Nucl. Instrum. Methods **266**, 549 (2008).
15. Fitch, F. T., Russel, D. S.: The separation of the rare earths by ion-exchange procedures. Can. J. Chem. **29**, 363 (1951).
16. Wang, Z. H., Ma, G. X., Lu, J, Liao, W. P., Li, D. Q.: Separation of heavy rare earth elements with extraction resin containing 1-hexyl-4-ethyloctyl isopropylphosphonic acid. Hydrometallurgy **66**, 95 (2002).
17. Schwantes, J. M., Rundberg, R. S., Taylor, W. A., Vieira, D. J.: Rapid, high-purity, lanthanide separations using HPLC. J. Alloys and Compounds **418**, 189 (2006).
18. Xianglan, W., Wei, L., Deqian, L.: Extraction and stripping of rare earths using mixtures of acidic phosphorus based reagents. J. Rare Earth **29**, 413 (2011).
19. Kala, R., Mary Gladis, J., Prasada Rao, T.: Pre concentrative separation of erbium from Y, Dy, Ho, Tb and Tm by using ion imprinted polymer particles via solid phase extraction. Anal. Chim. Acta **518**, 143 (2004).
20. Nadi, H., Sadeghi, M., Enferadi, M., Sarabadani, P.: Cyclotron production of ^{169}Yb: a potential radiolanthanide for brachytherapy. J. Radioanal. Nucl. Chem. **289**, 361 (2011).
21. Ziegler, J. F., Ziegler, M. D., Biersack, J. P.: SRIM—the stopping and range of ions in matter. Nucl. Instrum. Methods B **268**, 1818 (2010).
22. Sadeghi, M., Enferadi, M., Aref, M., Jafari, H.: Nuclear data for the cyclotron production of ^{66}Ga, ^{86}Y, ^{76}Br, ^{64}Cu and ^{43}Sc in PET imaging. Nukleonika **55**, 293 (2010).
23. Sadeghi, M., Alipoor, Z., Kakavand, T.: Target preparation of RbCl on a copper substrate by sedimentation method for cyclotron production. Nukleonika **55**, 303 (2010).
24. Firestone, R. B., Ekström, L. P.: WWW Table of radioactive isotopes. http://ie.lbl.gov/toi/perchart.htm (2004).

25. Koning, A. J., Rochman, D.: TENDL-2010: TALYS-based evaluated nuclear data library. Nuclear Research and Consultancy Group (NRG) Petten, The Netherlands, http://www.talys.eu/tendl-2010 (2010).
26. Koning, A. J., Hilaire, S. D., Duijvestijn, M. C.: TALYS-1.0: A nuclear reaction program. Nuclear Research and Consultancy Group (NRG) Petten, The Netherlands, http://www.talys.eu/download-talys. Accessed 21 December 2007.
27. Herman, M., Capote, R., Zerkin, V., Trkov, A., Wienke, H., Sin, M., Carlson, B. V., Matoon, C., Young-Sik, Cho: EMPIRE modular system for nuclear reaction calculations (version: 3.1 Rivoli) https://ndclx4.bnl.gov/gf/project/empire/ (2011).

4.3 Evaluation of the cyclotron production of ^{165}Er by different reactions

Authors: Nadia Zandi, Mahdi Sadeghi, Hossein Afarideh

Journal of Radioanalytical and Nuclear Chemistry, 295:923–928 (2013)

Highlights: ^{165}Er with a half-life of 10.3 h decays by electron capture to the ground state of stable isotope ^{165}Ho, and it is an appropriate radio-lanthanide for Auger electron therapy. In this study, excitation function of some major reaction channels such as ^{nat}Er(p,x)^{165}Tm→^{165}Er, ^{166}Er(p,2n)^{165}Tm→^{165}Er, ^{165}Ho(p,n)^{165}Er and ^{165}Ho(d,2n)^{165}Er reactions were calculated using ALICE/ASH (Hybrid and GDH models) and EMPIRE 3.1 codes. Moreover, target thickness and physical yield were evaluated with attention to stopping power, excitation function, and SRIM code. Then, ^{165}Er was produced using the sedimentation technique through the ^{nat}Er(p,x)^{165}Tm reaction channel. The target was irradiated with 15 MeV proton beams at 20 μA proton beam current for 1 h. The ^{165}Tm production yield was obtained 26 MBq/ μA h at EOB.

Contributions: In this study, I performed the theoretical calculations using ALICE, EMPIRE, and SRIM codes. I also performed the sedimentation technique to prepare the target. Furthermore, I wrote the manuscript.

J Radioanal Nucl Chem (2013) 295:923–928
DOI 10.1007/s10967-012-2116-0

Evaluation of the cyclotron production of ^{165}Er by different reactions

Nadia Zandi · Mahdi Sadeghi · Hossein Afarideh

Received: 9 May 2012 / Published online: 23 August 2012

Abstract Erbium-165 with 10.3 h physical half-life decays completely by electron capture to the ground state of stable isotope ^{165}Ho and it is an ideal radio lanthanide for Auger electron therapy. Excitation function of ^{165}Er via ^{nat}Er(p,x)^{165}Tm → ^{165}Er, ^{166}Er(p,2n)^{165}Tm → ^{165}Er, ^{165}Ho(p,n)^{165}Er and ^{165}Ho(d,2n)^{165}Er reactions were calculated using ALICE/ASH (Hybrid and GDH models) and EMPIRE 3.1 codes and then were compared with the reported measurement by experimental data and TENDL-2011. Physical yield and target thickness were evaluated with attention to excitation function, stopping power and SRIM code. ^{165}Er was produced using the sedimentation technique through the ^{nat}Er (p,x)^{165}Tm → ^{165}Er reaction. The deposited target was irradiated with 15 MeV proton beams at 20 μA current for 1 h. The ^{165}Tm production yield was 26 MBq/μA h at the end of bombardment.

Keywords ^{165}Er · Auger electron · Excitation function · EMPIRE-3.1 · ALICE/ASH · Physical yield · Production yield

Introduction

^{165}Er (10.3 h), decaying by electron capture to stable ^{165}Ho, offers an excellent promise for use in diagnostic nuclear medicine especially in conjunction with multi-wire proportional-counter cameras [1], and also is a potent nuclide for targeted radionuclide therapy [2]. New cancer targeted therapies that make use therapeutic antibodies or small molecules have made treatment more tumors specific and less toxic. Auger-emitting radio-nuclides have potential for the therapy of cancer due to their high level of cytotoxicity and short-range biological effectiveness [3].

Certain Auger electron emitters are particularly promising for targeted therapies because they deposit most of their decay radiation energy very locally (few micrometer to tens of micrometer range in soft tissue). Hence the therapeutic effect can be concentrated onto single cells or even onto the cell's nucleus (DNA) if selectively internalizing carriers are found [4].

In the previous works we evaluated cyclotron production of ^{167}Tm, ^{142}Pr, ^{85}Sr, ^{119}Sb and ^{61}Cu by ALICE/ASH, TALYS-1.0 and TALYS-1.2 codes and compared to existing data and TENDL-2010 [5–11]. The aim of this work was investigation of excitation functions of ^{nat}Er(p,x)^{165}Tm → ^{165}Er, ^{166}Er(p,2n)^{165}Tm → ^{165}Er,^{165}Ho(p,n)^{165}Er and ^{165}Ho(d,2n)^{165}Er reactions and comparison of them with EXFOR database and TENDL-2011 [12, 13]. Also with attention to the excitation functions and stopping powers of projectiles in erbium oxide (using SRIM code) [14], we calculated theoretical physical yield and target thickness. Eventually ^{165}Er was produced using ^{nat}Er(p,x)^{165}Tm → ^{165}Er reaction and production yield at the end of bombardment was compared with theoretical physical yield and the previous published results.

Excitation functions

In this part of work we employed new calculation code (EMPIRE 3.1 Rivoli) [15, 16] and excitation functions of

N. Zandi · M. Sadeghi · H. Afarideh
Department of Nuclear Engineering and Physics, Amir-kabir, University of Technology, P.O. Box 4155-4494, Tehran, Iran

M. Sadeghi (✉)
Agricultural, Medical & Industrial Research School, Nuclear Science and Technology Research Institute,
P.O. Box 31485/498, Karaj, Tehran, Iran
e-mail: msadeghi@nrcam.org

some reactions to produce ^{165}Er using ALICE/ASH and EMPIRE 3.1codes have been studied. According to results an optimum energy range was determined and employed to avoid the formation of radionuclide impurities and decrease the excitation functions of inactive impurities as far as possible.

EMPIRE 3.1 code

The EM PIRE (version 3.1 Rivoli), the latest version of the EM PIRE code, is a modular system of nuclear reaction codes comprised of various nuclear models and designed to perform nuclear reaction calculations over a wide range of energies and incident particles. The covered energy range is from resonance region (~keV) to several hundreds of MeV, and the projectile could be any nucleon, ion (including heavy ion) or a photon. EMPIRE is equipped with a complex system of codes to describe all the important nuclear reaction mechanisms It consists of a number of linked FORTRAN codes, input parameter libraries, and the experimental data library [15–17]. The code accounts for the major nuclear reaction mechanisms, including direct, pre-equilibrium and compound nucleus ones. The optical model and the direct reaction calculations were performed by the ECIS-03 code [18]. The optical model, discrete levels and deformation parameters were retrieved from the RIPL-2 library [19]. The direct channel calculations were performed by using the coupled channels model or the distorted wave Born approximation (DWBA) method. EMPIRE contains both the quantum mechanical (MSD/MSC) and classical models (DEGAS, PCROSS, HMS) to describe pre-equilibrium reactions. The option of EMPIRE-specific level densities was selected for all the calculations. An improved version of the Hauser–Feshbach theory was used for compound nucleus reactions. The 3.1 version of the EMPIRE code is equipped with the module that makes use the information contained in the Atlas of neutron resonances to produce resonance files and related covariances for the ENDF-6 formatted files.

The ALICE/ASH code

The ALICE/ASH code is a modified and advanced version of the ALICE/91 code. This code has been written to study the interaction of intermediate energy nucleons and nuclei with target nuclei. The code calculates energy and angular distributions of particles emitted in nuclear reactions, residual nuclear yields, and total nonelastic cross-sections for nuclear reactions induced by particles and nuclei with energies up to 300 MeV [4]. The parameters used in the ALICE/ASH code are as follow: (i) the Weisskopf–Ewing model for equilibrium calculations [20] (ii) The hybrid model and geometry dependent hybrid model (GDH) for pre-equilibrium emissions [21] (iii) the Fermi gas level density with the level density parameter "a = A/y" (the default value of y was 9). The hybrid model and the geometry dependent hybrid model (GDH) can be used for the calculation of particle spectra.

Calculation of the physical yield and the target thickness

Theoretical physical yield can be calculated by the following equation:

$$Y = \frac{N_L H}{M} I\left(1 - \mathrm{e}^{-\lambda t}\right) \int_{E_1}^{E_2} \left(\frac{\mathrm{d}E}{\mathrm{d}(\rho x)}\right)^{-1} \sigma(E)\mathrm{d}E$$

where Y is the product activity (in Bq) of the product, N_L is the Avogadro number, H is the isotope abundance of the target nuclide, M is the mass number of the target element, $\sigma(E)$ is the cross-section at energy E, I is the projectile current, $\mathrm{d}E/\mathrm{d}(\rho x)$ is the stopping power, λ is the decay constant of the product and t is the time of irradiation.

To obtain the optimum physical dimensions of the target such as the thickness, some estimation from the SRIM code (the stopping and range of ions in matter); were performed. SRIM is a group of programs which calculate the stopping and range of ions (up to 2 GeV/amu) into matter using a quantum mechanical treatment of ion-atom collisions. This calculation is made very efficient by the use of statistical algorithms which allow the ion to make jumps between calculated collisions and then averaging the collision results over the intervening gap.

The physical thickness of the target layer is chosen in such a way for a 90° geometry beam/target to ensure that the incident beam exits the target layer with a predicted energy; so the required thickness of the layer will be smaller with a coefficient 0.1.

TENDL-2011

TENDL is a nuclear data library which provides the output of the TALYS nuclear model code system for direct use in both basic physics and applications. The last version is TENDL-2011, which is based on both default and adjusted TALYS calculations and data from other sources [13].

Results and discussion

^{nat}Er(p,x) ^{165}Tm → ^{165}Er reaction

Regarding to ALICE/ASH code data for ^{nat}Er(p,x) ^{165}Tm → ^{165}Er reaction, ^{165}Tm has a maximum cross-section of about

586 mb at 22 MeV; its beneficial excitation functions occur between 8 and 40 MeV (Fig. 1). As the natural erbium is composed of six stable isotopes (^{162}Er = 0.14 %; ^{164}Er = 1.61 %;^{166}Er = 33.6 %; ^{167}Er = 22.9 %; ^{168}Er = 26.8 %; ^{170}Er = 14.9 %), some isotopic impurities will be produced from different channels in this energy range. ^{168}Tm is a long lived radioisotope (93.1 days) and will be produced at the threshold energy of 16 MeV and also existence of it in prepared radio-medicine could be result in excessive dose to the patient, therefore 8-15 MeV energy range was considered. For this reaction, the cross section measurements have been published by Tarkanyi et al. [22]. As can be seen in Fig. 2, The ALICE/ASH (Hybrid and GDH models) and EMPIRE-3.1 calculated results codes are in good agreement with the cross section values reported by Tarkanyi et al. [22].

^{166}Er(p,2n) ^{165}Tm → ^{165}Er reaction

Excitation function of the proton induced reaction on ^{166}Er was calculated and evaluation of the acquired data showed that the range of energy to produce ^{165}Tm is 12–27 MeV. ALICE/ASH code predicted the maximum cross section to be about 1,234 mb at 21 MeV (Fig. 3). In this energy range there are two isotopic impurities (^{164}Tm and ^{166}Tm). Production of radionuclidic impurities can be avoided by choosing 16–23 MeV energy range, therefore ^{166}Er(p,2n) ^{165}Tm → ^{165}Er reaction can be represented as the best reaction to produce ^{165}Er due to very high cross section to produce ^{165}Tm in no-carrier added form [23]. The results obtained from ALICE/ASH (Hybrid and GDH models) and EMPIRE-3.1 codes agree well with the measured data from Tarkanyi et.al [24] (Fig. 4). The physical yield and recommended target thickness was calculated using the SRIM code (Table 1).

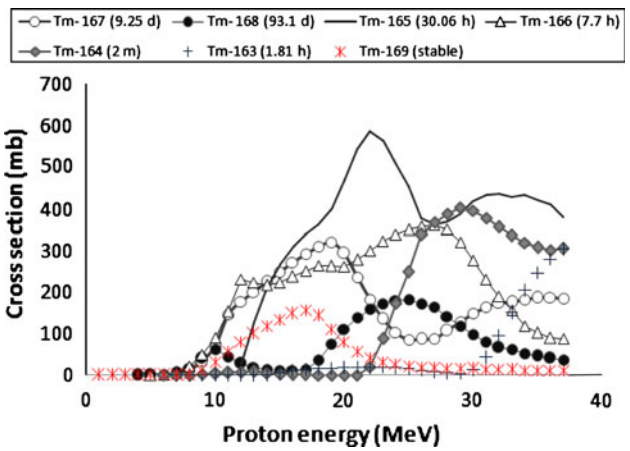

Fig. 1 Excitation function of ^{nat}Er(p,x)^{165}Tm → ^{165}Er reaction calculated by ALICE/ASH (Hybrid model) code

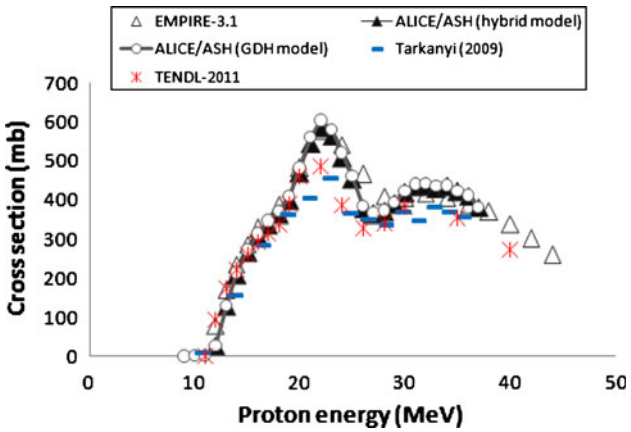

Fig. 2 Excitation function of ^{nat}Er(p,x)^{165}Tm → ^{165}Er reaction calculated by ALICE/ASH (Hybrid and GDH models) and EMPIRE-3.1 codes and experimental data

^{165}Ho(p,n)^{165}Er reaction

Excitation functions based on ALICE/ASH code calculation are shown in Fig. 5 at different decay channels after proton bombardment of holmium-165. Using this reaction, the best range of incident energy to produce ^{165}Er was assumed 7–11 MeV whose maximum cross section by ALICE/ASH code is 112 mb at 9 MeV. In this energy range a stable isotope ^{164}Er is simultaneously produced and could not be separated by chemical methods; therefore 7–9 MeV energy range should be considered to production of ^{165}Er in no-carrier-added state. Figure 6 shows the comparison between cross section values reported by Tarkanyi and Beyer [25, 26] and the results of nuclear model calculations employing the different theoretical calculations. It should be noted that the cross section values obtained by nuclear model calculation ALICE/ASH (Hybrid and GDH models) and TENDL-2011

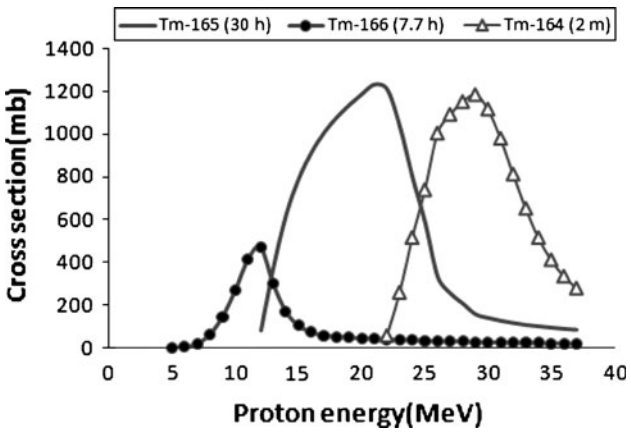

Fig. 3 Excitation function of ^{166}Er(p,2n)^{165}Tm → ^{165}Er reaction calculated by ALICE/ASH (Hybrid model) code

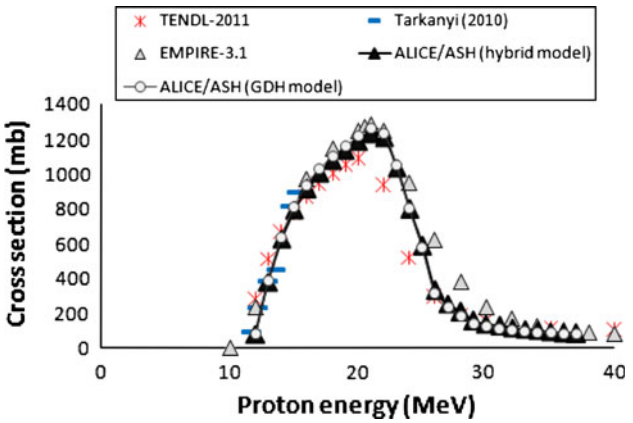

Fig. 4 Excitation function of $^{166}Er(p,2n)^{165}Tm \rightarrow {}^{165}Er$ reaction calculated by ALICE/ASH (Hybrid and GDH models) and EMPIRE-3.1 codes and experimental data

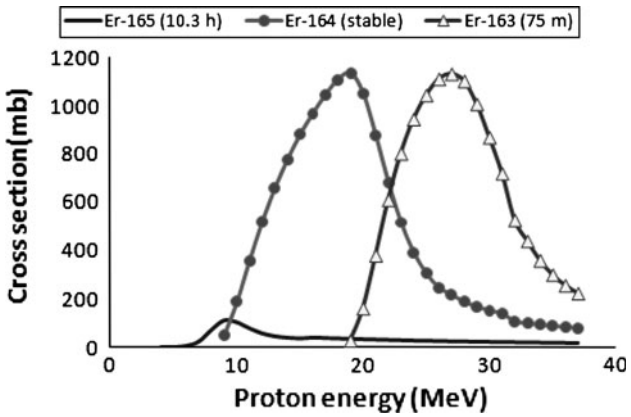

Fig. 5 Excitation function of $^{165}Ho(p,n)^{165}Er$ reaction calculated by ALICE/ASH (Hybrid model) code

Table 1 ^{165}Er physical yield and target thickness for various reactions

Reaction	Energy range (MeV)	Target thickness (μm)	Yield (MBq/μA h)	Reference
$^{nat}Er(p,x)^{165}Tm \rightarrow {}^{165}Er$	15–8	50.0	26.0	This work
	15–8	–	27.7	Theoretical calculation
	15–10	–	25.0	Tarkanyi [19]
$^{166}Er(p,2n)^{165}Tm \rightarrow {}^{165}Er$	23–16	60.7	315.2	Theoretical calculation
$^{165}Ho(p,n)^{165}Er$	11–7	21.1	29.4	Theoretical calculation
$^{165}Ho(d,2n)^{165}Er$	11–8	10.6	37.4	Theoretical calculation

are lower than experimental data reported by Tarkanyi and Beyer [25, 26] and also EMPIRE-3.1 code is more close to the experimental data and gives gradually higher maximum cross section value at 9 MeV compared to other calculational codes. As mentioned above, these discrepancies between the codes are due to the different models for description of the mechanisms and cross section depends on the type of model that describes these mechanisms, therefore results can vary. Also the hybrid model and geometry dependent hybrid model (GDH) are designed for pre-equilibrium emissions and the probability of pre-equilibrium mechanism reduces in this energy range. The physical yield of ^{165}Er was obtained 29.4 MBq/μA. h and the required thickness of target is 21.1 μm for $\mathring{6}$ geometry beam toward the target (Table 1).

$^{165}Ho(d,2n)^{165}Er$ reaction

Through this reaction to produce ^{165}Er, the best range of incident energy was assumed 8–18 MeV that maximum cross-section is 645 mb at 12 MeV. In this energy range $^{164/166}Er$ impurities are simultaneously produced (Fig. 7). These impurities are stable isotopes and could not be separated by chemical methods, therefore to limit production of stable isotopes and to production of ^{165}Er in no-carrier added form as far as possible, 8–11 MeV energy range are considered. As can be seen on

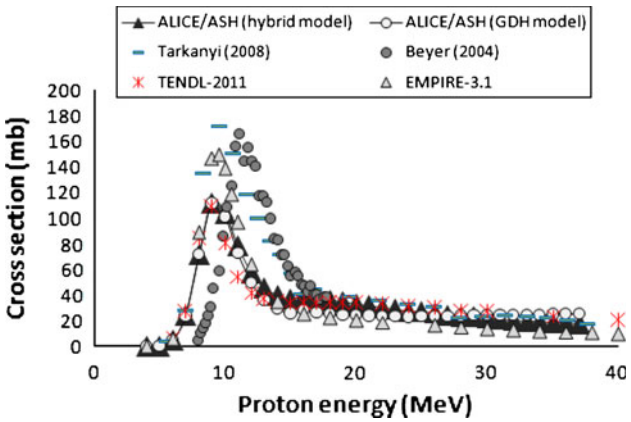

Fig. 6 Excitation function of $^{165}Ho(p,n)^{165}Er$ reaction calculated by ALICE/ASH (Hybrid and GDH models) and EMPIRE-3.1 codes and experimental data

Fig. 8, ALICE (Hybrid and GDH models) and EMPIRE-3.1 calculated results codes are in acceptable agreement with the cross section values reported by Tarkanyi et al. [27] and TENDL-2011. Theoretical physical yield in view of the chosen energy range is 37.4 MBq/μA h and by considering SRIM data, recommended thickness of the target is 10.6 μm for 6° geometry beams toward the target (Table 1).

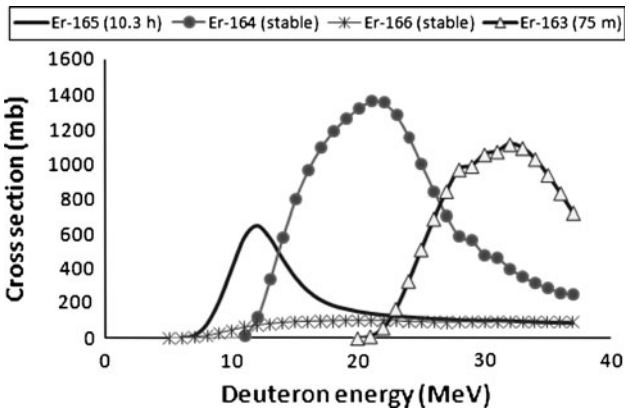

Fig. 7 Excitation function of ^{165}Ho(d,2n)^{165}Er reaction calculated by ALICE/ASH (Hybrid model) code

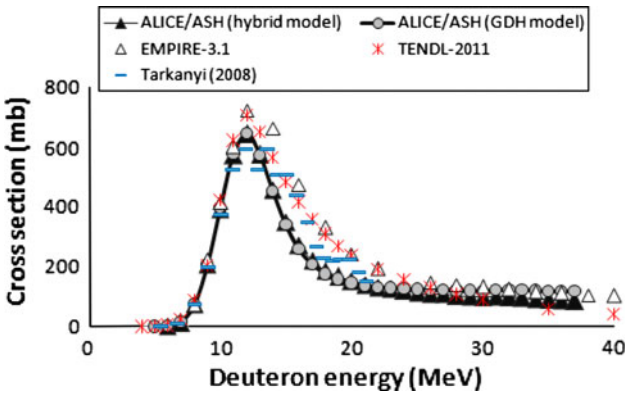

Fig. 8 Excitation function of ^{165}Ho(d,2n)^{165}Er reaction calculated by ALICE/ASH (Hybrid and GDH models) and EMPIRE-3.1 codes and experimental data

Target preparation and production yield

With respect to existing facilities, the ^{nat}Er(p,x) ^{165}Tm → ^{165}Er reaction was employed to produce ^{165}Tm radionuclide that leads to ^{165}Er production. It should be noted that medical application require highly enriched ^{166}Er target.

The $^{nat}Er_2O_3$ target was prepared by the stack foil technique first reported by Chandra et al. [28] and improved by Tarkanyi et al. [29] and Hermanne et al. [30]. High purity ^{nat}Er foils were stacked with Al backing.

In this study we employed sedimentation technique to prepare natural erbium oxide target.

A suspension of ethyl cellulose ($C_{20}H_{38}O_{11}$, Aldrich), $^{nat}Er_2O_3$ (Aldrich, 99.99 %) and acetone was employed to prepare a $^{nat}Er_2O_3$ layer deposited on copper substrate [7, 31].

The coated natural $^{nat}Er_2O_3$ target was introduced into a target holder and bombarded with 15 MeV protons at current of 20 μA for 1 h to reduce the proton beam energy from 15 to 8 MeV. Through the irradiation of natural target, the yield of ^{165}Tm was obtained about 26 MBq/μA h. This experimental yield is slightly lower because of the use of $^{nat}Er_2O_3$ target as compared to ^{nat}Er target assumed in calculations (Table 1).

Conclusion

In order to study practicality of the cyclotron production ^{165}Er, excitation function of ^{nat}Er(p,x)^{165}Tm → ^{165}Er, ^{166}Er(p,2n) ^{165}Tm → ^{165}Er, ^{165}Ho(p,n)^{165}Er and ^{165}Ho(d,2n)^{165}Er reactions were calculated by ALICE/ASH and EMPIRE-3.1 codes, and compared with the data taken from the TENDL-2011 and EXFOR database. By virtue of excitation function and SRIM code, physical yield and target thickness were calculated for each reaction.

By investigation the results, high yield production of ^{165}Er in no carrier added form can be obtained through the ^{166}Er(p,2n)^{165}Tm → ^{165}Er reaction; therefore it can be considered as the best reaction to produce ^{165}Er among the possibilities.

References

1. Roa DV, Hallee GJ, Ottlinger ME, Sastry KS (1997) Radiations emitted in the decay of ^{165}Er: a promising medical radionuclide. J Med phys 4:177–186
2. Donoghue JAO, Wheldon TE (1996) Targeted radiotherapy using Auger electron emitters. Phys Med Biol 41:1973–1992
3. Dorrer H, Ghezzi C, Haddad F, Jensen M, Köster U, Müller C, Pichler B, Rolle A M, Schibli R, et al. (2011) Novel diagnostic and therapeutic radio-nuclides for the development of innovative radiopharmaceuticals. European organization for nuclear research
4. Broeders C H M, Konobeyev A Yu, Korovin Yu A, Lunes V P, Blann M (2006) ALICE/ASH–Pre-compound and evaporation model code system for calculation of excitation functions, energy and angular distributions of emitted particles in nuclear reaction at intermediate energies, FZK-7183, http://bibliothek.fzk.de/zb/berichte/FZKA7183.pdf
5. Koning AJ, Hilaire SD, Duijvestijn MC (2007) TALYS-1.0. A nuclear reaction program NRG, The Netherlands, http://www.talys.eu/download-talys. Accessed 22 December 2007
6. Koning AJ, Hilairey S, Duijvestijn M (2009) TALYS-1.2: A nuclear reaction program. User manual, NRG, The Netherlands, http://www.talys.eu/download-talys. Accessed 22 December 2009
7. Sadeghi M, Zandi N, Afarideh H (2011) Targetry and specification of ^{167}Tm production parameters by different reactions. J Radioanal Nucl Chem 291:731–738
8. Sadeghi M, Zandi N, Bakhtiari M (2011) Nuclear model calculation for cyclotron production of ^{61}Cu as a PET imaging. J Radioanal Nucl Chem. doi:10.1007/s10967-011-1557-1
9. Sadeghi M, Bakht MK, Mokhtari L (2011) Practicality of the cyclotron production of radio lanthanide ^{142}Pr: a potential for therapeutic application and biodistribution studies. J Radioanal Nucl Chem 288:937–942
10. Sadeghi M, Enferadi M (2011) Nuclear model calculation on the production of ^{119}Sb via various nuclear reactions. J Ann Nucl Energy 38:824–825
11. Kakavand T, Sadeghi M, Alipoor Z (2010) Nuclear model calculation on charge particle induced reactions to produce ^{85}Sr for diagnostic and endtherapy. Kerntechnick 75:263–270
12. Experimental nuclear reaction data (EXFOR) (2012) http://www.nds.iaea.org/exfor/. Database Version of 2012

13. Koning A J, Rochman D (2011) TENDL-2011: TALYS-based evaluated nuclear data library, Nuclear Research and Consultancy Group (NRG) Petten, The Netherlands, http://www.talys.eu/tendl-2011
14. Ziegler JF, Ziegler MD, Biersack JP (2010) SRIM: the stopping and range of ions in matter. Nucl Instrum Methods B 268: 1818–1823
15. Herman M, Capote R, Sin M, Trkov A, Carlson BV, et al. (2012) EMPIRE-3.1 Rivoli: modular system for nuclear reaction calculations and nuclear reaction evaluation. NNDC, Brookhaven National Laboratory, Upton. Accessed 8 February, 2012
16. Herman H, Capote R, Carlson BV, Oblozinsky P, Sin M, Trkov A, Wienke H, Zerkin V (2007) EMPIRE: nuclear reaction model code system for data evaluation. Nucl Data Sheets 108: 2655–2715
17. Herman M, Oblozinsky P (2005) NNDC, Brookhaven National Laboratory. http://www.nndc.bnl.gov/empire219. Accessed September, 2005
18. Raynal J (1994) Notes on ECIS-94, CEA Saclay Report No. CEA-N-2772
19. Belgya T, Bersillon O, Capote R, Fukahori T, Zhigang G, Goriely S, Herman M, Ignatyuk AV, Kailas S, Koning A, Obložinský P, Plujko V, Young P, (2006) Handbook for calculations of nuclear reaction data, Reference input parameter library-2. Tech. Rep. IAEA-TECDOC-1506, IAEA, Vienna, pp 1–159. http://www-nds.iaea.or.at/RIPL-2
20. Weisskopf VF, Ewing DH (1940) On the yield of nuclear reactions with heavy elements. Phys Rev 57:472–485
21. Blann M (1991) ALICE-91, Statistical model code system with fission competition, RSIC code, PACKAGE PSR-146
22. Tárkányi F, Takács S, Hermanne A, Ditrói F, Király B, Baba M, Ohtsuki T, Kovalev SF, Ignatyuk AV (2009) Investigation of production of the therapeutic radioisotope ^{165}Er by proton induced reactions on erbium in comparison with other production routes. Appl Radiat Isot 67:243–247
23. de Goeij JJM, Bonardi ML (2005) How do we define the concepts specific activity, radioactive concentration, carrier, carrier-free and no-carrier-added. J Radioanal Nucl Chem 263:13–18
24. Tárkányi F, Hermanne A, Takács S, Király B, Spahn I, Ignatyuk AV (2010) Experimental study of the excitation functions of proton induced nuclear reactions on ^{167}Er for production of medically relevant ^{167}Tm. Appl Radiat Isot 68:250–255
25. Beyer GJ, Zeisler SK, Becker DW (2004) The auger electron emitter Er-165: excitation function of the Ho-165(p, n)Er-165 process. Radiochim Acta 92:219–223
26. Tárkányi F, Hermanne A, Takács S, Ditrói F, Király B (2008) Experimental study of the 165Ho(p, n) nuclear reaction for production of the therapeutic radioisotope 165Er. Nucl Instrum Methods B 266:3346–3352
27. Tárkányi F, Takács S, Hermanne A, Ditrói F (2008) Experimental study of the ^{165}Ho(d,2n) and ^{165}Ho(d, p) nuclear reactions up to 20 MeV for production of the therapeutic radioisotopes ^{165}Er and ^{166}gHo. Nucl Instrum Methods B 266:3529–3534
28. Chandra R, Braunstein P, Thein A (1972) Production of ^{167}Tm for medical use. Appl Radiat Isot 23:553
29. Tárkányi F, Takács S, Hermanne A, Ditrói F, Király B, Bab M, Ohtsuki T, Kovalev SF, Ignatyuk AV (2008) Study of activation cross sections of proton induced reactions on erbium for practical applications. Nucl Instrum Methods B 266:4872–4876
30. Hermanne A, Adam Rebeles R, Tarkanyi F, Takács S, Király B, Ignatyuk AV (2011) Cross sections for production of longer lived $^{170,\ 168,\ 167}$Tm in 16 MeV proton irradiation of ^{nat}Er. Nucl Instrum Methods Phys Res B 269:695–699
31. Sadeghi M, Alipoor Z, Kakavand T (2010) Target preparation of RbCl on a copper substrate by sedimentation method for cyclotron production. Nuklenika 55:303–306

4.4 Investigation of the production of the Auger electron emitter ^{135}La using medical cyclotrons

Authors: Jerzy Jastrzębski, Nadia Zandi, Jaroslaw Choinski, Mateusz Sitarz, Anna Stolarz, Agnieszka Trzcinska, Mehran Vagheian

Journal of Acta Physica Polonica B, 5:861-866 (2020)

Highlights: ^{135}La with a half-life of 19.5 h and almost 100% decay to the stable ^{135}Ba is one of the interesting radionuclides for Auger electron therapy and emits low-intensity gamma rays (predominantly 480.5 keV, 1.5%), which leads the patient dose at a negligible level. In this study, possible reactions leading to the production of ^{135}La were discussed in detail, and afterward, corresponding theoretical yields calculated using MCNPX code were presented. Finally, the ^{135}La production was performed employing a PETtrace cyclotron and a $^{nat}BaCO_3$ target.

Contributions: In this study, I contributed to the production of ^{135}La and theoretical calculations. Furthermore, I wrote the manuscript.

INVESTIGATION OF THE PRODUCTION OF THE AUGER ELECTRON EMITTER ^{135}La USING MEDICAL CYCLOTRONS*

J. Jastrzębski[a,†], N. Zandi[a], J. Choiński[a], M. Sitarz[a,b]
A. Stolarz[a], A. Trzcińska[a], M. Vagheian[c]

[a]Heavy Ion Laboratory, University of Warsaw, 02-093 Warszawa, Poland
[b]Faculty of Physics, University of Warsaw, 02-093 Warszawa, Poland
[c]Department of Energy Engineering and Physics
Amirkabir University of Technology, Tehran, Iran

(Received January 8, 2020)

Possible reactions leading to the production of ^{135}La are discussed in this study and corresponding theoretical yields calculated using Monte-Carlo (MCNPX) code are presented. The pilot ^{135}La production was performed employing the 16 MeV protons provided by a PETtrace cyclotron and a $^{nat}BaCO_3$ target.

DOI:10.5506/APhysPolB.51.861

1. Introduction

The Auger electron therapy is one of the most promising and important cancer therapies due to delivery of radiation dose only to individual cells [1]. Its effectiveness has been recently summarized in Refs. [2–4]. The Auger electron emitters cause much less off-target effects than β emitters [4]. ^{135}La with the half-life of 19.5 h and almost 100% decay to the stable ^{135}Ba [1] by electron capture is one of the important candidates for this kind of therapy. It also emits only low-intensity gamma rays (predominantly 480.5 keV, 1.5%) which contribute to the patient dose at a negligible level.

^{135}La can be produced using proton or deuteron bombardment of barium via ^{135}Ba$(p,n)^{135}$La, ^{136}Ba$(p,2n)^{135}$La, ^{134}Ba$(d,n)^{135}$La, ^{135}Ba$(d,2n)^{135}$La reactions and alpha bombardment of cesium ^{133}Cs$(\alpha,2n)^{135}$La.

* Presented at the XXXVI Mazurian Lakes Conference on Physics, Piaski, Poland, September 1–7, 2019.

† Deceased.

In 2015 and 2018, respectively, Mansel [5] and Fonslet [1] reported production of ^{135}La using protons bombarding a barium target. Nevertheless, to date, only few research works have been performed to study ^{135}La production routes. The cross sections are reported only for: ^{nat}Ba(d,x), ^{nat}Ba(p,x), ^{nat}La(p,x) and ^{133}Cs$(\alpha,2n)$ [2–10]. In this work, some possible routes of ^{135}La radionuclide production have been analysed in terms of production yield regarding the small medical cyclotron facilities and cost of targets needed for the discussed reaction. The production yield was calculated using the Monte Carlo N-Particle eXtended (MCNPX) code [11, 12].

2. Materials and methods

2.1. Theoretical calculations of TTY

The assessment of the applicability of a ^{135}La production route was mainly based on evaluation of Thick Target Yield (TTY) describing number of the produced radionuclides (activity) per unit of time and current of the applied beam. Theoretical TTY for production of the radionuclide of interest can be calculated using the following equation [13, 14]:

$$\mathrm{TTY} = \frac{H N_\mathrm{A} \lambda}{M Z e} \int_{E_1}^{E_2} \frac{\sigma(E)}{\mathrm{d}E/\mathrm{d}(x\rho)} \mathrm{d}E\,, \tag{1}$$

where TTY is thick target production yield [Bq/Ah], N_A is the Avogadro number [1/mol], H is the isotope abundance of the target nuclide [%], M is the molar mass of the target element [g/mol], $\sigma(E)$ is the cross section at energy E [cm^2], $\mathrm{d}E/\mathrm{d}(x\rho)$ is the stopping power [MeV/(mg/cm^2)], λ is the decay constant of the product [1/h], $E_1 - E_2$ is the energy deposited in the target material [MeV], Z is the atomic number of the projectile, and e is the elementary charge [As].

In our calculations, we used the cross sections from the TENDL-2017 nuclear data library based on the TALYS code [15]. The stopping powers used in the calculation were derived from the SRIM 2013 code (Stopping and Range of Ions in Matter) [16].

The activity produced at the given irradiation time or the irradiation time needed to produce the required activity can be calculated from the following relation (considering decays of the produced radionuclide):

$$A_\mathrm{EOB} = \mathrm{TTY}\, I \frac{1}{\lambda} \left(1 - \mathrm{e}^{-\lambda t_\mathrm{irr}}\right), \tag{2}$$

where A_EOB — activity at the End Of Bombardment, I — beam current, λ — decay constant, t_irr — irradiation time.

2.2. TTY predictions for ^{135}La production

$^{135}Ba(p,n)^{135}La$ and $^{136}Ba(p,2n)^{135}La$ reactions

The optimal proton energy range for the $^{135}Ba(p,n)^{135}La$ reaction is of 16 to 5 MeV [15]. Since the natural abundance of ^{135}Ba is relatively low (6.5%) (Table I), a highly enriched barium target would be necessary for efficient production of ^{135}La in this reaction. The best energy range for the $^{136}Ba(p,2n)^{135}La$ reaction is between 35 to 12 MeV, however, it is worth mentioning that for the energy corresponding to the best range of the first reaction, the ^{135}La production yield is of comparable level. In other words, using natural barium both ^{135}La production channels have to be considered. The theoretical calculation shows the production yield at 16 to 5 MeV of proton energy range for the 100% enriched isotopes, ^{135}Ba and ^{136}Ba equals to 165.48 MBq/μAh and 151 MBq/μAh, respectively and 16 MBq/μAh for a natural Ba target (Table II).

TABLE I

Natural abundance of barium isotopes.

Isotope	^{132}Ba	^{134}Ba	^{135}Ba	^{136}Ba	^{137}Ba	^{138}Ba
Abundance [%]	0.1	2.4	6.5	7.8	11.2	71.7

TABLE II

^{135}La theoretical production yield in various reactions.

Reaction	Target yield [MBq/μAh] 100% enrichment	Target yield [MBq/μAh] Natural target	Energy range [MeV]
$^{135}Ba(p,n)^{135}La$	165.48	16*	16 → 5
$^{136}Ba(p,2n)^{135}La$	151.20		16 → 12
$^{135}Ba(d,2n)^{135}La$	570.45		35 → 8
$^{134}Ba(d,n)^{135}La$	33.27		14 → 8
$^{133}Cs(\alpha,2n)^{135}La$	38.28		40 → 16

*This TTY value was calculated for 16 → 5 MeV proton energy range, taking into account the contribution of the $^{135}Ba(p,n)^{135}La$ and $^{136}Ba(p,2n)^{135}La$ reactions.

Taking into account composition of the natural barium, it makes the ^{135}La production efficiency relatively high and considering the energy of protons delivered by cyclotrons such as PETtrace, C18/9 or Eclipse^{TM}RD, this production route seems to be the most effective for the ^{135}La production in PET centres.

^{135}Ba$(d, 2n)^{135}$La reaction

The efficient energy range for the ^{135}La production in ^{135}Ba$(d, 2n)^{135}$La reaction is between 35 to 8 MeV. The theoretical calculation shows that the production yield in this energy range is 570.45 MBq/μAh (Table II). However, it requires high-energy deuterons that are not provided by the medical cyclotrons most commonly installed in the PET centres.

^{134}Ba$(d, n)^{135}$La reaction

The production energy range for the ^{134}Ba$(d, n)^{135}$La reaction is of 14 to 8 MeV [15]. The theoretical calculation shows that the production yield in the mentioned energy range equals 33.27 MBq/μAh (Table II). Due to the limited production efficiency and the very low abundance of ^{134}Ba in natural barium (2.4%), which would require the use of expensive enriched target material, the reaction cannot be considered as a good candidate for the efficient production of ^{135}La.

^{133}Cs$(\alpha, 2n)^{135}$La reaction

Regarding the best energy range of ^{133}Cs$(\alpha, 2n)^{135}$La production route (40–16 MeV), the calculation shows that the production yield equals 38.28 MBq/μAh (Table II). Taking into account that the yield is very low compared to other possible production routes, this reaction cannot be considered as a reasonable candidate.

2.3. Pilot production of ^{135}La using PETtrace cyclotron

2.3.1. Proton beam energy and beam current measurements

The verification of the experimental results requires measurements of the proton energy and the current of extracted beam. This is needed as well to optimize a target thickness and to reduce the radiation dose originating from the isotopes produced inside reactions [17].

Using the method proposed by Gagnon *et al.* [17], we verified the proton energy to be 15.98 ± 0.03 MeV. The beam current was measured by irradiating the copper and titanium foils of the same thickness (11 μm) and evaluating the activity of each radionuclide (^{62}Zn, ^{65}Zn and ^{48}V) produced respectively in Cu and Ti [18]. The obtained average beam current was 9.41 ± 1.85 μA which we found consistent with Faraday Cup measurements (10.2 ± 0.1 μA).

2.3.2. Target and irradiation condition

Considering the above TTY calculations and energy of protons delivered by PETtrace installed at HIL UW, the production of the ^{135}La via the ^{nat}Ba$(p, x)^{135}$La reaction was tested. Natural barium carbonate target ($BaCO_3$) with thickness of 427 mg/cm^2 prepared as a pellet [19] was

bombarded for 10 minutes at the PETtrace cyclotron solid state target station [20] with a proton beam of 15.7 MeV energy and 9.4 μA intensity. The foils of Cu (11 μm) and Ti (11 μm) were placed in front of the barium carbonate pellet for off-line beam current verification. Target activity after irradiation was measured with a HPGe detector. Moreover, due to the fact that natural barium is composed of 6 stable isotopes (Table I), the co-produced impurities were also investigated.

3. Results and discussion

The activity of ^{135}La produced in our pilot irradiation was equal to 9.57 MBq at EOB what corresponds to about 6 MBq/μAh of TTY (Fig. 1, left panel). The activities of coproduced impurities (Fig. 1, right panel) namely ^{132}La and ^{132}Cs were measured as 0.43 MBq and 0.83 MBq, respectively (Table III).

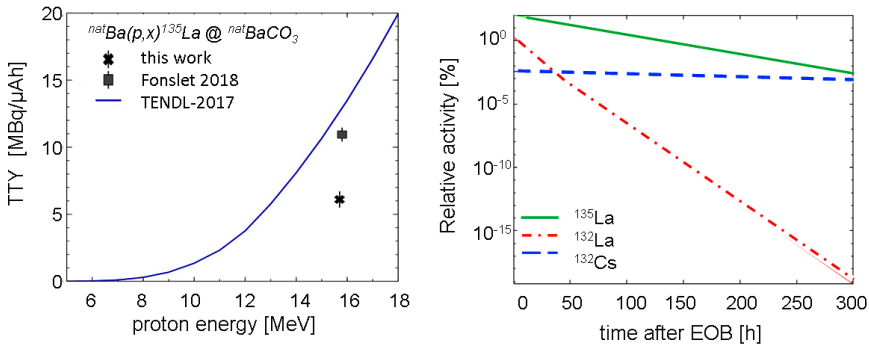

Fig. 1. Thick target yield for $^{\mathrm{nat}}\mathrm{Ba}(p,x)^{135}\mathrm{La}$ reaction and measured evolution of ^{135}La activity relative to the activity of coproduced impurities.

TABLE III

Activity of ^{135}La and impurities produced in natural Ba target.

Isotope	Half-life	Activity at EOB
^{135}La	19.5 h	9.57 ± 0.20 MBq
^{132}La	4.72 h	0.43 ± 0.18 MBq
^{132}Cs	6.48 d	0.83 ± 0.31 MBq

4. Conclusion

The most important ^{135}La production routes were considered based on the production yield and natural isotope abundance. The theoretical production yield for each reaction was obtained using the MCNPX code and

the results showed that $^{nat}Ba(p,x)^{135}La$ reaction represents a reasonable production route considering common facilities of the PET centres. The activity of ^{135}La produced by bombarding a natural barium target with protons of 15.7 MeV (attenuated by Cu and Ti foils) for 10 minutes with the beam current of 9.4 μA was equal to 9.57 MBq with impurities on the level below 1% at EOB.

Work completed with ENSAR2 (grant agreement No. 654002) support.

REFERENCES

[1] J. Fonslet *et al.*, *Phys. Med. Biol.* **63**, 015026 (2018).
[2] A.L. Kassis, *J. Nucl. Med.* **44**, 1479 (2003).
[3] F. Buchegger, F. Perillo-Adamer, Y.M. Dupertuis, A.B. Delaloye, *J. Nucl. Med. Mol. Imaging* **33**, 1352 (2006).
[4] B. Cornelissen, K.A. Vallis, *Curr. Drug Discov. Technol.* **7**, 263 (2010).
[5] A. Mansel, K. Franke, *Radiochim. Acta* **103**, 759 (2015).
[6] F. Tarkanyi *et al.*, *Nucl. Instrum. Methods Phys. Res. B* **414**, 18 (2018).
[7] F. Tarkanyi *et al.*, *Appl. Radiat. Isot.* **68**, 1869 (2010).
[8] K. Prescher *et al.*, *Nucl. Instrum. Methods Phys. Res. B* **53**, 105 (1991).
[9] F. Tarkanyi, A. Hermanne, F. Ditroi, S. Takacs, *J. Radioanal. Nucl. Chem.* **312**, 691 (2017).
[10] N.P.M. Sathik, M. Afzal Ansari, B.P. Singh, R. Prasad, *Pramana* **47**, 401 (1996).
[11] MCNPX User's manual, version 2.4.0, Los Alamos National Laboratory, New Mexico, 2002.
[12] A. Infantino, C. Hoehr, *AIP Conf. Proc.* **1845**, 020009 (2017).
[13] M. Sitarz *et al.*, *Instruments* **3**, 7 (2019).
[14] M. Sadeghi, N. Zandi, H. Afarideh, *J. Radioanal. Nucl. Chem.* **291**, 731 (2012).
[15] A.J. Koning, D. Rochman, TENDL-2017: TALYS-based evaluated nuclear data library, Nuclear Research and Consultancy Group (NRG) Petten, The Netherlands, http://www.talys.eu/tendl-2017
[16] J.F. Ziegler, J.P. Biersack, U. Littmark, The code of SRIM — the stopping and range of ions in matter, IBM Research, New York 2006.
[17] K. Gagnon *et al.*, *Appl. Radiat. Isot.* **69**, 247 (2011).
[18] A. Hermanne *et al.*, *Nucl. Data Sheets* **148**, 338 (2018).
[19] A. Stolarz, *J. Radioanal. Nucl. Chem.* **299**, 913 (2014).
[20] UP RP patent No. P.227402.

4.5 Study on a new design of Tehran Research Reactor for radionuclide production based on fast neutrons using MCNPX code

Authors: Nadia Zandi, Hossein Afarideh, Mohammad Reza Aboudzadeh, Saeed Rajabifar

Journal of applied radiation and isotopes, 132:67-71 (2018)

Highlights: The aim of this study is to increase the magnitude of the fast neutron flux inside the flux trap in nuclear research reactors where radionuclides are produced. For this demand, three new designs of the flux trap are proposed, and the obtained fast and thermal neutron fluxes are compared in each design. In the first and second designs, a sealed cube containing air and D_2O respectively was proposed, and the results of calculated production yield all indicated the superiority of the latter one by a factor of 55% compared to the first design. The third proposed design was introduced based on changing the surrounding of the sealed cube by locating two fuel plates around it. In this case, regarding the results, the production yield increased up to 70%.

Contributions: In this study, I performed the theoretical calculations and also I wrote the manuscript.

Applied Radiation and Isotopes 132 (2018) 67–71

Contents lists available at ScienceDirect

Applied Radiation and Isotopes

journal homepage: www.elsevier.com/locate/apradiso

Study on a new design of Tehran Research Reactor for radionuclide production based on fast neutrons using MCNPX code

Nadia Zandi[a], Hossein Afarideh[a,*], Mohammad Reza Aboudzadeh[b], Saeed Rajabifar[b]

[a] Department of Energy engineering and Physics, Amirkabir University of Technology, Tehran, Iran
[b] Radiation Application Research School, Nuclear Science and Technology Research Institute (NSTRI), P.O. Box 14395-836, Tehran, Iran

HIGHLIGHTS

- Medical isotope production using fast neutron flux is investigated.
- Tehran Research Reactor is considered for radionuclide production.
- New flux trap designs are proposed to enhance the fast neutron flux.
- MCNPX code is employed to investigate the results.
- The results all indicate a significant enhancement in production yield.

ARTICLE INFO

Keywords:
Radionuclide production
Fast neutron flux
MCNPX code
Flux trap design

ABSTRACT

The aim of this work is to increase the magnitude of the fast neutron flux inside the flux trap where radionuclides are produced. For this purpose, three new designs of the flux trap are proposed and the obtained fast and thermal neutron fluxes compared with each other.

The first and second proposed designs were a sealed cube contained air and D_2O, respectively. The results of calculated production yield all indicated the superiority of the latter by a factor of 55% in comparison to the first proposed design.

The third proposed design was based on changing the surrounding of the sealed cube by locating two fuel plates near that. In this case, the production yield increased up to 70%.

1. Introduction

Most radionuclides are produced by exposing suitable target materials to the neutron flux in a nuclear reactor for an appropriate time. Thermal neutron capture nuclear reactions are currently used for major radionuclide production. Thermal neutrons are those which are in thermal equilibrium with molecules/atoms of the surrounding medium (Manual for reactor produced radioisotopes, 2003). One of the most important factors for radionuclide production is a neutron flux intensity which should be optimized by considering special places within the reactor core or its surrounding (Mele, 1990).

Tehran research reactor (TRR) is commonly used to produce radionuclides via thermal neutrons (Aboudzadeh et al., 2015; Khalafi and Gharib, 2005; Deilami-nezhad et al., 2016). But it is noteworthy to mention that, production of some radionuclides such as ^{64}Cu and ^{67}Cu requires as large fast neutron flux as possible owing to their energy thresholds (Johnsen et al., 2015). In the case of being thermal reactor, it is not easily accessible to produce medical radionuclide via fast neutrons by considering the traditional design of the flux trap which contains only water that normally increases thermal to fast neutron flux ratio. So, some considerations should be taken and some new design should be introduced to produce efficiently.

In this study, some new design was taken to improve fast neutron flux in the central flux trap to produce medical radionuclides as high as possible in the TRR. Accordingly, MCNPX code (MCNPX User''s manual, 2002) was employed for both benchmarking and simulating the reactor core and then was used to design the proposed different flux trap for reaching to the best results. For this purpose, this paper is organized in 5 sections: In the second section, descriptions of TRR are presented briefly. In the third section, simulation of the reactor core and benchmarking of the obtained results against experimental measurements are carried out. The new proposed designing of the flux trap along with the calculated results, including thermal and fast neutron fluxes have been presented in the section four. Eventually, the fifth section gives the

* Corresponding author.
E-mail address: hafarideh@aut.ac.ir (H. Afarideh).

https://doi.org/10.1016/j.apradiso.2017.11.006
Received 31 July 2017; Received in revised form 30 October 2017; Accepted 5 November 2017
Available online 06 November 2017
0969-8043/

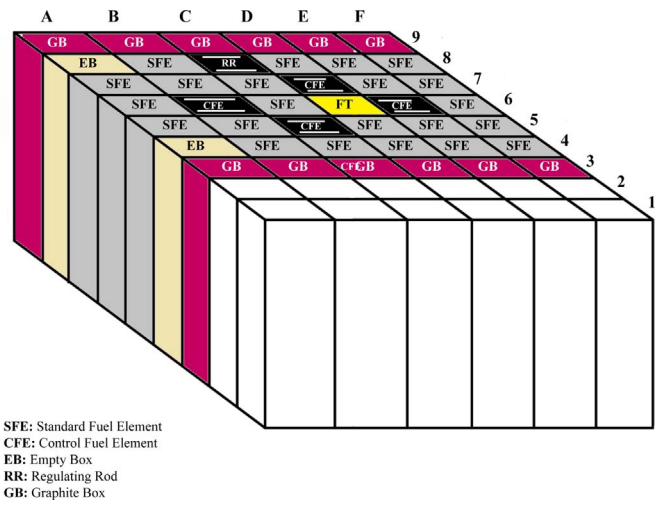

Fig. 1. The TRR core configuration used for designing.

conclusion.

2. Description of Tehran Research Reactor

Tehran Research Reactor is the only facility for reactor-based production of radionuclides which is needed for the extensive usage in all hospitals and medical centers in the country. This reactor is a 5 MW pool-type light-water moderated, heterogeneous solid fuel reactor in which the water is also used for cooling and shielding (AEOI, 1989, 2001). Its core configuration consists of MTR-type fuel elements which are inserted in the specific grid plate assemblies (Khalafi and Gharib, 2005; Lashkari et al., 2012).

There are two types of low enriched uranium (LEU) fuel elements: Standard Fuel Element (SFE) and Control Fuel Element (CFE). In terms of fuel elements, they both consist of enriched ^{235}U (approximately 20%) which are 19 plates for SFE and 14 for CFE, but in terms of configuration, CFEs also house fork-type control rods which are illustrated as white lines (Fig. 1). Also, it is worth to point out that the fuel is made of U_3O_8 powder dispersed in a pure aluminum matrix (Lashkari et al., 2012).

The arrangement of fuel assemblies including both SFEs and CFEs in the reactor core always is considered 9 × 6 array. Moreover, it is apparent and obvious in the figure that, some graphite boxes are located in the core surrounding as efficient reflectors for reaching to the much more neutron economy (Lashkari et al., 2012).

3. Methodology and results

3.1. Validation and benchmarking

In this section of the study, validation of simulation has been presented. On this basis, the first operating core of TRR was modelled and the results were compared with experimental measurements (Zaker, 2004). Table 1 reflects the comparison between the obtained results and the experimental measurements.

Table 1
Comparison of the calculated neutronic parameters and their RPEs with the experimental data for the first operating core.

Parameters (pcm)	MCNPX	Reference (Zaker, 2004)	RPE(%)
Excess reactivity	6844	7461	8.27
Worth of Safety Rod 1	6052	5670	6.74
Worth of Safety Rod 2	5883	5471	7.53
Worth of Safety Rod 3	4778	4633	3.13
Worth of Safety Rod 4	4840	4711	2.74
Worth of Regulating Rod	504	476	5.88

Table 2
Data of CFE and SFE (AEOI, 1989, 2001).

	CFE	SFE
Enrichment	20%	20%
Number of fuel plates	14	19
Total fuel plate thickness	0.15 cm	0.15 cm
Meat thickness	0.07 cm	0.07 cm
Cladding thickness	0.04 cm	0.04 cm
Water channel thickness	0.27 cm	0.27 cm
Meat width	6 cm	6 cm
Meat length	61.5 cm	61.5 cm
Side wall thickness	0.45 cm	0.45 cm
Inner distance between side wall	6.7 cm	6.7 cm
Meat material	U_3O_8-Al	U_3O_8-Al
FP cladding and side wall material	Al 6061	Al 6061
Absorber material for Shim Safety Rods	Ag-In-Cd	–
Absorber material for Fine Regulating Rods	AlSl 316L	–
Material in the gap between Cladding and Absorber	He at 1 atm	–
Guide Plates Material	Al 6061	–
Cladding material for absorber plate	AlSl 316L	–

Regarding Table 1, the calculated Relative Percent Errors (RPE) which can be defined as Eq. (1), are below 9% and consequently the validation of the results can be confirmed (Lashkari et al., 2015).

$$RPE\,(\%) = \frac{calculated\ \ value - reference\ value}{reference\ value} \times 100 \quad (1)$$

4. Procedure of new design

In order to design the flux trap and perform the corresponding calculations and simulations, first it is necessary to consider an operational core. On this basis, the core which is shown in Fig. 1 has been considered (Khalafi and Gharib, 1999).

As shown in the Fig. 1, the core configuration includes 22 SFEs and 4 CFEs and one Regulating Rod (RR). The core simulation was also carried out using MCNPX code regarding Table 2 as the required input data.

Prior to applying the new design of the flux trap, the variation of thermal and fast neutron flux in central flux trap (FT) while filling with ordinary water, should be considered (Fig. 2). Accordingly, the MESH Tally card at MCNPX code was employed to draw the fast and thermal neutron fluxes along the D-line direction (see Fig. 2). Considering the figure, it is obvious that the thermal flux in central flux trap is higher than the fast flux due to the existing water inside the trap which moderates the fast neutrons (Fig. 2).

While this situation is appropriate for the production of radionuclide with thermal flux, it is not acceptable for those that need fast neutrons. Consequently, using the Monte Carlo code, we proposed 3

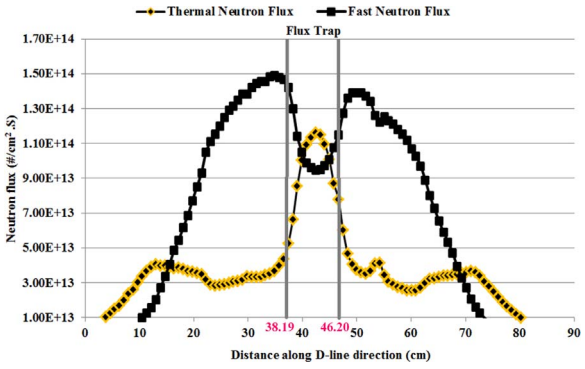

Fig. 2. Distribution of thermal and fast flux along D direction in the core when FT contained H_2O.

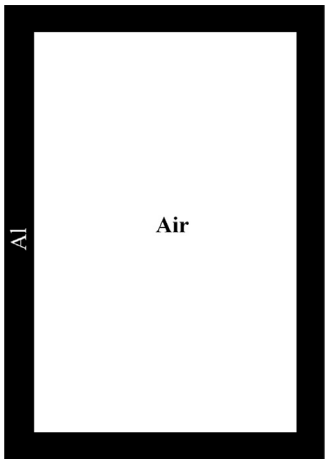

Fig. 3. The first proposed design of flux trap.

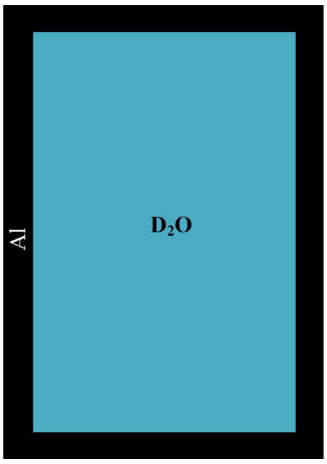

Fig. 5. The second proposed design of flux trap.

new designs which have the potential to change the above situation.

Firstly, we designed a sealed cube of aluminum alloy (AL 6061) with a thickness of 1 mm to prevent the water penetration. These features were based on the wall of the Empty Boxes (EBs) inside the reactor core which already were designed for the same purposes (see Fig. 3).

Moreover, the entire space of the sealed cube was filled with air that has lower moderation of neutrons owing to its much less density and scattering probability (owing to a higher atomic number of composing materials) compared with H_2O. So, it could reasonably be argued that due to the lack of water inside the sealed cube, it could be a suitable reservoir to place target materials to be bombarded with fast neutron (Fig. 7). Regarding the fact that the moderation of fast neutron in air is remarkably less than H_2O, the fast neutron flux of the latter case is higher than the former case. To be more precise, regarding Fig. 2 and Fig. 4, the ratio of the maximum fast neutron flux in the flux trap while filling with air is approximately 1.3 to the situation when the flux trap is filled with water and consequently by considering Eq. (2) (Lamarsh, 1965; Duderstadt and Hamilton, 1976) which shows the yield of a radionuclide produced in a reactor, we could reach 30% higher production yield.

$$Y_i = N_j \sigma_{j,g} \phi_g (1 - e^{-\lambda_i t}) \quad (2)$$

Where Y_i and λ_i indicate the production yield and decay constant of the produced isotope i, respectively. Moreover, in Eq. (2), ϕ_g is neutron flux in neutron energy group g and $\sigma_{j,g}$ is the microscopic neutron cross section of the target in the corresponding neutron energy group g. Also, N_j in the equation represents the atomic density of the bombardment target material.

Secondly, the entire space of the flux trap was filled with heavy water. This choice was partly due to the higher collision probability of D_2O than Air (because of the density) and lower moderation of D_2O than H_2O for the incident neutrons (Fig. 5) (Lamarsh, 1965; Duderstadt and Hamilton, 1976; Bell and Glasstone, 1970). In other words, when the collision probability increases by increasing the density, the number of neutrons pass through one cm^2 in one second will rise. Additionally, owing to the fact that, the moderation of deuterium nucleus is fewer than H_2O, the fast neutrons moderate less.

These features could somewhat help to increase the neutron flux compare with the situation when the sealed cube was filled with H_2O and Air. Fig. 6 shows the variation of the obtained fast and thermal neutron fluxes along the D-line direction of the reactor core when the flux trap contained D_2O.

Regarding Eq. (2) and performing simple mathematical calculations, it could be shown that the ratio of the production yield will be increased about 16% when the sealed cube contained D_2O instead of air. Moreover, it could easily be shown that the production yield could be increased about 75% when the sealed cube filled with D_2O rather than H_2O. Moreover, the calculated fast neutron fluxes have been illustrated in Fig. 7 in order to clarify the difference between the obtained results for the aforementioned proposed designs.

As can be argued, the last proposed design shows its highest capability to use for medical radionuclide production via fast neutrons. The explanation of the reasons for this behavior of the three materials has been presented previously and individually.

In order to increase the fast neutron flux as much as possible, we proposed the third new design. In this section of simulation, we extracted 17 fuel plates of one SFE and put the remained two fuel plates in the first and last empty positions in the guide plate. Then, we located the D_2O contained sealed cube in the middle of the guide plate based on the above obtained results which had the highest fast neutron flux

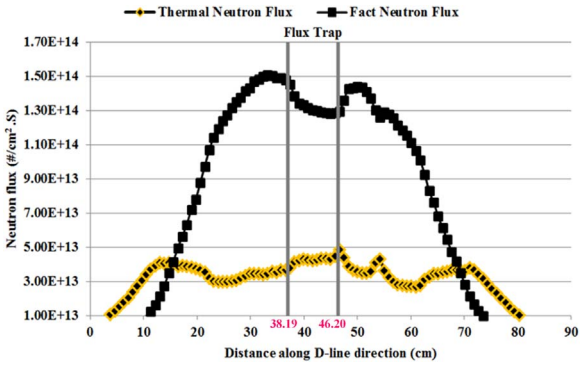

Fig. 4. Distribution of thermal and fast flux along D direction in the core when FT contained Air.

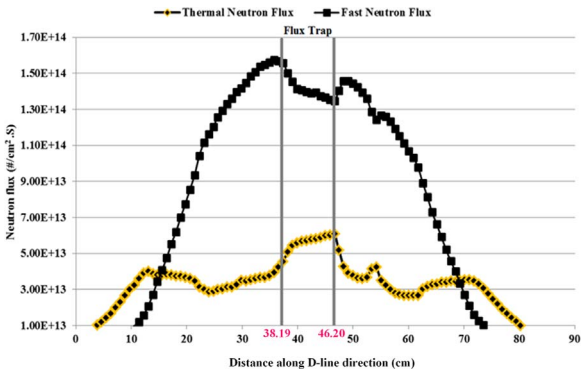

Fig. 6. Distribution of thermal and fast flux along D direction in the core when FT contained D_2O.

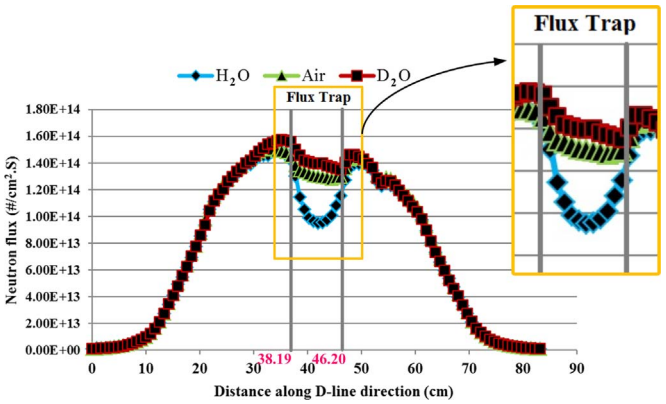

Fig. 7. Comparison between the obtained fast neutron flux while the sealed cube contained H_2O, Air and D_2O.

inside the flux trap (Fig. 8). This proposed design was a little more different from the previous ones where only the prevention of fast neutron moderation was the purpose. In fact, by locating the fuel plates near the sealed cube, the fast neutrons which be produced in the fuel plates could reach to the sealed cube with lower collisions and consequently lower moderation (Lamarsh, 1965; Duderstadt and Hamilton, 1976; Bell and Glasstone, 1970). The mentioned distance between fuel plates and sealed cube was equal to the half of the pitch (distance between two fuel plates) due to the required fuel plates cooling (Fig. 8) (Wakil, 1971). By considering the above points, the fast and thermal neutron fluxes have been calculated and illustrated in Fig. 9.

For facilitating comparison between the previous last proposed designs (sealed cube contained D_2O) and the current obtained results based on fuel plate's insertion, the variation of the fast neutron fluxes along the D-line direction in the flux trap have been shown in Fig. 10.

Regarding the Fig. 10, the latest new design has higher fast neutron flux in the entire flux trap and accordingly this proposed design based on insertion of fuel plates near the sealed cube which contained D_2O could be reasonably considered the best proposed design.

5. Conclusion

This paper deals with the development and enhancement of the Tehran Research Reactor for production of radionuclides based on the fast neutron flux using MCNPX code. For this purpose, some new designs were proposed both in terms of reducing the fast neutron

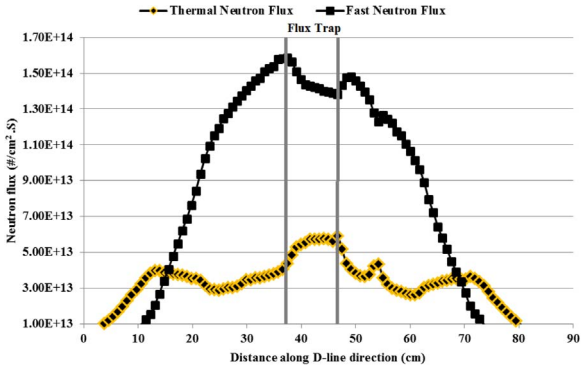

Fig. 9. Distribution of thermal and fast flux along D-line direction in the core based on the third proposed design.

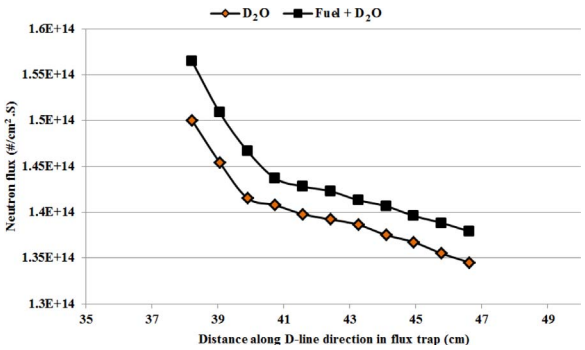

Fig. 10. Comparison of the fast neutron flux for all proposed designs.

moderation and increasing the fast neutron production. The first and second designs were comprised of a sealed cube contained air and D_2O instead of ordinary water (H_2O) to reduce the moderation of fast neutrons. Consequently, the production yield increased about 30% and 55%, respectively. Finally, the last design was proposed based on the insertion of 2 fuel plates near the flux trap contained D_2O. Although the production yield has been increased about 70% than the second proposed design, the difference was not considerable due to the limitation of distance between the inserted fuel plates and the sealed cube.

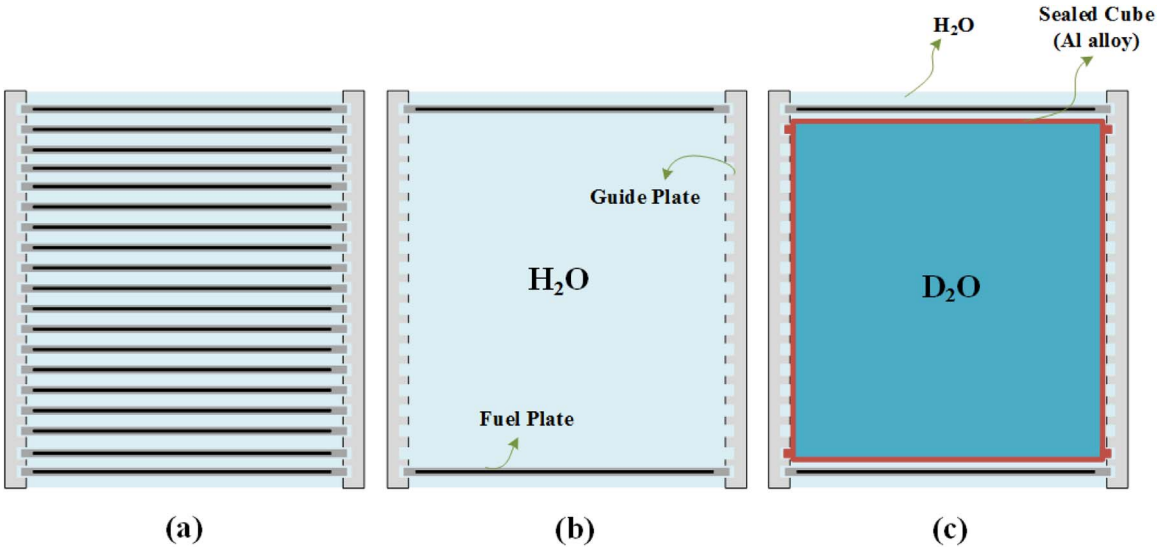

Fig. 8. Detailed scheme of the third new flux trap design.

Acknowledgements

This project was performed based on the IAEA coordinated research project (contract 21021) and the authors would like to express their gratitude to Nuclear Science and Technology Research Institute which sponsored the project under the scholarship program. The authors also would like to thank the IAEA for suggesting and supporting this research.

References

Aboudzadeh, M.R., Moassesi, M.E., Amiri, M., Shams, H., Alirezapour, B., Sadeghi, M., Fakhraei Sari, M., Keyvani, M., 2015. Preparation and Characterization of Chitosan-capped Radioactive Gold Nanoparticles: Neutron Irradiation Impact on Structural Properties…. Safety Analysis Report for the Tehran Research Reactor (HEU), Tehran-Iran (13, 339-345.AEOI, 1966).

AEOI, 1989. Tehran Research Reactor Amendment to the safety Report. Tehran-Iran.

AEOI, 2001. Safety Analysis Report for the Tehran Research Reactor (LEU). Tehran-Iran.

Bell, G.I., Glasstone, S., 1970. Nuclear Reactor Theory. Van Nostrand Reinhold Company, New York.

Deilami-nezhad, L., Moghaddam-Banaem, L., Sadeghi, M., Asgari, M., 2016. Production and purification of scandium-47: a potential radioisotope for cancer theranostics. Appl. Radiat. Isot. 118, 124–130.

Duderstadt, J.J., Hamilton, L.J., 1976. Nuclear Reactor Analysis, second ed. John. Wiley & Sons Inc, New York.

Johnsen, A.M., Heidrich, B.J., Durrant, C.B., Bascom, A.J., U¨nlu, K., 2015. Reactor production of 64Cu and 67Cu using enriched zinc target material. J. Radioanal. Nucl. Chem. 305, 61–71.

Khalafi, H., Gharib, M., 1999. Calculational tools to conduct experimental optimization in Tehran research reactor. Ann. Nucl. Energy 26, 1601–1610.

Khalafi, H., Gharib, M., 2005. Optimization of 60Co production using neutron flux trap in the Tehran research reactor. Ann. Nucl. Energy 32, 331–341.

Lamarsh, J.R., 1965. Introduction to Nuclear Reactor Theory. Addison-Wesley Publishing Company.

Lashkari, A., Khalafi, H., Mirvakili, S.M., Forughi, S., 2012. Neutronic analysis for Tehran Research Reactor mixed-core. Prog. Nucl. Energy 60, 31–37.

Lashkari, A.H., Khalafi, H., Kazeminejad, Keyvani, M., Ezzati, A., Hosnirokh, A., 2015. Experimental study of neutronic parameters in Tehran research reactor mixed-core. Prog. Nucl. Energy 83, 398–405.

Manual for reactor produced radioisotopes, 2003. International Atomic Energy Agency IAEA, IAEA-TECDOC-1340.

MCNPX User's manual, 2002. version 2.4.0, Los Alamos National Laboratory, New Mexico.

Mele, I., 1990. Optimization of TRIGA Reactor Operation Using Reactor Calculations. J. Stefan Report.

Wakil, M.M. El, 1971. Nuclear Heat Transport. The Haddon Craftsmen, Inc., Scranton, Pennsylvania, The United States.

Zaker, M., 2004. Conversion and Start up of Tehran Research Reactor with LEU Fuel. International Atomic Energy Agency, Vienna.

CHAPTER 5

CONCLUSION AND OUTLOOK

5.1 CONCLUSION

This Ph.D. thesis focused on the production and separation of the theranostic pair ^{61}Cu/^{67}Cu from Zn targets and radiolabeling of a peptide (DOTATOC). On this basis, we investigated the production of ^{61}Cu and ^{67}Cu and presented them in three steps, including: production, radiochemical separation, and radiolabeling.

In the first step, in chapter two, some possible reaction routes to the production of ^{61}Cu and ^{67}Cu were investigated. Regarding the results, ^{64}Zn(p,α)^{61}Cu and ^{68}Zn(γ,p)^{67}Cu reactions were concluded as the best reaction routes among all possible pathways to the production of ^{61}Cu and ^{67}Cu, respectively. Accordingly, for the ^{61}Cu production through the (p,α) nuclear reaction, an enriched ^{64}Zn target was irradiated by a proton cyclotron at SWAN Isotopen AG at Inselspital Bern. After that, the radionuclides contained in the irradiated target were quantified by gamma-ray spectroscopy. A dose calibrator (ISOMED 2010, Nuclear–Medizintechnik Dresden GmbH, Germany) was employed for quantitative measurement of ^{61}Cu due to the high level of activity, which could not be measured and quantified with the HPGe detector. Regarding the results, as was expected, ^{61}Cu could be obtained in sufficient quantity (about 2 GBq) required for the radiolabeling purpose. The advantage of this method is the feasibility of production in such high activity in medical cyclotrons, which are available mostly in nuclear medicine clinics. In the case of ^{67}Cu production, although some literature studied ^{67}Cu production using different methods such as cyclotron production and production with a nuclear reactor, both mentioned production routes are associated with some problems and cannot be used as cost-effective and routine production routes in hospitals and nuclear medicine clinics. On this basis, the most possible production pathways of ^{67}Cu were investigated in this project, and regarding that, the feasibility of producing ^{67}Cu using photonuclear reactions was considered. Afterward, the production of ^{67}Cu was performed via irradiations of ^{68}Zn with Bremsstrahlung generated by a 22 MeV Microtron at METAS (Federal Office of Metrology), and then the irradiated target was delivered to the radiochemistry laboratory at the University of Bern for measuring the gamma-ray spectra of the obtained Cu via an HPGe detector. However, due to the non-availability of high electron

energy and high power electron accelerator facilities in Switzerland, ^{67}Cu could not be obtained in sufficient activities (obtained only in kBq) which is not enough for labeling purposes.

In the second step (i.e., radiochemistry section), the obtained Cu was separated from the irradiated Zn target through a novel evaporation method based on the difference in vapor pressure temperatures of Cu and Zn. On this basis, a novel setup was designed for the implementation of the technique, and most of the radioactive Cu was separated from the Zn target. In the following, the residue of the evaporation process containing the Cu was dissolved with 8M HCl and H_2O_2 (30%), and transferred then to an automated extraction chromatography (with TK201 resin) using a Modular-Lab PharmTracer system (see Fig. 3.9) for removing remaining Zn and other impurities in the eluent. From the conjugated two chemical separation steps, the process was performed automatically, and all safety issues were considered for efficient chemical separation. According to the results, the obtained Cu (88% of the total radioactive Cu) was completely separated from the irradiated Zn target (no observation of Zn in the product).

In the third step of the project (i.e., radiolabeling section), it was demonstrated that the obtained activity of ^{61}Cu is adequate (compared with the obtained ^{67}Cu) for the labeling of biomolecules with a DOTA chelator. Based on the results, we could conclude that the DOTA-TOC coordinated and labeled well with the obtained Cu with more than 97% labeling yield.

In parallel to this study, the production of further potential radionuclides such as ^{167}Tm, ^{165}Er, and ^{135}La were investigated as potential candidates for applications in nuclear medicine. In the case of ^{167}Tm, cyclotron production of ^{167}Tm and radiochemical studies of the obtained Tm from the irradiated Er target through the solvent extraction technique were investigated. Regarding the results, the radiochemical yield of ^{167}Tm was obtained with about 80±5% yield using n-hexane/HDEHP (1 M). In the case of ^{165}Er, the excitation function of some major reaction channels leading to ^{165}Er production was investigated using ALICE/ASH (Hybrid and GDH models) and EMPIRE 3.1 codes. Moreover, targetry through the sedimentation technique and then cyclotron production was performed. However, due to using a natural Er target, the activity was not obtained in a sufficient amount. In the case of ^{135}La, cyclotron production and theoretical investigation of ^{135}La as a candidate radionuclide in Auger electron therapy were investigated.

However, due to limited activities (not reachable in GBq quantity), ^{135}La cannot satisfy the demand and replace prominent auger electrons emitting radionuclides such as ^{111}In and ^{67}Ga for further use in clinical applications. In the case of ^{67}Cu production, some new designs in the flux trap of research reactors to increase the magnitude of the fast neutron flux inside the flux trap where radionuclides are produced were investigated. These new designs can be employed for the production of some radionuclides, such as ^{67}Cu, which cannot be produced in the thermal flux in nuclear reactors.

5.2 OUTLOOK

This study's realm focused on the theranostic pair ^{61}Cu/^{67}Cu production and purification for use in clinical applications. The diagnostic, ^{61}Cu was obtained in adequate quantities for clinical applications, while ^{67}Cu could not be obtained in sufficient quantities using the Microtron facility at METAS due to irradiation with a low energy and low power electron beam. So, for follow-up experiments, in the near future, we intend to reduce the distance between the sample target and converter at the Microtron facility at METAS to increase the number of photons reaching the target. On these terms, higher activity of ^{67}Cu can be obtained. However, another possibility can be purchasing a high electron beam power and energy accelerator (such as Rhodotron, model TT300-HE) in Switzerland to suffice ^{67}Cu production demand, which can significantly increase the ^{67}Cu production activity. It is worth to point out that a Rhodotron is commercially available by the company IBA; however, the required photonuclear irradiation setup has not been yet developed and is under design and development in our group. Additionally, as a shared project in collaboration with SWAN Isotopen AG (as part of the University of Bern), we decided to start an investigation of the experimental cross-section measurements of ^{61}Cu during the irradiation with the cyclotron. This demand arises from the incompatibility between theoretical yield and experimentally obtained activity at EOB in addition to the lack of sufficient experimental measurements in the literature.

In the radiochemistry section, we reached the desired goal in the research area, furthermore, this automated setup can be used for the first time in a GMP (Good Manufacturing Practice) environment. Moreover, due to the fast and promising implementation of the entire automated developed setup, which is more crucial, particularly for ^{61}Cu (with half-life of 3.3 h), a large-scale production could be easily accessible. In foreseen plan in the future, we desire to complete the automated systems in other parts such as using an automated lift table instead of a labor-boy, which decreases dose exposure during the experiment. It is worth pointing out that the developed setup based on the evaporation technique is potentially able to be applied for the separation of other elements that have a difference in their vapor pressure temperatures. Moreover, by the use of the developed setup, one can prepare highly pure solid targets in different shapes and dimensions. More precisely, the collected powder around the cooling finger (which is purer than the original purchased material) can be recovered easily and be used for solid target preparation in different shapes and dimensions.

Within the radiolabeling section, the immediate plan stands on setting-up a High-performance liquid chromatography (HPLC) equipment to confirm the obtained results in the case of radiolabeling yield. Higher quantities of available ^{67}Cu radioactivity would facilitate investigations towards radiolabeling a DOTA chelator with ^{67}Cu. Additionally, we plan to start research on other possible chelators and peptides such as DOTA-TATE, which could increase the application of ^{61}Cu/^{67}Cu theranostic pairs in different preclinical studies. Based on the promising radiolabeling results obtained within this thesis, the ^{61}Cu/^{67}Cu theranostic pair has the potential to be used for the first time in human studies in the future.

Finally, as the other proposed plan in the near future, we decided to start an investigation on ^{64}Cu production using the SWAN cyclotron. On this topic, first, we plan to look into different possible production pathways, and regarding the results, we would move towards the best possible reaction route. Also, we plan to work on the theranostic pair ^{64}Cu/^{67}Cu and make a comparison with the ^{61}Cu/^{67}Cu pair for a better understanding of their function as theranostics pairs and select the most efficient one for future clinical studies.

REFERENCES

[1] McIntosh, J.R., Understanding Cancer, an Introduction to the biology, medicine, and societal implications of this disease. Garland Science (first Edition), United States (2019).

[2] Hassan, G., Seno, M., Blood and cancer: cancer stem cells as origin of hematopoietic cells in solid tumor microenvironments. Cells 9:1293 (2020).

[3] Liu, D., Tumors and cancers head–neck–heart–lung–gut, Taylor & Francis Group, Unite States (2018).

[4] Bombardieri, E., Seregni, E., Evangelista, L., Chiesa, C., Chiti, A., Clinical applications of nuclear medicine targeted therapy. Springer International Publishing AG, part of Springer Nature (2018).

[5] Goldsmith, S.J., Targeted radionuclide therapy: a historical and personal review. Seminars in Nuclear Medicine, 50:1-11 (2019).

[6] Ersahin, D., Doddamane, I., and Cheng, D., Targeted radionuclide therapy. Cancers 3, 3838-3855 (2011).

[7] Khan, F.M., Gibbons, J.P., Khan's the physics of radiation therapy (fifth edition), Wolters Kluwer, United States (2014).

[8] Xia, P., Godley, A., Shah, C., Videtic, G.M.M., and Suh, J.H., Strategies for radiation therapy treatment planning. Springer Publishing Company, United States (2019).

[9] Link, W., Principles of cancer treatment and anticancer drug development. Springer Nature Switzerland AG (2019).

[10] Zimmermann, R., Nuclear medicine radioactivity for diagnosis and therapy (second edition), EDP Sciences, France (2017).

[11] Washington, C.M., Leaver, D., Principles and practice of radiation therapy (fourth edition). Elsevier Inc. United States (2016).

[12] Pawlicki, T., Scanderbeg, D.J., Starkschall G., Hendee's radiation therapy physics (fourth edition), John Wiley & Sons, Inc., United States (2016).

[13] Heath, A., Radiation therapy study guide: a radiation therapist's review. Springer, United States (2016).

[14] Kamath, A.V., Translational pharmacokinetics and pharmacodynamics of monoclonal antibodies, Drug Discovery Today: Technologies, 21:75-83 (2016).

[15] Dash, A., Knapp, F.F., and Pillai, M.R.A., Targeted radionuclide therapy - an overview. Current Radiopharmaceuticals 6, 000-000 (2013).

[16] Wagener, C., Stocking, C., and Müller, O., Cancer signaling from molecular biology to targeted therapy. Wiley-VCH Verlag GmbH & Co. KGaA, Weinheim, Germany (2017).

[17] Ruigrok, E.A.M., Weerden, W.M., Nonnekens, J., and Jong, M., The future of PSMA-targeted radionuclide therapy: An overview of recent preclinical research. Pharmaceutics 11, 560 (2019).

[18] Piroozfar, B., Raisali, G., Alirezapour, B., Mirzaii, M., The Effect of ^{111}In Radionuclide Distance and Auger Electron Energy on Direct Induction of DNA Double Strand Breaks: A Monte Carlo Study Using Geant4-toolkit. International Journal of Radiation Biology 94(4):385-393 (2018).

[19] Ku, A., Facca, V.J., Cai, Z., and Reilly, R.M., Auger electrons for cancer therapy – a review, EJNMMI Radiopharmacy and Chemistry 4:27 (2019).

[20] Murshed, H., Fundamentals of radiation oncology (third edition): chapter 3 - radiation biology 57-87, United States (2019).

[21] Mettler, F.A., Guiberteau, F.F., Essentials of nuclear medicine and molecular imaging (seventh Edition). Elsevier, Inc. United States (2019).

[22] Dash, A., Pillai, M.R.A., and Knapp, F.F., Production of ^{177}Lu for targeted radionuclide therapy: available options. Nuclear Medicine and Molecular Imaging 49:85–107 (2015).

[23] Sgouros, G., Bodei, L., McDevitt, M.R., and Nedrow, J.R., Radiopharmaceutical therapy in cancer: clinical advances and challenges. Nature Reviews | Drug Discovery 19:589-608 (2020).

[24] IAEA radioisotopes and radiopharmaceuticals series No. 5: Yttrium-90 and Rhenium-188 radiopharmaceuticals for radionuclide therapy. International Atomic Energy Agency, Austria (2015).

[25] Müller, C., Meulen, N.P., Benesov, M., and Schibli, R., Therapeutic radiometals beyond ^{177}Lu and ^{90}Y: production and application of promising α-Particle, β^--Particle, and Auger Electron Emitters. Journal of Nuclear Medicine 58:91S–96S (2017).

[26] Tafreshi, N.K., et al., Development of targeted alpha particle therapy for solid tumors. Molecules 24, 4314 (2019).

[27] Zhao-Hui, J., et al., ^{67}Cu-Radiolabeling of a multimeric RGD peptide for αVβ3 integrin-targeted radionuclide therapy. Nuclear Medicine Communications 38: 347-355 (2017).

[28] Aliev, R.A., et al., Photonuclear production and radiochemical separation of medically relevant radionuclides: ^{67}Cu. Journal of Radioanalytical and Nuclear Chemistry 321: 125-132 (2019).

[29] Inagaki, M., et al., Production of ^{47}Sc, ^{67}Cu, ^{68}Ga, ^{105}Rh, ^{177}Lu, and ^{188}Re using electron linear accelerator. Journal of Radioanalytical and Nuclear Chemistry 322:1703–1709 (2019).

[30] Poty, S., Francesconi, L.C., McDevitt, M.R., Morris M.J., and Lewis J.S., α-Emitters for radiotherapy: from basic radiochemistry to clinical studies—Part 1. Journal of Nuclear Medicine 59:878–884 (2018).

[31] Ferrier, M.G., Radchenko, V., An appendix of radionuclides used in targeted alpha therapy, Journal of Medical Imaging and Radiation Sciences, 50: 58-65 (2019).

[32] Chabner, B.A., Longo D.L., Cancer chemotherapy, immunotherapy and biotherapy principles and practice. Wolters Kluwer, United States (2019).

[33] Chu, E., DeVita, Jr V.T., Physicians' cancer chemotherapy drug manual 2021. Jones & Bartlett Learning, United States (2021).

[34] Rachel A., Cancer chemotherapy. Wiley-Blackwell, United States (2009).

[35] Summerhayes, M., Daniels, S., Practical chemotherapy - a multidisciplinary guide. Chapman and Hall/CRC, United States (2018).

[36] Wickham L., Degrais P.M., Radiumtherapy. Cassell and Company, LTD., United Kingdom (1910).

[37] Chandra, R., Rahmim, A., Nuclear medicine physics: the basics. Lippincott Williams & Wilkins (LWW), United States (2017).

[38] IAEA TECDOC No. 1925: Industrial Applications of Sealed Radioactive Sources. International Atomic Energy Agency, Austria (2020).

[39] Brudecki, K., Kluczewska-Gałka, A., Zagrodzk, P., Jarząb, B., Gorzkiewicz, K., Mróz, T., ^{131}I thyroid activity and committed dose assessment among family members of patients treated with radioactive iodine. Radiation and Environmental Biophysics 59:559–564 (2020).

[40] Seidlin, S.M., Oshry, E., Yalow, A.A., Spontaneous and experimentally induced uptake of radioactive iodine in metastases from thyroid carcinoma; a preliminary report. 8:423-32 (1948).

[41] Society of Nuclear Medicine. The benefits of nuclear medicine, 1995. Available from http://interactive.snm.org/docs/whatisnucmed.pdf.

[42] Bailey, J.L., Humm, A., Todd-Pokropek, A., van Aswegen A., Nuclear medicine physics a handbook for teachers and students. International Atomic Energy Agency, Austria (2014).

[43] Mathematics and Physics of Emerging Biomedical Imaging. National Research Council (US) and Institute of Medicine (US) Committee on the Mathematics and Physics of Emerging Dynamic Biomedical Imaging. Washington (DC): National Academies Press (US); (1996).

[44] Gambhir, S. S. and Yaghoubi, S. S., Molecular Imaging with Reporter Genes (Cambridge University Press,), p. 120 (2010).

[45] See: https://www.lbic.lu.se/basic-principles-petct-and-spectct

[46] Rahmim, A., Lodge, M., Karakatsanis, N., et al., Dynamic whole-body PET imaging: principles, potentials and applications. Journal of Nuclear Medicine 59:1158 (2018).

[47] Bone, P., Single photon emission CT (SPECT) applies tomographic technology to radionuclide scanning, enabling a cross-sectional image to be obtained and enhancing conspicuity of a lesion. (Second Edition), 277-307, (2012).

[48] Ahmadzadehfar, H., SPECT, Technology, Procedures and Applications (2014).

[49] Duran, C., et al., in Vascular Medicine: A Companion to Braunwald's Heart Disease (Second Edition), (2013).

[50] Abeyasinghe, P., Structure-Function Relationship of the Brain: A comparison between the 2D Classical Ising model and the Generalized Ising model. Thesis, Western Ontario University, (2015).

[51] Delbeke, D., Coleman R.E., Guiberteau, M.J., et al., Procedure guideline for SPECT/CT imaging1.0. Journal Nuclear Medicine. 47:1227-1234, (2006).

[52] James, A., Turkington, T.G., SPECT/CT Physical Principles and Attenuation Correction. Journal of Nuclear Medicine Technology March, 36:1-10, (2008).

[53] Ahmadzadehfar, H., et al., Clinical applications of SPECT-CT. Springer International Publishing. ISBN: 978-3-030-65849-6, (2021).

[54] Utsunomiya, D., et al., Object-specific Attenuation Correction at SPECT/CT in Thorax: Optimization of Respiratory Protocol for Image Registration 1. Radiology 237:662-9, (2005).

[55] Carminati, M., et al., SPECT/MRI INSERT Compatibility: Assessment, Solutions, and Design Guidelines. Computer Science. IEEE Transactions on Radiation and Plasma Medical Sciences. 2:369-379, (2018).

[56] Schulz, V., et al., SiPM based preclinical PET/MR insert for a human 3T MR: First imaging experiments. IEEE NSS/MIC Conf., Valencia, Spain, pp. 4467–4469, (2011).

[57] Schneider, A., et al., Biomedical Engineering in Gastrointestinal Surgery. 87-220, ISBN 9780128032305, (2017).

[58] Townsend, D.W., Dual-Modality Imaging: Combining Anatomy and Function. Journal of Nuclear Medicine. 49, (2008).

[59] Ehman, E.C., et al., PET/MRI: Where might it replace PET/CT? Journal of Magnetic Resonance Imaging. 46: 1247–1262, (2017).

[60] Ciarmiello, A., Mansi, L., PET-CT and PET-MRI in Neurology. Springer, ISBN: 978-3-319-31612-3. (2016).

[61] Dahlbom, M., Physics of PET and SPECT Imaging (first edition). CRC Press, United States (2021).

[62] Tsechanski, A., Bielajew, A.F., Archambault, J.P., and Mainegra-Hing, E., Electron accelerator-based production of molybdenum-99: Bremsstrahlung and photoneutron generation from molybdenum vs. tungsten. Nuclear Instruments and Methods in Physics Research B 366 124-139 (2016).

[63] Fedorchenko, D.V., and Tsechanski, A., Photoneutronic aspects of the molybdenum-99 production by means of electron linear accelerators. Nuclear Instrument and Methods in Physics Research B 438:6-13 (2019).

[64] IAEA-TECDOC- 1065, Production technologies for molybdenum-99 and technetium-99m. Austria, (1999).

[65] IAEA radioisotopes and radiopharmaceuticals reports No. 2, Cyclotron Produced Radionuclides: Emerging Positron. Austria, (2017).

[66] IAEA-Technical Report No468, Cyclotron produced radionuclides: physical characteristics and production methods. Austria, (2009).

[67] Coenen, H.H., et al., Radioionidation Reactions for Pharmaceuticals: Compendium for Effective Synthesis Strategies. Springer, ISBN: 9781402045615, (2006).

[68] Cherry, S.R., Sorenson, J.A, and Phelps, M.E., Physics in nuclear medicine (fourth edition), Saunders, an imprint of Elsevier Inc., United States (2012).

[69] See: https://en.wikipedia.org/wiki/Stable_nuclide

[70] Leadbeater, T., Parker, D.J, A positron camera with flexible geometry for the study of industrial processes. 5th World Congress on Industrial Process Tomography, Bergen, Norway (2015).

[71] Gambhir, S.S., Molecular imaging of cancer with positron emission tomography. Nature Reviews Cancer 2:683-693 (2002).

[72] IAEA radioisotopes and radiopharmaceuticals reports No. 3. Cyclotron Produced Radionuclides: Guidance on Facility Design and Production of [18F]Fluorodeoxyglucose (FDG), Vienna, (2012).

[73] Ranajit, K.B., et al., Production of [^{11}C]carbon dioxide via the ^{11}B(p, n)^{11}C reaction and [^{18}F]fluoride via the ^{18}O(p, n)^{18}F reaction for radiopharmaceutical Development. Applied Radiation and Isotopes. 42:683-686, (1991).

[74] Iguchi, S., Moriguchi, T., Yamazaki, M. et al., System evaluation of automated production and inhalation of ^{15}O-labeled gaseous radiopharmaceuticals for the rapid ^{15}O-oxygen PET examinations. European Journal of Nuclear Medicine and Molecular Imaging. 5, 37 (2018).

[75] Pandey, M.K., et al., Cyclotron production of ^{68}Ga via the ^{68}Zn(p,n)^{68}Ga reaction in aqueous solution. Nuclear Medicine and Molecular Imaging, 4:303–310, (2014).

[76] Kambali, I., Wibowo, F.N., Comparison of gallium-68 production yields from (p,2n),

(α,2n) and (p,n) nuclear reactions applicable for cancer diagnosis. Journal of Physics. 1198 (2019).

[77] Nucleonica GmbH, Nucleonica Nuclear Science Portal (www.nucleonica.com), Version Version 3.0.297.0001, Karlsruhe (2020).

[78] Gargaud, M., et al., Branching Ratio. Encyclopedia of Astrobiology. Springer, Berlin, Heidelberg (2011).

[79] Knapp, F.F., Dash, A., Radiopharmaceuticals for therapy. Springer India (2016).

[80] Lewis, J.S., Windhorst, A.D., Zeglis, B.M., Radiopharmaceutical chemistry. Springer Nature Switzerland AG (2019).

[81] Kowalsky, R.j., Falen, S., Radiopharmaceuticals in Nuclear Pharmacy & Nuclear Medicine American Public Health Association Press, United States, (2004).

[82] Sun, X., et al., Positron emission tomography imaging using radiolabeled inorganic nanomaterials. 48: 286–294, (2015).

[83] Cooper, M.S., Sabbah, E., & Mather, S.J., Conjugation of chelating agents to proteins and radiolabeling with trivalent metallic isotopes. Nature Protocols 1:314-317 (2006).

[84] Calabria, F., Schillaci, O., Radiopharmaceuticals a guide to PET/CT and PET/MRI. Springer Nature Switzerland AG (2020).

[85] Sarko, D., Eisenhut, M., Haberkorn, U., and Mier, W., Bifunctional chelators in the design and application of radiopharmaceuticals for oncological diseases. Current Medicinal Chemistry 19, 2667-2688 (2012).

[86] Kostelnik, T.I., and Orvig, C., Radioactive main group and rare earth metals for imaging and therapy. Chemical Reviews 119 (2), 902-956 (2019).

[87] Owunwanne, A., Patel, M., Sadek, S., The handbook of radiopharmaceuticals, Chapman & Hall, United Kingdom (1995).

[88] Feijtel, D., Jong, M., and Nonnekens, J., Peptide receptor radionuclide therapy: looking back, looking forward. Current Topics in Medicinal Chemistry 20, 2959-2969 (2020)

[89] Saha, G.B., Fundamentals of nuclear pharmacy (third edition). Springer Science+Business Media, LLC, (2010).

[90] Kręcisz, P., et al., Radiolabeled peptides and antibodies in medicine. Bioconjugate Chemistry 32, 25−42 (2021).

[91] Nunn, A.D., Drugs and the pharmaceutical sciences Vol.55: Radiopharmaceuticals chemistry and pharmacology. Marcel Dekker, Inc. United States (1992).

[92] Cardinale, J., et al., Preclinical evaluation of ^{18}F-PSMA-1007, a new prostate-specific membrane antigen ligand for prostate cancer imaging. The Journal of Nuclear Medicine 58: 425-431 (2017).

[93] Liu, S., et al., Impact of PKM linkers on biodistribution characteristics of the ^{99m}Tc-labeled cyclic RGDfK dimer. Bioconjugate Chemistry. 17: 1499–1507, (2006).

[94] Chakraborty, S., Liu, S., (^{99m})Tc and (^{111})In-labeling of small biomolecules: bifunctional chelators and related coordination chemistry. Current topics in medicinal chemistry. 10. 1113-34, (2010).

[95] Forthal, D.N., Functions of Antibodies. microbiology spectrum. 2(4):1-17 (2014).

[96] Steinitz, M., Human monoclonal antibodies: methods and protocols. Springer New York. ISBN: 9781493989584, (2019).

[97] Lu, R.M., et al., Development of therapeutic antibodies for the treatment of diseases. Journal of Biomedical Science. 27, (2020).

[98] Barbet, J., et al., Radiolabeled antibodies for cancer imaging and therapy. Methods in Molecular Biology 907:681-97 (2012).

[99] Shokeen, M., Wadas, T.J., The Development of copper radiopharmaceuticals for imaging and therapy. Medicinal Chemistry 7, 413-429 (2011).

[100] Weber, J., Haberkorn, U., and Mier, W., Cancer stratification by molecular imaging. International Journal of Molecular Sciences 16, 4918-4946 (2015).

[101] Boinapally, S., et al., A prostate-specific membrane antigen (PSMA)-targeted prodrug with a favorable in vivo toxicity profile, Scientific Reports 11:7114 (2021).

[102] Eichenberger, L.S., Patra, M., and Holland, J.P., Photoactive chelates for radiolabeling proteins. Chemical Communications 55, 2257-2260 (2019).

[103] Geoffrey, S., et al., Neuro-oncology. Elsevier, ISBN: 978-0-7506-7516-1, 36:1-461, (2021).

[104] Kim, Y.H., et al., Diffusely increased ^{18}F-FDG uptake in the thyroid gland and risk of thyroid dysfunction: A cohort study. Journal of Clinical Medicine 8, 443 (2019).

[105] Moudi, M.A., Sun, Z. H., Diagnostic value of (18)F-FDG PET in the assessment of myocardial viability in coronary artery disease: A comparative study with (99m)Tc SPECT and echocardiography. Journal of Geriatric Cardiology 11(3):229-36 (2014).

[106] Rahman, W.T., et al., The impact of infection and inflammation in oncologic 18F-FDG PET/CT imaging. Biomedicine & Pharmacotherapy 117, 109168 (2019).

[107] Pruthi, A., Choudhury, P.S., Gupta, M., Taywade, S., Does the intensity of diffuse thyroid gland uptake on F-18 fluorodeoxyglucose positron emission tomography/computed tomography scan predict the severity of hypothyroidism? Correlation between maximal standardized uptake value and serum thyroid. Indian Journal of Nuclear Medicine 30(1):16-20 (2015).

[108] Cocolios, T.E., Cleeren, F.,Targeted Alpha Therapy research in Belgium: qualifying the 225Ac pipeline. CERN Document Server (2021).

[109] Gudkov, S.V., Shilyagina, N.Y., Vodeneev, V.A., and Zvyagin, A.V., Targeted Radionuclide Therapy of Human Tumors. International Journal of Molecular Sciences 17:33 (2015).

[110] Tan, H., Yeong, c.h., Wong, Y.H., Mckenzie, M., et al., Neutron-activated theranostic radionuclides for nuclear medicine. Nuclear Medicine and Biology 90:55-68. (2020).

[111] Yordanova, A., Eppard, E., Kürpig, S., Bundschuh, R.A., Schönberger, S., Gonzalez-Carmona, M., Feldmann, G., Ahmadzadehfar, H., and Essler , M., Theranostics in nuclear medicine practice. Onco Targets and Therapy 10:4821-4828 (2017).

[112] Türler, A., Matched pair theranostics. Chimia (Aarau) 1;73(11):947-949 (2019) PMID: 31753079**,** DOI: 10.2533/chimia.2019.947

[113] Pretze, M., et al., Ac-EAZY! Towards GMP-Compliant module syntheses of 225Ac-labeled peptides for clinical application. Journal of Pharmaceuticals 14:652 (2021).

[114] Meyer, C, et al., Radiation dosimetry and biodistribution of 68Ga-FAPI-46 PET imaging in cancer patients. European Journal of Nuclear Medicine 61, 1171-1177, (2020).

[115] Ali, S.K.I., Khandaker M.U., Dababneh, S., Kassim, H.A., Evaluation of production cross-sections for 61Cu non-standard PET radionuclide via light-ion-induced nuclear reactions on Co, Ni, Zn targets. Nuclear Instrument and Methods in Physics Research B 436: 221-235 (2018).

[116] Technical report No. 468, Cyclotron produced radionuclides: physical characteristics and production methods. International Atomic Energy Agency, Austria (2009).

[117] Chandramani, K., Basic physics. New Delhi: PHI Learning Private Ltd. ISBN 978-8120337084. (2009).

[118] Lee, S., Accelerator physics. World Scientific Publishing Co. Pte. Ltd, Singapore (2004).

[119] Nemenov, L.M., The history of the development of the cyclotron over fifty years (1930–1980). Soviet Physics Uspekhi 24:231-242. (1981).

[120] Friedlander, G., Hermann, G., Handbook of nuclear chemistry. Springer. ISBN: 9781441907202, (2011).

[121] Kleeven, W., Injection and extraction for cyclotrons. Ion Beam Applications (IBA), CAS - CERN Accelerator School: small accelerators. Cern, Switzerland (2016).

[122] El-Saftawy, A.A., Regulating the performance parameters of accelerated particles. Ph.D. thesis, Zagazig University (2020).

[123] IAEA Technical report No. 465, Cyclotron Produced Radionuclides: Principles and Practice. Vienna, (2008).

[124] IAEA-TECDOC-1340: Manual for reactor produced radioisotopes. International Atomic Energy Agency, Austria (2003).

[125] Adelstein, S.J., Manning, F.J., Isotopes for medicine and the life sciences, The National Academies Press, United States (1995).

[126] Technical reports series No. 389: Radiological characterization of shut down nuclear reactors for decommissioning purposes. International Atomic Energy Agency, Austria (1998).

[127] Heat powered cycles conferences. University of Bayreuth, Germany (2018).

[128] Schwellenbach, D., Basics of RF linear accelerators, Nevada National Security Site New Mexico Operations, Los Alamos UNLV (2018).

[129] Varlamov, A.V., Varlamov, V.V., Rudenko, D.S., Stepanov, M.E., Atlas of giant dipole resonances (INDC(NDS)-394). International Atomic Energy Agency, Austria (1999).

[130] Rotsch, D.A., et al., Production of medical isotopes with electron linacs. Proceeding of NAPAC, United States (2016).

[131] High power linacs for isotope production. Brochure, high energy isotope linac (2010).

[132] Zhu, T.C., Wang, K.H., Linear Accelerators (LINAC). In: Brady L.W., Yaeger T.E. (eds) Encyclopedia of Radiation Oncology. Springer, Berlin, Heidelberg (2013).

[133] Rigla, J.P., Design and characterization of magnetic systems in race-track microtrons. Thesis for: Doctorate. Instituto de Técnicas Energéticas Universidad Politécnica de Cataluña (2013).

[134] Hamm, R.W., and Hamm, M.E., Industrial accelerators and their applications, World Scientific Publishing Co. Pte. Ltd, Singapore (2012).

[135] Korenev, S., The concept of beam lines from Rhodotron for radiation technologies. Proceedings of the 2003 Particle Accelerator Conference,1015-1016 (2003).

[136] Ahmedova, A., Todorov, B., Burdzhiev, N., Goze, C., Copper radiopharmaceuticals for theranostic applications. European Journal of Medicinal Chemistry 157, 1406-1425 (2018).

[137] Ali, S.K.I., Khandaker M.U., Dababneh S., Kassim, H.A., Evaluation of production cross-sections for ^{61}Cu non-standard PET radionuclide via light-ion-induced nuclear reactions on Co, Ni, Zn targets. Nuclear Instrument and Methods in Physics Research B 436, 221-235 (2018).

[138] Williams, H.A., Robinson, S., Julyan, P., Zweit, J., Hastings, D., A comparison of PET imaging characteristics of various copper radioisotopes. European Journal of Nuclear Medicine and Molecular Imaging 32, 1473-1480 (2005).

[139] Hao, G., Mastren, T., Silvers, W., Hassan, G., Öz, O.K., Sun, X., Copper-67 radioimmunotheranostics for simultaneous immunotherapy and immuno-SPECT. Scientific Reports. 11:3622 (2021).

[140] Technical reports series No. 468, Cyclotron produced radionuclides: physical characteristics and production methods. IAEA, Austria (2009).

[141] Beneficial Uses and production of isotopes. Nuclear Energy Agency, France (2000).

[142] Szelecsènyi, F., et al., Comments on the feasibility of ^{61}Cu production by proton irradiation of ^{nat}Zn on a medical cyclotron. Applied Radiation and Isotopes 64, 789-791 (2006).

[143] Asabella A.N., et al., The copper radioisotopes: a systematic review with special interest to ^{64}Cu. Journal of Biomedicine and Biotechnology 3, 786463 (2014).

[144] Rowshanfarzad, P., Sabet, M., Jalilian, A.R., Kamalidehghan, M., An overview of copper radionuclides and production of ^{61}Cu by proton irradiation of ^{nat}Zn at a medical cyclotron. Applied Radiation and Isotopes 64, 1563-1573 (2006).

[145] Asad, A:H., Smith, S.V., Morandeau, L.M., Chan, S., Jeffrey, C.M., Price, R.I., Production of ^{61}Cu by the ^{nat}Zn(p,α) reaction: improved separation and specific activity determination by titration with three chelators. Brookhaven national laboratory, BNL-108191-2015-JA, (2015).

[146] McCarthy D.W., et al., High purity production and potential applications of copper-60 and copper-61. Nuclear Medicine & Biology 26, 351-358 (1999).

[147] Sadeghi, M., Zandi, N., Bakhtiari, M., Nuclear model calculation for cyclotron production of ^{61}Cu as a PET imaging. Journal of Radioanalytical and Nuclear Chemistry 292, 777–783 (2012).

[148] Thieme, S., et al., High specific activity ^{61}Cu via ^{64}Zn(p,α)^{61}Cu reaction at low proton energies. Applied Radiation and Isotopes 72, 169-176 (2013).

[149] Broeders, C.H.M., Konobeyev, A.Y., Korovin, Y.A., Lunes, V.P., Blann, M., ALICE/ASH–Pre-compound and evaporation model code system for calculation of excitation functions, energy and angular distributions of emitted particles in nuclear reaction at intermediate energies, FZK-7183, Forschungszentrum Karlsruhe GmbH, Germany (2006).

[150] Koning, A.J., Hilairey, S., Duijvestijn M., TALYS-1.2: a nuclear reaction program. User manual, NRG, Netherlands (2009).

[151] Pupillo, G., et al., New production cross sections for the theranostic radionuclide ^{67}Cu. Nuclear Inst. and Methods in Physics Research B 415, 41-47, (2018).

[152] Qaim, S.M., Nuclear data for production and medical application of radionuclides: present status and future needs, Nuclear Medicine and Biology 44, 31–49 (2017).

[153] Koning, A.J., et al., TENDL: Complete Nuclear Data Library for Innovative Nuclear Science and Technology, Nuclear Data Sheets 155 (2019).

[154] Koning, A.J., Rochman, D., TENDL-2019: TALYS-based evaluated nuclear data library. Nuclear Research and Consultancy Group (NRG) Petten, The Netherlands, http://www.talys.eu/ tendl-2019.

[155] Synowiecki, M.A., Perk, L.R., and FNijsen., J.F.W., Production of novel diagnostic radionuclides in small medical cyclotrons. EJNMMI Radiopharmacy and Chemistry 3 (2018).

[156] Schwarzbach, R., Zimmermann, K., Novak-Hofer, I., Schubiger, P.A., A comparison of ^{67}CU production by proton (67 to 12 MeV) induced reactions on NATZN and on enriched ^{68}Zn/^{70}Zn. Journal of Labelled Compounds and Radiopharmaceuticals 44, S809–S811 (2001).

[157] Kastleiner, S.,Coenen, H.H., Qaim,S.M., Possibility of production of ^{67}Cu at a small-sized cyclotron via the(p,α) reaction on enriched ^{70}Zn. Radiochimica Acta 84, 107-110 (1999).

[158] Pupillo, G., et al., Production of ^{67}Cu by enriched ^{70}Zn targets: first measurements of formation cross sections of ^{67}Cu, ^{64}Cu, ^{67}Ga, ^{66}Ga, ^{69m}Zn and ^{65}Zn in interactions of ^{70}Zn with protons above 45 MeV. Radiochimica Acta 108, 593-602 (2020).

[159] Skakun, Y.E., Qaim, S.M., Excitation function of the 64Ni(a,p)67Cu reaction for production of ^{67}Cu. Applied Radiation and Isotopes 60, 33-39 (2004).

[160] Ohya, T., et al., Small-scale production of 67Cu for a preclinical study via the ^{64}Ni(α, p)^{67}Cu channel. Nuclear Medicine and Biology 59, 56-60 (2018).

[161] Gopalakrishna, A., Suryanarayana, S.V., Naik, H., et. al. Production, separation and supply prospects of ^{67}Cu with the development of fast neutron sources and photonuclear technology. Radiochimica Acta 106, 549–557 (2018).

[162] Johnsen, A., Heidrich, B., Durrant, C.B., et al. Reactor production of ^{64}Cu and ^{67}Cu using enriched zinc target material. Journal of Radioanalytical and Nuclear Chemistry 305, 61-71, (2015).

[163] Luo, W., Babeica, M., Filipescu, D., Gheorghe, L., Niculae, D., Balabanski, D.L., Productions of radioisotopes of medical interest by photonuclear reaction using ELI-NP gamma ray beam. Acta Physica Polonica B 47, 763 (2016).

[164] Johnson, T., Introduction to health physics. McGraw-Hill Education. ISBN: 9780071835275, (2017).

[165] IAEA-TECDOC-1178, Handbook on photonuclear data for applications: cross-sections and spectra, International Atomic Energy Agency, Austria (2000).

[166] Haug, E., Nakel, W., The elementary process of bremsstrahlung, World Scientific Publishing Co., Singapore (2004).

[167] Pelowitz, D.B., MCNPX Users Manual Version 2.7.0 LA-CP-11-00438 (2011).

[168] Ayzatskiy, N.I., et al., Comparison of Cu-67 production at cyclotron and electron accelerator, Cyclotrons and Their Applications, Eighteenth International Conference. Physical copies currently on shelf in CERN Central Library, Instituto Nazionale di Fisica Nucleare 243-245 (2007).

[169] Koning, A.J., Rochman, D., TENDL-2020: TALYS-based evaluated nuclear data. Nuclear Research and Consultancy Group (NRG) Petten, The Netherlands (2010).

[170] L'annunziata, M.F., Handbook of radioactivity analysis (Second Edition), Academic Press. United States (2003).

[171] Azizi, A., Nozhati, R.A., Sillanpää, M. Solvent extraction of copper and zinc from sulfate leach solution derived from a porcelain stone tailings sample with chemorex CP-150 and D2EHPA. Journal of Sustainable Metallurgy 6, 250–258 (2020).

[172] Tylkowski, B., Wieszczycka, K., Reactive extraction at liquid–liquid systems. Physical Sciences Reviews. 3. 10:141, (2018).

[173] Gopalakrishna, A., Suryanarayana, S.V., Naik, H., et. al., Production, separation and supply prospects of 67Cu with the development of fast neutron sources and photonuclear technology. Radiochimica Acta 106, 549–557 (2018).

[174] Nicholas, N., Organic chemistry lab techniques. LibreTexts publisher, United States (2021).

[175] Horwitz, E.P., Dietz, M.L., Chiarizia, R., Diamond, H., Maxwell, I.S.L., Nelson, M.R., Separation and preconcentration of actinides by extraction chromatography using a supported liquid anion exchanger: application to the characterization of high-level nuclear waste solutions. Analytica Chimica Acta 310, 63–78 (1995).

[176] Extraction chromatography, technical documentation. TRISKEM International (2015), www.triskem.com

[177] Weiss, j., Handbook of Ion chromotography. Wiley-VCH, Germany (2004).

[178] Breton, E.J., Schlechten, A.W., Separation of copper from zinc by ion exchange. Journal of The Minerals, Metals & Materials Society 3, 517–521 (1951).

[179] IAEA-TECDOC-1955, Production of emerging radionuclides towards theranostic applications: copper-61, scandium-43 and -44, and yttrium-86. International Atomic Energy Agency, Austria (2021).

[180] Dorfner, K., Ion Exchangers. Walter de Gruyter, Germany, (1991).

[181] Muraviev, D., Gorshkov, V., Warshawsky, A., Ion exchange M. Dekker, New York, (2000).

[182] See: ttp://wiki.biomine.skelleftea.se/wiki/index.php/Ion-exchange

[183] Yunjian, M., Keqiang, Q., Separation and recovery of zinc from copper-based alloy scraps under vacuum conditions. Vacuum 106, 5-10 (2014).

[184] Eychenne, R., Bouvry, C., Bourgeois, M., Loyer, P., Benoist, E., Lepareur, N., Overview of radiolabeled somatostatin analogs for cancer imaging and therapy. Molecules 25, 4012 (2020).

[185] Follacchio, G.A., De Feo, M.S., De Vincentis, G., Monteleone, F., Liberatore, M., Radiopharmaceuticals labelled with copper radionuclides: clinical results in human beings. Current Radiopharmaceuticals 11(1), 22-33 (2018).

[186] Toshimitsu, F., Kazuhiro, O., Szelecsényi, F., Kovács, Z., Suzuki, K., Practical production of 61Cu using natural Co target and its simple purification with a chelating resin for 61CU-ATSM. Radiochimica Acta. 92, 209-214 (2004).

[187] Mirzaei, S., Revheim, ME., Raynor, W. et al. 64Cu-DOTATOC PET-CT in patients with neuroendocrine tumors. Oncology and Therapy 8, 125–131 (2020).

[188] Delpassand, E., et al., 64Cu-DOTATATE PET/CT for imaging patients with known or suspected somatostatin receptor–positive neuroendocrine tumors: results of the first U.S. prospective, reader-masked clinical trial. J Nucl Med., 61,890–896 (2020).

[189] Hennrich, U., Benešová, M., [^{68}Ga]Ga-DOTA-TOC: the first FDA-approved ^{68}Ga-radiopharmaceutical for PET imaging. Pharmaceuticals 13, 38 (2020).

[190] do Carmo, S. J. C., Alves, V. H. P., Alves, F., Abrunhosa, A. J., Fast and cost-effective cyclotron production of 61Cu using a natZn liquid target: an opportunity for radiopharmaceutical production and R&D. Dalton Transactions 46(42):14556-14560 (2017).

[191] SzelecsÈnyi, F., Kov·cs, Z., Suzuki, K., Okada, K., van der Walt, T.N., Steyn, G.F., Mukherjee, S., Production possibility of ^{61}Cu using proton induced nuclear reactions on zinc for PET studies. Journal of Radioanalytical and Nuclear Chemistry 263, 539–546 (2005).

[192] Rowshamfarzad, P., Sabet, M., Jalilian, A.M., An overview of copper radionuclides and production of Cu-61 by proton irradiation of Zn-nat at a medical cyclotron. Applied Radiation and Isotopes 64(12):1563-73 (2007).

[193] Talip, Z., et al., A Step-by-Step Guide for the Novel Radiometal Production for Medical Applications: Case Studies with 68Ga, 44Sc, 177Lu and 161Tb. Molecules 25(4):966 (2020).

[194] Asad, A:H., Smith, S.V., Morandeau, L.M., Chan, S., Jeffrey, C.M., Price, R.I., Production of ^{61}Cu by the ^{nat}Zn(p,α) reaction: improved separation and specific activity determination by titration with three chelators. Brookhaven national laboratory, BNL-108191-2015-JA, (2015).

[195] Čepa A., et al., Radiolabeling of the antibody IgG M75 for epitope of human carbonic anhydrase IX by ^{61}Cu and ^{64}Cu and its biological testing. Applied Radiations and Isotopes 143: 87-97 (2019).

[196] Jalilian, A. R., et al., Radiosynthesis and evaluation of [61Cu]-9,10-phenanthrenequinone thiosemicarbazone in fibrosarcoma-bearing animals for PET imaging. Radiochimica Acta 98, 175-181 (2010).

[197] Follacchio, G.A., De Feo, M.S., Vincentis, G., Monteleone, F., and Liberatore, M., Radiopharmaceuticals labelled with copper radionuclides: clinical results in human beings. Current Radiopharmaceuticals 11, 22-33 (2018).

[198] Kozempel, J., Gibson, A.K., Holzwarth, U., Simonelli, F., A Novel Method for 67Cu Production. In: Terachem 2010; 07 September 2010; Bressannone (Italy). Nuclear medicine and biology 37 (6); 2010.p. 717, (2012).

[199] Pupillo G., et al., Cyclotron production of ^{67}Cu: a new measurement of the ^{68}Zn(p,2p)^{67}Cu, ^{68}Zn(p,2n)^{67}Ga and ^{68}Zn(p,3n)^{66}Ga nuclear cross sections. Nucleus N^0 63 (2018).

[200] Johnsen, A.M., et al. Reactor production of ^{64}Cu and ^{67}Cu using enriched zinc target material. Journal of Radioanalytical and Nuclear Chemistry 305:61–71 (2015).

[201] Hovhannisyan G.H., Bakhshiyan T.M., Dallakyan R.K., Photonuclear production of the medical isotope ^{67}Cu. Nuclear Inst. and Methods in Physics Research, B 498 48-51 (2021).

[202] Smith N.A., Bowers D.L., Ehst D.A., The production, separation, and use of ^{67}Cu for radioimmunotherapy: A review. Applied Radiation and Isotopes 70(10) 2377-2383 (2012).

[203] Merrick M.J., et al., Imaging and dosimetric characteristics of ^{67}Cu. Physics in Medicine & Biology 66 035002 (2021).

[204] Medvedev D.G., et al., Development of a large scale production of ^{67}Cu from ^{68}Zn at the high energy proton accelerator: Closing the ^{68}Zn cycle. Applied Radiation and Isotopes 70:423-429 (2012).

[205] Norenberg J, Staples P, Atcher R et al. Workshop on the nation's need for isotopes: present and future. Department of Energy, Rockville (2008).

[206] Ayzatskiy, N.I., et al. Comparison of Cu-67 production at cyclotron and electron accelerator. Cyclotrons and their applications, Eighteenth International Conference (2007).

[207] Jin, Z.H., et al., ^{67}Cu-Radiolabeling of a multimeric RGD peptide for αVβ3 integrin-targeted radionuclide therapy: stability, therapeutic efficacy, and safety studies in mice. Nuclear Medicine Communications 38(4):347-355 (2017).

[208] Hao G., et al., Copper-67 radioimmunotheranostics for simultaneous immunotherapy and immuno-SPECT. Scientific Reports 11:3622 (2021).

[209] Gopalakrishna, A., et al., Production, separation and supply prospects of ^{67}Cu with the development of fast neutron sources and photonuclear technology. Radiochimica Acta, 106: 549-557 (2018).

[210] Skliarova, H., et al., Medical cyclotron solid target preparation by ultrathick film magnetron sputtering deposition instruments. MDPI, *Instruments 3*,21 (2019).

[211] Thieme, S., Walther, M., Preusche, S., Rajander, J., Pietzsch, H., Lill, J., Kaden, M., Solin, O., Steinbach, J., High specific activity ^{61}Cu via ^{64}Zn(p,α)^{61}Cu reaction at low proton energies. Applied Radiation and Isotopes 72, 169-176 (2013).

[212] Carzaniga, S.T., Production of non-standard medical radio-isotopes with solid targets. Thesis, University of Bern (2019).

[213] Stucki, G., Recent activities in measurements standards and dosimetry at METAS 2005-2007 Report to the 18th meeting of the CCRI May (2007).

[214] do Carmo, S. J. C., Alves, V. H. P., Alves, F., Abrunhosa, A. J., Fast and cost-effective cyclotron production of ^{61}Cu using a ^{nat}Zn liquid target: an opportunity for radiopharmaceutical production and R&D. Dalton Transactions 46(42):14556-14560 (2017).

[215] Aliev, R.A., et al., Photonuclear production and radiochemical separation of medically relevant radionuclides: ^{67}Cu. Journal of Radioanalytical and Nuclear Chemistry, 321, 125–132 (2019).

[216] Hovhannisyan, G.H., Bakhshiyan, T.M., Dallakyan, R.K., Photonuclear production of the medical isotope ^{67}Cu. Nuclear Inst. and Methods in Physics Research, B 498, 48-51 (2021).

[217] Svedjehed, J., Kutyreff C.J., Engle, J.W., Gagnon, K., Automated, cassette-based isolation and formulation of high-purity [61Cu]CuCl2 from solid Ni targets. EJNMMI Radiopharmacy and Chemistry, 5, 21 (2020).

[218] Ziegler JF, Biersack JP, Littmark U, The code of SRIM— the stopping and range of ions in matter. IBM Research, New York (2006).

[219] Zandi, N., et al., Targetry and specification of ^{167}Tm production parameters by different reactions. Journal of Radioanalytical and Nuclear Chemistry 291:731–738, (2012).

List of Figures

List of Tables

ABBREVIATONS

IAEA	Atomic Energy Agency
NCDs	Non-Communicable Diseases
METAS	Federal Institute of Metrology
PET	Positron Emission Tomography
SPECT	Single-Photon Emission Computed Tomography
MRI	Magnetic resonance imaging
LET	Linear Energy Transfer
PSMA	Prostate-Specific Membrane Antigen
DOTA	Dodecane Tetraacetic Acid
BFCA	Bifunctional Chelating Agents
FDA	Food and Drug Administration
^{18}FDG	Fluorodeoxyglucose
PMT	Photomultiplier Tube
LINAC	Linear Accelerators
DC	Direct Current
GDR	Giant Dipole Resonances
MCNP	Monte Carlo N-Particle Transport
HPGe	High Pure Germanium
SLM	4-fold Module
HRM	Heater Reaction Module
SYM	Syringe Module
TLC	Thin Layer Chromatography
BR	Branching Ratio
HPLC	High-performance liquid chromatography

ACKNOWLEDGEMENT

First of all, I would like to thank Prof. Dr. Andreas Türler, my supervisor, for accepting me as a Ph.D. student to his radiochemistry group and provide me the opportunity to start working on this promising topic. Prof. Andreas Türler always inspired the students to start deeply thinking about novel ideas based on different approaches. His outstanding knowledge in the field helped the project to progress in the right and effective direction. For me, it was a great chance to join his group and working on copper radiopharmaceuticals. He always supported me in attending practical courses that were along with my Ph.D. thesis. I am really thankful for his mentoring approach that is beneficial in my future carrier.

I am really grateful to other collaborative colleagues (Dr. Niurka Menses Moreno, Dr. Tais Bernabeu, Ronal Zingg, and Dr. Maruta Bunka) who supported me in the implementation of this project and were a part of the community. It was a great chance for me to know them, that I could always count on their support.

I want to thank Prof. Saverio Braccini's group and his genus Ph.D. Student Gaia Dellepiane at SWAN Isotopen AG for assisting us in the production section. They really had an essential role in performing this project.

I would also like to express my thankfulness to Dr. Christian Kottler and Dr. Matthias Lüthi at METAS, who support us in the production section. Dr. Matthias Lüthi generously spent time assisting us in the target irradiation section.

Finally, I would like to express special thanks to my husband (Mehran Vagheian), who always motivated me to continue my project, especially whenever I was depleted and exhausted. Thanks, Mehran, for being with me for all the moments.

Batch Report

Device:	HJZM0G2	Procedure:	chemical seperation
Batch:	B20210209001	Half life:	3.3 h
Started:	2021-02-09 15:47:46	Nuclide:	Cu-61

Duration of synthesis: 01:39:44
User-ID: admin
Project path: C:\PROGRAM FILES (X86)\EUROTOPE\ML43SPLC\EDITOR\PROJECT ENGLISH\ZINC-COPPER_OVEN_NEW_FINAL_2 COLUMN TK201_REVISION\ZINC-COPPER_OVEN_NEW_FINAL_2 COLUMN TK201_REVISION.MDL
Project version: 0.0.6

Preparation steps:

1	instalation cassette Cu-Zn	Ok
2	column exist	Ok
3	conditioning of TK201	Ok
4	In big vial, tube should be at the end bottom?	Ok

Audit trail of process:

Timestamp	Object ID	Object Name	Process Step	Comment
2021-02-09 15:47:46	PCtrl	Flow Control	Batch control: start batch	
2021-02-09 15:47:46	Stop	Stop	Button switched from on to off	
2021-02-09 15:47:46	PCtrl	Flow Control	Batch control: start audit trail	
2021-02-09 15:47:47	PCtrl	Flow Control	Msg: water and 8 M connected?	
2021-02-09 15:47:47	Stop	Stop	Button switched from off to on	
2021-02-09 15:47:54	PCtrl	Flow Control	Msg was confirmed	
2021-02-09 15:47:54	Stop	Stop	Button switched from on to off	
2021-02-09 15:47:54	PCtrl	Flow Control	Msg: cassette contains water?	
2021-02-09 15:47:55	Stop	Stop	Button switched from off to on	
2021-02-09 15:48:03	PCtrl	Flow Control	Msg was confirmed	
2021-02-09 15:48:03	Stop	Stop	Button switched from on to off	
2021-02-09 15:48:04	PCtrl	Flow Control	Msg: Remove column 2?	
2021-02-09 15:48:04	Stop	Stop	Button switched from off to on	
2021-02-09 15:48:07	PCtrl	Flow Control	Msg was confirmed	
2021-02-09 15:48:07	Stop	Stop	Button switched from on to off	
2021-02-09 15:48:07	Set string	Set string	String: Comment1 = Conditioning (const.)	
2021-02-09 15:48:07	FOF-SM1	FOF-SM1	Valve switched to direction 2-3	
2021-02-09 15:48:07	FOF-SM2	FOF-SM2	Valve switched to direction 1-3	
2021-02-09 15:48:07	FOF-SM3	FOF-SM3	Valve switched to direction 1-2	
2021-02-09 15:48:07	FOH-SM1	FOH-SM1	Valve switched to direction 1-3	
2021-02-09 15:48:07	FOH-SM2	FOH-SM2	Valve switched to direction 1-3	
2021-02-09 15:48:07	FOH-SM3	FOH-SM3	Valve switched to direction 1-3	
2021-02-09 15:48:07	FOI-SM1	FOI-SM1	Valve switched to direction 1-3	
2021-02-09 15:48:07	GQY-HR	GQY-HR	normal mode, Wait 200 ms Tsp: 0 C	
2021-02-09 15:48:23	GQW-SY	GQW-SY	Syringe starts, volume: 7000 ul, speed: 450 ul/s	
2021-02-09 15:48:28	timer_1	Timer 1	Wait 5.00 s	
2021-02-09 15:48:28	FOF-SM1	FOF-SM1	Valve switched to direction 1-3	
2021-02-09 15:48:28	FOF-SM2	FOF-SM2	Valve switched to direction 1-3	
2021-02-09 15:48:28	FOF-SM3	FOF-SM3	Valve switched to direction 2-3	
2021-02-09 15:48:28	FOG-SM1	FOG-SM1	Valve switched to direction 1-2	
2021-02-09 15:48:29	FOG-SM2	FOG-SM2	Valve switched to direction 2-3	
2021-02-09 15:48:29	FOG-SM3	FOG-SM3	Valve switched to direction 1-3	
2021-02-09 15:48:29	FOH-SM1	FOH-SM1	Valve switched to direction 1-3	
2021-02-09 15:48:29	FOH-SM2	FOH-SM2	Valve switched to direction 1-3	
2021-02-09 15:48:29	FOH-SM3	FOH-SM3	Valve switched to direction 1-3	
2021-02-09 15:48:29	FOI-SM1	FOI-SM1	Valve switched to direction 1-3	
2021-02-09 15:48:29	FOI-SM2	FOI-SM2	Valve switched to direction 1-3	
2021-02-09 15:48:29	FOI-SM3	FOI-SM3	Valve switched to direction 1-2	
2021-02-09 15:48:29	GQY-HR	GQY-HR	normal mode, Wait 200 ms Tsp: 0 C	
2021-02-09 15:52:09	GQW-SY	GQW-SY	Syringe starts, volume: -7000 ul, speed: 32 ul/s	
2021-02-09 15:52:14	timer_1	Timer 1	Wait 5.00 s	
2021-02-09 15:52:14	FOF-SM1	FOF-SM1	Valve switched to direction 1-3	
2021-02-09 15:52:14	FOF-SM2	FOF-SM2	Valve switched to direction 2-3	
2021-02-09 15:52:14	FOF-SM3	FOF-SM3	Valve switched to direction 1-2	
2021-02-09 15:52:45	GQW-SY	GQW-SY	Syringe starts, volume: 6000 ul, speed: 200 ul/s	
2021-02-09 15:52:50	timer_1	Timer 1	Wait 5.00 s	

Batch Report (cont.)

Timestamp	Object ID	Object Name	Process Step	Comment
2021-02-09 15:52:50	FOF-SM1	FOF-SM1	Valve switched to direction 1-3	
2021-02-09 15:52:50	FOF-SM2	FOF-SM2	Valve switched to direction 1-3	
2021-02-09 15:52:50	FOF-SM3	FOF-SM3	Valve switched to direction 2-3	
2021-02-09 15:52:50	FOG-SM1	FOG-SM1	Valve switched to direction 1-2	
2021-02-09 15:52:50	FOG-SM2	FOG-SM2	Valve switched to direction 2-3	
2021-02-09 15:52:50	FOG-SM3	FOG-SM3	Valve switched to direction 1-3	
2021-02-09 15:52:50	FOH-SM1	FOH-SM1	Valve switched to direction 1-3	
2021-02-09 15:52:50	FOH-SM2	FOH-SM2	Valve switched to direction 1-3	
2021-02-09 15:52:50	FOH-SM3	FOH-SM3	Valve switched to direction 1-3	
2021-02-09 15:52:50	FOI-SM1	FOI-SM1	Valve switched to direction 1-3	
2021-02-09 15:52:50	FOI-SM2	FOI-SM2	Valve switched to direction 1-3	
2021-02-09 15:52:50	FOI-SM3	FOI-SM3	Valve switched to direction 1-2	
2021-02-09 15:52:50	GQY-HR	GQY-HR	normal mode, Wait 200 ms Tsp: 0 C	
2021-02-09 15:55:59	GQW-SY	GQW-SY	Syringe starts, volume: -6000 ul, speed: 32 ul/s	
2021-02-09 15:56:04	timer_1	Timer 1	Wait 5.00 s	
2021-02-09 15:56:04	PCtrl	Flow Control	Msg: change column 2?	
2021-02-09 15:56:05	Stop	Stop	Button switched from off to on	
2021-02-09 15:57:21	PCtrl	Flow Control	Msg was confirmed	
2021-02-09 15:57:21	Stop	Stop	Button switched from on to off	
2021-02-09 15:57:21	FOF-SM1	FOF-SM1	Valve switched to direction 2-3	
2021-02-09 15:57:21	FOF-SM2	FOF-SM2	Valve switched to direction 1-3	
2021-02-09 15:57:21	FOF-SM3	FOF-SM3	Valve switched to direction 1-2	
2021-02-09 15:57:21	FOH-SM1	FOH-SM1	Valve switched to direction 1-3	
2021-02-09 15:57:21	FOH-SM2	FOH-SM2	Valve switched to direction 1-3	
2021-02-09 15:57:21	FOH-SM3	FOH-SM3	Valve switched to direction 1-3	
2021-02-09 15:57:21	FOI-SM1	FOI-SM1	Valve switched to direction 1-3	
2021-02-09 15:57:21	GQY-HR	GQY-HR	normal mode, Wait 200 ms Tsp: 0 C	
2021-02-09 15:57:38	GQW-SY	GQW-SY	Syringe starts, volume: 7000 ul, speed: 450 ul/s	
2021-02-09 15:57:43	timer_1	Timer 1	Wait 5.00 s	
2021-02-09 15:57:43	FOF-SM1	FOF-SM1	Valve switched to direction 1-3	
2021-02-09 15:57:43	FOF-SM2	FOF-SM2	Valve switched to direction 1-3	
2021-02-09 15:57:43	FOF-SM3	FOF-SM3	Valve switched to direction 2-3	
2021-02-09 15:57:43	FOG-SM1	FOG-SM1	Valve switched to direction 1-2	
2021-02-09 15:57:43	FOG-SM2	FOG-SM2	Valve switched to direction 2-3	
2021-02-09 15:57:43	FOG-SM3	FOG-SM3	Valve switched to direction 1-3	
2021-02-09 15:57:43	FOH-SM1	FOH-SM1	Valve switched to direction 1-3	
2021-02-09 15:57:43	FOH-SM2	FOH-SM2	Valve switched to direction 1-3	
2021-02-09 15:57:43	FOH-SM3	FOH-SM3	Valve switched to direction 1-3	
2021-02-09 15:57:43	FOI-SM1	FOI-SM1	Valve switched to direction 1-3	
2021-02-09 15:57:43	FOI-SM2	FOI-SM2	Valve switched to direction 1-3	
2021-02-09 15:57:43	FOI-SM3	FOI-SM3	Valve switched to direction 1-2	
2021-02-09 15:57:44	GQY-HR	GQY-HR	normal mode, Wait 200 ms Tsp: 0 C	
2021-02-09 16:01:23	GQW-SY	GQW-SY	Syringe starts, volume: -7000 ul, speed: 32 ul/s	
2021-02-09 16:01:28	timer_1	Timer 1	Wait 5.00 s	
2021-02-09 16:01:28	FOF-SM1	FOF-SM1	Valve switched to direction 1-3	
2021-02-09 16:01:28	FOF-SM2	FOF-SM2	Valve switched to direction 2-3	
2021-02-09 16:01:28	FOF-SM3	FOF-SM3	Valve switched to direction 1-2	
2021-02-09 16:02:00	GQW-SY	GQW-SY	Syringe starts, volume: 6000 ul, speed: 200 ul/s	
2021-02-09 16:02:05	timer_1	Timer 1	Wait 5.00 s	
2021-02-09 16:02:05	FOF-SM1	FOF-SM1	Valve switched to direction 1-3	
2021-02-09 16:02:05	FOF-SM2	FOF-SM2	Valve switched to direction 1-3	
2021-02-09 16:02:05	FOF-SM3	FOF-SM3	Valve switched to direction 2-3	
2021-02-09 16:02:05	FOG-SM1	FOG-SM1	Valve switched to direction 1-2	
2021-02-09 16:02:05	FOG-SM2	FOG-SM2	Valve switched to direction 2-3	
2021-02-09 16:02:05	FOG-SM3	FOG-SM3	Valve switched to direction 1-3	
2021-02-09 16:02:05	FOH-SM1	FOH-SM1	Valve switched to direction 1-3	
2021-02-09 16:02:05	FOH-SM2	FOH-SM2	Valve switched to direction 1-3	
2021-02-09 16:02:05	FOH-SM3	FOH-SM3	Valve switched to direction 1-3	
2021-02-09 16:02:05	FOI-SM1	FOI-SM1	Valve switched to direction 1-3	
2021-02-09 16:02:05	FOI-SM2	FOI-SM2	Valve switched to direction 1-3	
2021-02-09 16:02:05	FOI-SM3	FOI-SM3	Valve switched to direction 1-2	
2021-02-09 16:02:06	GQY-HR	GQY-HR	normal mode, Wait 200 ms Tsp: 0 C	
2021-02-09 16:05:14	GQW-SY	GQW-SY	Syringe starts, volume: -6000 ul, speed: 32 ul/s	
2021-02-09 16:05:19	timer_1	Timer 1	Wait 5.00 s	
2021-02-09 16:05:19	PCtrl	Flow Control	Msg: put (8 M+H2O2) LEFT	

Batch Report (cont.)

Timestamp	Object ID	Object Name	Process Step	Comment
2021-02-09 16:05:20	Stop	Stop	Button switched from off to on	
2021-02-09 16:43:40	PCtrl	Flow Control	Msg was confirmed	
2021-02-09 16:43:40	PCtrl	Flow Control	Msg: Chemical separation start?	
2021-02-09 16:43:40	Stop	Stop	Button switched from on to off	
2021-02-09 16:43:41	Stop	Stop	Button switched from off to on	
2021-02-09 16:44:05	PCtrl	Flow Control	Msg was confirmed	
2021-02-09 16:44:06	PCtrl	Flow Control	Msg: Put column 1 and 2?	
2021-02-09 16:44:06	Stop	Stop	Button switched from on to off	
2021-02-09 16:44:06	Stop	Stop	Button switched from off to on	
2021-02-09 16:45:36	PCtrl	Flow Control	Msg was confirmed	
2021-02-09 16:45:36	Stop	Stop	Button switched from on to off	
2021-02-09 16:45:37	PCtrl	Flow Control	Msg: Change valve argon to syringe?	
2021-02-09 16:45:37	Stop	Stop	Button switched from off to on	
2021-02-09 16:45:46	PCtrl	Flow Control	Msg was confirmed	
2021-02-09 16:45:46	Stop	Stop	Button switched from on to off	
2021-02-09 16:45:47	Set string	Set string	String: Comment1 = Load Oven 1th (const.)	
2021-02-09 16:45:47	PCtrl	Flow Control	Msg: put HCl with H2O2?	
2021-02-09 16:45:47	Stop	Stop	Button switched from off to on	
2021-02-09 16:45:57	PCtrl	Flow Control	Msg was confirmed	
2021-02-09 16:45:57	Stop	Stop	Button switched from on to off	
2021-02-09 16:45:58	FOF-SM1	FOF-SM1	Valve switched to direction 2-3	
2021-02-09 16:45:58	FOF-SM2	FOF-SM2	Valve switched to direction 1-3	
2021-02-09 16:45:58	FOF-SM3	FOF-SM3	Valve switched to direction 1-2	
2021-02-09 16:45:58	FOH-SM1	FOH-SM1	Valve switched to direction 1-3	
2021-02-09 16:45:58	FOH-SM2	FOH-SM2	Valve switched to direction 1-3	
2021-02-09 16:45:58	FOH-SM3	FOH-SM3	Valve switched to direction 1-3	
2021-02-09 16:45:58	FOI-SM1	FOI-SM1	Valve switched to direction 1-3	
2021-02-09 16:45:58	GQY-HR	GQY-HR	normal mode, Wait 200 ms Tsp: 0 C	
2021-02-09 16:46:05	GQW-SY	GQW-SY	Syringe starts, volume: 3000 ul, speed: 450 ul/s	
2021-02-09 16:46:08	timer_1	Timer 1	Wait 2.00 s	
2021-02-09 16:46:08	FOF-SM1	FOF-SM1	Valve switched to direction 1-3	
2021-02-09 16:46:08	FOF-SM2	FOF-SM2	Valve switched to direction 1-3	
2021-02-09 16:46:08	FOF-SM3	FOF-SM3	Valve switched to direction 1-2	
2021-02-09 16:46:08	FOH-SM1	FOH-SM1	Valve switched to direction 2-3	
2021-02-09 16:46:08	FOH-SM2	FOH-SM2	Valve switched to direction 1-3	
2021-02-09 16:46:08	FOH-SM3	FOH-SM3	Valve switched to direction 1-3	
2021-02-09 16:46:08	GQY-HR	GQY-HR	normal mode, Wait 200 ms Tsp: 0 C	
2021-02-09 16:46:15	GQW-SY	GQW-SY	Syringe starts, volume: -3000 ul, speed: 450 ul/s	
2021-02-09 16:56:15	timer_1	Timer 1	Wait 600.00 s	
2021-02-09 16:56:15	FOF-SM1	FOF-SM1	Valve switched to direction 1-3	
2021-02-09 16:56:15	FOF-SM2	FOF-SM2	Valve switched to direction 1-3	
2021-02-09 16:56:15	FOF-SM3	FOF-SM3	Valve switched to direction 1-2	
2021-02-09 16:56:15	FOH-SM1	FOH-SM1	Valve switched to direction 2-3	
2021-02-09 16:56:15	FOH-SM2	FOH-SM2	Valve switched to direction 1-3	
2021-02-09 16:56:15	FOH-SM3	FOH-SM3	Valve switched to direction 1-3	
2021-02-09 16:56:16	GQY-HR	GQY-HR	normal mode, Wait 200 ms Tsp: 0 C	
2021-02-09 16:56:38	GQW-SY	GQW-SY	Syringe starts, volume: 10000 ul, speed: 450 ul/s	
2021-02-09 16:56:43	timer_1	Timer 1	Wait 5.00 s	
2021-02-09 16:56:43	FOF-SM1	FOF-SM1	Valve switched to direction 1-3	
2021-02-09 16:56:43	FOF-SM2	FOF-SM2	Valve switched to direction 1-3	
2021-02-09 16:56:43	FOF-SM3	FOF-SM3	Valve switched to direction 1-2	
2021-02-09 16:56:43	FOH-SM1	FOH-SM1	Valve switched to direction 2-3	
2021-02-09 16:56:43	FOH-SM2	FOH-SM2	Valve switched to direction 1-3	
2021-02-09 16:56:43	FOH-SM3	FOH-SM3	Valve switched to direction 1-3	
2021-02-09 16:56:44	GQY-HR	GQY-HR	normal mode, Wait 200 ms Tsp: 0 C	
2021-02-09 16:57:06	GQW-SY	GQW-SY	Syringe starts, volume: -10000 ul, speed: 450 ul/s	
2021-02-09 16:57:11	timer_1	Timer 1	Wait 5.00 s	
2021-02-09 16:57:11	FOF-SM1	FOF-SM1	Valve switched to direction 1-3	
2021-02-09 16:57:12	FOF-SM2	FOF-SM2	Valve switched to direction 1-3	
2021-02-09 16:57:12	FOF-SM3	FOF-SM3	Valve switched to direction 1-2	
2021-02-09 16:57:12	FOH-SM1	FOH-SM1	Valve switched to direction 2-3	
2021-02-09 16:57:12	FOH-SM2	FOH-SM2	Valve switched to direction 1-3	
2021-02-09 16:57:12	FOH-SM3	FOH-SM3	Valve switched to direction 1-3	
2021-02-09 16:57:12	GQY-HR	GQY-HR	normal mode, Wait 200 ms Tsp: 0 C	
2021-02-09 16:57:34	GQW-SY	GQW-SY	Syringe starts, volume: 10000 ul, speed: 450 ul/s	

Batch Report (cont.)

Timestamp	Object ID	Object Name	Process Step	Comment
2021-02-09 16:57:39	timer_1	Timer 1	Wait 5.00 s	
2021-02-09 16:57:40	FOF-SM1	FOF-SM1	Valve switched to direction 1-3	
2021-02-09 16:57:40	FOF-SM2	FOF-SM2	Valve switched to direction 1-3	
2021-02-09 16:57:40	FOF-SM3	FOF-SM3	Valve switched to direction 1-2	
2021-02-09 16:57:40	FOH-SM1	FOH-SM1	Valve switched to direction 2-3	
2021-02-09 16:57:40	FOH-SM2	FOH-SM2	Valve switched to direction 1-3	
2021-02-09 16:57:40	FOH-SM3	FOH-SM3	Valve switched to direction 1-3	
2021-02-09 16:57:40	GQY-HR	GQY-HR	normal mode, Wait 200 ms Tsp: 0 C	
2021-02-09 16:58:03	GQW-SY	GQW-SY	Syringe starts, volume: -10000 ul, speed: 450 ul/s	
2021-02-09 16:58:03	timer_1	Timer 1	Wait 0.00 s	
2021-02-09 16:58:03	FOF-SM1	FOF-SM1	Valve switched to direction 1-3	
2021-02-09 16:58:03	FOF-SM2	FOF-SM2	Valve switched to direction 1-3	
2021-02-09 16:58:03	FOF-SM3	FOF-SM3	Valve switched to direction 1-2	
2021-02-09 16:58:03	FOH-SM1	FOH-SM1	Valve switched to direction 2-3	
2021-02-09 16:58:03	FOH-SM2	FOH-SM2	Valve switched to direction 1-3	
2021-02-09 16:58:03	FOH-SM3	FOH-SM3	Valve switched to direction 1-3	
2021-02-09 16:58:03	GQY-HR	GQY-HR	normal mode, Wait 200 ms Tsp: 0 C	
2021-02-09 16:58:26	GQW-SY	GQW-SY	Syringe starts, volume: 10000 ul, speed: 450 ul/s	
2021-02-09 16:58:31	timer_1	Timer 1	Wait 5.00 s	
2021-02-09 16:58:31	FOF-SM1	FOF-SM1	Valve switched to direction 1-3	
2021-02-09 16:58:31	FOF-SM2	FOF-SM2	Valve switched to direction 1-3	
2021-02-09 16:58:31	FOF-SM3	FOF-SM3	Valve switched to direction 1-2	
2021-02-09 16:58:31	FOH-SM1	FOH-SM1	Valve switched to direction 2-3	
2021-02-09 16:58:31	FOH-SM2	FOH-SM2	Valve switched to direction 1-3	
2021-02-09 16:58:31	FOH-SM3	FOH-SM3	Valve switched to direction 1-3	
2021-02-09 16:58:31	GQY-HR	GQY-HR	normal mode, Wait 200 ms Tsp: 0 C	
2021-02-09 16:58:54	GQW-SY	GQW-SY	Syringe starts, volume: -10000 ul, speed: 450 ul/s	
2021-02-09 16:58:54	timer_1	Timer 1	Wait 0.00 s	
2021-02-09 16:58:54	FOF-SM1	FOF-SM1	Valve switched to direction 1-3	
2021-02-09 16:58:54	FOF-SM2	FOF-SM2	Valve switched to direction 1-3	
2021-02-09 16:58:54	FOF-SM3	FOF-SM3	Valve switched to direction 1-2	
2021-02-09 16:58:54	FOH-SM1	FOH-SM1	Valve switched to direction 2-3	
2021-02-09 16:58:54	FOH-SM2	FOH-SM2	Valve switched to direction 1-3	
2021-02-09 16:58:54	FOH-SM3	FOH-SM3	Valve switched to direction 1-3	
2021-02-09 16:58:54	GQY-HR	GQY-HR	normal mode, Wait 200 ms Tsp: 0 C	
2021-02-09 16:59:17	GQW-SY	GQW-SY	Syringe starts, volume: 10000 ul, speed: 450 ul/s	
2021-02-09 16:59:22	timer_1	Timer 1	Wait 5.00 s	
2021-02-09 16:59:22	FOF-SM1	FOF-SM1	Valve switched to direction 1-3	
2021-02-09 16:59:22	FOF-SM2	FOF-SM2	Valve switched to direction 1-3	
2021-02-09 16:59:22	FOF-SM3	FOF-SM3	Valve switched to direction 1-2	
2021-02-09 16:59:22	FOH-SM1	FOH-SM1	Valve switched to direction 2-3	
2021-02-09 16:59:22	FOH-SM2	FOH-SM2	Valve switched to direction 1-3	
2021-02-09 16:59:22	FOH-SM3	FOH-SM3	Valve switched to direction 1-3	
2021-02-09 16:59:23	GQY-HR	GQY-HR	normal mode, Wait 200 ms Tsp: 0 C	
2021-02-09 16:59:45	GQW-SY	GQW-SY	Syringe starts, volume: -10000 ul, speed: 450 ul/s	
2021-02-09 16:59:45	timer_1	Timer 1	Wait 0.00 s	
2021-02-09 16:59:45	PCtrl	Flow Control	Msg: put 8M HCl left?	
2021-02-09 16:59:46	Stop	Stop	Button switched from off to on	
2021-02-09 17:00:23	PCtrl	Flow Control	Msg was confirmed	
2021-02-09 17:00:23	Stop	Stop	Button switched from on to off	
2021-02-09 17:00:23	Set string	Set string	String: Comment1 = Load Oven 2nd (const.)	
2021-02-09 17:00:23	FOF-SM1	FOF-SM1	Valve switched to direction 2-3	
2021-02-09 17:00:24	FOF-SM2	FOF-SM2	Valve switched to direction 1-3	
2021-02-09 17:00:24	FOF-SM3	FOF-SM3	Valve switched to direction 1-2	
2021-02-09 17:00:24	FOH-SM1	FOH-SM1	Valve switched to direction 1-3	
2021-02-09 17:00:24	FOH-SM2	FOH-SM2	Valve switched to direction 1-3	
2021-02-09 17:00:24	FOH-SM3	FOH-SM3	Valve switched to direction 1-3	
2021-02-09 17:00:24	FOI-SM1	FOI-SM1	Valve switched to direction 1-3	
2021-02-09 17:00:24	GQY-HR	GQY-HR	normal mode, Wait 200 ms Tsp: 0 C	
2021-02-09 17:00:32	GQW-SY	GQW-SY	Syringe starts, volume: 3000 ul, speed: 450 ul/s	
2021-02-09 17:00:34	timer_1	Timer 1	Wait 2.00 s	
2021-02-09 17:00:34	FOF-SM1	FOF-SM1	Valve switched to direction 1-3	
2021-02-09 17:00:34	FOF-SM2	FOF-SM2	Valve switched to direction 1-3	
2021-02-09 17:00:34	FOF-SM3	FOF-SM3	Valve switched to direction 1-2	
2021-02-09 17:00:34	FOH-SM1	FOH-SM1	Valve switched to direction 2-3	

Batch Report (cont.)

Timestamp	Object ID	Object Name	Process Step	Comment
2021-02-09 17:00:34	FOH-SM2	FOH-SM2	Valve switched to direction 1-3	
2021-02-09 17:00:34	FOH-SM3	FOH-SM3	Valve switched to direction 1-3	
2021-02-09 17:00:34	GQY-HR	GQY-HR	normal mode, Wait 200 ms Tsp: 0 C	
2021-02-09 17:00:41	GQW-SY	GQW-SY	Syringe starts, volume: -3000 ul, speed: 450 ul/s	
2021-02-09 17:10:41	timer_1	Timer 1	Wait 600.00 s	
2021-02-09 17:10:41	FOF-SM1	FOF-SM1	Valve switched to direction 1-3	
2021-02-09 17:10:42	FOF-SM2	FOF-SM2	Valve switched to direction 1-3	
2021-02-09 17:10:42	FOF-SM3	FOF-SM3	Valve switched to direction 1-2	
2021-02-09 17:10:42	FOH-SM1	FOH-SM1	Valve switched to direction 2-3	
2021-02-09 17:10:42	FOH-SM2	FOH-SM2	Valve switched to direction 1-3	
2021-02-09 17:10:42	FOH-SM3	FOH-SM3	Valve switched to direction 1-3	
2021-02-09 17:10:42	GQY-HR	GQY-HR	normal mode, Wait 200 ms Tsp: 0 C	
2021-02-09 17:11:04	GQW-SY	GQW-SY	Syringe starts, volume: 10000 ul, speed: 450 ul/s	
2021-02-09 17:11:09	timer_1	Timer 1	Wait 5.00 s	
2021-02-09 17:11:09	FOF-SM1	FOF-SM1	Valve switched to direction 1-3	
2021-02-09 17:11:09	FOF-SM2	FOF-SM2	Valve switched to direction 1-3	
2021-02-09 17:11:10	FOF-SM3	FOF-SM3	Valve switched to direction 1-2	
2021-02-09 17:11:10	FOH-SM1	FOH-SM1	Valve switched to direction 2-3	
2021-02-09 17:11:10	FOH-SM2	FOH-SM2	Valve switched to direction 1-3	
2021-02-09 17:11:10	FOH-SM3	FOH-SM3	Valve switched to direction 1-3	
2021-02-09 17:11:10	GQY-HR	GQY-HR	normal mode, Wait 200 ms Tsp: 0 C	
2021-02-09 17:11:33	GQW-SY	GQW-SY	Syringe starts, volume: -10000 ul, speed: 450 ul/s	
2021-02-09 17:11:38	timer_1	Timer 1	Wait 5.00 s	
2021-02-09 17:11:38	FOF-SM1	FOF-SM1	Valve switched to direction 1-3	
2021-02-09 17:11:38	FOF-SM2	FOF-SM2	Valve switched to direction 1-3	
2021-02-09 17:11:38	FOF-SM3	FOF-SM3	Valve switched to direction 1-2	
2021-02-09 17:11:38	FOH-SM1	FOH-SM1	Valve switched to direction 2-3	
2021-02-09 17:11:38	FOH-SM2	FOH-SM2	Valve switched to direction 1-3	
2021-02-09 17:11:38	FOH-SM3	FOH-SM3	Valve switched to direction 1-3	
2021-02-09 17:11:38	GQY-HR	GQY-HR	normal mode, Wait 200 ms Tsp: 0 C	
2021-02-09 17:12:01	GQW-SY	GQW-SY	Syringe starts, volume: 10000 ul, speed: 450 ul/s	
2021-02-09 17:12:06	timer_1	Timer 1	Wait 5.00 s	
2021-02-09 17:12:06	FOF-SM1	FOF-SM1	Valve switched to direction 1-3	
2021-02-09 17:12:06	FOF-SM2	FOF-SM2	Valve switched to direction 1-3	
2021-02-09 17:12:06	FOF-SM3	FOF-SM3	Valve switched to direction 1-2	
2021-02-09 17:12:06	FOH-SM1	FOH-SM1	Valve switched to direction 2-3	
2021-02-09 17:12:06	FOH-SM2	FOH-SM2	Valve switched to direction 1-3	
2021-02-09 17:12:06	FOH-SM3	FOH-SM3	Valve switched to direction 1-3	
2021-02-09 17:12:07	GQY-HR	GQY-HR	normal mode, Wait 200 ms Tsp: 0 C	
2021-02-09 17:12:29	GQW-SY	GQW-SY	Syringe starts, volume: -10000 ul, speed: 450 ul/s	
2021-02-09 17:12:29	timer_1	Timer 1	Wait 0.00 s	
2021-02-09 17:12:29	FOF-SM1	FOF-SM1	Valve switched to direction 1-3	
2021-02-09 17:12:29	FOF-SM2	FOF-SM2	Valve switched to direction 1-3	
2021-02-09 17:12:29	FOF-SM3	FOF-SM3	Valve switched to direction 1-2	
2021-02-09 17:12:29	FOH-SM1	FOH-SM1	Valve switched to direction 2-3	
2021-02-09 17:12:29	FOH-SM2	FOH-SM2	Valve switched to direction 1-3	
2021-02-09 17:12:29	FOH-SM3	FOH-SM3	Valve switched to direction 1-3	
2021-02-09 17:12:30	GQY-HR	GQY-HR	normal mode, Wait 200 ms Tsp: 0 C	
2021-02-09 17:12:53	GQW-SY	GQW-SY	Syringe starts, volume: 10000 ul, speed: 450 ul/s	
2021-02-09 17:12:58	timer_1	Timer 1	Wait 5.00 s	
2021-02-09 17:12:58	FOF-SM1	FOF-SM1	Valve switched to direction 1-3	
2021-02-09 17:12:58	FOF-SM2	FOF-SM2	Valve switched to direction 1-3	
2021-02-09 17:12:58	FOF-SM3	FOF-SM3	Valve switched to direction 1-2	
2021-02-09 17:12:58	FOH-SM1	FOH-SM1	Valve switched to direction 2-3	
2021-02-09 17:12:58	FOH-SM2	FOH-SM2	Valve switched to direction 1-3	
2021-02-09 17:12:58	FOH-SM3	FOH-SM3	Valve switched to direction 1-3	
2021-02-09 17:12:58	GQY-HR	GQY-HR	normal mode, Wait 200 ms Tsp: 0 C	
2021-02-09 17:13:21	GQW-SY	GQW-SY	Syringe starts, volume: -10000 ul, speed: 450 ul/s	
2021-02-09 17:13:21	timer_1	Timer 1	Wait 0.00 s	
2021-02-09 17:13:21	FOF-SM1	FOF-SM1	Valve switched to direction 1-3	
2021-02-09 17:13:21	FOF-SM2	FOF-SM2	Valve switched to direction 1-3	
2021-02-09 17:13:21	FOF-SM3	FOF-SM3	Valve switched to direction 1-2	
2021-02-09 17:13:21	FOH-SM1	FOH-SM1	Valve switched to direction 2-3	
2021-02-09 17:13:21	FOH-SM2	FOH-SM2	Valve switched to direction 1-3	
2021-02-09 17:13:21	FOH-SM3	FOH-SM3	Valve switched to direction 1-3	

Batch Report (cont.)

Timestamp	Object ID	Object Name	Process Step	Comment
2021-02-09 17:13:21	GQY-HR	GQY-HR	normal mode, Wait 200 ms Tsp: 0 C	
2021-02-09 17:13:44	GQW-SY	GQW-SY	Syringe starts, volume: 10000 ul, speed: 450 ul/s	
2021-02-09 17:13:49	timer_1	Timer 1	Wait 5.00 s	
2021-02-09 17:13:49	FOF-SM1	FOF-SM1	Valve switched to direction 1-3	
2021-02-09 17:13:49	FOF-SM2	FOF-SM2	Valve switched to direction 1-3	
2021-02-09 17:13:49	FOF-SM3	FOF-SM3	Valve switched to direction 1-2	
2021-02-09 17:13:49	FOH-SM1	FOH-SM1	Valve switched to direction 2-3	
2021-02-09 17:13:49	FOH-SM2	FOH-SM2	Valve switched to direction 1-3	
2021-02-09 17:13:49	FOH-SM3	FOH-SM3	Valve switched to direction 1-3	
2021-02-09 17:13:50	GQY-HR	GQY-HR	normal mode, Wait 200 ms Tsp: 0 C	
2021-02-09 17:14:12	GQW-SY	GQW-SY	Syringe starts, volume: -10000 ul, speed: 450 ul/s	
2021-02-09 17:14:12	timer_1	Timer 1	Wait 0.00 s	
2021-02-09 17:14:12	Set string	Set string	String: Comment1 = Load Column (const.)	
2021-02-09 17:14:12	FOF-SM1	FOF-SM1	Valve switched to direction 1-3	
2021-02-09 17:14:12	FOF-SM2	FOF-SM2	Valve switched to direction 1-3	
2021-02-09 17:14:12	FOF-SM3	FOF-SM3	Valve switched to direction 1-2	
2021-02-09 17:14:12	FOH-SM1	FOH-SM1	Valve switched to direction 2-3	
2021-02-09 17:14:12	FOH-SM2	FOH-SM2	Valve switched to direction 1-3	
2021-02-09 17:14:12	FOH-SM3	FOH-SM3	Valve switched to direction 1-3	
2021-02-09 17:14:13	GQY-HR	GQY-HR	normal mode, Wait 200 ms Tsp: 0 C	
2021-02-09 17:14:47	GQW-SY	GQW-SY	Syringe starts, volume: 10000 ul, speed: 300 ul/s	
2021-02-09 17:14:57	timer_1	Timer 1	Wait 10.00 s	
2021-02-09 17:14:57	FOF-SM1	FOF-SM1	Valve switched to direction 1-3	
2021-02-09 17:14:57	FOF-SM2	FOF-SM2	Valve switched to direction 1-3	
2021-02-09 17:14:57	FOF-SM3	FOF-SM3	Valve switched to direction 2-3	
2021-02-09 17:14:57	FOG-SM1	FOG-SM1	Valve switched to direction 1-2	
2021-02-09 17:14:57	FOG-SM2	FOG-SM2	Valve switched to direction 2-3	
2021-02-09 17:14:57	FOG-SM3	FOG-SM3	Valve switched to direction 1-3	
2021-02-09 17:14:57	FOH-SM1	FOH-SM1	Valve switched to direction 1-3	
2021-02-09 17:14:57	FOH-SM2	FOH-SM2	Valve switched to direction 1-3	
2021-02-09 17:14:57	FOH-SM3	FOH-SM3	Valve switched to direction 1-3	
2021-02-09 17:14:57	FOI-SM1	FOI-SM1	Valve switched to direction 1-3	
2021-02-09 17:14:57	FOI-SM2	FOI-SM2	Valve switched to direction 1-3	
2021-02-09 17:14:57	FOI-SM3	FOI-SM3	Valve switched to direction 1-2	
2021-02-09 17:14:57	GQY-HR	GQY-HR	normal mode, Wait 200 ms Tsp: 0 C	
2021-02-09 17:20:11	GQW-SY	GQW-SY	Syringe starts, volume: -10000 ul, speed: 32 ul/s	
2021-02-09 17:20:16	timer_1	Timer 1	Wait 5.00 s	
2021-02-09 17:20:36	timer_1	Timer 1	Wait 20.00 s	
2021-02-09 17:20:36	PCtrl	Flow Control	Msg: put NaCl solution right?	
2021-02-09 17:20:36	Stop	Stop	Button switched from off to on	
2021-02-09 17:20:46	PCtrl	Flow Control	Msg was confirmed	
2021-02-09 17:20:46	Stop	Stop	Button switched from on to off	
2021-02-09 17:20:46	FOF-SM1	FOF-SM1	Valve switched to direction 1-3	
2021-02-09 17:20:46	FOF-SM2	FOF-SM2	Valve switched to direction 2-3	
2021-02-09 17:20:46	FOF-SM3	FOF-SM3	Valve switched to direction 1-2	
2021-02-09 17:21:07	GQW-SY	GQW-SY	Syringe starts, volume: 4000 ul, speed: 200 ul/s	
2021-02-09 17:21:11	Stop	Stop	Button switched from off to on	
2021-02-09 17:23:48	timer_1	Timer 1	Wait 5.00 s	
2021-02-09 17:23:48	FOF-SM1	FOF-SM1	Valve switched to direction 1-3	
2021-02-09 17:23:48	FOF-SM2	FOF-SM2	Valve switched to direction 1-3	
2021-02-09 17:23:48	FOF-SM3	FOF-SM3	Valve switched to direction 2-3	
2021-02-09 17:23:48	Stop	Stop	Button switched from on to off	
2021-02-09 17:23:48	FOG-SM1	FOG-SM1	Valve switched to direction 1-2	
2021-02-09 17:23:49	FOG-SM2	FOG-SM2	Valve switched to direction 2-3	
2021-02-09 17:23:49	FOG-SM3	FOG-SM3	Valve switched to direction 1-3	
2021-02-09 17:23:49	FOH-SM1	FOH-SM1	Valve switched to direction 1-3	
2021-02-09 17:23:49	FOH-SM2	FOH-SM2	Valve switched to direction 1-3	
2021-02-09 17:23:49	FOH-SM3	FOH-SM3	Valve switched to direction 1-3	
2021-02-09 17:23:49	FOI-SM1	FOI-SM1	Valve switched to direction 1-3	
2021-02-09 17:23:49	FOI-SM2	FOI-SM2	Valve switched to direction 1-3	
2021-02-09 17:23:49	FOI-SM3	FOI-SM3	Valve switched to direction 1-2	
2021-02-09 17:23:49	GQY-HR	GQY-HR	normal mode, Wait 200 ms Tsp: 0 C	
2021-02-09 17:25:56	PCTRLHMI	PCTRLHMI	The running process breaks, because of an error	Error
2021-02-09 17:25:57	Stop	Stop	Button switched from off to on	
2021-02-09 17:27:30	Stop	Stop	Button switched from on to off	

Batch Report (cont.)

Charts:

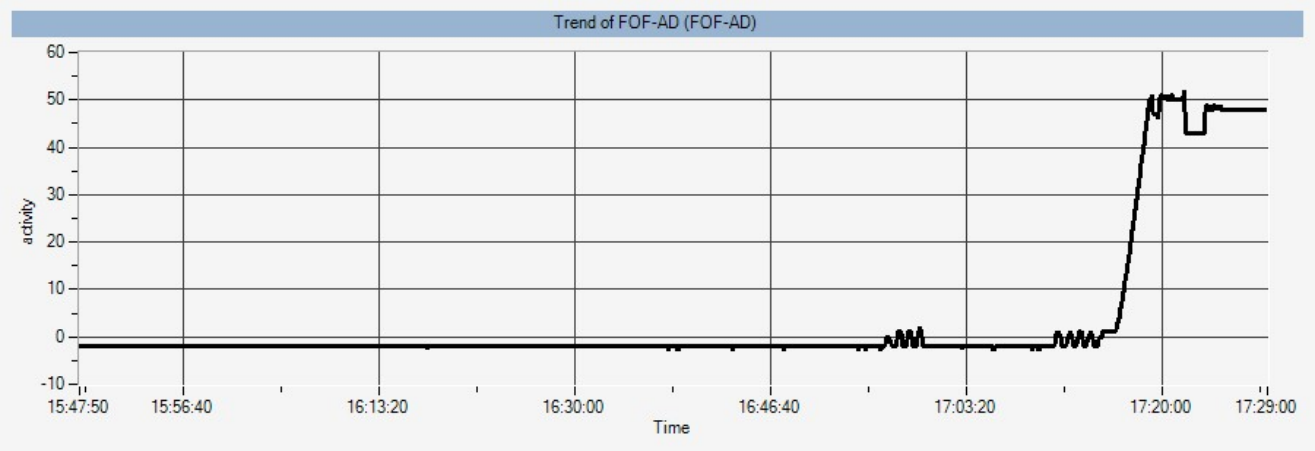

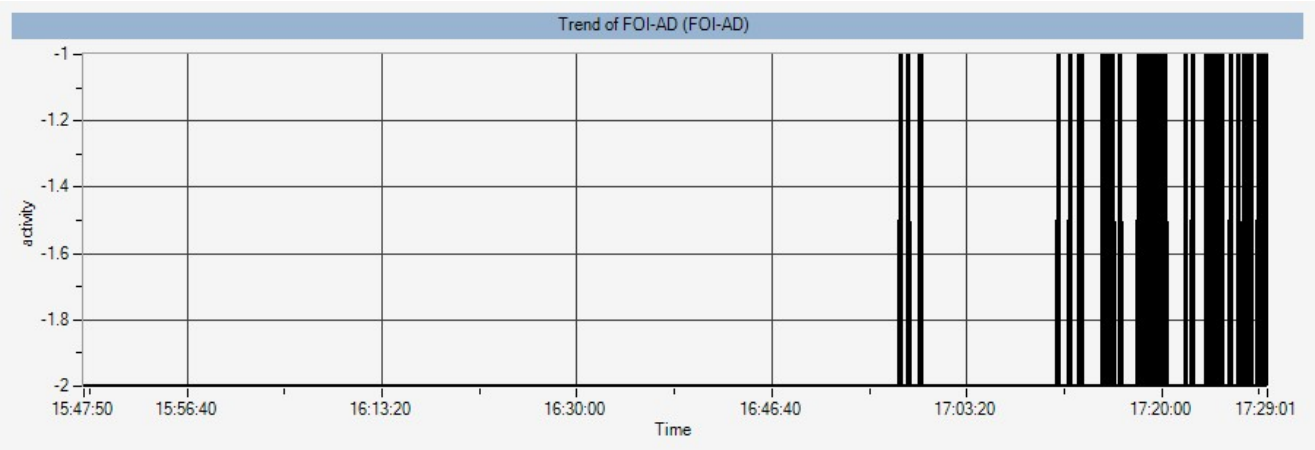

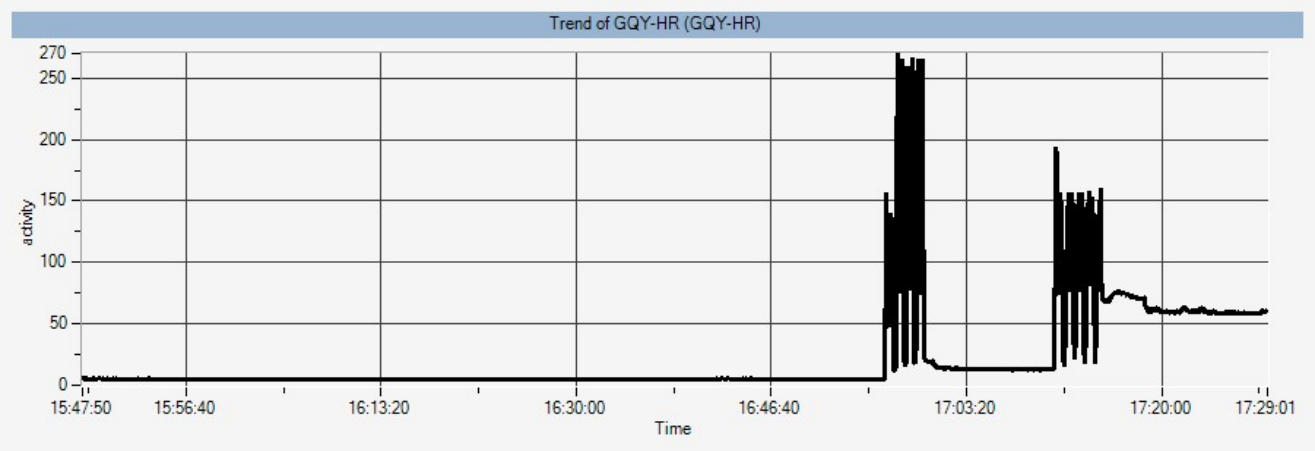

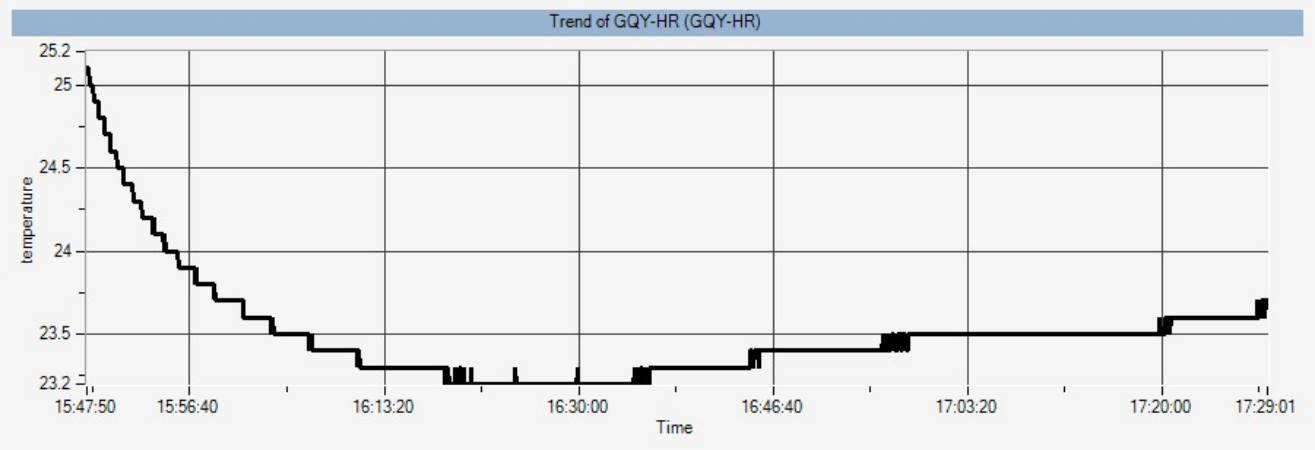

Batch Report (cont.)

Errors and messages:

Functionbloc	Object Name	Kind	Error Description	Timestamp	Detected at / by	Quitted at / by
SYRINGEHM	GQW-SY	Error	Position error	2021-02-09 17:25:56	00:00:00 by none	00:00:00 by none

Appendix B

Radioactivity

Radioactivity is a process that occurs when an unstable atomic nucleus loses energy by emitting energy in the form of emitted particles of ionizing radiation or electromagnetic waves, called radiation. With the passage of time, the number of parent nuclei remaining decreases (due to nuclear disintegrations). Radioactivity, or simply activity (A), can be defined as the number of disintegrations per second (dps) of a given sample of a radionuclide [164]. The unit of radioactivity is the Becquerel (1 Bq=1 dps) or Curie (Ci) (1 mCi=37 MBq, 1 Ci is the activity of 1g ^{226}Ra) .

The number of decay events (−*dN*), that is expected to occur in a small interval of time (*dt*), is proportional to the number of atoms present *N*:

$$-\frac{dN}{N} = \lambda dt,$$

where λ is decay constant and is the inverse of the lifetime.

$t_{1/2} = \frac{\ln 2}{\lambda}$.

The solution to this first-order differential equation is the function:

$N = N_0\ e^{-\lambda t}$,

where N_0 is the number of atoms at time $t = 0$.

Specific activity

Specific activity is the activity per quantity of a radionuclide and the units are Bq/mg or Ci/mg.